Universität Rostock
Traditio et Innovatio

Faculty of Mechanical Engineering and Marine Technology
Chair of Mechatronics

DISSERTATION

Advanced Control Designs for Output Tracking of Hydrostatic Transmissions

Ngoc Danh Dang
2021

https://doi.org/10.18453/rosdok_id00003429

Advanced Control Designs for Output Tracking of Hydrostatic Transmissions

Dissertation

zur
Erlangung des akademischen Grades

Doktor-Ingenieur (Dr.-Ing.)

der Fakultät für Maschinenbau und Schiffstechnik
an der Universität Rostock

vorgelegt von
M. Sc. Ngoc Danh Dang
geb. am 05.12.1982 in Nghe An, Vietnam

Gutachter:

Prof. Dr.-Ing. Harald Aschemann
Lehrstuhl für Mechatronik
Universität Rostock

Prof. Dr.-Ing. Paolo Mercorelli
Institut für Produkt- und Prozessinnovation
Leuphana Universität Lüneburg

Tag der Verteidigung: 19. November 2021

Lehrstuhl für Mechatronik der Universität Rostock
2021

Acknowledgements

This dissertation is my achievement after a five-year research program at the Chair of Mechatronics at the Faculty of Mechanical Engineering and Marine Technology at the University of Rostock, Germany. This research program was partly sponsored by Vietnam Ministry of Education and Training upon the recommendation of Vietnam National University of Agriculture.

Throughout the research process, I have made a huge effort on my own to reach this final result. However, as we all know, a completed study could not be done without any assistance. For the personal and scientific support I have received, I would like to mention my supervisor, Professor Dr.-Ing. Harald Aschemann – Head of the Chair of Mechatronics. He is serious but friendly, careful but enthusiastic. His dynamism, vision, sincerity and motivation have deeply inspired me. He has provided me a valuable scientific guidance. He has taught me the methods to carry out and to present the research works as clearly as possible. Especially, I am extremely grateful for the invaluable support he has offered me in the hard time of the Covid-19 pandemic that gives me the opportunity to complete the research program. Thereby, I would like to express my deep and sincere gratitude to him.

I would like to thank Prof. Paolo Mercorelli – Leuphana University of Lüneburg – for his interest in my work and the second review.

I also extend my thanks to the secretary staffs, who helped me a lot with the paperwork, and to all other research members in the Chair of Mechatronics for their sincerely and friendly interactions.

Finally, this achievement is dedicated to all members in my great family.

Rostock, November 2021

Ngoc Danh Dang

Abstract

Hydrostatic transmissions, in comparison to conventional mechanical transmission systems, expose many advantages. They provide continuously variable transmission ratios, high power density, low inertia, efficient operation in a wide range of torque-to-speed ratios and they can serve as a dynamic braking system. The spatial arrangement of a hydrostatic transmission is very flexible also, the power can be transmitted from a single prime mover to several load locations, even in the cases where the position and orientation of the load units change. In industrial applications, hydrostatic transmission systems are widely used in specialized working vehicles such as construction, agriculture, excavation machinery and off-road vehicles where high drive torques are required. In other transport vehicles, passenger cars for instance, the applications of hydrostatic transmissions are less common. Recently, in the trend of emission reduction and environment-friendly applications, the hydrostatic transmissions gain more and more contribution in high-performance transport vehicles with the invention of power-split gearboxes, energy recovery systems in hybrid drive trains and also in green energy systems such as ocean energy systems and wind turbines, etc.

The limitation of hydrostatic transmissions in high-performance applications is caused by the energy efficiency and control issues. From a control point of view, they are characterized by high nonlinearity, disturbance and physical parameter uncertainty caused by many operational and structural aspects such as fluid viscosity, temperature variation, leakage oil flow and the elasticity of the connecting hoses, etc. Currently, PID (proportional-integral-derivative) controllers are still predominant in HST applications but their performance, however, is not sufficient to attain an accurate control result in the wide range of HST operation. Therefore, advanced control approaches become more favorable.

In the last decade, many nonlinear control approaches have been proposed, those are diverse in terms of control strategy, control objective and design principle. Based on the existing control techniques that have been proposed generally for uncertain nonlinear systems, the work in this dissertation focuses on the design and the validation of advanced control approaches for the output tracking of HST systems.

Taking the practical considerations as a guideline, the work addresses simple but efficient model descriptions in a combination with advanced control and estimation approaches to achieve an accurate tracking of the desired trajectories. The proposed control designs are capable of fully exploiting the wide operation range of HSTs within the system configuration limits. The dissertation develops a new trajectory planning scheme for the output tracking of HST systems that efficiently and simultaneously uses both the primary and secondary control inputs. Based on this control scheme, simple design models or even purely data-driven models are envisaged and deployed to develop and investigate several advanced control approaches for HST systems: optimal control, estimator-based feedback linearization control, active disturbance rejection control and model-free control approaches. The use of tracking differentiators – which can be interpreted as a model-free way to determine time derivatives of noise-afflicted measurements and substitute classical state transformations corresponding to a classical model-based approach – is investigated in many of the mentioned control structures. Thereby, a practical view on the applicability of such technical measures for effective and robust control designs on HST systems is provided. Successful study results are obtained by means of both simulations and experiments on a real test rig of the hydrostatic transmission – which is built for validation tests at the Chair of Mechatronics, University of Rostock.

Zusammenfassung

Hydrostatische Getriebe bieten im Vergleich zu herkömmlichen mechanischen Getrieben viele Vorteile. Sie ermöglichen stufenlos verstellbare Übersetzungsverhältnisse, eine hohe Leistungsdichte, ein geringes Trägheitsmoment, einen effizienten Betrieb in einem weiten Bereich von Drehmoment-Drehzahl-Verhältnissen, und sie können als dynamisches Bremssystem dienen. Die räumliche Anordnung eines hydrostatischen Getriebes ist ebenfalls sehr flexibel, die Leistung kann von einer einzigen Antriebsmaschine auf mehrere Laststellen übertragen werden, auch wenn sich die Position und Ausrichtung der Lasteinheiten ändert. In der Industrie werden die hydrostatische Getriebesysteme häufig in speziellen Arbeitsfahrzeugen wie Bau-, Landwirtschafts-, Bagger- und Geländefahrzeugen eingesetzt, die hohe Antriebsmomente erfordern. In anderen Transportfahrzeugen, z.B. in Personenkraftwagen, ist der Einsatz hydrostatischer Getriebe weniger verbreitet. In jüngster Zeit gewinnen hydrostatische Getriebe im Zuge des Trends zur Emissionsreduzierung für leistungsstarke Transportfahrzeuge und umweltfreundlichen Anwendungen mit der Entwicklung von leistungsverzweigten Getrieben, Energierückgewinnungssystemen in Hybridantriebssträngen und auch in umweltfreundlichen Energiesystemen wie Meeresenergiesystemen und Windturbinen immer mehr an Bedeutung.

Die Grenzen des hydrostatischen Getriebes in Hochleistungsanwendungen liegen in der Energieeffizienz und der Regelung. Aus regelungstechnischer Sicht sind sie durch hohe Nichtlinearität, Störungen und Unsicherheiten der physikalischen Parameter gekennzeichnet, die durch zahlreiche betriebliche und strukturelle Aspekte wie Flüssigkeitsviskosität, Temperaturschwankungen, Leckölströme und Elastizitäten der Verbindungsschläuche usw. verursacht werden. Gegenwärtig sind PID-Regler (proportional-integral-differenzierend) in HST-Anwendungen immer noch vorherrschend, aber ihr Leistungsvermögen reicht nicht aus, um in dem weiten Bereich des HST-Betriebs ein genaues Regelungsverhalten zu erzielen. Daher werden fortschrittliche Regelungsansätze immer bedeutender.

Im letzten Jahrzehnt wurden viele nichtlineare Regelungsansätze vorgeschlagen, die sich in Bezug auf Regelungsstrategie, Regelungsziel und Entwurfsprinzip unterscheiden. Basierend auf den bestehenden Entwurfstechniken, die im Allg. für unsichere nichtlineare Systeme vorgeschlagen wurden, konzentriert sich diese Dissertation auf den Entwurf und die Validierung von fortgeschrittenen Regelungsansätzen für die Ausgangsfolgeregelung von HST-Systemen.

Unter Berücksichtigung praktischer Erwägungen werden in dieser Arbeit einfache, aber effiziente Modellbeschreibungen in Kombination mit fortschrittlichen Regelungs- und Schätzmethoden verwendet, um eine genaue Verfolgung der gewünschten Trajektorien zu erreichen. Die vorgeschlagenen Regelungskonzepte sind in der Lage, den weiten Betriebsbereich von HSTs innerhalb der Grenzen der Systemkonfiguration voll auszunutzen. In der Dissertation wird ein neues Schema für die Trajektorienplanung für die Ausgangsfolge von HST-Systemen entwickelt, das sowohl die primären als auch die sekundären Steuereingänge effizient und gleichzeitig nutzt. Auf der Grundlage dieses Strukturierung werden einfache Entwurfsmodelle oder sogar rein datengetriebene Modelle in Betracht gezogen und eingesetzt, um mehrere fortschrittliche Regelungsansätze für HST-Systeme zu entwickeln und zu untersuchen: optimale Regelung, schätzungsbasierte Linearisierungsverfahren im Rückführzweig, aktive Störungsunterdrückung und modellfreie Regelungsansätze. Die Verwendung von Tracking-Differenzierern – die als modellfreier Weg zur Bestimmung von Zeitableitungen störungsbehafteter Messungen interpretiert werden können und klassische Zustandstransformationen, die einem klassischen modellbasierten Ansatz entsprechen, ersetzen – wird in vielen der genannten Regelungsstrukturen untersucht. Dadurch wird ein praktischer Blick auf die Anwendbarkeit solcher technischer Maßnahmen für

effektive und robuste Regelungsentwürfe auf HST-Systemen ermöglicht. Erfolgreiche Untersuchungsergebnisse werden sowohl mittels Simulationen als auch durch Experimente an einem realen Prüfstand des hydrostatischen Getriebes – der für Validierungstests am Lehrstuhl für Mechatronik der Universität Rostock aufgebaut ist – erzielt.

Contents

List of Figures

List of Tables

Abbreviations

ADR	Active disturbance rejection
AFC	Adaptive feedforward compensation
APE	Adaptive parameter estimation
CMAC	Cerebellar model articulation controller
DARE	Discrete algebraic Riccati equation
DLQR	Discrete linear quadratic regulator
ESO	Extended state observer
FBO	Takagi-Sugeno Fuzzy-based optimal control
FEL	Feedback error learning
Fig.	Figure
GPI	Generalized-proportional-integral
HJB	Hamilton-Jacobi-Bellman
HST	Hydrostatic transmission
iPD	Intelligent proportional-derivative control
LQR	Linear quadratic regulator
LTD	Linear tracking differentiator
LTD2	Second-order linear tracking differentiator
LTD3	Third-order linear tracking differentiator
LTD4	Fourth-order linear tracking differentiator
LMI	Linear matrix inequality
MIMO	Multiple input-multiple output
MISO	Multiple input-single output
MLP	Multiple layer perceptron network
MPC	Model predictive control
NMPC	Nonlinear model predictive control
P	Proportional control
PD	Proportional-derivative control
PI	Proportional-integral control
PID	Proportional-integral-derivative control
RDO	Reduced-order state and disturbance observer
RBF	Radial basic function
RMS	Root mean square
SDRE	State-dependent Riccati equation
SIF	State-dependent integral feedback control
SISO	Single input-single output
SMC	Sliding mode control
Tab.	Table
TD	Tracking differentiator
UKF	Unscented Kalman filter
w.r.t.	with respect to

List of Symbols

The list is split into parts according to the structure of the content. Note that supplementary, intermediate, and auxiliary variables are not explicitly listed, but specified at the place of their first usage.

Modeling and Trajectory Planning for the HST System

Mathematical Model of the HST system

q_P	Hydraulic pump flow rate
q_M	Hydraulic motor flow rate
ω_P	Hydraulic pump angular velocity
ω_M	Hydraulic motor angular velocity
V_P	Volumetric displacement of hydraulic pump
V_M	Volumetric displacement of hydraulic motor
$\tilde{V}_P$	Maximal volumetric displacement of hydraulic pump
$\tilde{V}_M$	Maximal volumetric displacement of hydraulic motor
α_P	Swash-plate angle of hydraulic pump
$\alpha_{P,max}$	Maximal swash-plate angle of hydraulic pump
$\tilde{\alpha}_P$	Normalized swash-plate angle of hydraulic pump
α_M	Bent-axis angle of hydraulic motor
$\alpha_{M,max}$	Maximal bent-axis angle of hydraulic motor
$\tilde{\alpha}_M$	Normalized bent-axis angle of hydraulic motor
ϵ_M	Lower bound of hydraulic motor bent-axis angle
A_P	Effective piston area of hydraulic pump
D_P	Piston circle diameter of hydraulic pump
N_P	Number of piston in hydraulic pump displacement unit
A_M	Effective piston area of hydraulic motor
D_M	Piston circle diameter of hydraulic motor
N_M	Number of piston in hydraulic motor displacement unit
Δp	Difference pressure in the hydraulic circuit
q_U	Lumped leakage flow disturbance
τ_U	Lumped torque disturbance
T_{uP}	Time constant of hydraulic pump actuator
T_{uM}	Time constant of hydraulic motor actuator
k_P	Proportional gain of hydraulic pump actuator
k_M	Proportional gain of hydraulic motor actuator
u_P	Analog control signal of hydraulic pump
u_M	Analog control signal of hydraulic motor
J_V	Mass moment of inertial at hydraulic motor shaft

d_V	Damping coefficient at hydraulic motor shaft
$\tilde{\alpha}_{Md}$	Desired trajectory of motor bent-axis angle
ω_{Md}	Desired trajectory of motor angular velocity
$\omega_{Md,max}$	Maximal desired value of motor angular velocity
ω_{max}	Physically-limited value of motor angular velocity
a	User-defined threshold for motor displacement activation
b	Limit parameter for desired trajectory design

Advanced Output Control Designs

Optimization-Based Approaches

Model Predictive Control

N	Number of point in prediction horizon
J	Cost function
w_j	Weighting scalars, $j = \{1, 2, 3, 4\}$
k	Time index
p	Design parameter
$\mathbf{x}$	Full system state vector
$\tilde{\Upsilon}$	Lyapunov function candidate
$\mathbf{f}$	System dynamics vector function
$\mathbf{C}_m$	Output matrix
$\mathbf{x}_e$	Extended system state vector
Ψ	Extended system dynamics vector function
α, κ, β	Design parameters
$\hat{\mathbf{x}}_e$	Estimate of extended system state vector
$\mathbf{Q}_K$	Process noise covariance matrix
$\mathbf{R}_K$	Measurement noise covariance matrix
$\mathbf{K}_K$	Kalman gain matrix
$\mathbf{L}_x$	State covariance matrix
$\tilde{\mathbf{L}}_x$	Error covariance matrix
$\tilde{\mathbf{L}}_y$	Measurement error covariance matrix
$\mathbf{L}_{xy}$	Cross-covariance matrix
τ_h	Motor hydraulic torque
τ_{hd}	Desired value of hydraulic torque

Takagi-Sugeno Fuzzy-Based Optimal Control Design for Torque Tracking Control

$y_\tau = \tau_h$	Output torque
$\mathbf{x}_\tau$	Torque-controlled system state vector
v	Lump disturbance input
$\mathbf{A}$	Quasi-linear system matrix
$\mathbf{b}$	Input matrix
$\mathbf{d}$	Disturbance input matrix
$\mathbf{c}$	Output matrix

$\mathbf{A}_{d,1}, \mathbf{A}_{d,2}$	Discretized vertex system matrices
$\mathbf{b}_d$	Discretized input matrix
$\mathbf{d}_d$	Discretized disturbance input matrix
$\mathbf{K}_C$	Kalman controllability criterion matrix
$\mathbf{A}_1, \mathbf{A}_2$	Vertex system matrices
h_1, h_2	Weighting functions
$\mathbf{S}_1, \mathbf{S}_2$	DARE solutions matrices
$\mathbf{A}_{c,1}, \mathbf{A}_{c,2}$	Vertex closed-loop system matrices
$\mathbf{A}_c$	Closed-loop system matrix
$\mathbf{k}_1, \mathbf{k}_2$	Vertex optimal feedback gain vectors
$\mathbf{k}$	Optimal feedback gain vector
$\mathbf{P}_L$	Common Lyapunov function
J_τ	Quadratic cost function
$\mathbf{Q}$	State weighting matrix
r	Control input weighting scalar
T_s	Sampling time
$k_{F,0}, k_{F,1}, k_{F,2}$	Feedforward gains
$k_{D,0}, k_{D,1}$	Disturbance compensation gains
z	z-transform variable
$y_{\tau,d} = \tau_{hd}$	Desired value of output torque
a_M	System matrix of motor dynamics
b_M	Input vector of motor dynamics system
a_{dM}	Discretized system matrix of motor dynamics
b_{dM}	Discretized input vector of motor dynamics system
k_M	Optimal feedback gain of motor control
b_M	Input vector of motor dynamics system
$k_{MF,0}, k_{MF,1}$	Feedforward gains of motor control

State-Dependent Integral State Feedback Control

$\bar{\mathbf{x}}$	Augmented state vector
$\bar{\mathbf{A}}$	Augmented system matrix
$\bar{\mathbf{b}}$	Augmented input matrix
$\bar{\mathbf{e}}$	Reference input matrix
$\bar{\mathbf{c}}$	Augmented output matrix
w_τ	Integral state
$\bar{\mathbf{K}}_C$	Kalman controllability matrix
$\bar{\mathbf{A}}_d$	Discretized augmented system matrix
$\bar{\mathbf{b}}_d$	Discretized augmented input matrix
$\bar{\mathbf{k}}$	State-dependent feedback gain vector
$\bar{\mathbf{Q}}$	Weighting matrix of augmented state vector
$\bar{r}$	Weighting scalar of feedback control input
u_{SFB}	Feedback control input
$\bar{J}_\tau$	Quadratic cost function
$\bar{\mathbf{S}}$	SDRE solution matrix
$\bar{\mathbf{A}}_c$	Close loop system matrix
$\bar{\mathbf{A}}_{d,i}$	Vertex discretized system matrices, $i = \{1, 2, 3, 4\}$

$\bar{\mathbf{A}}_{c,i}$	Vertex close loop system matrices, $i = \{1, 2, 3, 4\}$
$\bar{\mathbf{k}}_i$	Vertex system feedback gain vectors, $i = \{1, 2, 3, 4\}$
$\bar{\mathbf{P}}_L$	Common Lyapunov function matrix
$\tilde{\mathbf{A}}_c$	State feedback close loop system matrix
$k_{V,0}, k_{V,1}$	State-dependent disturbance compensation gains
u_{SDC}	Disturbance compensation control input
J_e	Quadratic cost function for observer design
$\mathbf{K}_e$	Kalman observability criterion matrix
$\mathbf{Q}_e$	Weighting matrix of estimation error
$\mathbf{R}_e$	Weighting matrix of measurement error
$\mathbf{A}_{ed}$	Discretized extended system matrix
$\mathbf{B}_{ed}$	Discretized extended system matrix
$\mathbf{S}_e$	SDRE solution for observer design
$\mathbf{H}_e$	State-dependent observer gain matrix
$\mathbf{H}_{e,i}$	Vertex observer gain matrix, $i = \{1, ..., 8\}$
$\mathbf{O}_{e,i}$	Vertex observer system matrix, $i = \{1, ..., 8\}$
$\mathbf{P}_e$	Common Lyapunov function matrix

Estimator-Based Feedback Linearization

ς_i	State variables of tracking differentiator $i = 1, 2, ..., n$
$c_{\varsigma n,i}$	Tracking differentiator coefficients ,$i = 1, 2, ...n$
$R_{\varsigma n}$	Tuning parameter for tracking differentiator
r_x	Tracked signal
$\mathbf{y}$	System state vector
V	Lyapunov function candidate
λ_0, λ_1, k	Feedback-linearized control parameters
e	Tracking error
f	Nonlinearity function
$c_{\varsigma 3,i}$	LTD3 coefficients ,$i = 1, 2, 3$
$R_{\varsigma 3}$	Tuning parameter for LTD3

Nonlinearity Compensation Using a State and Disturbance Observer

$\hat{\mathbf{q}}$	Estimated state vector of RDO
$\mathbf{p}$	Internal state vector of RDO
$\mathbf{H}$	Observer gain matrix of RDO
$\mathbf{y}_m$	Measurement vector
$\mathbf{u}$	Control input vector
ξ	Estimation error vector of RDO
Φ	Nonlinear function of RDO
$\mathbf{J}_\xi$	Jacobian matrix of estimation error dynamics of RDO
$\mathbf{f}_1, \mathbf{f}_2$	System dynamics vector functions
$\mathbf{I}$	Identity matrix
$k_{\alpha M}$	Feedback gain of hydraulic motor control

Nonlinearity Compensation by Adaptive Parameter Estimation

s	Laplace domain variable
$\bar{f}$	Alternative presentation of nonlinearity function in adaptive control
$\bar{k}$	Adaptive control design parameter
$\hat{a}_1$	Adaptive parameters, $i = \{0, 1, 2, 3, 4\}$
γ_i	Adaptation rate for parameter estimation, $i = \{0, 1, 2, 3, 4\}$
$y_d = \omega_{Md}$	Desired value of angular velocity

Nonlinearity Compensation by a Neural Network

F_N	Output function of neural network
$\tilde{k}$	Feedback control design parameter
$\tilde{f}$	Alternative presentation of nonlinearity function in neural feedback control
$\mathbf{w}$	Neural network output weight vector
$\mathbf{V}$	Neural network hidden-layer weight matrix
σ	Neural network activation function
$M_w, \boldsymbol{M}_v, \kappa, \kappa_r$	Neural network tuning parameter
Θ	Augmented weighting matrix of neural network
θ	Bound of augmented weighting matrix norm
Q	Norm bound of desired trajectory
u_δ	Robust term of neural network control
$\mathbf{x}_N$	Neural network synapsis input vector

Active Disturbance Rejection Approaches

Observer-Based ADR Control Design

ζ	Estimation errors of ESO
$\hat{y}$	System states estimated by ESO
χ_1, χ_2	Extended states of ESO
$\tilde{F}$	Total disturbance in ADR control
l_i	Gains of ESO, $i = \{0, 1, 2, 3, 4\}$
α_i	Feedback gains of ADR control, $i = \{0, 1, 2\}$
t, τ	Time variable
P_0	Characteristic polynomial of ESO
P_e	Characteristic polynomial of linear feedback controller

Flat-Filtering ADR Control Design

e_{uP}	Control input error
β_i	Flat-filtering network gains, $i = \{0, 1, 2, 3, 4, 5\}$
P_β	Characteristic polynomial

Model-Free approaches

y	Output of phenomenological model
u	Input of phenomenological model
F	Piece-wise constant function of disturbance in ultra-local model
K	User-defined system parameter

Sliding Mode Control

$\hat{F}$	Estimate of disturbance in ultra-local model
$\tilde{\xi}$	Disturbance estimation error
$\bar{L}$	Disturbance estimation error bound
ϑ	Sliding variable
ρ_0, ρ_1, ρ_2	Sliding manifold design parameters
$\bar{\eta}, \bar{\rho}, \bar{\gamma}$	Sliding control design parameters
$\bar{V}$	Lyapunov function candidate
$R_{\varsigma 4}$	LTD4 parameter
$c_{\varsigma 4,i}$	LTD4 parameters, $i = \{1, 2, 3, 4\}$

Neural Network Compensation Using Feedback Error Learning

k_0, k_1, k_2	Feedback control gains
$R_{\varsigma 3}$	LTD3 parameter
$c_{\varsigma 3,i}$	LTD3 parameters, $i = \{1, 2, 3\}$
$\mathbf{W}$	Weight matrix of neural network
$\mathbf{w}$	Output layer weight vector of neural network
$\mathbf{V}$	Hidden layer weight matrix of neural network
$\mathbf{x}_N$	Synaptic input vector
P	Number of neurons
η, η_w, η_v	Learning rates

Adaptive Feedforward Compensation Using Neural Networks

L	Number of neurons
v_i	Input weights, $i = \{1, ..., L\}$
w_i	Output weights, $i = \{1, ..., L\}$
η_1, η_2	Learning rates
k_P, k_D, k_{2D}	Feedback control gains

1 Introduction

1.1 Principle of Hydrostatic Transmissions

Hydrostatic transmission (HST) systems basically consist of a hydraulic pump, a hydraulic motor and other possible components such as pressure valves, charge pumps, fluid tanks and hydraulic accumulators. The presence of these components in an HST system depends on the specific configuration of the application. The working principle of an HST system is based on a transformation between mechanical power and hydraulic power, which typically involves the operation of hydraulic pumps and hydraulic motors in a fluid circuit connected by means of hydraulic hoses.

The hydraulic pump is coupled to a prime mover that can be an internal combustion engine, an electrical motor or a wind turbine. The mechanical power from the prime mover in form of kinetic energy of rotational shaft is supplied into the hydraulic pump, at the output port of the hydraulic pump, a pressurized fluid flow is created and transmitted along the connection hose to the input port of the hydraulic motor. Here, the hydraulic motor works in the reverse mode to the pump converting the hydraulic power back into the mechanical power at the rotational output shaft, which is coupled to the load.

1.2 HST System Configurations

HST systems, regarding the circuit construction, are classified into two categories – open-circuit and closed-circuit transmissions [1]. In an open-circuit system, the inlet of the hydraulic pump and the outlet of the hydraulic motor are connected to the hydraulic reservoir as depicted in Fig. 1.1, the hydraulic flow from the pressure port on the pump is directed to power the motor and, then, returned back to the reservoir. This type of circuit construction is generally less

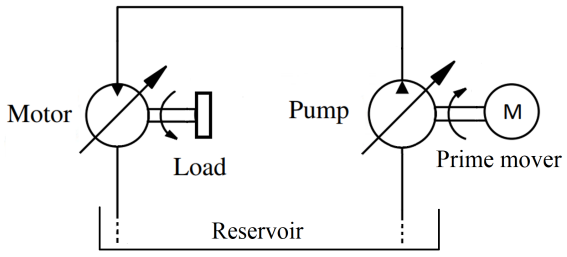

Figure 1.1: Open-circuit HST systems.

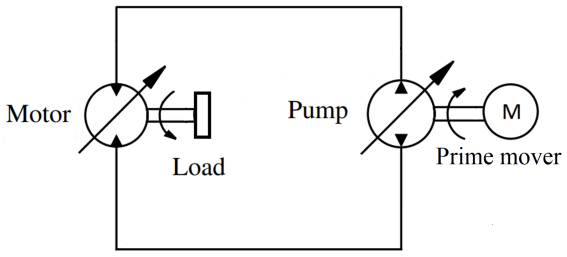

Figure 1.2: Closed-circuit HST systems.

expensive, better for lower pressure applications, simple to maintain and easier to diagnose problems [2]. Contrarily, in a closed-circuit HST system, the motor outlet is connected directly to the hydraulic pump inlet instead of returning to the reservoir, see Fig. 1.2, which forms a

closed-loop of the fluid lines. In this case, a charge pump is required to supplement the fluid into the system for leakage compensation. This type of HST system is generally applied in mobile applications and mainly used with higher-pressure piston hydraulic pumps and motors. Closed-circuit HST systems are generally more expensive, more difficult to diagnose and repair, however, they offer many advantages: able to run at higher pressures with less fluid flow – which requires smaller hydraulic lines, direction reversion without the use of valves, more control options are available [2].

According to the transmission ratio, there are four types of HST systems corresponding to four possible combinations of the hydraulic pumps and motors in an HST circuit related to the structure (fixed or variable displacement) of the used pump/motor [1], see Fig. 1.3

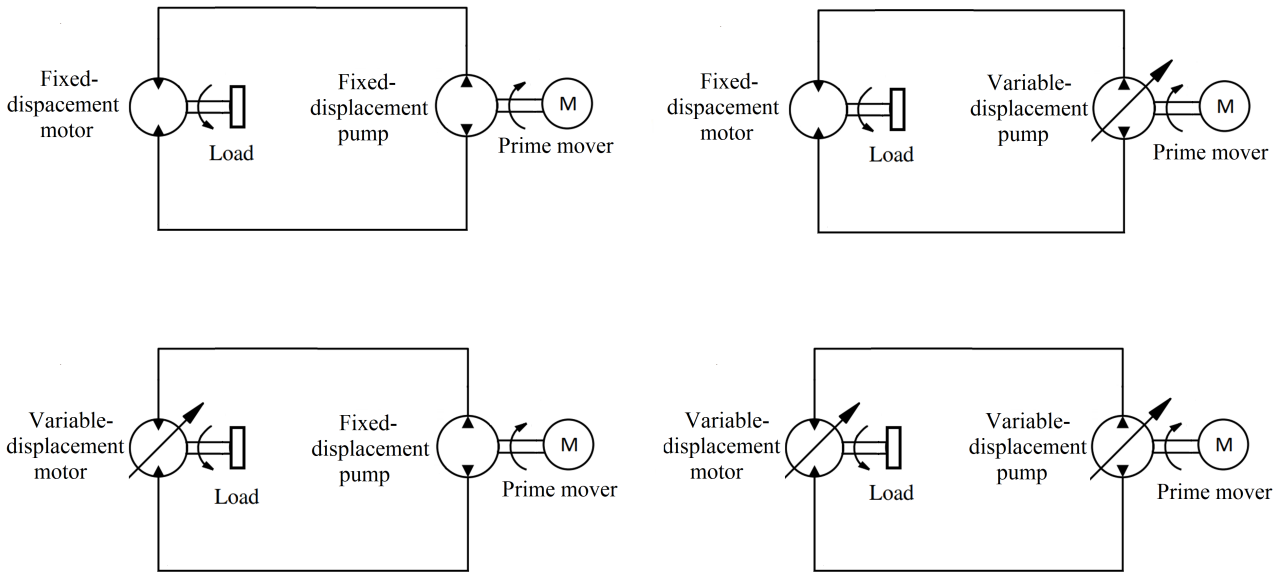

Figure 1.3: Possible types of an HST system.

In a fixed-displacement pump and fixed-displacement motor configuration, the transmission ratio is constant. The motor angular velocity, therefore, can be varied by altering only the angular velocity of the prime mover that is directly connected to the pump. This HST type is least flexible for applications with a fixed transmission ratio, fixed hydraulic torque and power. An HST that uses a variable-displacement pump in a combination with a fixed-displacement motor constitutes the most popular configuration [1] and can be regarded as a continuously-variable transmission. By changing the pump displacement, a constant torque is generated at the motor shaft, whereas the motor angular velocity and the output power vary accordingly. The reversion motion is also possible by a negative displacement of the pump. In a circuit where a fixed-displacement pump and a variable-displacement motor are used, the power generated by the pump is constant. Different angular velocities of the motor can be achieved by altering the motor displacement, which varies the hydraulic torque as well. This configuration is not very popular in practice due to the limitation of the motor displacement range, which should be kept at a large value enough to maintain the circuit pressure and the motor angular velocity in safe limits. The most flexible configuration in practice is an HST system that consists of both variable displacement pumps and motors. The system power, angular velocity and torques are able to be freely changed by regulating displacements of both components. This configuration can be regarded as an infinitely variable transmission. In this case, the transmission ratio,

theoretically, can smoothly vary from $-\infty$ to $+\infty$. However, regarding the safety in operation, the transmission ratio is limited in an acceptably wide interval [1]. In modern applications, this configuration is found more and more common relying on the flexibility in operation and control, many application studies regarding this type of HSTs can be exposed in [3–7].

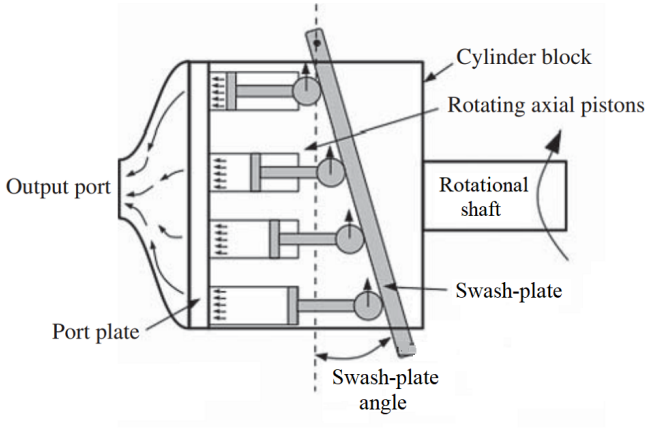

Figure 1.4: Structural principle of a swash-plate type pump/motor (adapted from [1]).

Hydraulic pumps and motors are main components of an HST system, they are also diversity in structure. Some typical structures include: gear types, gerotor types, vane types, radial- and axial-piston types. In fluid power industry, the radial- and axial-piston types are found most popular [1] taking their advantages over other structures such as high efficiency, low moment of inertia, high operating pressure. The axial-piston type, especially, with swash-plate or bent-axis structures offers the highest degree of variability, which benefits the most for control [8].

Fig. 4.36 and Fig. 1.5 show the structural principle of the swash-plate and bent-axis types of the hydraulic pumps/motors. The volumetric displacement of the unit is easily varied independent of the shaft angular velocity by altering the tilt angle of the swash plate or the bent angle of the cylinder block.

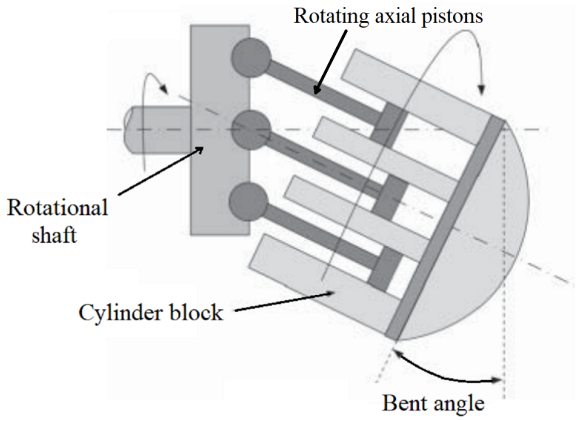

Figure 1.5: Structural principle of a bent-axis type pump/motor (adapted from [1]).

The positioning of the swash plate or the tilt angle of cylinder blocks is made possible by means of servo control mechanisms, which can use either the mechanical, hydraulic or electrical

methods. Fig. 1.6 shows a diagram of the servo system for regulating the bent-axis angle of the Rexroth A6VM motor using electrical inputs.

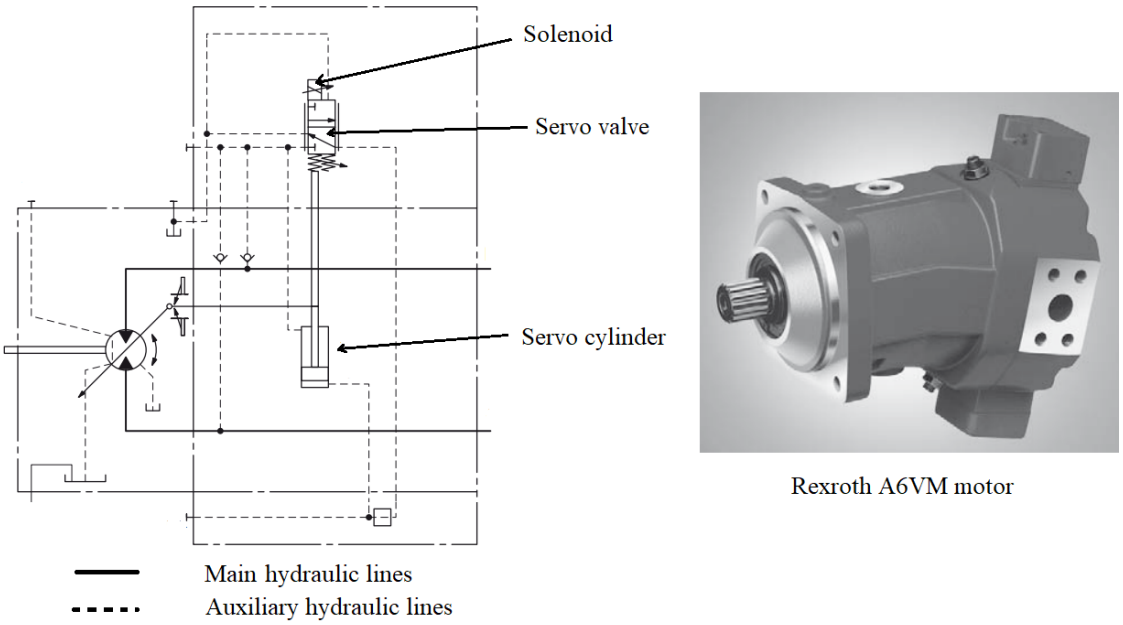

Figure 1.6: A servo mechanism for tilt angle control [13].

1.3 Applications of HST Systems

HST systems offer many advantages over the other forms of power transmissions such as, [12]:

- High power density – HST systems can transmit a high power in a compact design;
- Efficient operation over a wide range of torque-to-speed ratios, high output torques can be achieved at very low velocity;
- Providing a continuously variable transmission ratio in a wide range;
- Smooth motion reversion without changing gears;
- Able to maintain desired speeds within the design limits regardless of loads;
- Low moment of the inertia – which requires low starting torques and exhibits a fast response;
- Able to transmit power from a single prime mover to several load units, even if the position and orientation of the load unit change;
- Providing dynamic braking;
- Long component lifetime with the use of fluids – which can serve as the lubricant and coolant reducing wear and heat in the system.

They are widely used in heavy working machines and off-road vehicles such as harvesters, wheel loaders, excavators, telehandlers, construction and agriculture machinery [9–11]. In recent years, HSTs become trend in the applications with the new designs of high performance working vehicles, in modern automobiles and in green energy power plants [1, 3, 4, 9].

In heavy working equipment like tractors, cranes, bulldozers and other heavy-duty machines, HST systems benefit from the capability of changing the transmission ratio and reversion of the vehicle motion without shifting gears. The flexibility in spatial arrangement also provides a huge advantage, where the pumps and motors can be placed arbitrarily on the chassis, which makes several specialized equipment become possible. A hydraulic bucket lift as an example,

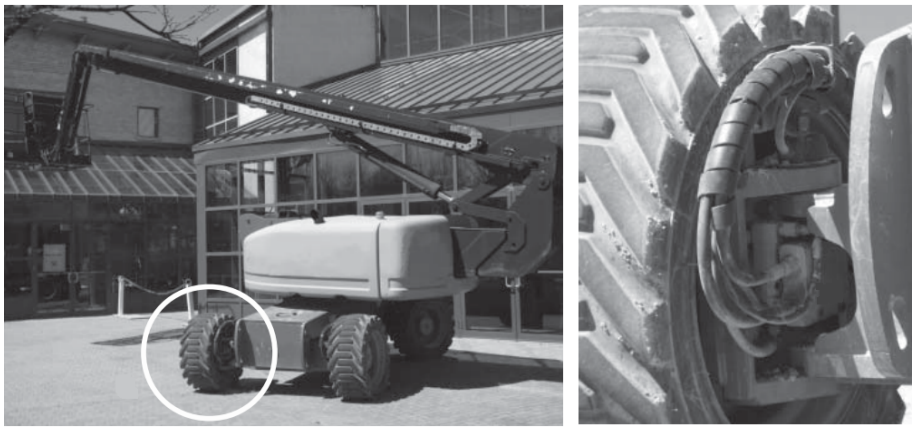

Figure 1.7: A bucket lift: the drive engine is mounted on a rotary platform, hydraulic motors are placed at the wheels [1].

Fig. 1.7, where the cabin and the engine are placed on a turning platform, which is impossible with the use of mechanical transmission systems [1]. In lifting equipment, an HST is used in energy storage systems with hydraulic accumulators, which recover the energy when lowering the load and reproduce power in duty. As an infinitely variable transmission, an HST system allows the drive engine to work at a constant angular velocity – where the maximum energy efficiency is reached regardless of loads, which benefits most in applications like bulldozers, tractors [1, 4].

For automobile applications, in the demand of reducing power consumption due to increased fuel costs and environmental issues regarding fossil fuel emission, higher performance transmission systems with the use of HSTs are in development. By exploiting the advantage of HSTs as the infinitely variable transmission, which allows to change the car speed and to keep the engine running at a fixed angular velocity – where the high performance of combustion engines is achieved, many options to construct such high performance transmissions have been proposed [1, 3, 14, 15] as illustrated in Fig. 1.8 and Fig. 1.9.

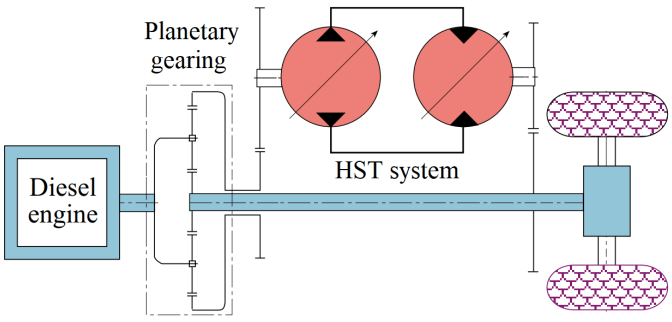

Figure 1.8: Power-split gearboxes [14].

In power-split gearboxes, Fig. 1.8, joining the operation of HSTs and mechanical gears allows

for a possibility to keep the output power and velocity in a desired range without a sophisticated gearbox. This configuration splits the transmitted power into a hydrostatic power flow in parallel with a mechanical one. At low output speeds, the power is mostly transmitted through the hydrostatic system, which provides a better performance for vehicle acceleration and deceleration. As the output speed increases, more power flow is transmitted through the mechanical system for a higher energy efficiency. Fig. 1.9 presents the concept of a hydraulic-mechanical

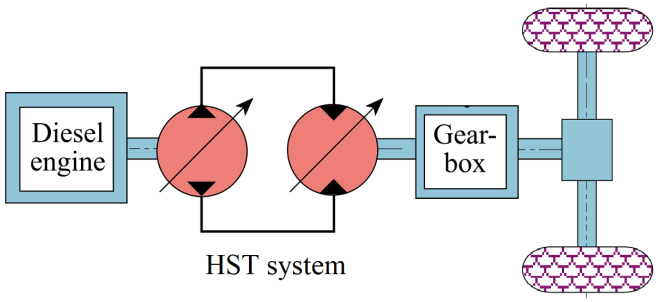

Figure 1.9: Serial connection of an HST with a gearbox [14].

series connection, which is to overcome the limitation of a pure HST concept in high power capacity applications. The serial connection of an HST with a mechanical gearbox provides a possibility to increase the transmission ratio for high power transmissions without the need of increasing the size of components [14].

HSTs also come into play on hybrid vehicles, the concept is shown in Fig. 1.10. When the

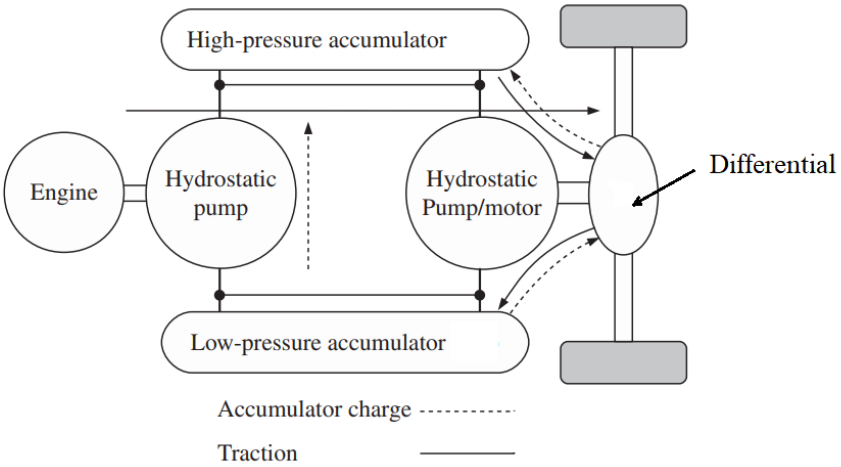

Figure 1.10: Serial hydraulic hybrid transmission systems [1].

vehicle is in charge mode, energy can be stored by pumping the fluid from the low-pressure accumulator into the high-pressure one, which can be done by either the pump connected to the drive engine or by the motor connected to the differential (the motor connected to the differential now works in the pump mode). In the traction mode, the hydraulic motor is driven by the power discharged from the high-pressure accumulator.

In wind power plants, an HST system is used to replace the conventional gearbox, Fig. 1.11, which speeds up the angular velocity to the required value of generators. The use of HST

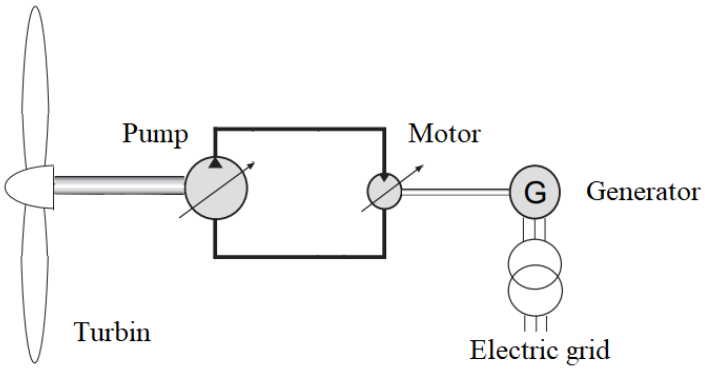

Figure 1.11: HSTs in wind power plants [9].

systems makes it possible to keep the generator rotor at a constant angular velocity while the angular velocity of the turbine may change due to wind speed variation. Moreover, the hydrostatic units (pump and motor) can be arranged separately from one another – which is convenient for construction, assembly and maintenance.

1.4 Disadvantages of HSTs

As previously mentioned, HSTs are recognized in various industrial applications and gaining more and more contributions in other practical applications in the near future. These future applications expose the requirement of high-performance transmission systems. However, beside a variety of remarkable advantages, which puts HST systems into interest, many issues regarding the operation of HST systems are still need to be addressed. They expose several drawbacks, which limit the use of HST systems in general such as [16–18]:

- System components are expensive due to high precise manufacturing technology;
- Flammable hazards, dirty due to fluid leakage;
- Working liquid is very sensitive to pollution;
- They are bulky and noisy;
- Heavy weight components;
- Low energy efficiency due to pressure loss, volume loss and friction loss.

From the control point of view, the control of HST systems is sophisticated, which results from the high non-linearity, disturbance and unavoidable uncertainty in the system caused by many physically-related aspects such as [9, 19–21]:

- The variation in the fluid temperature;
- The change of kinematic viscosity;
- The elasticity of the hydraulic hoses;
- The oil leakage flow;
- The friction disturbance.

Therefore, advanced control approaches are required for an accurate control result. In the last decays, researches on the control of HST systems are very active in both academic and industrial fields. From an overall perspective, the most common strategy for controlling hydraulic systems is still the primary control [14], namely, the output angular velocity of the hydraulic motor shaft is controlled by regulating the displacement of hydraulic pumps. In later development stages, the secondary control concept was introduced, which uses a variable volumetric displacement motor as a second controlled element to achieve the required output speeds or torques [14, 22–25]. The control of HST systems in the most flexible configuration with both variable volumetric displacement pumps and motors are still limited in number. For the development of HST applications, more researches on this control interest are obviously beneficial, which inspires the contribution of this thesis.

1.5 HST Control Literature Review

1.5.1 Classical Proportional-Integral-Derivative (PID) Control

PID is the earliest strategy for the control in industry, which realizes the control law without the use of a controlled plant model. The controller is very effective from the practical point of view due to simple structure. More than 95% of controllers used in industry are PID and most of them are PI controllers [26]. The derivative term is not usually used in practice due to the noise that comes from the measurement signal. Taking the derivative of a measurement signal magnifies the noise, which may reduce the lifetime of actuators even deteriorate the controllers. For HST systems, the application of PID controller is very limited due to an insufficient control performance.

J. Kwaśniewski et al. [20] performed researches on the properties of a pump-controlled HST with different controllers. Here, a PI and a cascade PI controllers were in turn. The tests have been performed with different speeds and oil temperature. The results showed a poor performance of the PI controller while the cascade PI controller could provide a better solution. However, as the final conclusion of the authors, it is very difficult to control the object. HST systems are highly nonlinear and not time-invariant due to the change of fluid viscosity as a function of temperature. The higher temperature results in a better control performance, however, the PI controllers can work well at one particular working point only.

J. Ambuel et al. [27] has developed a PI controller for the output speed tracking of HST systems, which uses a variable displacement pump and a fixed displacement motor. The author performed many tests on the real system. For practical reasons, the control parameters were tuned empirically. The results showed that the set of control parameters with the proportional gain $K_p = 0.2$ and the integral gain $K_i = 0.1$ results in an under-damped control, whereas the set of gains with $K_p = 0.1$ and $K_i = 0.05$ results in an over-damped response. An interesting point has been found in the experiments that the previously over-damped control changes to an under-damped one after a relocation of the test bed, according to the author, this shows that the PI control is very sensitive to the changes of HST system characteristics.

K. Huhtala [28] and S. Tikkanen et al. [29] performed similar researches and discussed the application of the PI controller for an HST system. By analyzing the system model, the research results showed a strong dependence of the PI controller gains on the hydraulic unit

displacements. The authors also concluded that a controller with fixed gains could not provide a sufficient control performance over the wide operation range of the system. Moreover, it was pointed out that controlling the hydraulic motor by a PID controller is much more difficult than controlling the hydraulic pump. A controller tuned at low speed settings results in an under-damped response at high speed, in vice-versa, a controller tuned at high speeds results in an over-damped one at low speed regions. Similarly, A. V. Akkaya [31] performed simulation researches on the effect of the bulk modulus on the performance of HST system controls. The results proved a poor control performance of the PID controller under the variation of hydraulic aspects in the system.

1.5.2 Fuzzy Logic Control

It is similar in comparison to PID controllers, fuzzy logic controllers do not require the model of the controlled plant. The qualitative knowledge, however, is necessary to generate the control rules. Fuzzy-Based controllers provide better solutions for the control of nonlinear systems over the PID controls. Particularly for HST systems, the control results are significantly improved, which have been confirmed in many researches.

J. Ambuel et al. [27] developed a fuzzy-PI controller for the speed control of HST systems, which comprises a PI controller and a rule-based controller. The rule-based controller is activated when the tracking error is larger than a predefined value, if the tracking error drops below this value, then, the conventional PI controller in turn drives the error to zero. The authors used the speed tracking error and the motor torque as the inputs for the decision making and the rule set was designed based on the system understanding and test data. The results showed a significant improvement of the tracking performance and a reduction of the control sensitivity to the system changes for the proposed fuzzy-PI controller.

K. Huhtala [28] also presented a fuzzy-based adaptive PI controller, namely, the adaptive characteristics of the PI controller is achieved through the gain scheduling using fuzzy rules, which are applied on both the pump and the motor. The rules were designed based on the actual and desired values of the output speed. The result showed a great improvement of the fuzzy-based controller over the conventional PID one. Similar result was also confirmed by researches of S. Tikkanen et al. [29]. The fuzzy rules in this design were based on the output error and its change rate, the resulting fuzzy controller performed much better for both the control of pumps and motors over the PI controller.

A self-organizing fuzzy logic controller for the speed control of a hydraulic motor has been developed by I. A. Njabeleke et. al. [30]. In this design, the control rules were adaptive, i.e., they were modified online upon the system parameters. The test results illustrated the benefit of the self-organizing fuzzy logic over the linear control, as the author concluded. A similar adaptive control design and test result can be found also in the work of A. Nawrocka and J. Kwasniewski [19]. A. V. Akkaya [31] designed a fuzzy logic speed control for testing of a pump-controlled motor under the effects of the bulk modulus. The control rules were defined based on two input values: the tracking error and its derivative. A similar control structure can be found in the work of A. Q. Hussien et al. [32], which controls the output speed of a hydraulic motor by regulating the pump displacement using a DC servo motor. The results from these two works showed an achievable tracking performance of the fuzzy controllers.

1.5.3 Model-Based Control

As the need of HSTs increases in industrial applications, advanced control approaches obviously are required to obtain a sufficient control performance, which is not achievable with the conventional linear controls. Characteristics and dynamics of HST system components become more and more a great interest of researchers resulting in an advanced modeling of HST systems, which forms the basis for advanced model-based control designs.

J. Lennevi and J. 0. Palmberg [33] analyzed the components of an HST system, which comprises both variable volumetric displacement pumps and motors. A nonlinear dynamic model has been established. This system model, however, was linearized and simplified by using only the pump displacement for actuation, whereas the motor displacement was considered as a parameter. The linear quadratic regulator (LQR), then, was deployed for a motor angular velocity control design and a Kalman filter was used for estimation of the feedback states. The control structure was evaluated with a step response. The results showed that the LQR technique is adequate for the control of HST systems, however, as seen from the test when the system changes (by changing the motor displacement), the control performance degrades. The authors suggested that the LQR is still beneficial, however, the method is not an automatic process, therefore, the model of the system should be fully known for a successful control result for the implemented controller.

H. W. Wu and C. B. Lee [34] proposed a self-tuning adaptive controller for the speed control of HST systems. The authors reduced the nonlinear system model to a second-order linear one by neglecting the dynamics of the displacement mechanisms and of the relief valves. The model, then, was described by a transfer function. The adaptive controller was constructed by deploying the recursive least square (RLS) parameter estimation technique to estimate the parameters in the model transfer function. The adaptive gains were defined by pole-placements. The resulting adaptive controller was tested for the control of velocity on three different HST configurations – pump-controlled, motor-controlled and both pump- and motor-controlled settings – under the variation of pump speeds, system pressure and load torques. The evaluation was performed with a rectangular response, the results showed a satisfactory control performance for the pump-controlled- and both pump- and motor-controlled HST systems. However, for the motor-controlled configuration the result was not achievable under the effects of system changes.

I. A. Njabeleke et al. [35] proposed an H_∞ control structure for high speed HST systems. The system operation was divided into two regions corresponding to a low- and a high-speed range of the motor angular velocity, and the controllers were designed for each range separately. According to the authors' investigation results, the proposed dual mode controller is effective providing robustness over the entire speed range. H. Berg and M. Ivantysynova [24] conducted researches on a new design of a linear control structure for the secondary control of a HST system. Based on the linear model of system components, the authors deployed LQR techniques to derive a control structure that comprises an inner and an outer loop. The inner loop controls the swash plate aiming at a fast response of the displacement unit, the outer loop controls the velocity and position of the motor shaft. By analyzing the test results, the authors pointed out that the response of the displacement units is the key to improve the performance of the overall system and the implemented structure provide a high-bandwidth control, which results in a fast response of the system dynamics.

L. D. Re et al. [36] conducted researches on a multiple objective optimal control (optimizing both energy efficiency and dynamic response) for HST systems by combining the primary

control (pump-controlled) and the secondary control (motor-controlled). For the simplicity in assessments of the control effect, the system models were reduced to linear ones. Based on these linear models the energy performance index was constructed and deployed in the optimization algorithm of the model reference linearization method. The solution of this method was also compared to the approximate solution of the Hamilton-Jacobi-Bellman (HJB) equation, the evaluation of the results was performed in simulation only. As indicated by the simulation results, the primary control provides the best energy efficiency, whereas the secondary control provides fast response. The combination of both control strategies results in a trade-off solution. For a realistic test, the proposed structure was directed to control the original nonlinear model. The results, however, degraded significantly. It even became unstable for the case of the HJB solution. The authors concluded that the HJB solution is more effective but less robust than the reference model linearization method.

A. Nawrocka and J. Kwasniewski [37] proposed a model predictive controller based on a neural network for the velocity control of an HST system. In this structure, a feedforward neural network was trained off-line to copy the behavior of the controlled plant, the neural network model afterward was implemented in the optimization algorithm. The simulation result showed a satisfactory response of the system to a step command. A. J. Humadi et al. [38] performed a simulation study for the velocity control of a pump-controlled HST system using a radial basic function (RBF) neural network. The neural network took the tracking error and its first derivative as the synaptic inputs, and the parameters of the neural network were chosen to generate a proper control surface that drives the system error to zero. The simulation results, which were compared to the ones of a PID controller, showed that the neural network based controller performs better, it exposes a higher load disturbance rejection capability and is more robust than the PID controller.

H. T. Do and K. K. Ahn [39] proposed a fuzzy-based sliding mode controller (SMC) for the secondary control of the velocity tracking for HST systems. The design was based on a second-order nonlinear system model, which takes into account the effects of the dead zone and the saturation of displacement mechanisms. An equivalent control was designed to drive the sliding variable toward zero, however, due to the uncertainty of system parameters, this equivalent control was simulated by a fuzzy logic system. The error that is defined by the difference between the equivalent control and the fuzzy-simulated control was compensated by a switching robust term. The whole control law was derived based on Lyapunov stability theory, which guaranteed a stable controller. The experiments with the proposed controller were carried out in the conditions of disturbance loads, and compared to the ones of a conventional PID controller. The results demonstrated that the fuzzy-based SMC outperforms the PID controller and provides a higher performance for the velocity control of secondary-controlled HST systems.

M. E. Hasan et al. [10] researched on a control technique, which used model inversion to control the velocity of a pump-controlled motor. The model of the system was derived using Bond graph method, then, was inverted to achieve the required pump displacement. The study result confirmed the applicability of such techniques and the authors concluded that, by using system inversion techniques, the motor speed could be brought back to the previous value. However, there was no evaluation on the dynamic response of the proposed technique. C. S. Kim and C. O. Lee [40] proposed a robust speed controller for a secondary-controlled HST system. This design was based on a linear system model. The design procedure resulted in a linear controller, and the robustness of this controller was provided by a feedforward disturbance compensation law, which uses an observer for disturbance estimation. As concluded from the test results, the controller shows the robustness and an improved performance in comparison to the conventional

PID ones.

H. Aschemann et al. [11] developed a control-oriented model for an HST drive-train. The authors took into account the dynamics of pump and motor displacement units, which are presented by first-order differential equations including the saturation of actuators. The lump disturbance torque acting on the motor and the lump leakage flow in the system were also introduced. The pressure in the system was characterized by the difference between the low and high pressure sides and the angular velocity of the motor was considered as a system state variable. Thereby, a fourth-order nonlinear dynamic system was established. For control design purpose, the displacement variables were approximated by the control inputs, which resulted in a flat system with the system difference pressure and the motor angular velocity as the flat outputs. Based on this model, a Lyapunov-based controller has been developed, which acted simultaneously the primary and secondary controls on the system to track the desired value of both the difference pressure and the motor angular velocity. The disturbance torque, which is required by the controller, was estimated using a nonlinear reduced-order disturbance observer. The simulation study results demonstrated a good quality of the closed-loop performance with a small tracking error for both output variables. The experimental validation of the proposed controller can be found in [41].

H. Sun and H. Aschemann [42] implemented a robust controller for HST systems based on the mathematical model developed in [11]. The model, however, was modified with an introduction of the lump leakage flow as a separate disturbance variable along with the lump torque disturbance. These two variables were estimated by a reduced-order disturbance observer. By explicitly considering the actuator dynamics, the authors derived the dynamic relations between the output variables and the control inputs, which can be inverted to obtain the control law. To deal with the actuator uncertainty, the control law was extended by a robustifying term that is designed based on the Lyapunov stability theory. For implementation, the desired trajectory of the motor angular velocity was formulated by a high-order polynomial, whereas the desired trajectory of the difference pressure was calculated from the desired value of the angular velocity. The simulation results proved that the presented approach leads to an outstanding tracking performance. In a similar control structure, an adaptive version of this controller can be found in [43], where the robustifying term was replaced by an adaptive mechanism, which is also derived directly from Lyapunov stability theory. Based on the assumption of bounded uncertainties of the actuators as presented in [44], the mentioned authors provided an alternative control solution – a sliding mode control – using the same system dynamics modeling for HSTs. The simulation results showed an equivalent performance to the ones of previous control approaches.

An innovative control structure has been proposed by H. Aschemann and H. Sun in [45]. Based on the system model developed in [42], the authors divided the system dynamics into two subsystems: a linear subsystem characterizes the dynamics of the hydraulic motor actuator, whereas a nonlinear one presents the dynamics of remaining system variables. The control designs were applied separately to each subsystem. This approach allowed for a simplicity in design and implementation by reducing the multiple-input multiple-output (MIMO) problem to a single-input single-output (SISO) one. Moreover, the control performance was magnificently improved. For the speed control, the authors proved that the motor angular velocity is a flat output, based on this derivation a flatness-based controller was proposed, which involves three different control actions: a fast control of the motor actuator – which tracks the desired trajectory of the bent-axis angle, a control loop for trajectory tracking of the motor angular velocity, and a reduced-order disturbance observer – which estimates the leakage flow as well

as the unknown load torque allowing for a disturbance compensation. The simulation results proved an excellent control performance. An experimental validation of the robust version of this flatness-based control can be exposed in [46]. As the basis, this decentralized control scheme was exploited in many control designs thereafter. In [47, 48] two versions of the model predictive control were proposed. Passivity-based, optimal control and back-stepping control approaches can be found in [49], [50] and [51], respectively. The SMC and its variations were presented in [52–55].

R. Prabel and H. Aschemann [56] designed a decentralized control approach for the hydraulic torque tracking of HST systems based on an extended linearization technique. A flatness-based controller was deployed for the control of the hydraulic motor to follow the predefined value of the bent-axis angle, whereas the extended linearization technique was exploited for a design of the motor torque control. The motor torque controller is comprised of three components: a feedforward control, a feedforward disturbance compensation, and a state feedback regulator. The states for feedback and the disturbance variables were estimated by a sliding mode observer. This control design exploited the pole-placement method based on a quasi-linear system model. The effectiveness of the proposed control structure was demonstrated by simulations and experiments. Further advanced control approaches that exploit the dynamic model developed in [42] have been conducted by N. D. Dang and H. Aschemann, which can be found in [57–62]. In [63,65,66], N. D. Dang and H. Aschemann proposed new control concepts, where the authors treated the design procedure for HST system control in a multiple-input single-output (MISO) framework.

P. Zeman et al. [67] designed a model predictive controller for the speed control of a secondary-controlled HST system. By taking into account the electro-mechanical relationship of the motor displacement components, the authors derived a nonlinear model of the system. This model was employed in a gradient projection optimization algorithm for the prediction. The unmeasurable states of the system were estimated by an extended Kalman filter. Nevertheless, the static friction in the system was not considered in the control design but resolved by introducing a dither signal to keep the valve spool in permanent motion, which eliminates the static friction. The results of the control implementation showed a very good tracking performance of the model predictive control with high robustness.

P. Zips et al. [68] presented a design of an optimization-based control concept for real-time applications for the torque control of HST systems, which comprises both variable displacement pumps and motors. Based on a reduced-order mathematical model of the controlled system, an optimization-based feedforward control and a flatness-based control were derived in a cascade structure. The optimization-based control planed the desired trajectories for the system pressure and the motor bent-axis angle, which are subject to minimize the torque tracking error and control efforts. These trajectories were fed into the flatness-based feedback controller that produces the control inputs to the system. The states that are required for feedback (the system difference pressure, pump wash-plate angle and motor bent-axis angle) were estimated using two separate observers. The proposed control structure was successfully implemented on a micro-controller. The experiment results, in comparison to the one of PID controller, showed a good tracking performance and an improvement of power loss.

1.5.4 Modeling and Trajectory Planning

The modeling of HST systems has been briefly mentioned in previous subsection. In this subsection, the discussion focuses on more detail reviews of the recently-developed nonlinear

modeling of HST systems with both variable displacement pumps and motors in the multi-variable framework, which is relevant to the encouragement of the works in this dissertation.

E. Carlsson [69] in 2006 developed a nonlinear model of HSTs for a forest vehicle. The hydraulic pumps and motors of the system have servo actuator mechanisms, which use solenoid valves and are controlled by electric currents. However, in this development, the author neglected the dynamics of system actuators. The input currents were related to the tilt angles by empirically-static functions. The nonlinear relation between the tilt angles and the unit displacements was omitted as well, which significantly reduces the complexity of the system model. Actually, the author used directly the displacements as the control inputs without considering any internal disturbance aspects such as leakage flow and disturbance torques.

In the work of H. Schulte [6] in 2007, a new control-oriented nonlinear model of a general HST, which is based on a parallel distributed compensation scheme using the Takagi-Sugeno approach, was introduced. The system uses electro-servo mechanisms for actuation, which is popular in modern applications. The resulting system model consisted of three states: the pressure of high pressure side, the pressure of low pressure side, and the motor angular velocity. The electrical voltage signals were used as the control inputs, which are linearly related to the volumetric displacements the hydraulic units. That means the dynamics of the actuators were not considered and the nonlinearity of the displacements in relation to the actuation mechanism was also neglected. The improvement in this model was that the leakage losses in the system are taken into account that makes sense in real applications.

In 2009, H. Aschemann et al. [11] presented an innovative modeling of an HST that has the same physical configuration as the one used in [6] with elector-servo systems, which can be controlled by electronic devices. A fourth-order nonlinear model was proposed with four system states: the normalized swash-plate angle, the normalized bent-axis angle, the difference pressure, and the motor angular velocity. In this innovative model, the internal losses in the system were fully considered including the leakage flow and the disturbance torque. The dynamics of actuators that presents the behavior of the displacement units upon the control input voltages were explicitly taken into account. Only the nonlinear relation between the tilt angles and the volumetric displacements was simplified by a reasonable assumption of small tilt angles.

T. H. Ho and K. K. Ahn, in 2010 [70], proposed a simulation model of HST systems with hydraulic accumulators for an energy recovery system. Both variable volumetric displacement pumps and motors are used. The authors took into account the actuator dynamics presented by the first-order lag behavior in the same manner as used in the work of H. Aschemann et al. [11]. The losses of fluid flow were accounted as well. The relation between control input voltages and the displacement units, however, was linearly applied, which results in a simplified system model. In 2014, H. Schulte and S. Georg [9] developed a nonlinear control model of wind turbines with an HST. This model basically relies on the nonlinear model proposed in [6], and was combined with the turbine dynamic model. The difference of the new development was that this model uses the difference pressure as a system state – which is already used in [11] – instead of the high and low pressures in the hydraulic circuit. Moreover, the actuator dynamics was also explicitly considered. Y. Wang et al. [71], in 2014, modeled an HST on an unmanned ground vehicle for the motor angular velocity control purpose in an MISO framework. In this model, the actuator dynamics was considered, however, the nonlinear relation between the actuators and displacements of hydraulic units, and the internal disturbances were all omitted.

The work of H. Sun [73] in 2015 introduced a modified version of the one developed by H. Aschemann et al. [11] for a general HST system. The model has been fully validated on the

test bench and proved to be efficient for control designs. The system model consists of four states: the normalized swash-plate angle, the normalized bent-axis angle, the difference pressure and the motor angular velocity. In this modification, though the nonlinear relation between the tilt angles and the volumetric displacements of the hydraulic units was still simplified, the leakage fluid flow in the system was considered as an unknown disturbance beside the unknown disturbance torque. The performance of the control design was improved by using a model-based observer to estimate both the unknown disturbances.

The configuration of HSTs with both variable volumetric displacement pumps and motors forms a multi-variable control system with two inputs of the hydraulic pump and the hydraulic motor. The output of the system – depending on the purpose of the applications and the control design approaches as well – may be single or multiple. Therefore, the trajectory planning for the controls of pumps and motors is also variant in many ways.

In several applications of HSTs, the pump and the motor are usually controlled in parallel to reach the control objective. In these cases, the system output consists of two controlled variables, which constitutes the MIMO control framework. As presented in [5, 23, 70, 72], the motor angular velocity and the system pressure are the two controlled outputs, where the hydraulic pump was manipulated to regulate the pressure in the hydraulic circuit, and the motor was controlled to obtain the desired angular velocity. Contrarily, the control plan could be exchanged between the hydraulic pump and motor as used in [71], where the pump was controlled to follow the desired angular velocity while the motor was used to keep the system pressure in a predefined range. In [9, 11] the HST control system was designed to track the desired angular velocity. To realize the control law, an additional system output – the difference pressure – was required for the design, which is calculated based on some physical considerations. In [68], the hydraulic torque was considered as the single output of the controlled system, the system became over-actuated, therefore, the authors introduced the efficiency as an additional output variable to utilize the system.

The control of HST systems in an MISO scheme can be found also in other applications. As mentioned in [3], the hydraulic efficiency can be the single controlled objective. In this case, both the hydraulic pump and the hydraulic motor are simultaneously planned to follow the optimal trajectories, which maximize the hydraulic efficiency based on a characteristic map. Similarly, the trajectories of the pump and the motor can be optimized to produce maximal energy efficiency for the whole system as presented in [75]. In the case where the motor angular velocity serves as the single output of the system, pumps and motors are usually controlled in different stages – which is referred to as the standard speed control [75]. At the first stage, the pump is controlled to follow the desired value of motor angular velocity. When the pump displacement reaches its maximum, the second stage begins with the hydraulic motor. In this stage, the motor takes action to continue tracking the desired output value. This control plan can be found in [21] and [75] as well.

In [73], the author introduced a decentralize control scheme, which decomposes the multi-variable HST system into a combination of multiple SISO subsystems. Each subsystem corresponds to the control of the hydraulic pump and the hydraulic motor in a separate manner. In this control scheme, the hydraulic motor is controlled to follow a desired trajectory of the bent-axis angle while the hydraulic pump is regulated to track the desired output – the angular velocity or the torque. The study result proved a very high tracking accuracy for the system outputs, however, the way that was used to plan the desired trajectory for hydraulic motor has not been addressed.

1.6 Summary

The advantages put HST systems into the interest of industrial applications, however, the disadvantages prevent the widespread of HST systems in practice, specially from the control point of view. Advanced controls are needed, nevertheless, the researches are still open. The literature review research, as presented, obviously is not able to cover all the related works in HST system control. The available result, however, provides an understanding of the state-of-the-art in the field. As can be concluded, conventional PID controllers are not adequate in the wide operation range for the control of HST systems, whereas model free approaches, like fuzzy controllers, and advanced model-based controllers are much more beneficial. Most of recent researches focus on the control of HST systems in primary or secondary control modes. Some limited number of them act on both the primary and secondary controls simultaneously. It is suggested by many researchers that the primary control is most efficient while the secondary control provides fast dynamic response. The controller that acts both the primary and secondary controls offers a trade-off result, see [34, 36], however, good performance can be achieved as demonstrated in [11, 34, 36, 42].

1.7 Contribution and Outline

A lot of researches on advanced control approaches have been performed and published in the last decades as demonstrated in the literature review. Nevertheless, some directions are still worth of a deeper consideration. From a practical point of view, for example, the design model should be simple to reduce the modeling effort as well as the number of parameters to be identified experimentally. Nevertheless, the resulting tracking performance of the closed-loop system should be high according to certain quality criteria, which has to be guaranteed by dedicated components of the control structure and appropriate design techniques. Moreover, due to aging or degradation, models established for a new device are prone to become less accurate during its lifetime. It may be expected that this drawback is more critical for a highly sophisticated design model. The idea is, hence, to base the control design instead on a simple design model that captures only the most decisive characteristics of the real system, like the relative degree, and to estimate the resulting modeling errors online as well as to use them for compensation purposes. Based on the existing control techniques that have been proposed generally for uncertain nonlinear systems, the work in this dissertation focuses on the design and the validation of advanced control approaches for the output tracking of HST systems. The control strategy is derived from the practical point of view in such a way that both the pump and the motor work synchronically to provide the required output, which corresponds to a multiple-input single-output (MISO) control scheme. The proposed control designs fully exploit the wide operation range of the HSTs – in the limits of physical configuration – under the effect of disturbance, uncertainty and high nonlinearity. Accordingly, the dissertation provides the following contributions:

- Development of a new trajectory planning scheme for the output tracking of HST systems, which efficiently uses both the primary and secondary control inputs;
- Following the idea of simple design models or even purely data-driven models, the following control approaches are developed and investigated in detail for the HST system:
  - Optimal control: Here, a model-based approach to HST control is followed, where the control law is derived by optimization techniques. Using model predictive control,

state and input constraints can be addressed properly and included in the control design. Moreover, gain-scheduled tracking controllers can be derived using Takagi-Sugeno fuzzy techniques in a combination with optimal control or state-dependent Riccati equation techniques based on system descriptions with state-dependent matrices and vectors;

  - Estimator-based feedback linearization: In this class of design techniques, known model parts are included in the right-hand side of the state-space representation of the design model, whereas unknown model parts – typically sophisticated nonlinear descriptions for nonlinearities or uncertainties – are considered by different kinds of estimators. Thereby, both the robustness and the accuracy are improved.

  - Active disturbance rejection control (ADRC): In this approach, mainly the complete right-hand side of the state-space representation of the design model is considered as unknown. Different techniques are applied to provide either observer-based estimates for the unknown model part or to design a compensator using flat-filtering techniques;

  - Model-free control approaches: Here, the control designs are completely data-driven and based on either output measurements or tracking errors as well as its time derivatives. The robustness and performance of such control structures are investigated and validated in both simulations and experiments.

- The use of tracking differentiators is investigated in all the control structures above – if applicable. Tracking differentiators can be interpreted as a model-free way to determine time derivatives of noise-afflicted measurements and substitute classical state transformations corresponding to a classical model-based approach.

- All the developed control approaches are implemented on a dedicated test rig and validated by experiments. The performance of the individual solution is assessed and quantified.

The remaining part of this dissertation covers the following topics:

- Section 2 - Modeling and proposed trajectory planning for HST systems: A part of this section provides the knowledge contained in the HST model, which serves as the basis for the model-based control design as well as for the analysis and simulation purposes. The remaining content presents the development of a new trajectory planning scheme for the output tracking of HST systems that renders the framework of designed control structures.

- Section 3 - Advanced control designs: This section covers the main scientific contribution of the present work. All the proposed control structures are detailed with a corresponding analysis and a description of the design procedure.

- Section 4 - Control design validation: Simulation tests and experimental validations are demonstrated in this section. The results are summarized and evaluated by means of a common performance index – the root-mean-square error – for a valuable assessment of the control performance, which provides an overall view of the applicability and the potential of each control approach.

- Section 5 - Conclusion: The section draws some perspectives – from the author's point of view – on the achievable results and further improvements, which may be taken in the future to attain more valuable contributions.

2 Modeling and Trajectory Planning for the HST System

2.1 Mathematical Model of the HST

All the work in the dissertation is aimed at the validation by real-time implementation on the test equipment, which is set up at the Chair of Mechatronics at the University of Rostock, Fig. 2.1. The principle configuration is shown in Fig. 2.2 The system consists of both variable

Figure 2.1: The HST test equipment [73].

volumetric displacement pumps and motors, the pump is of axial-piston swash-plate types and the motor is of axial-piston bent-axis types. The hydraulic connection between the in-port and out-port of these two components forms a closed fluid circuit. An electrical motor is used to drive the pump, the angular velocity of the hydraulic pump can be kept constant or varied depending on the study purposes. The hydraulic motor is coupled to a second electrical motor which can generate a constant or varying load torque. The difference pressure in the circuit and the angular velocity of the pump and the motor are measurable by pressure gauges and speed sensors. The mathematical model of HST systems has been developed by H. Aschemann

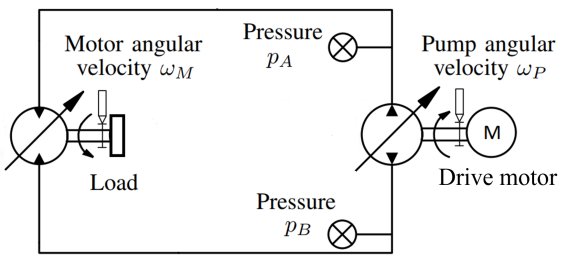

Figure 2.2: Principle configuration of the test rig.

and H. Sun in [45] and detailed by H. Sun in [73], which serves as the basis for control designs. The derivation of this system model is briefly represented in the sequel.

2.1.1 Hydraulic System Dynamics

Pump Flow Rate

The structural principle of a hydraulic pump is depicted in Fig. 2.3. The rate of fluid flow generated by the pump

$$q_P = \frac{V_P(\alpha_P)\omega_P}{2\pi} \tag{2.1}$$

is proportional to the pump angular velocity ω_P. The displacement $V_P(\alpha_P)$ depends on the inclined angle of the swash plate α_P and is presented by a nonlinear equation:

$$V_P(\alpha_P) = N_P\, A_P\, D_P\, \tan(\alpha_{P,\max} \cdot \tilde{\alpha}_P)\,, \tag{2.2}$$

with $\tilde{\alpha}_P = \alpha_P/\alpha_{P,\max}$ denoting the normalized swash-plate angle and $\alpha_{P,\max}$ as the maximum of the swash-plate angle. A_P stands for the effective piston area, D_P is the diameter of the piston circle and N_P presents the number of pistons in the unit.

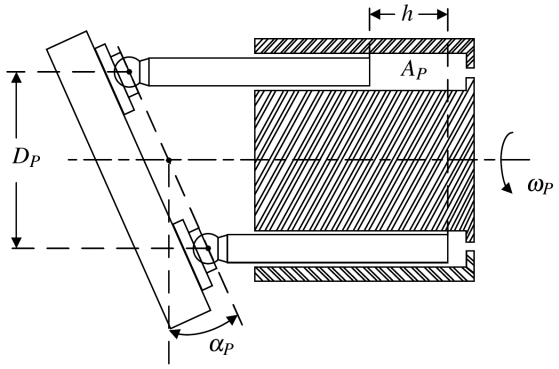

Figure 2.3: Structural principle of the hydraulic pump [73].

By denoting $\tilde{V}_P = \frac{N_P A_P D_P}{2\pi}$ as the maximal volumetric displacement, the flow rate through the hydraulic pump can be represented as follows

$$q_P = \tilde{V}_P \tan\left(\alpha_{P,\max} \cdot \tilde{\alpha}_P\right) \omega_P. \tag{2.3}$$

Motor Flow Rate

The motor volume flow rate, q_M, depends on the motor angular velocity, ω_M, in the same manner as of the hydraulic pump, namely:

$$q_M = \frac{V_M(\alpha_M)\omega_M}{2\pi}. \tag{2.4}$$

Provided that the structural parameters N_M, A_M, and D_M are defined, see Fig. 2.4, the nonlinear relation of the motor volumetric displacement to the bent-axis angle, α_M, is presented by

$$V_M(\alpha_M) = N_M\, A_M\, D_M\, \sin(\alpha_{M,\max} \cdot \tilde{\alpha}_M), \tag{2.5}$$

hence, the flow rate of the hydraulic motor becomes

$$q_M = \tilde{V}_M \sin\left(\alpha_{M,\max} \cdot \tilde{\alpha}_M\right) \omega_M, \tag{2.6}$$

where, $\tilde{\alpha}_M = \alpha_M/\alpha_{M,\max}$ represents the normalized bent-axis angle, $\alpha_{M,\max}$ stands for the maximum of the bent-axis angle and $\tilde{V}_M = \frac{N_M A_M D_M}{2\pi}$ denotes the maximum value of the motor displacement.

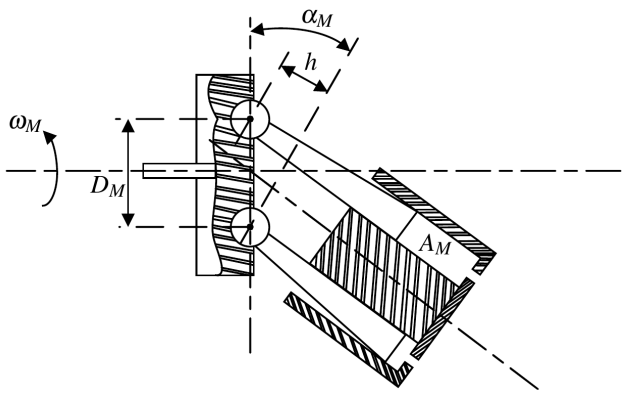

Figure 2.4: Structural principle of the hydraulic motor [73].

Dynamics of Fluid Pressure

For practical reasons, the difference pressure between the low and high pressure sides (p_A and p_B, see Fig. 2.2) in the hydraulic circuit is introduced as a state variable, which allows for a smaller order of the system model. Moreover, the assumption of symmetric physical conditions is applied and the pressure losses in the hydraulic circuit are also neglected. The difference pressure, hence, can be expressed as follows

$$\Delta\dot{p} = \tfrac{2}{C_H}\left(\tilde{V}_P \tan\left(\alpha_{P,\max}.\tilde{\alpha}_P\right)\omega_P - \tilde{V}_M \sin\left(\alpha_{M,\max}.\tilde{\alpha}_M\right)\omega_M\right) - \tfrac{q_U}{C_H} \ , \tag{2.7}$$

where the unknown disturbance term q_U accounts for the leakage, and C_H presents the capacitance of the hydraulic oil.

2.1.2 Actuator Dynamics

The dynamics of the actuators for both the hydraulic pumps and motors is approximated by a first-order differential equation as follows

$$\begin{aligned} T_{uP}\dot{\tilde{\alpha}}_P + \tilde{\alpha}_P &= k_P u_P \ , \\ T_{uM}\dot{\tilde{\alpha}}_M + \tilde{\alpha}_M &= k_M u_M \end{aligned} \tag{2.8}$$

with T_{uP} and T_{uM} presenting the time constants of actuator dynamics for the pump and the motor respectively, k_P and k_M denoting the proportional gains and the two analog control inputs of the servo valves which drives the actuators denoted by u_P and u_M . Both the control inputs and the tilt angles of the actuators are bounded according to the physical limitations: $u_P \in [-1, 1]$, $u_M \in [\epsilon_M, 1]$, $\tilde{\alpha}_P \in [-1, 1]$ and $\tilde{\alpha}_M \in [\epsilon_M, 1]$ with $\epsilon_M > 0$.

2.1.3 Mechanical System Dynamics

The rotational dynamics of the motor shaft can be derived by deploying the torque balance equation

$$J_V\dot{\omega}_M + d_V\omega_M = \tilde{V}_M\Delta p \ \sin(\alpha_{M,\max}\cdot\tilde{\alpha}_M) - \tau_U \ , \tag{2.9}$$

which is equivalent to

$$\dot{\omega}_M = \frac{\tilde{V}_M}{J_V} \ \sin(\alpha_{M,\max}\cdot\tilde{\alpha}_M)\Delta p - \frac{d_V}{J_V}\omega_M - \frac{\tau_U}{J_V} \ , \tag{2.10}$$

where d_V stands for the damping coefficient and J_V is the mass moment of the inertia. The disturbance of the load torque as well as the model uncertainty are taken into account by an introduction of the lumped disturbance term τ_U.

2.1.4 The Nonlinear Model of the Overall System

The description of a dynamic model for the overall system now can be established by combining all the dynamic components derived above. The resulting nonlinear system is presented in a fourth-order state-space model as follows

$$\begin{bmatrix} \dot{\tilde{\alpha}}_M \\ \dot{\tilde{\alpha}}_P \\ \Delta\dot{p} \\ \dot{\omega}_M \end{bmatrix} = \begin{bmatrix} -\frac{1}{T_{uM}}\tilde{\alpha}_M + \frac{k_M}{T_{uM}}u_M \\ -\frac{1}{T_{uP}}\tilde{\alpha}_P + \frac{k_P}{T_{uP}}u_P \\ \frac{2\tilde{V}_P}{C_H}\tan(\alpha_P)\omega_P - \frac{2\tilde{V}_M}{C_H}\sin(\alpha_M)\omega_M - \frac{q_U}{C_H} \\ -\frac{d_V}{J_V}\omega_M + \frac{\tilde{V}_M}{J_V}\sin(\alpha_M)\Delta p - \frac{\tau_U}{J_V} \end{bmatrix}. \tag{2.11}$$

For a succinct representation, the notation replacements $\alpha_M = \tilde{\alpha}_M \cdot \alpha_{M,\max}$ and $\alpha_P = \tilde{\alpha}_P \cdot \alpha_{P,\max}$ are used.

2.2 Motivation of the Trajectory Planning Method

The operation range of a HST system, which uses simultaneously both the variable volumetric displacement pump and motor, can be divided into two principle speed intervals corresponding to a low- and a high-speed range, as illustrated in Fig. 2.5.

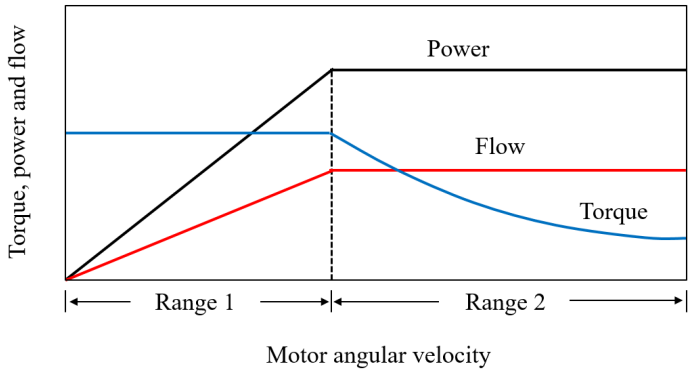

Figure 2.5: Operational characteristics of the HST.

In the low-speed range – range 1 – the volumetric displacement of the hydraulic motor is fixed to the maximal value, and an increasing of the motor angular velocity is possible by altering the pump volumetric displacement from zero to its maximal value. In this range, as the displacement of the hydraulic pump increases to gain speed, the hydraulic torque generated at the motor shaft remains constant, but both the volume flow and the power depend proportionally on the angular velocity of the motor. When the hydraulic pump reaches its maximal displacement, the high-speed range – range 2 – begins. At this point, if a further increasing of the motor angular velocity is required then the motor displacement needs to be reduced. Within this range, while the hydraulic torque varies inversely to the motor angular velocity, the power

and the flow rate remain constant, cf. [74]. Changing the motor angular velocity in this manner is referred to as the standard speed control for HST systems in mobile applications [75–77]. Fig. 2.6 shows the variation of the motor angular velocity upon the changes of the pump and motor displacements in the corresponding operation ranges at a constant pump angular velocity.

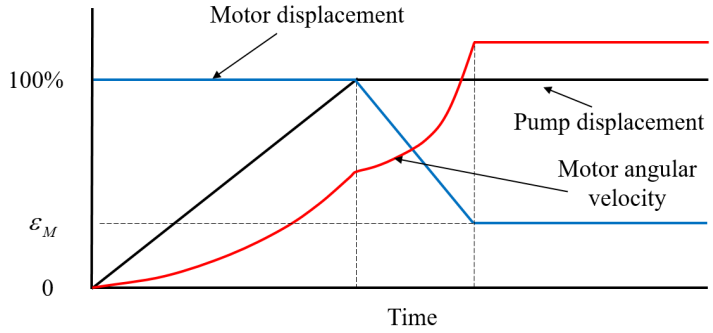

Figure 2.6: Variation of the motor angular velocity upon the motor and pump displacements at a constant pump velocity.

In practical applications with HST systems, it is typically desired to attain the highest torque possible at the output shaft of the hydraulic motor. Specially at low speeds, when starting, a high torque is required for a larger acceleration of the vehicles [3] or during the loading phase of working machines [78]. Moreover, the hydraulic motor also offers a higher volumetric efficiency at large displacements [75]. Thereby, it is favorable to keeping the volumetric displacement of the hydraulic motor as large as possible. Aiming at this, the control plan is proposed as follows:

- The primary control – hydraulic pump control – is prioritized which provides efficiency, see Sect. 1.6. The pump displacement unit is controlled to track the output value accurately;
- The secondary control, i.e., the hydraulic motor control, is actuated only when it is required to gain the proper transmission ratio, which depends on the desired value of the motor angular velocity output.

The design is now turned into the framework of MISO systems. In this thesis, most of the control designs are based on decentralized schemes (except the model predictive control which will be detailed later), in that case the resulting control structure is similar to the one developed in [45,73]. However, the difference is that with the proposed control allocation – unlike in [45,73] where the trajectory of the motor bent-axis angle is treated as an independent reference value, namely, it is specified regardless of the performance of the generated hydraulic torque – the highest torque possible is produced at the motor shaft, which offers higher performance and efficiency for practical applications.

2.3 Synchronized Trajectory Planning for the Bent-Axis Angles of the Hydraulic Motors

Based on the control allocation discussed previously, the desired trajectory of the hydraulic motor bent-axis angle is planned dependent on the reference trajectory, namely, it follows an empirical expression which is related to the desired values of the motor angular velocity. The idea is to prioritize the pump control to achieve a higher efficiency. The control of hydraulic motor is exploited only when the control of the hydraulic pump is no longer authorized due to

actuator saturation. The expression is chosen as follows [66]

$$\tilde{\alpha}_{Md} = 1 - c \cdot \sin\left(\frac{\pi}{2} d\right) \tag{2.12}$$

with $\tilde{\alpha}_{Md}$ denoting the desired values of the motor bent-axis angle.

The intermediate variable d is defined by the reference value of the system output, which is evaluated with the following rule

$$d = \begin{cases} \dfrac{\omega_{Md} - a}{b \cdot \omega_{\max} - a} & \text{if} \quad \omega_{Md} > a, \\ \\ 0 & \text{if} \quad \omega_{Md} \leqslant a. \end{cases} \tag{2.13}$$

In the definition (2.13):

- ω_{Md} represents the desired values of the motor angular velocity.
- The parameter a is a user-defined parameter which specifies a threshold value of the angular velocity where the hydraulic motor control is activated. If the desired value of the motor angular velocity becomes larger than a, then the bent-axis angle of the hydraulic motor is required to decrease in order to gain the proper transmission ratio. Thereby, the variation of the motor displacement unit is synchronized with the motor desired angular velocity in the high-speed region. The chosen value of the parameter a results in a trade-off between the efficiency and the smoothness of the system behavior. If a is chosen too small – that means the motor control is activated too early – then the efficiency is degraded. If a has too large values, then very fast changes of the motor displacement are caused, and the motor angular velocity may undergo oscillations.
- $b < 1$ is a fixed design parameter which is used to avoid a saturation of the hydraulic pump swash-plate angle aiming at maintaining the control authority for the tracking accuracy. A small value of b narrows the speed range of the HST system, whereas a too large value of b may cause a saturation of the hydraulic pump actuator.
- $\omega_{\max}$ is an experimental parameter, which determines the highest angular velocity possible based on the given physical limitations of the real system.
- The calculation of the parameter c is provided by

$$c = 1 - \epsilon_M, \tag{2.14}$$

  where ϵ_M represents the lower bound of motor bent-axis angle.

The desired trajectory of the system output – the hydraulic motor angular velocity – is also designed to satisfy the compliant requirement of the operational limitations on the real system in order to avoid any saturation of both hydraulic pump and motor displacement units, namely, the maximum of $\omega_{Md,max} = b \cdot \omega_{max}$. This results in $d \in [0, 1]$.

The function $\sin(\cdot)$ is used in (3.92) to generate a smooth transition of the motor displacement unit. Moreover, it keeps mapping the value of d onto the range $[0, 1]$. As a consequence, the desired value of the motor bent-axis angle $\tilde{\alpha}_{Md}$ fits into the range $[1, \epsilon_M]$, which is in compliance with the limited working range of the motor displacement unit.

3 Advanced Output Control Designs

Based on the analysis of the system model and by following the basic ideas stated in Subsect. 1.7 as a guideline, the advanced control designs in the remaining part of the thesis may be classified into four principle groups, where in each group several variants of the control methods are investigated. Fig. 3.1 provides an outlook on the control design classification.

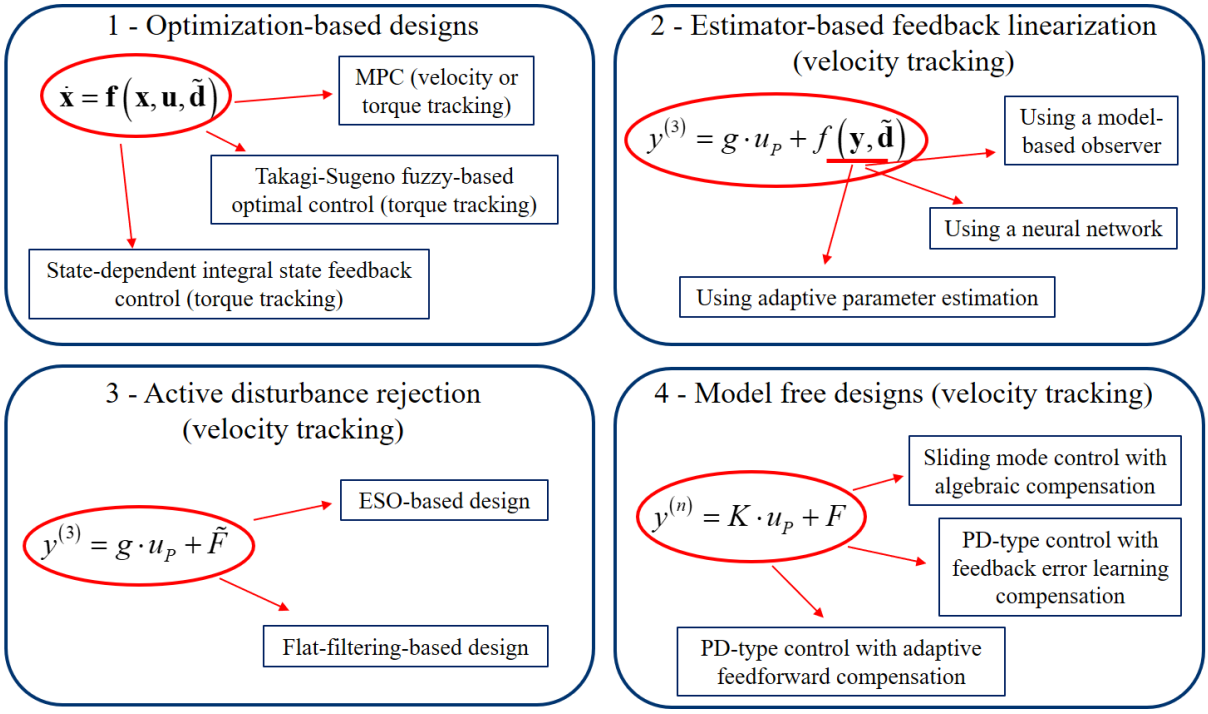

Figure 3.1: Classification of the control designs.

- Optimization-based approaches: This group consists of model-based control designs with three control variants: nonlinear model predictive control – which is deployed for either angular velocity or torque control; Takagi-Sugeno fuzzy-based optimal control – which is designed for torque control; and state-dependent integral state feedback control deployed for torque control as well. The system model is described by the nonlinear function of the state vector $\mathbf{x}$, the control vector $\mathbf{u}$ and the disturbances $\tilde{\mathbf{d}}$. Moreover, the control laws of these control designs are derived directly from the solution of optimization problems like in nonlinear model predictive control, or – in the case of linear quadratic problems – from the solution of algebraic Riccati equations like in Takagi-Sugeno fuzzy-based optimal control and state-dependent integral state feedback control, see [58, 59, 61, 63, 64].
- Estimator-based feedback linearization: In this group, the feedback linearization framework is applied to realize tracking controllers for tracking of angular velocity. Considering

the nonlinear input-output relationship, different alternatives of estimator are investigated for the compensation of nonlinearities and disturbances – which is described by the nonlinear function $f(\mathbf{y}, \tilde{\mathbf{d}})$. The compensated dynamics results in an integrator chain, the linear methods, subsequently, can be applied to stabilize the tracking error, [57]. The variants of estimator include: a reduced-order disturbance observer – which relies on a complete model of the system; adaptive parameter estimation – which allows for a reduction of model knowledge by the incorporated adaptive parameters that account for the parameter uncertainty and disturbances in the system; a neural network that produces the correct compensation signal through the learning process.

- Active disturbance rejection (ADR) control: This control approach originates from classical PID control, where advantages of PID controls, like the robustness and the simplicity in control design, are exploited and extended to a higher complexity level toward the generalized PID control for nonlinear and uncertain systems that can be presented in Brunovsky form. For its application, only knowledge or assumptions on the relative degree of an input-output relation are necessary. Two control methods are demonstrated for tracking of angular velocity – a standard approach with use of an extended state observer and the flat-filtering approach, [62]. ADR control is basically a model-free control approach but treated as a separate class in this work.
- Model-free control approaches: This group comprises three control approaches – a sliding mode control and two control applications using a multiple layer neural network, where the control designs do not require a complete model knowledge and may result in data-driven control structures, [60, 65, 66]. The designs rely on the ultra-local model instead, where the relative order n and the parameter K are empirically chosen. The term "model-free" refers to a particular control approach proposed in [79] which is similar to active disturbance rejection approaches. It comes, however, from a different mathematical point of view and was originally developed as an algebraic version of active disturbance rejection control, see [96]. These control designs are established for velocity tracking also.

Most of control designs address velocity tracking. The reason for this is that a direct measurement of the output torque is not available at the dedicated test rig of the hydrostatic transmission system. The hydraulic torque must be calculated instead using the system model, therefore control designs, where the complete model of the system is not used, become irrelevant for torque control. In the sequel, control design approaches are detailed in the order of reducing the model knowledge required for developing of the control structure.

3.1 Optimization-Based Approaches

The control designs in this group exploit a full model of the system. Based on optimization techniques, the control inputs are determined in such a way that some predefined criteria are minimized. Usually, the controlled system output or the state variables and the control inputs are regarded so that the system is asymptotically stable and shows an acceptable error convergence. This approach takes important roles in industrial practice leading to two popular control approaches which are known as linear quadratic regulator (LQR) and model predictive control (MPC) [126]. In this thesis, these two control approaches are of interest for HST systems.

3.1.1 Model Predictive Control (MPC)

Defining the cost function The design of a nonlinear model predictive control (NMPC) relies on a discretized nonlinear model of the system. By exploiting the complete system model, the evolution of the system states in the future are predicted along a finite moving horizon using the current values of system states and corresponding inputs. At each discrete time interval, a cost function is minimized over the prediction horizon resulting in a sub-optimal solution sequence of the control inputs. Only the first action of the resulting control sequence is employed to the system. This numerical procedure is repeatedly performed in the next time intervals. Fig. 3.2 depicts the principle of an MPC control.

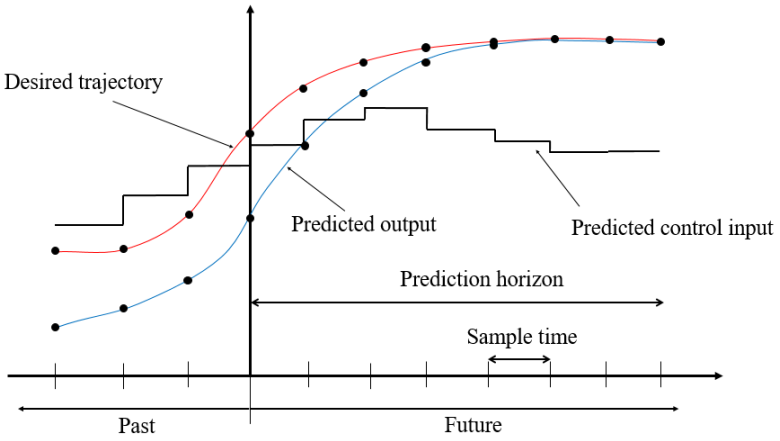

Figure 3.2: Principle of model predictive control.

Defining a cost function is the first step in an NMPC design. In a standard procedure, a quadratic function of both system states and control inputs is employed as a cost function to be minimized. In the present design, the system is considered in the MISO framework. It turns out that the choice of a proper cost function – which is not described in the standard form – becomes crucial in order to achieve the desired tracking performance for the MISO scheme w.r.t. the proposed control strategy. The mentioned cost function is defined as follows

$$J = \sum_{k=1}^{N} \left[w_1(\omega_{Md}(k) - \omega_M(k))^2 + w_2(\tilde{\Delta}p(k))^2 + w_3(1 - \tilde{\alpha}_M(k))^2 + w_4(p - \tilde{\alpha}_P(k))^2 \right]. \quad (3.1)$$

Here, the positive scalars w_1, w_2, w_3, w_4 represent the corresponding weighting factors for each individual cost term. In the second term, $\tilde{\Delta}p = \Delta p(k+1) - \Delta p(k)$ is the change in system pressure. N is the number of time points in the prediction horizon and the time instance is denoted by the index k. The meaning of each term in (3.1) is explained in the sequel:

- The first term in the cost function corresponds to the penalization of the tracking error, which is defined by the difference between the reference value ω_{Md} and the output ω_M. This penalization forces the system output to track the desired value.
- The second term produces a smoothing effect on the transition of the actuators to avoid too fast changes in the pressure, which reduces oscillations in the system.
- The third term is responsible for maintaining the largest motor displacement possible to produce the highest torque possible at the motor shaft as expected by penalizing the deviation of the bent-axis angle $\tilde{\alpha}_M$ from its maximum.

- The last term, which regards the swash-plate angle $\tilde{\alpha}_P$ with a fixed design parameter $p \in [0, 1]$, is a practical measure to smoothen transitions between the two actuators of the hydraulic pump and motor.

It is also assumed that the desired value ω_{Md} is constant within the prediction horizon. Note that the penalization cost of control input is usually a contribution in the cost function of model predictive control. In the proposed definition of the cost function, the control inputs u_M and u_P are not present. Instead they are addressed indirectly by penalizing the variables $\tilde{\alpha}_M$ and $\tilde{\alpha}_P$ taking advantage of the close relations between the inputs and these variable, whose dynamics are characterized by first-order lag behaviors with small time constants.

Numerical optimization methods The computational issue regarding a high load of online optimization problems is still one of the most difficult obstacle in a real-time application of NMPC, particularly for applications to fast mechatronic systems. In the case of HSTs, the system model comprises four state variables and two control inputs, which requires a consideration of selected optimization techniques for the real-time implementation of the NMPC algorithm regarding the configuration of the available hardware. Aiming at a small real-time computational load, the optimization algorithm is properly formulated in such a way that it allows for a transformation of a dynamic optimization problem into a static one by numerical evaluation of the cost function w.r.t. the system dynamic constraints. Then, the well-known Newton-Raphson algorithm is deployed with its favorable convergence properties. Here, the box constraints that define the feasible ranges of the system states and control inputs are also included within the proposed numerical process [63].

The numerical implementation of the proposed algorithm involves the discretization of the system dynamics. Several popular discretization techniques can be named such as explicit Euler, Euler-Heun or Runge-Kutta schemes. They offer different results regarding the accuracy and the computational burden. As mentioned before, the computational load related to the discretization method needs to be taken into account for both implementation capability and the numerical accuracy on the available hardware. For an evaluation of a suitable choice for the discretization method, simulation tests have been performed. The performance of three methods is presented in Table 3.1.

Table 3.1: Performance of discretization methods

	Method		
Performance	***Euler***	***Euler-Heun***	***Runge-Kutta***
RMS error	4.279e-1	2.571e-1	2.219e-1

Based on the statistics in the Table 3.1 it can be seen that, in comparison to the simplest method – explicit Euler, Runge-Kutta integration achieves a significant reduction of the RMS by 48%, whereas the Euler-Heun method reduces the error by 40%. However, given the larger computational effort that requires a higher number of evaluations of the state equations using the Runge-Kutta method, the Euler-Heun method becomes obviously a better choice.

As the discretization method has been designated, the system model is now discretized in an predictor-corrector scheme. With the system state vector $\mathbf{x} = \begin{bmatrix} \tilde{\alpha}_M & \tilde{\alpha}_P & \Delta p & \omega_M \end{bmatrix}^T$ and the control input vector $\mathbf{u} = \begin{bmatrix} u_M & u_P \end{bmatrix}^T$, the continuous-time nonlinear function according to

(2.11)

$$\mathbf{f}(\mathbf{x},\mathbf{u}) = \begin{bmatrix} -\frac{1}{T_{uM}}\tilde{\alpha}_M + \frac{k_M}{T_{uM}}u_M \\ -\frac{1}{T_{uP}}\tilde{\alpha}_P + \frac{k_P}{T_{uP}}u_P \\ \frac{2\tilde{V}_P}{C_H}\tan(\alpha_P)\omega_P - \frac{2\tilde{V}_M}{C_H}\sin(\alpha_M)\omega_M - \frac{q_U}{C_H} \\ -\frac{d_V}{J_V}\omega_M + \frac{\tilde{V}_M}{J_V}\sin(\alpha_M)\Delta p - \frac{\tau_U}{J_V} \end{bmatrix} \tag{3.2}$$

is implemented using the corresponding discrete-time description. The system state variables evaluated at each discrete time instance k are denoted with the time index by $\mathbf{x}(k)$ and $\mathbf{f}(\mathbf{x}(k),\mathbf{u}(k))$. The prediction model now reads

$$\mathbf{x}(k+1) = \mathbf{x}(k) + T_s\,\frac{\mathbf{f}\left(\mathbf{x}(k),\mathbf{u}(k)\right) + \mathbf{f}\left(\bar{\mathbf{x}}(k),\mathbf{u}(k)\right)}{2}\,, \tag{3.3}$$

where

$$\bar{\mathbf{x}}(k) = \mathbf{x}(k) + T_s\,\mathbf{f}\left(\mathbf{x}(k),\mathbf{u}(k)\right) \tag{3.4}$$

represents an Euler step with the sampling time T_s. The value of the cost function J according to (3.1) is accumulated while the future system evolution is predicted in the prediction horizon.

The Newton-Raphson optimization algorithm is deployed based on the numerical evaluation of both the Hessian and the gradient of the cost function J w.r.t. the optimization variables. In the implemented algorithm, the control input sequences $u_M(k)$ and $u_P(k)$ represents the optimization variables, and they are stacked in a single vector $\tilde{\mathbf{u}}_{opt}$ as follows

$$\tilde{\mathbf{u}}_{opt} = [\tilde{u}_1, ..., \tilde{u}_N, \tilde{u}_{N+1}, ..., \tilde{u}_{2N}]\,, \tag{3.5}$$

where the first N control elements from $\tilde{u}_1, ..., \tilde{u}_N$ correspond to the motor control input u_M and the remaining N ones, $\tilde{u}_{N+1}, ..., \tilde{u}_{2N}$, are related to the pump control input u_P.

The prediction horizon comprises N time points. With two control inputs, the optimization variables result in a number of $2N$, therefore, the resulting Hessian matrix has the dimension of $2N$ x $2N$. Regarding the issue with the dimension of the optimization problem, the expense for a full Hessian matrix computation would be quite large. However, it is worth to note that each individual control element in the optimization sequence may have an arbitrary value in the feasible region, which is independent of the others. Moreover, the assumption of the convexity for the local optimization problem is also taken into account. Therefore, the large computational cost of the full gradient and Hessian matrix calculations can be avoided. By exploiting the optimizing-over-some-variables technique [127], the gradient of the cost function J w.r.t. the corresponding element in $\tilde{\mathbf{u}}_{opt}$ is reduced to the first derivative, whereas the Hessian matrix is reduced to a scalar as the second derivative of the cost function. These effective reductions provide a small optimization load and, as a consequence, a large number of Newton steps is allowed within the given time interval. That offers the real-time implementation capability for the proposed NMPC algorithm on fast mechatronic systems such as HSTs with a 50 ms sampling time. Fig. 3.3 provides a demonstration of the optimization process using the mentioned technique. As illustrated, in each sample time interval, a certain number of the Newton-Raphson iterations are performed. At each iteration, one variable is updated after the other, the process is repeated until the search reaches the vicinity of the minimum. This search process is similar to the pattern search – or Hooke-Jeeves – algorithm [128].

The derivatives of the cost function J w.r.t. the $j-th$ element of the optimization vector $\tilde{\mathbf{u}}_{opt}$

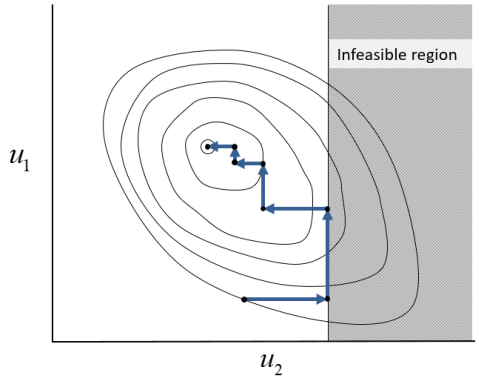

Figure 3.3: Illustration example of the convex optimization process using the idea of optimizing-over-some-variables for a two-dimensional case.

can be evaluated using the central difference formula [129] as follows

$$\begin{aligned} \frac{\partial J}{\partial \tilde{u}_j} &= \frac{J_{\tilde{u}_j+\Delta\tilde{u}} - J_{\tilde{u}_j-\Delta\tilde{u}}}{2\Delta\tilde{u}}, \\ \frac{\partial^2 J}{\partial \tilde{u}_j^2} &= \frac{J_{\tilde{u}_j+\Delta u} - 2J_{\tilde{u}_j} + J_{\tilde{u}_j-\Delta\tilde{u}}}{\Delta\tilde{u}^2}. \end{aligned} \tag{3.6}$$

Here, $\Delta\tilde{u}$ is a small perturbation which is used to disturb the control element $\tilde{u}_j$ for numerical evaluations, and $J_{\tilde{u}_j}$ denotes the value of the cost function corresponding to the control action $\tilde{u}_j$. Similarly, $J_{\tilde{u}_j+\Delta\tilde{u}}$ and $J_{\tilde{u}_j-\Delta\tilde{u}}$ present the values of the cost function when the perturbed element $\tilde{u}_j + \Delta\tilde{u}$ and $\tilde{u}_j - \Delta\tilde{u}$ are applied, respectively. The update rule, which considers the box constraints of control inputs, is given as follows

$$\tilde{u}_j^{*(i+1)} = \tilde{u}_j^{(i)} - \frac{\partial J}{\partial \tilde{u}_j}\left(\frac{\partial^2 J}{\partial \tilde{u}_j^2}\right)^{-1},$$

$$\tilde{u}_j^{(i+1)} = \begin{cases} b_l, & \text{if } \tilde{u}_j^{*(i+1)} < b_l, \\ \tilde{u}_j^{*(i+1)}, & \text{if } b_l \leq \tilde{u}_j^{*(i+1)} \leq b_u, \\ b_u, & \text{if } \tilde{u}_j^{*(i+1)} > b_u. \end{cases} \tag{3.7}$$

In the update law (3.7), the index i specifies the $i-th$ iteration of the algorithm. The values b_l and b_u define the lower and upper bounds of the control inputs, respectively.

For the HST system, the constraints are applied only to two state variables – the normalized motor bent-axis angle $\tilde{\alpha}_M$ and the normalized pump swash-plate angle $\tilde{\alpha}_P$. These constraints are identical to the ones of the control inputs. It is worth to point out that the dynamics of these two state variables are described by the first-order lag systems with proportional gains $k_P = 1$ and $k_M = 1$. This obviously implies that the given constraints of these two states are satisfied automatically as long as the values of control inputs are in their feasible regions.

Summary of the numerical optimization algorithm

Initialization $\tilde{\mathbf{u}}_{opt} = \mathbf{0}$

Reading the current state vector $\mathbf{x}(k)$ and disturbance values from the Kalman filter

For $i = 1$ to maximal iteration step i_{max}
  For $j = 1$ to $2N$
  - Evaluation of the derivatives:
    - ◇ Initialization of the cost function $J = 0$
    - ◇ Disturbing the control element $\tilde{u}_j$ with $\Delta\tilde{u}$
    - ◇ Prediction of the state $\mathbf{x}(k+1)$ in the horizon using (3.3)
    - ◇ Accumulation of the cost function according to (3.1)
    - ◇ Calculation of the derivatives using (3.6)
  - Control input update for $\tilde{u}_j^{(i+1)}$ using (3.7)

  End
End
Apply the first control action to the HST system: $[u_M, u_P]^T = [\tilde{u}_1, \tilde{u}_{N+1}]^T$.

Stability analysis The success of MPC has been confirmed in various industrial applications. Issues regarding the stability of the proposed algorithm needs still to be addressed. Several systematic works have been conducted to provide proofs of stability for MPC algorithms. Nevertheless, the applicability of the corresponding results is not guaranteed in general [130], hence, they are limited to specific cases. In this application study, the cost function is not formulated in a standard form, which makes the stability proof even harder. Therefore, the stability analysis of the proposed control algorithm aims at finding evidence of a convergence instead. For this purpose, let's consider the cost function evaluated at each time step k within the prediction horizon

$$\bar{\Upsilon}(k) = w_1(\omega_{Md} - \omega_M(k))^2 + w_2(\tilde{\Delta}p(k))^2 + w_3(1 - \tilde{\alpha}_M(k))^2 + w_4(p - \tilde{\alpha}_P(k))^2. \tag{3.8}$$

As it is defined, this function is obviously positive definite and radially unbounded, hence, it can be considered as a Lyapunov function candidate. Then, the non-monotonic Lyapunov function theorem that is stated by A. A. Ahmadi et al. in [131] for the stability analysis of discrete-time nonlinear systems can be applied. Accordingly, the stability condition for the NMPC results in

$$\big(\bar{\Upsilon}(k+N) - \bar{\Upsilon}(k)\big) + ... + \big(\bar{\Upsilon}(k+1) - \bar{\Upsilon}(k)\big) < 0. \tag{3.9}$$

The criterion (3.9) is evaluated numerically along the prediction horizon w.r.t. to the optimal control input sequence $\tilde{\mathbf{u}}_{opt}$. As this criterion is satisfied with strictly negative values, the equation (3.9) implies decreasing values of the Lyapunov function candidate within the resulting control horizon, which indicates the convergence of the control algorithm according to [131].

System variable estimation The proposed NMPC algorithm requires a full feedback of all system state variables and the estimation of unknown disturbances q_U and τ_U for the implementation. Taking into account that the system possesses a high nonlinearity and is affected by disturbances and measurement noise, Kalman filters are employed in order to reconstruct these system variables. For nonlinear systems, the extended Kalman filter (EKF) and the unscented Kalman filter (UKF) [132, 133] are two variants that provide good performance for estimation. In this work, the unscented version is preferred because of its advantages and superior estimation results over the EKF. The UKF relies on nonlinear transformations of sample points without any Taylor linearizations. This is beneficial for the computational process as well because the Jacobians are not required anymore. Moreover, the approximation in UKFs are based on transformations of multiple points that provides better approximation of the nonlinear output distribution.

For the implementation of the UKF, the state vector of the system (2.11) is extended by two disturbance models for the leakage volume flow and the load torque. The resulting state vector becomes

$$\mathbf{x}_e = \begin{bmatrix} \tilde{\alpha}_M & \tilde{\alpha}_P & \Delta p & \omega_M & q_U & \tau_U \end{bmatrix}^T, \tag{3.10}$$

where integrator disturbance models are employed

$$\begin{bmatrix} \dot{q}_U \\ \dot{\tau}_U \end{bmatrix} = \begin{bmatrix} 0 \\ 0 \end{bmatrix}. \tag{3.11}$$

The system output vector is given by

$$\mathbf{y}_m = \begin{bmatrix} \Delta p \\ \omega_M \end{bmatrix} = \begin{bmatrix} 0 & 0 & 1 & 0 & 0 & 0 \\ 0 & 0 & 0 & 1 & 0 & 0 \end{bmatrix} \mathbf{x}_e = \mathbf{C}_m \mathbf{x}_e. \tag{3.12}$$

The Euler-Heun discretization method is again applied to the system model, and the resulting discrete-time presentation is given as follows

$$\mathbf{x}_e(k+1) = \mathbf{x}_e(k) + T_s \frac{\Psi\left(\mathbf{x}_e(k), \mathbf{u}(k)\right) + \Psi\left(\bar{\mathbf{x}}_e(k), \mathbf{u}(k)\right)}{2} \tag{3.13}$$

with an Euler prediction step defined by

$$\bar{\mathbf{x}}_e(k) = \mathbf{x}_e(k) + T_s \, \Psi\left(\mathbf{x}_e(k), \mathbf{u}(k)\right) \ . \tag{3.14}$$

Here, the nonlinear dynamics of the extended system is governed by the function Ψ as follows

$$\Psi = \begin{bmatrix} -\dfrac{1}{T_{uM}}\tilde{\alpha}_M + \dfrac{k_M}{T_{uM}} u_M \\ -\dfrac{1}{T_{uP}}\tilde{\alpha}_P + \dfrac{k_P}{T_{uP}} u_P \\ \dfrac{2\tilde{V}_P}{C_H}\tan(\alpha_P)\omega_P - \dfrac{2\tilde{V}_M}{C_H}\sin(\alpha_M)\omega_M - \dfrac{q_U}{C_H} \\ -\dfrac{d_V}{J_V}\omega_M + \dfrac{\tilde{V}_M}{J_V}\sin(\alpha_M)\Delta p - \dfrac{\tau_U}{J_V} \\ 0 \\ 0 \end{bmatrix}. \tag{3.15}$$

The structure of the UKF is detailed in [133]. The design process involves the choice of $2n+1$ sigma points forming a matrix χ with its $i-th$ column defined by

$$\chi_i = \begin{cases} \mathbf{x}_e, & i = 0 \\ \mathbf{x}_e + \left(\sqrt{\mu \mathbf{L}_x}\right)_i, & i = 1, ..., n \\ \mathbf{x}_e - \left(\sqrt{\mu \mathbf{L}_x}\right)_i, & i = n+1, ..., 2n \end{cases} \tag{3.16}$$

where $\left(\sqrt{\mathbf{L}_x}\right)_i$ represents the $i-th$ column of the matrix square root of $\mathbf{L}_x$, which can be evaluated using the Cholesky decomposition [133]. n is the dimension of the extended system state vector and the scaling factor μ is given as follows

$$\mu = \alpha^2 \left(n + \kappa\right). \tag{3.17}$$

The design parameters α and κ are related to the spread of the sigma points. The associated weights of the state variables and the covariances are given by

$$w_{m,i} = \begin{cases} \dfrac{\lambda}{\lambda+n}, & i=0 \\ \dfrac{1}{2(\lambda+n)}, & i=1,...,2n \end{cases}$$
$$w_{c,i} = \begin{cases} \dfrac{\lambda}{\lambda+n} + (1-\alpha^2+\beta), & i=0 \\ w_{m,i}, & i=1,...,2n \end{cases} \tag{3.18}$$

where $\lambda = \mu - n$. The scalar β characterizes the higher-order distribution of the sigma points, and $\beta = 2$ is optimal if a Gaussian distribution process is assumed [132]. Given the covariance matrices w.r.t. process noise $\mathbf{Q}_K$ and measurement noise $\mathbf{R}_K$, the UKF algorithm repeatedly performs the following steps at each time interval:

- UKF initialization
$$\mathbf{L}_x(k) = \mathbf{L}_0, \quad \hat{\mathbf{x}}_e(k) = \mathbf{x}_{e,0}$$

- Sigma points transformation and the mean value calculation
$$\chi(k+1) = \chi(k) + T_s \Psi\left(\hat{\mathbf{x}}_e(k), \mathbf{u}(k)\right)$$
$$\tilde{\mathbf{x}}_e(k+1) = \sum_{i=0}^{2n} w_{m,i}\chi_i(k+1)$$

- Error covariance matrix prediction
$$\tilde{\mathbf{L}}_x(k+1) = \sum_{i=0}^{2n} w_{c,i}\left(\chi_i(k+1) - \tilde{\mathbf{x}}_e(k+1)\right)\left(\chi_i(k+1) - \tilde{\mathbf{x}}_e(k+1)\right)^T + \mathbf{Q}_K$$

- Measurement prediction
$$\gamma(k+1) = \mathbf{C}_m\chi(k+1)$$
$$\tilde{\mathbf{y}}(k+1) = \sum_{i=0}^{2n} w_{m,i}\gamma_i(k+1)$$

- Measurement error covariance matrix prediction
$$\tilde{\mathbf{L}}_y(k+1) = \sum_{i=0}^{2n} w_{c,i}\left(\gamma_i(k+1) - \tilde{\mathbf{y}}(k+1)\right)\left(\gamma_i(k+1) - \tilde{\mathbf{y}}(k+1)\right)^T + \mathbf{R}_K$$

- Cross-covariance matrix update and the calculation of the Kalman gain $\mathbf{K}_K$
$$\mathbf{L}_{xy}(k+1) = \sum_{i=0}^{2n} w_{c,i}\left(\chi_i(k+1) - \tilde{\mathbf{x}}_e(k+1)\right)\left(\gamma_i(k+1) - \tilde{\mathbf{y}}(k+1)\right)^T$$
$$\mathbf{K}_K(k+1) = \mathbf{L}_{xy}(k+1)\mathbf{P}_y^{-1}(k+1)$$

- State vector and the error covariance matrix updates
$$\hat{\mathbf{x}}_e(k+1) = \tilde{\mathbf{x}}_e(k+1) + \mathbf{K}_K(k+1)\left(\mathbf{y}(k+1) - \tilde{\mathbf{y}}(k+1)\right)$$
$$\mathbf{L}_x(k+1) = \tilde{\mathbf{L}}_x(k+1) - \mathbf{K}_K(k+1)\tilde{\mathbf{L}}_y(k+1)\mathbf{K}_K^T(k+1)$$

The implementation of the proposed estimator-based NMPC is depicted in Fig. 3.2.

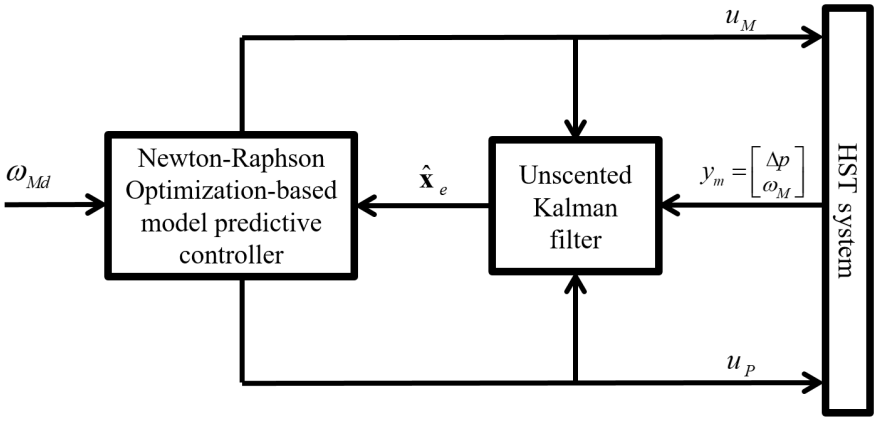

Figure 3.4: Implementation of the NMPC structure.

Adaptation for hydraulic torque control There is an interesting point in this proposed control design – that is, the control can easily be adapted for the control of hydraulic torque instead of the motor angular velocity. To do so, simply modify the first term of the cost function w.r.t. the hydraulic torque as the system output, the following cost function results in

$$J = \sum_{k=1}^{N} \left[w_1(\tau_{hd}(k) - \tau_h(k))^2 + w_2(\tilde{\Delta}p(k))^2 + w_3(1 - \tilde{\alpha}_M(k))^2 + w_4(p - \tilde{\alpha}_P(k))^2 \right], \tag{3.19}$$

where the hydraulic torque $\tau_h(k)$ is evaluated according to

$$\tau_h(k) = \tilde{V}_M \sin(\alpha_M(k))\Delta p(k) \tag{3.20}$$

and $\tau_{hd}(k)$ is the corresponding desired torque value. With the set of parameters chosen properly, a high hydraulic torque tracking performance can be achieved.

3.1.2 Takagi-Sugeno Fuzzy-Based Optimal Control Design for Torque Tracking (FBO)

The proposed control structure for a torque tracking is designed in a decentralized scheme where the controls of the hydraulic pumps and motors are independent of each other. The design is based on two separate subsystems: a first-order dynamic subsystem is responsible for the control of the bent-axis angle of the hydraulic motor, which allows for a simple control design. The second subsystem presents a nonlinear dynamics of the hydraulic torque, where the Takagi-Sugeno fuzzy techniques are deployed to control the output of the system [59].

- The subsystem for motor control design is given by a first-order lag behavior which describes the normalized motor bent-axis angle dynamics and corresponds to the first equation in the system model (2.11)

$$\dot{\tilde{\alpha}}_M = -\frac{1}{T_{uM}}\tilde{\alpha}_M + \frac{k_M}{T_{uM}}u_M. \tag{3.21}$$

- The subsystem that presents the relevant dynamics for the motor torque control design comprises the second and third differential equations in the system (2.11) resulting in

$$\begin{bmatrix} \dot{\tilde{\alpha}}_P \\ \Delta\dot{p} \end{bmatrix} = \begin{bmatrix} -\dfrac{1}{T_{uP}}\tilde{\alpha}_P + \dfrac{k_P}{T_{uP}}u_P \\ \dfrac{2\tilde{V}_P}{C_H}\tan(\alpha_P)\omega_P - \dfrac{2\tilde{V}_M}{C_H}\sin(\alpha_M)\omega_M - \dfrac{q_U}{C_H} \end{bmatrix}. \tag{3.22}$$

  In this subsystem, the normalized motor bent-axis angle $\tilde{\alpha}_M$ is considered as a gain-scheduling parameter. Moreover, $\alpha_M = \tilde{\alpha}_M \cdot \alpha_{M,\max}$ and $\alpha_P = \tilde{\alpha}_P \cdot \alpha_{P,\max}$ hold.

Pump Control Using Takagi-Sugeno Techniques

The application of the Takagi-Sugeno (TS) fuzzy techniques allows for an extension of classical linear control design approaches to nonlinear systems [134]. In order to obtain an exact TS representation, the subsystem (3.22) is rewritten in a quasi-linear form [135] as follows

$$\begin{aligned} \begin{bmatrix} \dot{\tilde{\alpha}}_P \\ \Delta\dot{p} \end{bmatrix} &= \begin{bmatrix} -\frac{1}{T_{uP}} & 0 \\ \frac{2\tilde{V}_P\omega_P \operatorname{sinc}(\alpha_P)\cdot\alpha_{P,\max}}{C_H\cos(\alpha_P)} & 0 \end{bmatrix} \begin{bmatrix} \tilde{\alpha}_P \\ \Delta p \end{bmatrix} + \begin{bmatrix} \frac{k_P}{T_{uP}} \\ 0 \end{bmatrix} u_P + \begin{bmatrix} 0 \\ -\frac{1}{C_H} \end{bmatrix} v, \\ y_\tau &= \begin{bmatrix} 0 & \tilde{V}_M \sin(\alpha_M) \end{bmatrix} \begin{bmatrix} \tilde{\alpha}_P \\ \Delta p \end{bmatrix}, \end{aligned} \tag{3.23}$$

where the lumped disturbance term v is defined by $v = 2\tilde{V}_M\omega_M \sin(\alpha_{M,\max}\cdot\tilde{\alpha}_M) + q_U$ and y_τ denotes the output torque. Using corresponding matrix notations, the system can be represented by

$$\begin{aligned} \dot{\mathbf{x}}_\tau &= \mathbf{A}(\tilde{\alpha}_P, \omega_P)\,\mathbf{x}_\tau + \mathbf{b}\,u_P + \mathbf{d}\,v, \\ y_\tau &= \mathbf{c}^T(\tilde{\alpha}_M)\,\mathbf{x}_\tau\ . \end{aligned} \tag{3.24}$$

The system matrix $\mathbf{A} = \mathbf{A}(\tilde{\alpha}_P, \omega_P)$ in (3.24) depends on the swash-plate angle $\tilde{\alpha}_P$ and the angular velocity ω_P of the pump, whereas the two vectors $\mathbf{b}$ and $\mathbf{d}$ are constant. The state variable $\tilde{\alpha}_M$ in this subsystem is considered as a gain-scheduling parameter.

To guarantee a successful control design for the selected quasi-linear presentation, Kalman's controllability criterion [141]

$$\begin{aligned} \mathbf{K}_C(\tilde{\alpha}_P, \omega_P) &= \begin{bmatrix} \mathbf{b} & \mathbf{A}(\tilde{\alpha}_P, \omega_P)\,\mathbf{b} \end{bmatrix}, \\ \det(\mathbf{K}_C(\tilde{\alpha}_P, \omega_P)) &\neq 0 \end{aligned} \tag{3.25}$$

must be ensured. Substituting the matrices $\mathbf{A}(\tilde{\alpha}_P, \omega_P)$ and $\mathbf{b}$ from (3.23) into (3.25) results in

$$\det(\mathbf{K}_C(\tilde{\alpha}_P, \omega_P)) = \frac{2\tilde{V}_P k_P^2 \omega_P \alpha_{P,\max} \operatorname{sinc}(\alpha_P)}{C_H T_{uP}^2 \cos(\alpha_P)}. \tag{3.26}$$

With $\omega_P > 0$, hence, the criterion is point-wise fulfilled. Note that this condition does not make any statement regarding nonlinear controllability, it only guarantees the solvability of the Riccati equation.

The state-dependent element of the system matrix $\mathbf{A}(\tilde{\alpha}_P, \omega_P)$ is now described succinctly by a nonlinear function $f(\tilde{\alpha}_P, \omega_P)$. Given its maximal and minimal values, f_{max} and f_{min}, the function $f(\tilde{\alpha}_P, \omega_P)$ can be exactly interpolated according to

$$f(\tilde{\alpha}_P, \omega_P) = f_{\max}\cdot p_1 + f_{\min}\cdot p_2, \tag{3.27}$$

where p_1 and p_2 are two membership functions which are defined as follows

$$\begin{aligned} p_1 &= \frac{f\left(\tilde{\alpha}_P, \omega_P\right) - f_{\min}}{f_{\max} - f_{\min}}, \\ p_2 &= \frac{f_{\max} - f\left(\tilde{\alpha}_P, \omega_P\right)}{f_{\max} - f_{\min}} \ . \end{aligned} \tag{3.28}$$

Moreover, two local system models corresponding to two system matrices $\mathbf{A}_1$ and $\mathbf{A}_2$ that result from the values f_{max} and f_{min} can also be established [136]. Given two membership functions and two local models, the weighting functions for the interpolation between the two local models and the membership functions become identical, namely

$$\begin{aligned} h_1 &= p_1, \\ h_2 &= p_2. \end{aligned} \tag{3.29}$$

The polytopic system representation formed by the local models with their corresponding contributions is written as follows

$$\mathbf{A}\left(\tilde{\alpha}_P, \omega_P\right) = \sum_{i=1}^{2} h_i\left(\tilde{\alpha}_P, \omega_P\right) \mathbf{A}_i \ . \tag{3.30}$$

Aiming at the discrete-time control design, the local system models are firstly discretized using explicit Euler method with a sample time T_s. The two corresponding discretized models can be stated as follows

$$\begin{aligned} \mathbf{x}_\tau(k+1) &= \left(\mathbf{I} + T_s\, \mathbf{A}_i\right) \mathbf{x}_\tau(k) + T_s\, \mathbf{b}\, u_P(k) + T_s\, \mathbf{d}\, v\left(k\right) \\ &= \mathbf{A}_{d,i} \mathbf{x}_\tau(k) + \mathbf{b}_d\, u_P(k) + \mathbf{d}_d\, v\left(k\right), \end{aligned} \tag{3.31}$$

where k is the time index, $\mathbf{A}_{d,i}$, $i \in \{1, 2\}$, are system matrices of local models and $\mathbf{b}_d$, $\mathbf{d}_d$ are the system vectors.

Based on the derived exact TS representation, the nonlinear control can be designed by means of linear optimal control techniques, which is applied to each discretized local model. The proposed torque tracking control consists of three components – an optimal feedback control, a feedforward control and a feedforward disturbance compensation. They are detailed in the sequel.

Optimal Feedback Control Design

For the design of the feedback control u_{FB}, the disturbance v in equation (3.31) is discarded, which will be compensated later, resulting in

$$\mathbf{x}_\tau(k+1) = \mathbf{A}_{d,i}\, \mathbf{x}_\tau(k) + \mathbf{b}_d\, u_{FB}(k). \tag{3.32}$$

At this point, a discrete-time LQR design (DLQR) is applied to find the feedback gain, which involves the minimization of a quadratic cost function

$$J_\tau = \sum_{k=1}^{\infty} \left[\mathbf{x}_\tau(k)^T\, \mathbf{Q}\, \mathbf{x}_\tau\left(k\right) + r\, u_{FB}^2\left(k\right) \right] , \tag{3.33}$$

where the positive definite matrix $\mathbf{Q}$ and the positive scalar r are the weighting factors of the state vector $\mathbf{x}$ and the scalar input u_{FB}, respectively. To find the solution of the optimization problem regarding the cost function (3.33), the corresponding discrete-time algebraic Riccati equations (DARE) are solved for each local model, which are given by

$$\mathbf{A}_{d,i}^T[(\mathbf{S}_i - \mathbf{P}_i\,\mathbf{b}_d(r + \mathbf{b}_d^T\mathbf{S}_i\mathbf{b}_d)^{-1}\mathbf{b}_d^T\mathbf{P}_i]\mathbf{A}_{d,i} + \mathbf{Q} = \mathbf{S}_i,\ i = 1, 2, \tag{3.34}$$

resulting in symmetric positive definite solutions $\mathbf{S}_i = \mathbf{S}_i^T > 0$. Given the solutions $\mathbf{S}_i$, the feedback gains corresponding to the local models can be determined as follows

$$\mathbf{k}_i^T = (r + \mathbf{b}_d^T\mathbf{S}_i\mathbf{b}_d)^{-1}\mathbf{b}_d^T\,\mathbf{S}_i\mathbf{A}_{d,i}\ , \tag{3.35}$$

which can be found by using the built-in "dlqr" routine of the implemented control software. The feedback gain for the overall system is determined by the weighted sum of the local ones

$$\mathbf{k}^T\left(\tilde{\alpha}_P, \omega_P\right) = \left[\ k_1 \quad k_2\ \right] = \sum_{i=1}^{2} h_i\left(\alpha_P, \omega_P\right)\mathbf{k}_i^T \tag{3.36}$$

and the feedback control law, finally, becomes

$$u_{FB}(k) = -\mathbf{k}^T\left(\tilde{\alpha}_P, \omega_P\right)\mathbf{x}_\tau(k)\ . \tag{3.37}$$

The resulting closed-loop system matrices $\mathbf{A}_{c,i} = \mathbf{A}_{d,i} - \mathbf{b}_d\,\mathbf{k}_i^T$, $i \in \{1, 2\}$, of the vertex models are constant. By using the weighting functions (3.29), the closed-loop matrix of the overall system results in

$$\mathbf{A}_c(\tilde{\alpha}_P, \omega_P) = \sum_{i=1}^{2} h_i(\tilde{\alpha}_P, \omega_P)\mathbf{A}_{c,i}. \tag{3.38}$$

The stability of the closed-loop system matrix (3.38) is proved using linear matrix inequalities (LMIs) [137], where a common Lyapunov function [134], $\mathbf{P}_L$, has been found by means of YALMIP and SeDuMi [138, 139], satisfying the following conditions

$$\mathbf{P}_L > 0,\ \mathbf{A}_{c,i}^T\,\mathbf{P}_L\,\mathbf{A}_{c,i} - \mathbf{P}_L < 0,\quad i \in \{1, 2\}\ . \tag{3.39}$$

Feedforward Control Design

The hydraulic torque y_τ generated by the hydraulic motor serves as the system output. According to (3.24) and (3.38), the transfer function presenting the response of the system can be calculated as follows

$$\begin{aligned} G_b\left(z\right) = \frac{Y_\tau\left(z\right)}{U_{FF}\left(z\right)} &= \mathbf{c}^T(z\mathbf{I} - \mathbf{A}_c)^{-1}\mathbf{b}_d \\ &= \frac{b_0\left(\tilde{\alpha}_M, \tilde{\alpha}_P, \omega_P\right)}{a_0\left(\tilde{\alpha}_P, \omega_P\right) + a_1\left(\tilde{\alpha}_P, \omega_P\right)\cdot z + a_2\left(\tilde{\alpha}_P, \omega_P\right)\cdot z^2}, \end{aligned} \tag{3.40}$$

where the coefficients in (3.40) are defined by

$$\begin{aligned} b_0 &= 2T_s^2\tilde{V}_M\tilde{V}_P\alpha_{P,\max}k_P\omega_P\,\mathrm{sinc}\left(\alpha_P\right)\sin\left(\alpha_M\right), \\ a_0 &= C_H\cos\left(\alpha_P\right)\left(T_{uP} - T_s + T_sk_P\cdot k_1\right) + 2\alpha_{P,\max}T_s^2\tilde{V}_Pk_P\cdot k_2\cdot\omega_P\,\mathrm{sinc}\left(\alpha_P\right), \\ a_1 &= C_H\cos\left(\alpha_P\right)\left(T_sT_{uP} - 2T_{uP} + T_sk_P\cdot k_1\right), \\ a_2 &= C_HT_{uP}\cos\left(\alpha_P\right). \end{aligned}$$

Transformed into the time domain, the system input-output relation between the output y_τ and the input signal u_{FF} in the form of a difference equation becomes

$$\begin{aligned} a_0\left(\tilde{\alpha}_P, \omega_P\right) y_\tau(k) + a_1\left(\tilde{\alpha}_P, \omega_P\right) y_\tau(k+1) + a_2\left(\tilde{\alpha}_P, \omega_P\right) y_\tau(k+2) \\ = b_0\left(\tilde{\alpha}_M, \tilde{\alpha}_P, \omega_P\right) u_{FF}(k) \ . \end{aligned} \tag{3.41}$$

The output $y_\tau(k)$ should be identical to the desired value $\tau_{hd}(k)$. Given $\omega_P > 0$ and $\alpha_M = \alpha_{M,\max} \cdot \tilde{\alpha}_M$, with $\tilde{\alpha}_M \in [\epsilon_M, 1]$ and $\epsilon_M > 0$, $b_0\left(\tilde{\alpha}_M, \tilde{\alpha}_P, \omega_P\right) \neq 0$, equation (3.41) is solvable. Substituting $y_\tau(k) = \tau_{hd}(k)$ in (3.41) and solving for the feedforward control input $u_{FF}(k)$ result in

$$u_{FF}(k) = k_{F,0}\ \tau_{hd}(k) + k_{F,1}\ \tau_{hd}(k+1) + k_{F,2}\ \tau_{hd}(k+2) \ , \tag{3.42}$$

where the gain-scheduled coefficients $k_{F,i}$ are defined by

$$k_{F,i} = \frac{a_i(\tilde{\alpha}_P, \omega_P)}{b_0(\tilde{\alpha}_M, \tilde{\alpha}_P, \omega_P)} \ , \ \text{with } i = 0, 1, 2 \ . \tag{3.43}$$

For a causal implementation of the control law (3.42), the desired trajectory $\tau_{hd}(k)$ is shifted by two sample steps in backward time direction. The feedforward control law finally becomes

$$u_{FF}(k) = k_{F,0}\, \tau_{Md}(k-2) + k_{F,1}\, \tau_{Md}(k-1) + k_{F,2}\, \tau_{Md}(k) \ . \tag{3.44}$$

Disturbance Compensation

For an accurate tracking result, the disturbance term v in (3.24) needs to be compensated. The transfer function describing the response of the controlled output y_τ upon the disturbance input v reads

$$\begin{aligned} G_e(z) = \frac{Y_\tau\left(z\right)}{V\left(z\right)} &= \mathbf{c}^T \left(z\mathbf{I} - \mathbf{A}_c\right)^{-1} \mathbf{d}_d \\ &= \frac{b_1\left(\tilde{\alpha}_M, \tilde{\alpha}_P\right) z + b_2\left(\tilde{\alpha}_M, \tilde{\alpha}_P\right)}{a_0\left(\tilde{\alpha}_P, \omega_P\right) + a_1\left(\tilde{\alpha}_P, \omega_P\right) \cdot z + a_2\left(\tilde{\alpha}_P, \omega_P\right) \cdot z^2} \ , \end{aligned} \tag{3.45}$$

with

$$\begin{aligned} b_1 &= -T_s \tilde{V}_M T_{uP} \cos\left(\alpha_P\right) \sin\left(\alpha_M\right) , \\ b_2 &= -T_s \tilde{V}_M T_{uP} \cos\left(\alpha_P\right) \sin\left(\alpha_M\right) \left(T_s - T_{uP} + T_s k_P \cdot k_1\right) . \end{aligned}$$

An ideal compensation becomes possible if the following condition is fulfilled

$$Y_\tau(z) = G_b(z) \cdot U_{DC}(z) + G_e(z) \cdot V(z) \stackrel{!}{=} 0 \ , \tag{3.46}$$

where $U_{DC}(z)$ is the disturbance compensation law which is chosen properly. Given $G_b(z) \neq 0$ according to (3.40), solving (3.46) for $U_{DC}(z)$ results in

$$\begin{aligned} U_{DC}(z) &= -\frac{G_e(z)}{G_b(z)} \cdot V(z) \\ &= \frac{-b_1\left(\tilde{\alpha}_M, \tilde{\alpha}_P\right) z - b_2\left(\tilde{\alpha}_M, \tilde{\alpha}_P\right)}{b_0\left(\tilde{\alpha}_M, \tilde{\alpha}_P, \omega_P\right)} \ . \end{aligned} \tag{3.47}$$

By denoting

$$\begin{aligned} k_{D,0}\left(\tilde{\alpha}_M, \tilde{\alpha}_P, \omega_P\right) &= \frac{-b_2\left(\tilde{\alpha}_M, \tilde{\alpha}_P\right)}{b_0\left(\tilde{\alpha}_M, \tilde{\alpha}_P, \omega_P\right)}, \\ k_{D,1}\left(\tilde{\alpha}_M, \tilde{\alpha}_P, \omega_P\right) &= \frac{-b_1\left(\tilde{\alpha}_M, \tilde{\alpha}_P\right)}{b_0\left(\tilde{\alpha}_M, \tilde{\alpha}_P, \omega_P\right)}, \end{aligned}$$

the compensation law can be presented as follows

$$u_{DC}(k) = k_{D,0}(\tilde{\alpha}_P, \omega_P)\, v(k-1) + k_{D,1}(\tilde{\alpha}_P, \omega_P)\, v(k) \ , \tag{3.48}$$

where the current and past values of the disturbance input are involved.

Finally, the control input signal applied to the system is evaluated as the summation of all individual contributions of the designed controls according to

$$u_p(k) = u_{FB}(k) + u_{FF}(k) + u_{DC}(k) \ . \tag{3.49}$$

Control Design for the Hydraulic Motor

The motor shaft at the test rig has only a small mass moment of inertial. A high output torque at the motor shaft, consequently, may result in a very high motor angular velocity. Therefore, for the control of the hydraulic torque, the motor needs to be synchronized properly to produce the required angular velocity. For this purpose, the corresponding desired motor angular velocity is calculated according to the dynamics of the system. Let's consider the last equation of the system model

$$\dot{\omega}_M = -\frac{d_V}{J_V}\omega_M + \frac{\tilde{V}_M}{J_V}\sin(\alpha_M)\Delta p - \frac{\tau_U}{J_V}, \tag{3.50}$$

where τ_U accounts for both the load torque and disturbance torques, and the hydraulic torque is defined by $\tau_h = \tilde{V}_M \sin(\alpha_M)\Delta p$. The total torque τ_M acting on the motor shaft is evaluated with $\tau_M = \tau_h - \tau_U$, the motor velocity dynamics is obtained from (3.50) as follows

$$J_V\dot{\omega}_M + d_V\omega_M = \tau_M. \tag{3.51}$$

The resulting motor angular velocity, then, is calculated by the following transfer function

$$\omega_M(s) = \frac{1}{J_V s + d_V}\tau_M(s), \tag{3.52}$$

which is represented in the discrete form by

$$\omega_M(z) = \frac{T_s}{J_V z + T_s \cdot d_V - J_V}\tau_M(z). \tag{3.53}$$

The desired value of the motor angular velocity that is required by the trajectory scheduling module can be calculated using (3.53) to produce the desired trajectory for the motor bent-axis angle with the substitution of $\tau_M = \tau_{hd} - \tau_U$. For the tracking of the desired trajectory of the bent-axis angle, a linear optimal tracking control is applied to the hydraulic motor, which is detailed in the sequel.

The dynamics of motor bent-axis angle is governed by a simple first-order lag behavior – equation (3.21) – which can be represented by

$$\dot{\tilde{\alpha}}_M = a_M\, \tilde{\alpha}_M + b_M\, u_M, \tag{3.54}$$

where $a_M = -\frac{1}{T_{uP}}$ and $b_M = \frac{k_M}{T_{uM}}$. The time discretization of (3.54) using the explicit Euler method results in

$$\begin{aligned} \tilde{\alpha}_M(k+1) &= (1 + T_s a_M)\, \tilde{\alpha}_M(k) + T_s b_M u_M(k) \\ &= a_{dM}\tilde{\alpha}_M(k) + b_{dM}u_M(k) \ , \end{aligned} \tag{3.55}$$

with the corresponding discrete-time system matrix and input vector a_{dM} and b_{dM}, which are scalar in the given case. Given the weighting factors r_M and q_M, a discrete-time optimal feedback control can be applied using the built-in "dlqr" routine. With the optimal feedback gain k_M, the feedback control law can be established as follows

$$u_{MFB}(k) = -k_M \tilde{\alpha}_M(k). \tag{3.56}$$

In order to follow the desired output $\tilde{\alpha}_{Md}$, a feedforward control can be easily designed. The mentioned feedforward control law is given by

$$u_{MFF}(k) = k_{MF,0}\, \tilde{\alpha}_{Md}(k) + k_{MF,1} \tilde{\alpha}_{Md}(k+1)\ , \tag{3.57}$$

where $k_{MF,0} = -\frac{a_{dM}}{b_{dM}}$ and $k_{MF,1} = \frac{1}{b_{dM}}$ are the feedforward gains. Similarly to the control design of the hydraulic pump, the desired trajectory $\tilde{\alpha}_{Md}(k)$ is shifted one time step backwards for a causal implementation of the control law

$$u_{MFF}(k) = k_{MF,0}\, \tilde{\alpha}_{Md}(k-1) + k_{MF,1} \tilde{\alpha}_{Md}(k)\ . \tag{3.58}$$

The overall control input for the hydraulic motor becomes

$$u_M(k) = u_{MFF}(k) + u_{MFB}(k). \tag{3.59}$$

UKF for State and Disturbance Estimation

The control designs for both the hydraulic pump and motor require a feedback of the system states $\tilde{\alpha}_P$, $\tilde{\alpha}_M$ and the estimation of the unknown disturbances q_U, τ_U. For this purpose, a UKF is deployed. Please refer to Sect. 3.1.1 for the details of a UKF design. Fig. 3.5 shows the whole implemented control structure.

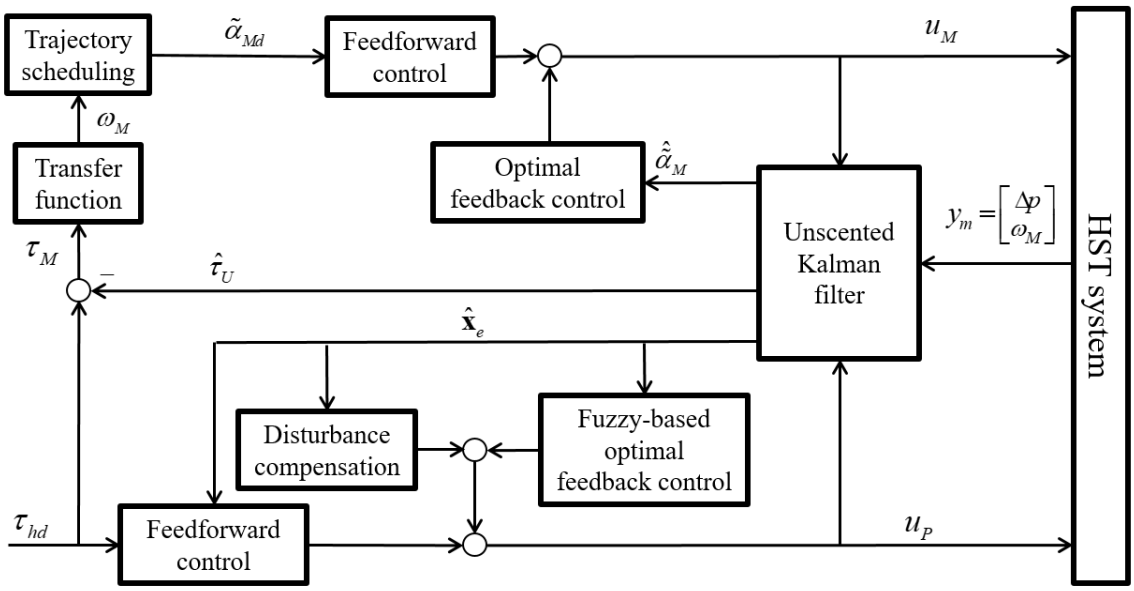

Figure 3.5: The control structure of the TS fuzzy-based LQR design.

3.1.3 State-Dependent Integral State Feedback for Torque Control (SIF)

This discrete-time control design possesses many similarities with the one in Sect. 3.1.2. In a decentralized control structure, the bent-axis angle and the torque of hydraulic motor are controlled separately. In previous design, the LQR design is applied by solving the Riccati equation off-line, and the feedback control gains are determined based on Takagi-Sugeno fuzzy methods. In the sequel, the LQR design is again used to address the nonlinear system, however, the technique is deployed for an online-solution of the state-dependent Riccati equation (SDRE) [140–142] to obtain the state-dependent feedback gains of an integral state feedback control [61].

State-Dependent Integral State Feedback Control for Hydraulic Pumps

For the control design of the hydraulic pump for the torque tracking, let's consider again the quasi-linear system (3.24)

$$\begin{aligned} \dot{\mathbf{x}}_\tau &= \mathbf{A}(\tilde{\alpha}_P, \omega_P)\, \mathbf{x}_\tau + \mathbf{b}\, u_P + \mathbf{d}\, v, \\ y_\tau &= \mathbf{c}^T(\tilde{\alpha}_M)\, \mathbf{x}_\tau \ , \end{aligned} \tag{3.60}$$

with

$$\mathbf{A}\left(\tilde{\alpha}_P, \omega_P\right) = \begin{bmatrix} -\dfrac{1}{T_{uP}} & 0 \\ \dfrac{2\tilde{V}_P \omega_P \operatorname{sinc}\left(\alpha_P\right) \cdot \alpha_{P,\max}}{C_H \cos\left(\alpha_P\right)} & 0 \end{bmatrix}, \mathbf{b} = \begin{bmatrix} \dfrac{k_P}{T_P} \\ 0 \end{bmatrix},$$
$$\mathbf{x}_\tau = \begin{bmatrix} \tilde{\alpha}_P \\ \Delta p \end{bmatrix}, \mathbf{d} = \begin{bmatrix} 0 \\ -\frac{1}{C_H} \end{bmatrix}, \mathbf{c} = \begin{bmatrix} 0 \\ \tilde{V}_M \sin\left(\alpha_M\right) \end{bmatrix}$$

and $v = 2\tilde{V}_M \omega_M \sin\left(\alpha_M\right) + q_U$.

The design of an integral state feedback control [143] in this work is based on the SDRE. The state-dependent system matrix, at each time step, is calculated and employed in the DLQR technique to obtain the corresponding feedback gains. For this purpose, the term v in (3.60) can be discarded, moreover the system is augmented with an integral w_τ which is defined by

$$\dot{w}_\tau = e_\tau = y_{\tau,d} - y_\tau, \tag{3.61}$$

where e stands for the torque tracking error, $y_{\tau,d}$ is the desired value and y_τ presents the controlled output. The augmented system becomes

$$\begin{aligned} \dot{\mathbf{x}}_a &= \bar{\mathbf{A}}(\tilde{\alpha}_M, \tilde{\alpha}_P, \omega_P)\, \mathbf{x}_a + \bar{\mathbf{b}}\, u_{SFB} + \bar{\mathbf{e}}\, y_{\tau,d} \ , \\ y_\tau &= \bar{\mathbf{c}}^T(\tilde{\alpha}_M)\, \mathbf{x}_a \ , \end{aligned} \tag{3.62}$$

with a new introduction of the feedback control signal u_{SFB}. The augmented system matrices are represented as follows

$$\begin{aligned} &\bar{\mathbf{A}}\left(\tilde{\alpha}_M, \tilde{\alpha}_P, \omega_P\right) = \begin{bmatrix} \mathbf{A}\left(\tilde{\alpha}_P, \omega_P\right) & \mathbf{0} \\ -\mathbf{c}^T(\tilde{\alpha}_M) & 0 \end{bmatrix}, \ \mathbf{x}_a = \begin{bmatrix} \mathbf{x}_\tau \\ w_\tau \end{bmatrix}, \\ &\bar{\mathbf{b}} = \begin{bmatrix} \mathbf{b} \\ 0 \end{bmatrix}, \ \bar{\mathbf{e}} = \begin{bmatrix} \mathbf{0} \\ 1 \end{bmatrix}, \ \bar{\mathbf{c}}^T(\tilde{\alpha}_M) = \begin{bmatrix} \mathbf{c}^T(\tilde{\alpha}_M) & 0 \end{bmatrix}. \end{aligned} \tag{3.63}$$

Similarly to previous optimal control design, for a successful SDRE control, the solvability of the Riccati equation must be guaranteed. Therefore, the chosen system matrix must fulfill

point-wise the Kalman's controllability criterion in the whole operating range

$$\begin{array}{l} \bar{\mathbf{K}}_C(\cdot) = \left[\begin{array}{ccc} \bar{\mathbf{b}} & \bar{\mathbf{A}}(\cdot)\,\bar{\mathbf{b}} & \bar{\mathbf{A}}^2(\cdot)\,\bar{\mathbf{b}} \end{array}\right], \\ \det\left(\bar{\mathbf{K}}_C(\cdot)\right) \neq 0. \end{array} \tag{3.64}$$

In the given case, this leads to

$$\det\left(\bar{\mathbf{K}}_C(\cdot)\right) = \frac{-4\tilde{V}_M\tilde{V}_P^2\alpha_{P,\max}^2 k_P^3\omega_P^2\,\mathrm{sinc}^2(\alpha_P)\sin(\alpha_M)}{C_H^2 T_{uP}^3\cos^2(\alpha_P)} \ .$$

Provided that $\alpha_M = \alpha_{M,\max}\cdot\tilde{\alpha}_M$, with $\tilde{\alpha}_M \in [\epsilon_M, 1]$, $\epsilon_M > 0$ and $\omega_P > 0$, Kalman's controllability criterion is fulfilled.

For the discrete-time control design, the system is discretized using the explicit Euler method. Thereby, the system can be transformed into the discrete form with time index k according to

$$\mathbf{x}_a(k+1) = \bar{\mathbf{A}}_d\mathbf{x}_a(k) + \bar{\mathbf{b}}_d\,u_{SFB}(k) \ , \tag{3.65}$$

with $\bar{\mathbf{A}}_d = \mathbf{I} + T_s\,\bar{\mathbf{A}}$, $\bar{\mathbf{b}}_d = T_s\,\bar{\mathbf{b}}$. The discrete-time optimal control technique – DLQR – is now employed resulting in a state- and parameter-dependent feedback gain vector $\bar{\mathbf{k}}^T(\tilde{\alpha}_M, \tilde{\alpha}_P, \omega_P)$, which is the solution of the minimization problem of a quadratic cost function

$$\bar{J}_\tau = \sum_{k=1}^{\infty}\left[\mathbf{x}_a^T(k)\,\bar{\mathbf{Q}}\,\mathbf{x}_a(k) + \bar{r}\,u_{SFB}^2(k)\right] \ , \tag{3.66}$$

where the positive definite matrix $\bar{\mathbf{Q}} > 0$ and the scalar $\bar{r} > 0$ are the weighting factors of the augmented system state vector $\mathbf{x}_a$ and the scalar input u_{SFB} respectively. The online solution of the algebraic Riccati equation

$$\bar{\mathbf{A}}_d^T[(\bar{\mathbf{S}} - \bar{\mathbf{S}}\,\bar{\mathbf{b}}_d(\bar{r} + \bar{\mathbf{b}}_d^T\bar{\mathbf{S}}\bar{\mathbf{b}}_d)^{-1}\bar{\mathbf{b}}_d^T\bar{\mathbf{S}}]\bar{\mathbf{A}}_d + \bar{\mathbf{Q}} = \bar{\mathbf{S}} \tag{3.67}$$

results in a symmetric, positive definite solution $\bar{\mathbf{S}} = \bar{\mathbf{S}}^T > 0$. Then, the feedback gains become

$$\bar{\mathbf{k}}^T = (\bar{r} + \bar{\mathbf{b}}_d^T\bar{\mathbf{S}}\bar{\mathbf{b}}_d)^{-1}\bar{\mathbf{b}}_d^T\,\bar{\mathbf{S}}\bar{\mathbf{A}}_d, \tag{3.68}$$

which are calculated by using the built-in routine "dlqr" in the control software. The feedback law finally results in

$$u_{SFB}(k) = -\bar{\mathbf{k}}^T(\tilde{\alpha}_M, \tilde{\alpha}_P, \omega_P)\,\mathbf{x}_a(k) \ . \tag{3.69}$$

The implementation of the state-dependent control concept is depicted in Fig. (3.6). Here, the feedback gain vector $\bar{\mathbf{k}}^T = \left[\begin{array}{cc} \mathbf{k}_\tau^T & k_I \end{array}\right]$ consists of two components - the component $\mathbf{k}_\tau^T$ corresponds to the feedback of $\mathbf{x}_\tau$ of the original system, whereas the component k_I is the corresponding feedback gain of the integrated tracking error w_τ.

The stability of SDRE approaches is till need to be addressed [144,145]. In this work, the closed-loop stability of the state-dependent system matrix $\bar{\mathbf{A}}_c = \bar{\mathbf{A}}_d - \bar{\mathbf{b}}_d\,\bar{\mathbf{k}}^T$ is analyzed by means of LMIs methods in a similar manner as proposed in [134] for Takagi-Sugeno fuzzy systems. For a stability analysis purpose, let's consider the two nonlinear functions of the augmented system matrix $\bar{\mathbf{A}}_d$

$$\begin{array}{c} f_A(\tilde{\alpha}_P, \omega_P) = \dfrac{2\tilde{V}_P\omega_P\,\mathrm{sinc}(\alpha_P)\cdot\alpha_{P,\max}}{C_H\cos(\alpha_P)}, \\ f_c(\tilde{\alpha}_M) = \tilde{V}_M\sin(\alpha_M) \ . \end{array} \tag{3.70}$$

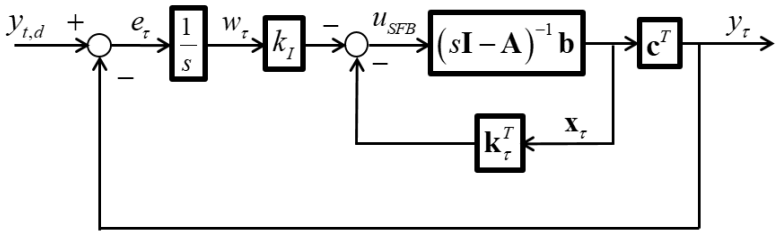

Figure 3.6: The block diagram of the feedback control (presented in continuous form).

Each of these function has a maximum and minimum value, so that the combinations of these values form four vertex system models, $\bar{\mathbf{A}}_{d,i}, i = \{1,2,3,4\}$. The DLQR technique can be applied to find the corresponding feedback gain vectors $\bar{\mathbf{k}}_i^T, i = \{1,2,3,4\}$, which result in the closed-loop system matrices $\bar{\mathbf{A}}_{c,i} = \bar{\mathbf{A}}_{d,i} - \bar{\mathbf{b}}_d\,\bar{\mathbf{k}}_i^T$. These four closed-loop system matrices cover the characteristics of the system in the whole working range. The stability of the closed-loop system at any working point is guaranteed, according to [134], by the existence of a common Lyapunov function for all vertex systems. This common Lyapunov function can be found by means of YALMIP and SeDuMi [138, 139], which satisfies the following set of inequalities

$$\bar{\mathbf{P}}_L > 0,\ \bar{\mathbf{A}}_{c,i}^T\,\bar{\mathbf{P}}_L\,\bar{\mathbf{A}}_{c,i} - \bar{\mathbf{P}}_L < 0, \quad i \in \{1,...,4\}\ . \tag{3.71}$$

Disturbance Compensation

A further improvement of the tracking performance can be achieved by compensating the disturbance term v in (3.60). The corresponding transfer function for disturbance compensation, which accounts only the state feedback loop, from the term v to the controlled output y_τ becomes

$$G_d(z) = \frac{Y_\tau(z)}{V(z)} = \mathbf{c}^T\left(z\mathbf{I} - \tilde{\mathbf{A}}_c\right)^{-1}\mathbf{d}_d\,. \tag{3.72}$$

Here,

$$\tilde{\mathbf{A}}_c = \mathbf{A}_d - \mathbf{b}_d\mathbf{k}_\tau^T,$$
$$\mathbf{A}_d = \mathbf{I} + T_s\,\mathbf{A}, \mathbf{b}_d = T_s\,\mathbf{b},\ \mathbf{d}_d = T_s\,\mathbf{d}$$

and $\mathbf{k}_\tau^T = \begin{bmatrix} k_{\tau,1} & k_{\tau,2} \end{bmatrix}$. Given a proper choice of the compensation law $U_{SDC}(z)$, an ideal rejection of the disturbance can be achieved by satisfying the following condition

$$Y_\tau(z) = G_c(z)\cdot U_{SDC}(z) + G_d(z)\cdot V(z) \stackrel{!}{=} 0\ , \tag{3.73}$$

where $G_c(z) = \mathbf{c}^T\left(z\mathbf{I} - \tilde{\mathbf{A}}_c\right)^{-1}\mathbf{b}_d$ holds. Solving (3.73) for $U_{DC}(z)$ results in the dynamic disturbance compensation law

$$U_{SDC}(z) = -\frac{G_d(z)}{G_c(z)}\cdot V(z)\ , \tag{3.74}$$

where

$$\begin{aligned} G_d(z) &= \frac{b_{\tau,1}\left(\tilde{\alpha}_M,\tilde{\alpha}_P\right)z + b_{\tau,2}\left(\tilde{\alpha}_M,\tilde{\alpha}_P\right)}{a_{\tau,0}\left(\tilde{\alpha}_P,\omega_P\right) + a_{\tau,1}\left(\tilde{\alpha}_P,\omega_P\right)\cdot z + a_{\tau,2}\left(\tilde{\alpha}_P,\omega_P\right)\cdot z^2}\ , \\ G_c(z) &= \frac{b_{\tau,0}\left(\tilde{\alpha}_M,\tilde{\alpha}_P,\omega_P\right)}{a_{\tau,0}\left(\tilde{\alpha}_P,\omega_P\right) + a_{\tau,1}\left(\tilde{\alpha}_P,\omega_P\right)\cdot z + a_{\tau,2}\left(\tilde{\alpha}_P,\omega_P\right)\cdot z^2} \end{aligned} \tag{3.75}$$

holds, with

$$
\begin{aligned}
b_{\tau,0} &= 2T_s^2 \tilde{V}_M \tilde{V}_P \alpha_{P,\max} k_P \omega_P \operatorname{sinc}(\alpha_P) \sin(\alpha_M), \\
b_{\tau,1} &= -T_s \tilde{V}_M T_{uP} \cos(\alpha_P) \sin(\alpha_M), \\
b_{\tau,2} &= -T_s \tilde{V}_M T_{uP} \cos(\alpha_P) \sin(\alpha_M) (T_s - T_{uP} + T_s k_P \cdot k_{\tau,1}).
\end{aligned}
$$

Provided that the physical parameters $b_{\tau,0} \neq 0$, $b_{\tau,1} \neq 0$ and $b_{\tau,2} \neq 0$, the system $G_c(z)$ can be inverted and leads to

$$
U_{SDC}(z) = \frac{-b_{\tau,1}(\tilde{\alpha}_M, \tilde{\alpha}_P) z - b_{\tau,2}(\tilde{\alpha}_M, \tilde{\alpha}_P)}{b_{\tau,0}(\tilde{\alpha}_M, \tilde{\alpha}_P, \omega_P)} V(z) \ . \tag{3.76}
$$

By denoting

$$
\begin{aligned}
k_{V,0}(\tilde{\alpha}_M, \tilde{\alpha}_P, \omega_P) &= \frac{-b_{\tau,1}(\tilde{\alpha}_M, \tilde{\alpha}_P)}{b_{\tau,0}(\tilde{\alpha}_M, \tilde{\alpha}_P, \omega_P)}, \\
k_{V,1}(\tilde{\alpha}_M, \tilde{\alpha}_P, \omega_P) &= \frac{-b_{\tau,2}(\tilde{\alpha}_M, \tilde{\alpha}_P)}{b_{\tau,0}(\tilde{\alpha}_M, \tilde{\alpha}_P, \omega_P)},
\end{aligned}
$$

the compensation law can be represented as follows

$$
u_{SDC}(k) = k_{V,0}(\tilde{\alpha}_P, \omega_P) v(k) + k_{V,1}(\tilde{\alpha}_P, \omega_P) v(k-1). \tag{3.77}
$$

The overall control for the output tracking is evaluated with the sum of the contributions from the feedback and disturbance compensation controls

$$
u_P = u_{SFB} + u_{SDC} \ . \tag{3.78}
$$

State and Disturbance Observer Design Using SDRE Techniques

The proposed control design involves the system state feedback and the estimate of the disturbance q_U for compensation according to (3.60), therefore, an observer is required. In this design, a state-dependent optimal observer is designed to construct the estimates for all required variables. For the design of the observer, the state vector in the system (2.11) is extended by the following disturbance models

$$
\begin{aligned}
\dot{\tau}_U &= 0, \\
\dot{q}_U &= 0 \ ,
\end{aligned} \tag{3.79}
$$

then, the extended state vector can be represented as follows

$$
\mathbf{x}_e = \begin{bmatrix} \tilde{\alpha}_P & \tilde{\alpha}_M & \Delta p & \omega_M & q_U & \tau_U \end{bmatrix}^T. \tag{3.80}
$$

The system outputs are defined by

$$
\mathbf{y}_m = \begin{bmatrix} \Delta p \\ \omega_M \end{bmatrix} = \begin{bmatrix} 0 & 0 & 1 & 0 & 0 & 0 \\ 0 & 0 & 0 & 1 & 0 & 0 \end{bmatrix} \mathbf{x}_e = \mathbf{C}_m \mathbf{x}_e. \tag{3.81}
$$

The observer is also designed based on the SDRE technique exploiting the duality principle in a similar manner as used in the SDRE design for the feedback control introduced before. For this purpose, the extended system model is rewritten in the form of state-dependent matrices as follows

$$
\dot{\mathbf{x}}_e = \mathbf{A}_e(\mathbf{x}_e) \mathbf{x}_e + \mathbf{B}_e \mathbf{u}, \tag{3.82}
$$

where the state-dependent system matrix $\mathbf{A}_e(\mathbf{x}_e)$ and the input matrix $\mathbf{B}_e$ read

$$\begin{aligned}\mathbf{A}_e &= \begin{bmatrix} -\frac{1}{T_{uP}} & 0 & 0 & 0 & 0 & 0 \\ 0 & -\frac{1}{T_{uM}} & 0 & 0 & 0 & 0 \\ f_1(\cdot) & f_2(\cdot) & 0 & 0 & -\frac{1}{C_H} & 0 \\ 0 & 0 & f_3(\cdot) & -\frac{d_V}{J_V} & 0 & -\frac{1}{J_V} \\ 0 & 0 & 0 & 0 & 0 & 0 \\ 0 & 0 & 0 & 0 & 0 & 0 \end{bmatrix}, \\ \mathbf{B}_e^T &= \begin{bmatrix} \frac{k_P}{T_{uP}} & 0 & 0 & 0 & 0 & 0 \\ 0 & \frac{k_M}{T_{uM}} & 0 & 0 & 0 & 0 \end{bmatrix}.\end{aligned} \tag{3.83}$$

The input is defined by $\mathbf{u} = \begin{bmatrix} u_P & u_M \end{bmatrix}^T$, the nonlinear functions are given by

$$\begin{aligned} f_1(\tilde{\alpha}_P, \omega_P) &= \frac{2\tilde{V}_P \omega_P \operatorname{sinc}(\alpha_P)\, \alpha_{P,max}}{C_H \cos(\alpha_P)}, \\ f_2(\tilde{\alpha}_M, \omega_M) &= \frac{-2\tilde{V}_M \omega_M \operatorname{sinc}(\alpha_M)\, \alpha_{M,max}}{C_H}, \\ f_3(\tilde{\alpha}_M) &= \frac{\tilde{V}_M \sin(\alpha_M)}{J_V}. \end{aligned}$$

Here, $\alpha_M = \alpha_{M,\max} \cdot \tilde{\alpha}_M$ and $\alpha_P = \alpha_{P,\max} \cdot \tilde{\alpha}_P$ hold.

The selection of the state-dependent presentation in (3.83) is not unique. For a successful design of an observer, however, Kalman's observability criterion [141] must be ensured, namely

$$\mathbf{K}_e(\cdot) = \begin{bmatrix} \mathbf{C}_m \\ \mathbf{C}_m \mathbf{A}_e(\cdot) \\ \mathbf{C}_m \mathbf{A}_e^2(\cdot) \\ \mathbf{C}_m \mathbf{A}_e^3(\cdot) \\ \mathbf{C}_m \mathbf{A}_e^4(\cdot) \\ \mathbf{C}_m \mathbf{A}_e^5(\cdot) \end{bmatrix} \tag{3.84}$$

must have full rank. Given the available measurements, the chosen form of the state-dependent system matrix (3.83) leads to $rank(\mathbf{K}_e) = 6$, which is equal to the order of the system matrix and fulfills the observability criterion. Please note again that this observability criterion only guarantees the solvability of the Riccati equation but does not make any statement regarding nonlinear observability. Independently, with measurements of the motor angular velocity and the different pressure nonlinear observability of the extended state vector can be proven.

The discretization of system matrices using explicit Euler method results in

$$\mathbf{x}_e(k+1) = \mathbf{A}_{ed}\, \mathbf{x}_e(k) + T_s \mathbf{B}_e \mathbf{u}(k), \tag{3.85}$$

with $\mathbf{A}_{ed} = \mathbf{I} + T_s \mathbf{A}_e$ and $\mathbf{B}_{ed} = T_s \mathbf{B}_e$. Finally, the observer equation is given in the following form [91, 92]

$$\hat{\mathbf{x}}_e(k+1) = \mathbf{A}_{ed} \hat{\mathbf{x}}_e(k) + \mathbf{B}_{ed} \mathbf{u}(k) + \mathbf{H}_e \left(\mathbf{y}_m - \mathbf{C}_m \hat{\mathbf{x}}_e(k) \right). \tag{3.86}$$

In equation (3.86), the observer gain matrix $\mathbf{H}_e$ is determined online by the DLQR technique which solve the optimization problem for the following cost function

$$J_e = \sum_{k=1}^{\infty} \left[\tilde{\mathbf{x}}_e^T(k)\, \mathbf{Q}_e \tilde{\mathbf{x}}_e(k) + \tilde{\boldsymbol{y}}_m^T(k)\, \mathbf{R}_e \tilde{\boldsymbol{y}}_m(k) \right], \tag{3.87}$$

where $\tilde{\mathbf{x}}_\mathbf{e}$ is the observation error vector and $\tilde{\boldsymbol{y}}_m$ is the measurement error vector. $\mathbf{Q}_e$ and $\mathbf{R}_e$ are the symmetric positive definite diagonal weighting matrices. The DLQR technique solves online the following discrete-time algebraic Riccati equation

$$\mathbf{A}_{ed}^T \left[(\mathbf{S}_e - \mathbf{S}_e \, \mathbf{C}_m (\mathbf{R}_e + \mathbf{C}_m^T \mathbf{S}_e \mathbf{C}_m)^{-1} \mathbf{C}_e^T \mathbf{S}_e \right] \mathbf{A}_{ed} + \mathbf{Q}_e = \mathbf{S}_e, \tag{3.88}$$

that results in a positive definite solution $\mathbf{S}_e = \mathbf{S}_e^T > 0$. The state-dependent optimal observer gain matrix $\mathbf{H}_e$ follows according to

$$\mathbf{H}_e = (\mathbf{R}_e + \mathbf{C}_m^T \mathbf{S}_e \mathbf{C}_m)^{-1} \mathbf{C}_m^T \mathbf{S}_e \mathbf{A}_{ed}, \tag{3.89}$$

which is also determined by exploiting the "dlqr" built-in routine of the test equipment driver.

For the stability analysis of the proposed observer, the same approach used in the control design is again exploited. Here, $2^3 = 8$ vertex models of the system – which corresponds to the number of the combination constituted from three functions f_1, f_2 and f_3 w.r.t. their minimum and maximum – are established resulting in 8 corresponding observer structures

$$\mathbf{O}_{e,i} = \mathbf{A}_{e,i} - \mathbf{H}_{e,i} \mathbf{C}_m, \quad i \in \{1, ..., 8\} \tag{3.90}$$

with $\mathbf{H}_{e,i}$ denoting the corresponding observer gain matrices of the vertex models. By means of YALMIP and SeDuMi [138,139], a joint Lyapunov function $\mathbf{P}_e$ has been found satisfying the following matrix inequalities

$$\mathbf{P}_e > 0, \; \mathbf{O}_{e,i}^T \, \mathbf{P}_e \, \mathbf{O}_{e,i} - \mathbf{P}_e < 0, \quad i \in \{1, ..., 8\} \; . \tag{3.91}$$

According to [134], the stability of the observer is guaranteed.

The implementation of the proposed control – in a combination with an optimal control for the hydraulic motor which is designed already in Takagi-Sugeno fuzzy-based optimal control design section – is depicted in Fig. 3.7

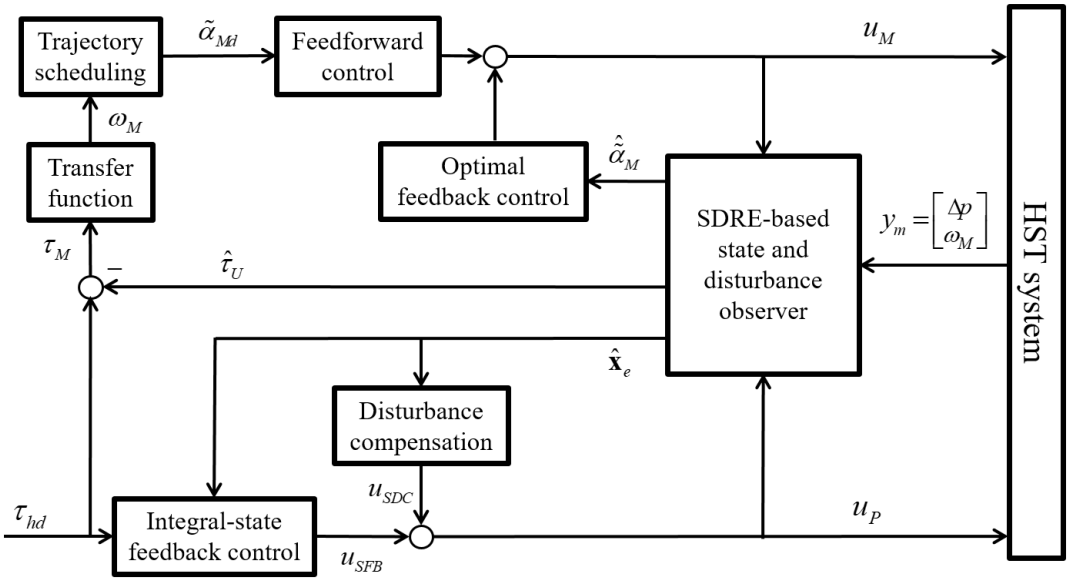

Figure 3.7: The block diagram of the implemented control structure.

3.2 Estimator-Based Feedback Linearization

The corresponding control designs are applied in a decentralized scheme. Accordingly, the system model is divided into two subsystems which serve as the basis for separate control designs of the hydraulic motor and the hydraulic pump.

- Subsystem for the control of the motor bent-axis angle – which is identical to (3.21)

$$\dot{\tilde{\alpha}}_M = -\frac{1}{T_{uM}}\tilde{\alpha}_M + \frac{k_M}{T_{uM}}u_M. \tag{3.92}$$

- Subsystem for the velocity control design

$$\begin{bmatrix} \dot{\tilde{\alpha}}_P \\ \Delta\dot{p} \\ \dot{\omega}_M \end{bmatrix} = \begin{bmatrix} -\frac{1}{T_{uP}}\tilde{\alpha}_P + \frac{k_P}{T_{uP}}u_P \\ \frac{2\tilde{V}_P}{C_H}\tan(\alpha_P)\omega_P - \frac{2\tilde{V}_M}{C_H}\sin(\alpha_M)\omega_M - \frac{q_U}{C_H} \\ -\frac{d_V}{J_V}\omega_M + \frac{\tilde{V}_M}{J_V}\sin(\alpha_M)\Delta p - \frac{\tau_U}{J_V} \end{bmatrix}, \tag{3.93}$$

  with the gain-scheduling parameter $\tilde{\alpha}_M$.

Feedback Linearization for Hydraulic Pump Control

The idea of feedback linearization is to cancel nonlinearities and to impose a desired linear dynamics. This approach has been successfully developed for applications belonging to a class of nonlinear systems whose dynamics can be described by the so-called companion form [88]. From this starting point, the application of feedback linearization to the velocity control of HST systems is straightforward as the system can be easily transformed into the companion form as presented subsequently.

In the second subsystem (3.93), which is responsible for the hydraulic pump control, the normalized bent-axis angle $\tilde{\alpha}_M$ is considered as a gain-scheduling parameter. According to the physical limitations on the real system, a small value of the hydraulic pump swash-plate angle ($|\alpha_P| \leq 18^o$) can be applied, hence, the basic trigonometric tangent function in the third equation of the system dynamics model can be approximated by

$$\tan(\alpha_P) \approx \alpha_P.$$

By applying $\alpha_P = \alpha_{P,\max} \cdot \tilde{\alpha}_P$, the corresponding dynamic subsystem for the motor angular velocity can be represented as follows

$$\begin{bmatrix} \dot{\tilde{\alpha}}_P \\ \Delta\dot{p} \\ \dot{\omega}_M \end{bmatrix} = \begin{bmatrix} -\frac{1}{T_{uP}}\tilde{\alpha}_P + \frac{k_P}{T_{uP}}u_P \\ \frac{2\tilde{V}_P}{C_H}\omega_P \cdot \alpha_{P,\max} \cdot \tilde{\alpha}_P - \frac{2\tilde{V}_M}{C_H}\sin(\alpha_M)\omega_M - \frac{q_U}{C_H} \\ -\frac{d_V}{J_V}\omega_M + \frac{\tilde{V}_M}{J_V}\sin(\alpha_M)\Delta p - \frac{\tau_U}{J_V} \end{bmatrix}. \tag{3.94}$$

It can be easily shown that the system is flat [73] by repeatedly differentiating the system output ω_M. By doing so, the third time derivative reveals the flatness property of the system output

$$\begin{aligned} \omega_M^{(3)} = &-\frac{2\tilde{V}_M^2\sin^2(\alpha_M)}{J_V C_H T_{uP}}\omega_M - \left(\frac{2\tilde{V}_M^2\sin^2(\alpha_M)}{J_V C_H} + \frac{d_V}{J_V T_{uP}}\right)\dot{\omega}_M \\ &- \left(\frac{d_V}{J_V} + \frac{1}{T_{uP}}\right)\ddot{\omega}_M - \frac{\tilde{V}_M\sin(\alpha_M)}{J_V C_H T_{uP}}q_U + \frac{2\tilde{V}_M\sin(\alpha_M)\alpha_{P,\max}\tilde{V}_P\omega_P k_P}{J_V C_H T_{uP}}u_P\,. \end{aligned} \tag{3.95}$$

The resulting relative degree is of three which is equal to the order of the subsystem, hence, no internal dynamics exists. This means that the system is stabilizable. Note that in the differentiations, terms regarding the derivatives of the disturbances appear, i.e. $\dot{\tau}_U$, $\ddot{\tau}_U$ and $\dot{q}_U$. However, for a simple design, they are discarded.

By defining

$$\mathbf{y} = \begin{bmatrix} y_0 \\ y_1 \\ y_2 \end{bmatrix} = \begin{bmatrix} \omega_M \\ \dot{\omega}_M \\ \ddot{\omega}_M \end{bmatrix} , \tag{3.96}$$

$$\begin{aligned} f\left(\mathbf{y}, q_U\right) = &-\frac{2\tilde{V}_M^2 \sin^2(\alpha_M)}{J_V C_H T_{uP}} y_0 - \left(\frac{2\tilde{V}_M^2 \sin^2(\alpha_M)}{J_V C_H} + \frac{d_V}{J_V T_{uP}}\right) y_1 \\ &- \left(\frac{d_V}{J_V} + \frac{1}{T_{uP}}\right) y_2 - \frac{\tilde{V}_M \sin(\alpha_M)}{J_V C_H T_{uP}} q_U \end{aligned} \tag{3.97}$$

and

$$g = \frac{2\tilde{V}_M \sin(\alpha_M) \alpha_{P,\max} \tilde{V}_P \omega_P k_P}{J_V C_H T_{uP}}, \tag{3.98}$$

the system can be presented in the companion form

$$y_0^{(3)} = g \cdot u_P + f\left(\mathbf{y}, q_U\right) \tag{3.99}$$

or in an equivalent controller normal form as follows

$$\begin{aligned} \dot{y}_0 &= y_1 \\ \dot{y}_1 &= y_2 \\ \dot{y}_2 &= f\left(\mathbf{y}, q_U\right) + g \cdot u_P \ . \end{aligned} \tag{3.100}$$

Provided that all parameters of the system model and the leakage disturbance q_U are perfectly known, it is possible to linearize the system by compensating all the nonlinearities and disturbances. For this purpose, an auxiliary control input υ is introduced according to

$$\upsilon = f\left(\mathbf{y}, q_U\right) + g \cdot u_P. \tag{3.101}$$

As a result, the feedback-linearized system (3.100) is described as an integrator chain of length three

$$\dot{\mathbf{y}} = \begin{bmatrix} \dot{y}_0 \\ \dot{y}_1 \\ \dot{y}_2 \end{bmatrix} = \begin{bmatrix} y_1 \\ y_2 \\ \upsilon \end{bmatrix} . \tag{3.102}$$

By using (3.102), any linear control design technique can be deployed. Here, a Lyapunov-based control is proposed.

As the relative degree of the HST system is three, the desired trajectory of the motor angular velocity is supposed to be sufficiently smooth to allow for a good tracking. Here, the time derivatives of the desired trajectory are available up to an order of three, i.e. $\dot{\omega}_{Md}$, $\ddot{\omega}_{Md}$ and $\dddot{\omega}_{Md}$ are available for the control design. To solve the tracking problem in the given case, the following Lyapunov function is introduced

$$V(\delta) = \frac{\delta^2}{2}, \tag{3.103}$$

with

$$\delta = \ddot{e} + \lambda_1 \dot{e} + \lambda_0 e \ . \tag{3.104}$$

Here, positive coefficients λ_0 and λ_1 represent the design parameters, the tracking error is given by $e = \omega_M - \omega_{Md}$, and the desired trajectory is denoted by ω_{Md}. Differentiating the variable δ results in

$$\dot{\delta} = \dddot{e} + \lambda_1 \ddot{e} + \lambda_0 \dot{e} = \dddot{\omega}_M - \dddot{\omega}_{Md} + \lambda_1 \ddot{e} + \lambda_0 \dot{e}. \tag{3.105}$$

The system can be stabilized using a feedback control law υ according to

$$\upsilon = \dot{x}_3 = \dddot{\omega}_M = \dddot{\omega}_{Md} - \lambda_1 \ddot{e} - \lambda_0 \dot{e} - k\delta \tag{3.106}$$

with the design parameter $k > 0$. Rearranging (3.106) yields

$$\dddot{\omega}_M - \dddot{\omega}_{Md} + \lambda_1 \ddot{e} + \lambda_0 \dot{e} + k\delta = 0. \tag{3.107}$$

By applying (3.105), the expression (3.107) can be equivalently presented by a first-order dynamics $\dot{\delta} + k\delta = 0$. As $k > 0$, the exponential convergence of δ toward zero is guaranteed. The tracking performance can be adjusted by tuning the positive parameters λ_0, λ_1 and k.

Finally, the system control input is defined by an inverse dynamics as follows

$$u_P = \frac{1}{g} \left[\upsilon - f\left(\mathbf{y}, q_U\right) \right]. \tag{3.108}$$

The control law requires the measurements of the angular velocity and its first two time derivatives, i.e. ω_M, $\dot{\omega}_M$ and $\ddot{\omega}_M$, to evaluate the error and for feedback linearization. This becomes possible by deploying the tracking differentiator (TD).

Tracking Differentiators

Like in feedback linearization, derivatives of output variables are required to evaluate the control law. The derivatives may be numerically approximated by means of given measurements of the output signal. Due to the unavoidable noise in the sensing process, which is magnified in the derivative signals, vibrations of the actuators may be induced, which reduces the lifetime of the mechanical structures, and clearly deteriorates the control performance. Therefore, the use of such numerically approximated derivatives in feedback control is less relevant and not recommended in practice.

To overcome this difficulty, tracking differentiators are developed for the estimation of derivatives of noisy measurement signals. In the literature, lots of alternative differentiation trackers can be found such as the high-gain observer-based differentiator, the super-twisting algorithm, Han's TD, the linear time-derivative tracker, and the robust exact differentiator. Among them, the robust exact differentiator and Han's TD seem to be superior.

The robust exact differentiator based on sliding mode techniques has been established by Levant in [80], and has been further developed in [81]. Nowadays, even a Matlab/Simulink toolbox for research and application has been created, see [82]. The differentiator has a nonlinear error dynamics, which promises a faster convergence of the estimated variables. Han's TD was proposed by Jingqing Han in 1989 and was detailed in [83] to support PID controllers with both nonlinear and linear versions available.

An nth-order nonlinear version of Han's TD has the following form

$$\begin{aligned}
\dot{\varsigma}_1 &= \varsigma_2 \\
\dot{\varsigma}_2 &= \varsigma_3 \\
&... \\
\dot{\varsigma}_n &= -R_{\varsigma n}^n \; f_\varsigma \left(\varsigma_1 - r_x, \frac{\varsigma_2}{R_{\varsigma n}}, ..., \frac{\varsigma_n}{R_{\varsigma n}^{n-1}} \right),
\end{aligned} \tag{3.109}$$

where $R_{\varsigma n} > 0$ is a tuning parameter and f_ς is a bounded nonlinear function chosen by the user. The solutions of the dynamic structure (3.109) ς_1, ς_2, ..., ς_n converge to r_x, $\dot{r}_x$,..., $r_x^{(n)}$, respectively.

Similarly, an nth-order linear version of Han' TD has been proposed as follows

$$\begin{aligned}
\dot{\varsigma}_1 &= \varsigma_2 \\
\dot{\varsigma}_2 &= \varsigma_3 \\
&... \\
\dot{\varsigma}_n &= -R_{\varsigma n}^n \left[c_{\varsigma n,1} \left(\varsigma_1 - r_x \right) + c_{\varsigma n,2} \frac{\varsigma_2}{R_{\varsigma n}} + ... + c_{\varsigma n,n} \frac{\varsigma_n}{R_{\varsigma n}^{n-1}} \right],
\end{aligned} \tag{3.110}$$

where $R_{\varsigma n} > 0$ holds, and the coefficients $c_{\varsigma n,1}$, $c_{\varsigma n,2}$,..., $c_{\varsigma n,n}$ are chosen to place the solutions of the characteristic polynomial

$$s^n + c_{\varsigma n,n} s^{n-1} + ... + c_{\varsigma n,1} = 0 \tag{3.111}$$

in the left half of the s-plane. Given properly defined parameters, the differentiator state variables ς_1, ς_2, ..., ς_n converge to r_x, $\dot{r}_x$,..., $r_x^{(n)}$, respectively.

The nonlinear tracking differentiator theoretically promises higher performance thanks to the nonlinear dynamics. In this work, however, the linear version of Han's TD (LTD) is preferred and implemented instead of other nonlinear ones due to many reasons, which are discussed in the sequel.

Firstly, the performance of a nonlinear version of the TD is still comparable to a linear one. A meaningful example for the second-order TD can be taken from [84], where the nonlinear TD is established as follows

$$\begin{aligned}
\dot{\varsigma}_1 &= \varsigma_2 \\
\dot{\varsigma}_2 &= -{R_2}^2 \left[c_1 \arctan\left(\gamma_1 (\varsigma_1 - r_x) \right) + c_2 \arctan(\gamma_2 \frac{\varsigma_2}{R_2}) \right].
\end{aligned} \tag{3.112}$$

Here, $R_2, c_1, c_2, \gamma_1, \gamma_2$ are tuning parameters. A corresponding linear version can be stated as follows

$$\begin{aligned}
\dot{\varsigma}_1 &= \varsigma_2 \\
\dot{\varsigma}_2 &= -R_{\varsigma n}^2 \left[c_{\varsigma 2,1} \left(\varsigma_1 - r_x \right) + c_{\varsigma 2,2} \frac{\varsigma_2}{R_{\varsigma 2}} \right].
\end{aligned} \tag{3.113}$$

Comparing both dynamics 3.112 and 3.113, it can be seen that they result in a similar local behavior when the estimation errors become small because near the origin the arctan function behaves linearly. The corresponding results can be found in more detail in [84]. Moreover, based on the literature research and dedicated tests made by the author of this work, it turned out

that the choice of the nonlinear function f_ς and the parameters for Han's nonlinear TD is not a trivial task, especially for high-order cases, while most of the available nonlinear structures in the literature are developed for second-order TDs only, see [85–87]. On the contrary, the determination of the linear TD is straightforward based on the specification of the characteristic polynomial, see (3.111). The simplicity of the LTD in implementation in comparison to other ones such as the robust exact differentiator is beneficial as well.

Secondly, according to [83], Han's linear TD offers many advantages regarding stability, limit conditions of the input signal, etc. over the others. The LTD also has the advantage of smoothness in comparison to the chattering phenomenon often encountered with sliding-mode-based differentiators. Additionally, it has been shown that the TD is noise-tolerant in the linear case.

The final reason stems from the performance, which has been investigated on the test rig. As indicated by test results, the LTD provides more accurate and smoother estimation of derivative signals in experiments performed on the real equipment. The performance of the LTD in comparison to the ones of a sliding-mode-based differentiator and model-based state transformation is demonstrated in Fig. 3.8.

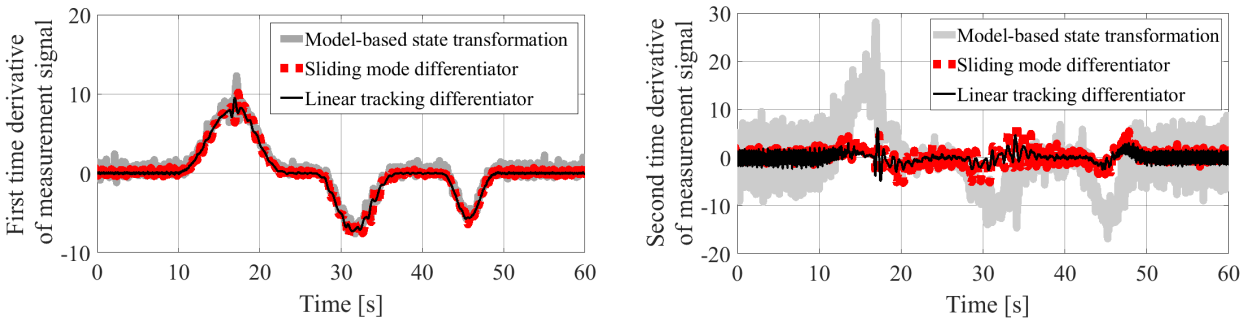

Figure 3.8: Experimental results for signal derivative estimation.

As can be seen from the Fig. 3.8, the linear tracking differentiator produces smoother signals with a slightly smaller delay in comparison to the sliding-mode-based one for both the first and second time-derivative estimates of the measurement signal, and its performance obviously outperforms the model-based state transformation as indicated in the test results.

The use of LTD for feedback control design in this work is straightforward as it has been developed for PID controller for a noise-tolerant derivative estimation [83]. For feedback linearization, the stability of closed-loop dynamics using an observer for the state feedback is discussed by A. N. Atassi et al. [91] and by A. E. Golubev et al. [89]. As an observer for state feedback – the derivatives in this case, the use of TD for feedback linearization is possible.

Back to the feedback of derivative signals for the proposed control design, a third-order LTD (LTD3) is deployed, which has the following form

$$\begin{aligned}\dot{\varsigma}_1 &= \varsigma_2\\ \dot{\varsigma}_2 &= \varsigma_3\\ \dot{\varsigma}_3 &= -R_{\varsigma 3}^3\left[c_{\varsigma 3,1}\left(\varsigma_1-\omega_M\right)+c_{\varsigma 3,2}\frac{\varsigma_2}{R_{\varsigma 3}}+c_{\varsigma 3,3}\frac{\varsigma_3}{R_{\varsigma 3}^2}\right]\end{aligned} \tag{3.114}$$

with parameters $c_{\varsigma 3,1}$, $c_{\varsigma 3,2}$ and $c_{\varsigma 3,3}$ defined according to (3.111) using pole-placement methods and $R_{\varsigma 3}$ properly chosen. Fig. 3.9 shows the principle of feedback linearization with the use of

an LTD3. Given the basic derivation above, in the sequel several estimators are investigated, which are used to address the uncertainty in the feedback linearization approach [57]:

- Reduced-order state and disturbance observer (RDO)
- Adaptive parameter estimation (APE)
- Online-trained multiple layer neural network (MLP)

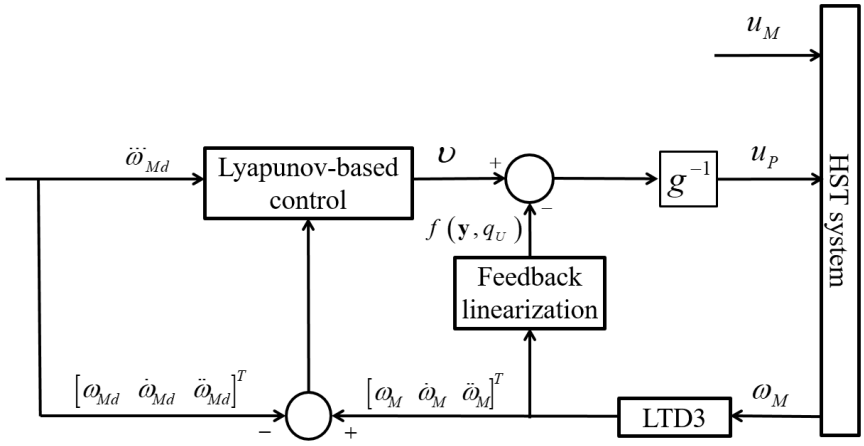

Figure 3.9: Proposed feedback linearization scheme.

3.2.1 Nonlinearity Compensation Using a State and Disturbance Observer

This control design exploits the full model of the system to realize an observer for the feedback linearization. As can be seen in the hydraulic pump control design in equation (3.97) and (3.98), the feedback loop requires the system state $\tilde{\alpha}_M$ and the disturbance q_U for nonlinearity and disturbance compensation as well as for construction of the function g. As the system states Δp and ω_M can be measured, a reduced-order disturbance observer (RDO) is employed for estimation of unmeasurable states and disturbance variables. Let's consider again the full system model (2.11), which is reintroduced here for convenience

$$\begin{bmatrix} \dot{\tilde{\alpha}}_M \\ \dot{\tilde{\alpha}}_P \\ \Delta\dot{p} \\ \dot{\omega}_M \end{bmatrix} = \begin{bmatrix} -\frac{1}{T_{uM}}\tilde{\alpha}_M + \frac{k_M}{T_{uM}}u_M \\ -\frac{1}{T_{uP}}\tilde{\alpha}_P + \frac{k_P}{T_{uP}}u_P \\ \frac{2\tilde{V}_P}{C_H}\tan(\alpha_P)\omega_P - \frac{2\tilde{V}_M}{C_H}\sin(\alpha_M)\omega_M - \frac{q_U}{C_H} \\ -\frac{d_V}{J_V}\omega_M + \frac{\tilde{V}_M}{J_V}\sin(\alpha_M)\Delta p - \frac{\tau_U}{J_V} \end{bmatrix}. \tag{3.115}$$

The equation of the observer output, as proposed in [91], reads

$$\hat{\mathbf{q}} = \mathbf{H} \cdot \mathbf{y}_m + \mathbf{p}, \tag{3.116}$$

where the following quantities are defined:

- The measured outputs are denoted by vector $\mathbf{y}_m$

$$\mathbf{y}_m = \begin{bmatrix} \Delta p \\ \omega_m \end{bmatrix}, \qquad \dot{\mathbf{y}}_m = \begin{bmatrix} \Delta \dot{p} \\ \dot{\omega}_m \end{bmatrix} = \mathbf{f}_1 \left(\mathbf{y}_m, \mathbf{q}, \mathbf{u} \right). \tag{3.117}$$

- The vector $\hat{\mathbf{q}}$ comprises the estimates of the unmeasurable states and the disturbance inputs, which are represented by the integrator disturbance models, i.e. $\dot{\tau}_U = 0$ and $\dot{q}_U = 0$.

$$\mathbf{q} = \begin{bmatrix} \tilde{\alpha}_M \\ \tilde{\alpha}_P \\ q_U \\ \tau_U \end{bmatrix}, \qquad \dot{\mathbf{q}} = \begin{bmatrix} \dot{\tilde{\alpha}}_M \\ \dot{\tilde{\alpha}}_P \\ 0 \\ 0 \end{bmatrix} = \mathbf{f}_2 \left(\mathbf{y}_m, \mathbf{q}, \mathbf{u} \right). \tag{3.118}$$

- $\mathbf{H}$ is the observer gain matrix, which has the following structure

$$\mathbf{H} = \begin{bmatrix} h_{11} & 0 & h_{31} & 0 \\ 0 & h_{22} & 0 & h_{42} \end{bmatrix}. \tag{3.119}$$

- The observer internal state vector $\mathbf{p}$ is obtained as the solution of a state equation according to

$$\dot{\mathbf{p}} = \mathbf{\Phi} \left(\mathbf{y}_m, \hat{\mathbf{q}}, \mathbf{u} \right) \ . \tag{3.120}$$

- $\mathbf{u} = [u_P, u_M]^T$ is the vector of control inputs.

The dynamic equation of the estimation error, ξ, is defined as follows

$$\dot{\xi} = \dot{\mathbf{q}} - \dot{\hat{\mathbf{q}}} = \dot{\mathbf{q}} - \mathbf{H}^T \dot{\mathbf{y}}_m - \dot{\mathbf{p}}. \tag{3.121}$$

The vector function $\mathbf{\Phi}$ follows from the design condition regarding a vanishing steady-state observer error. Substituting the definitions above into (3.121) yields the steady-state observer equation as follows

$$\mathbf{f}_2 \left(\mathbf{y}_m, \mathbf{q}, \mathbf{u} \right) - \mathbf{H}^T \mathbf{f}_1 \left(\mathbf{y}_m, \mathbf{q}, \mathbf{u} \right) - \mathbf{\Phi} \left(\mathbf{y}_m, \hat{\mathbf{q}}, \mathbf{u} \right) = \mathbf{0}. \tag{3.122}$$

Taking into account that the steady-state error $\xi = \mathbf{0}$ must be satisfied, equation (3.122) becomes

$$\mathbf{f}_2 \left(\mathbf{y}_m, \mathbf{q}, \mathbf{u} \right) - \mathbf{H}^T \mathbf{f}_1 \left(\mathbf{y}_m, \mathbf{q}, \mathbf{u} \right) - \mathbf{\Phi} \left(\mathbf{y}_m, \mathbf{q}, \mathbf{u} \right) = \mathbf{0}. \tag{3.123}$$

Solving (3.123) for the unknown function $\mathbf{\Phi}$ leads to

$$\mathbf{\Phi} \left(\mathbf{y}_m, \mathbf{q}, \mathbf{u} \right) = \mathbf{f}_2 \left(\mathbf{y}_m, \mathbf{q}, \mathbf{u} \right) - \mathbf{H}^T \mathbf{f}_1 \left(\mathbf{y}_m, \mathbf{q}, \mathbf{u} \right). \tag{3.124}$$

The convergence of the estimation error (3.121) is evaluated by the linearized dynamics. For this purpose, the Jacobian matrix $\mathbf{J}_\xi$ is derived as follows

$$\begin{aligned} \mathbf{J}_\xi &= \frac{\partial \left[\mathbf{f}_2 \left(\mathbf{y}_m, \mathbf{q}, \mathbf{u} \right) \right]}{\partial \xi} - \frac{\partial \left[\mathbf{H}^T \mathbf{f}_1 \left(\mathbf{y}_m, \mathbf{q}, \mathbf{u} \right) \right]}{\partial \xi} - \frac{\partial \left[\mathbf{\Phi} \left(\mathbf{y}_m, \hat{\mathbf{q}}, \mathbf{u} \right) \right]}{\partial \xi} \\ &= -\frac{\partial \left[\mathbf{\Phi} \left(\mathbf{y}_m, \mathbf{q} - \xi, \mathbf{u} \right) \right]}{\partial \xi} = \frac{\partial \left[\mathbf{\Phi} \left(\mathbf{y}_m, \mathbf{q} - \xi, \mathbf{u} \right) \right]}{\partial \left(\mathbf{q} - \xi \right)}. \end{aligned} \tag{3.125}$$

The asymptotic stability requires that all eigenvalues of $\mathbf{J}_\xi$ evaluated at $\xi = \mathbf{0}$ must be in the left half of the complex s-plane for all working conditions. Substituting the corresponding functions for $\mathbf{f}_1$ and $\mathbf{f}_2$ from the system model (3.115) into (3.124) results in

$$\mathbf{\Phi}\left(\mathbf{y}_m, \mathbf{q}, \mathbf{u}\right) = \begin{bmatrix} -\frac{1}{T_{uM}}\tilde{\alpha}_M + \frac{k_M}{T_{uM}}u_M \\ -\frac{1}{T_{uP}}\tilde{\alpha}_P + \frac{k_P}{T_{uP}}u_P \\ 0 \\ 0 \end{bmatrix} - \mathbf{H}^T \begin{bmatrix} \frac{2}{C_H}\tilde{V}_P \tan(\alpha_P)\omega_P - \frac{2}{C_H}\tilde{V}_M \sin(\alpha_M)\omega_M - \frac{q_u}{C_H} \\ -\frac{d_V}{J_V}\omega_M + \frac{\tilde{V}_M}{J_V}\Delta p \ \sin(\alpha_M) - \frac{\tau_u}{J_V} \end{bmatrix}. \tag{3.126}$$

The observer gain matrix $\mathbf{H}$ can be obtained by placing the eigenvalues of the Jacobian matrix according to (3.125) as follows

$$\det\left(s\mathbf{I} - \frac{\partial \mathbf{\Phi}\left(\mathbf{y}_m, \mathbf{q}, \mathbf{u}\right)}{\partial \mathbf{q}}\right) \doteq \prod_{i=1}^{4}(s + s_i), \tag{3.127}$$

where $s_i,\ i = \{1, 2, 3, 4\}$ are four positive design values which specify the negative eigenvalues of the desired characteristic polynomial. By comparing the characteristic polynomial with the desired one, the four unknown gains of the matrix $\mathbf{H}$ can be directly determined.

Control of the hydraulic motor The input-output relation of the motor bent-axis angle is characterized by the equation (3.92), it is reintroduced here for convenience.

$$\dot{\tilde{\alpha}}_M = -\frac{1}{T_{uM}}\tilde{\alpha}_M + \frac{k_M}{T_{uM}}u_M \ . \tag{3.128}$$

As the feedback of the bent-axis angle $\tilde{\alpha}_M$ is available from the RDO, this system can be stabilized using a flatness-based controller

$$u_M = \frac{1}{k_M}\tilde{\alpha}_M + \frac{T_{uM}}{k_M}\upsilon_M \ , \tag{3.129}$$

with $\upsilon_M = \dot{\tilde{\alpha}}_{Md} + k_{\alpha M} \cdot e_{\alpha M}$. Here, $k_{\alpha M}$ is a positive coefficient and $e_{\alpha M} = \tilde{\alpha}_{Md} - \tilde{\alpha}_M$ the tracking error, with $\tilde{\alpha}_{Md}$ representing the desired values.

As can be seen in (3.129), the control law requires the first time derivative $\dot{\tilde{\alpha}}_{Md}$ of the desired trajectory, which can be provided by a second-order LTD (LTD2) in the following form

$$\begin{aligned} \dot{\varsigma}_1 &= \varsigma_2 \\ \dot{\varsigma}_2 &= -R_{\varsigma 2}^2\left[c_{\varsigma 2,1}\left(\varsigma_1 - \tilde{\alpha}_{Md}\right) + c_{\varsigma 2,2}\frac{\varsigma_2}{R_{\varsigma 2}}\right] \ . \end{aligned} \tag{3.130}$$

With parameters $c_{\varsigma 2,1}$, $c_{\varsigma 2,2}$ defined by an eigenvalue placement according to the rules stated in (3.111) and $R_{\varsigma 2}$ properly chosen, the value $\dot{\tilde{\alpha}}_{Md}$ corresponds to the estimate ς_2.

Fig. 3.10 presents the whole control structure for the velocity tracking of HST systems exploiting feedback linearization by means of the RDO.

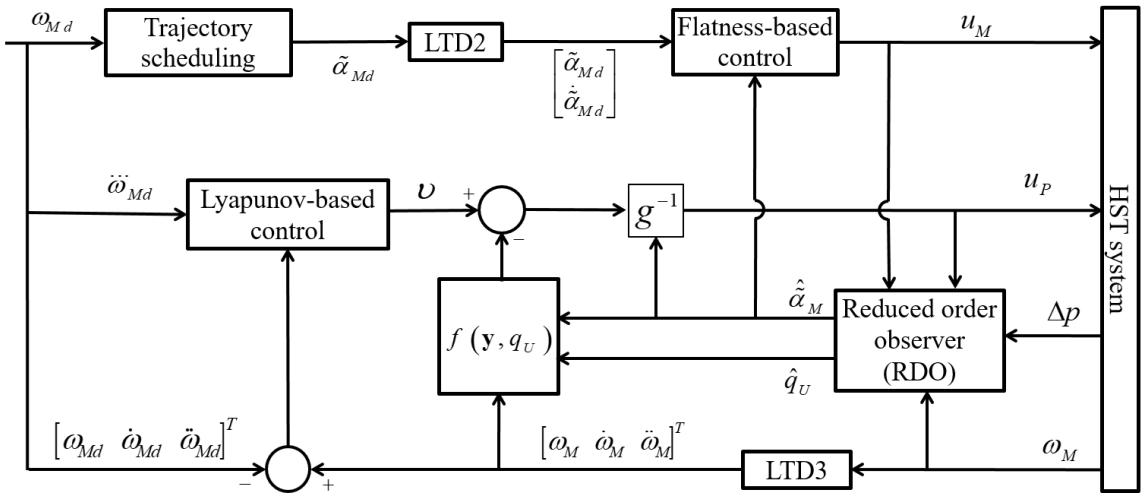

Figure 3.10: Feedback linearization implementation with the RDO.

3.2.2 Nonlinearity Compensation by Adaptive Parameter Estimation

Adaptive control for nonlinear systems using adaptive parameter estimation (APE) techniques is mentioned by E. Slotine and W. Li in [88]. This approach has been successfully developed for a class of nonlinear systems whose dynamics can be presented in companion form. Consequently, this technique is applicable to the velocity control of HST systems.

The adaptive control law presented in [88] is derived from a different control point of view. Nevertheless, it can be proved to be equivalent to the proposed feedback-linearized control scheme using some simple mathematical manipulations. For an analysis, let's consider again the HST system dynamics (3.99). Replacing the disturbance function $f(\mathbf{y}, q_U)$ according to 3.97 by a new function $\bar{f}(\mathbf{y})$ that contains adaptive parameters to be estimated results in a new expression as follows

$$y_0^{(3)} = g \cdot u_P + \bar{f}(\mathbf{y}) \ . \tag{3.131}$$

As suggested in [88], the adaptive control law is chosen as follows

$$u_P = \frac{1}{g} \cdot \bar{v} - \bar{k}\delta - \frac{1}{g}\bar{f}(\mathbf{y}), \tag{3.132}$$

where δ is defined as presented in (3.104), namely

$$\delta = \ddot{e} + \lambda_1 \dot{e} + \lambda_0 e \tag{3.133}$$

with $\bar{k} > 0$ and

$$\bar{v} = y_d^{(3)} - \lambda_1 \ddot{e} - \lambda_0 \dot{e} \ . \tag{3.134}$$

Here, $y_d^{(3)} = \dddot{\omega}_{Md}$ denotes the reference value of $\dddot{\omega}_M$. Substituting (3.134) into (3.132) results in

$$u_P = \frac{1}{g}\left[y_d^{(3)} - \lambda_1 \ddot{e} - \lambda_0 \dot{e}\right] - \bar{k}\delta - \frac{1}{g}\bar{f}(\mathbf{y}). \tag{3.135}$$

By choosing the parameter $\bar{k} = k/g$, where k is the parameter of the Lyapunov-based control in (3.106), equation (3.135) becomes

$$u_P = \frac{1}{g}\left[y_d^{(3)} - \lambda_1 \ddot{e} - \lambda_0 \dot{e} - k\delta - \bar{f}(\mathbf{y})\right]. \tag{3.136}$$

Applying equation (3.106) in (3.136) yields

$$u_P = \frac{1}{g}\left[\upsilon - \bar{f}\left(\mathbf{y}\right)\right], \tag{3.137}$$

where υ is the auxiliary control defined in (3.106). It can be seen from (3.137) that if the estimation of $\bar{f}\left(\mathbf{y}\right)$ produces a similar result corresponding to the feedback-linearized control (3.108). Then, the control law (3.137) guarantees the convergence of the tracking error toward zero. The compensation using $\bar{f}\left(\mathbf{y}\right)$ is possible by applying an adaptive parameter estimation technique. For this purpose, the overall control law (3.137) is represented in the compatible form with the one suggested in [88] as follows

$$u_P = \hat{a}_0 \frac{1}{g} \cdot \upsilon + \sum_{i=1}^{4} \hat{a}_i \cdot \bar{f}_i\left(\mathbf{y}\right). \tag{3.138}$$

In the inverse dynamics (3.138), the parameters $\hat{a}_i, i \in \{0,1,2,3,4\}$, are considered to be unknown and estimated online. Presenting the functions $\bar{f}_i$ in (3.138) in more detail w.r.t (3.97) and (3.98) results in

$$\begin{aligned} u_P = {} & \hat{a}_0 \frac{J_V C_H T_{uP}}{2\tilde{V}_M \sin(\alpha_M) \tilde{V}_P \alpha_{P,max} \omega_P k_P} \upsilon - \hat{a}_1 \frac{\tilde{V}_M \sin(\alpha_M)}{\tilde{V}_P \alpha_{P,max} \omega_P k_P} \omega_M \\ & - \hat{a}_2 \left(\frac{T_{uP} \tilde{V}_M \sin(\alpha_M)}{\tilde{V}_P \alpha_{P,max} \omega_P k_P} + \frac{C_H d_V}{2\tilde{V}_M \sin(\alpha_M) \tilde{V}_P \alpha_{P,max} \omega_P k_P} \right) \dot{\omega}_M \\ & - \hat{a}_3 \left(\frac{C_H T_{uP} d_V}{2\tilde{V}_M \sin(\alpha_M) \tilde{V}_P \alpha_{P,max} \omega_P k_P} + \frac{J_V C_H}{2\tilde{V}_M \sin(\alpha_M) \tilde{V}_P \alpha_{P,max} \omega_P k_P} \right) \ddot{\omega}_M \\ & - \hat{a}_4 \frac{1}{2\tilde{V}_M \sin(\alpha_M) \tilde{V}_P \alpha_{P,max} \omega_P k_P} \, . \end{aligned} \tag{3.139}$$

Thereby, the uncertainty and disturbance in the system model are compensated by the adaptive parameters $\hat{a}_i, i \in \{0,1,2,3,4\}$. A set of parameter values $\hat{a}_i = 1, i \in \{0,1,2,3\}$ and $\hat{a}_4 = 0$ – which corresponds to the nominal model of the system with a vanishing q_U – is used to initialize the estimation. This design requires a mathematical model of the system, however, as the disturbance and uncertainty are compensated by the adaptation of the estimated parameters, an observer is no longer needed, which simplifies the control structure and yields an improved robustness.

With the state vector $\mathbf{y} = [y_0, y_1, y_2]^T = [\omega_M, \dot{\omega}_M, \ddot{\omega}_M]^T$, obviously, (3.139) can be represented in the form of (3.138)

$$u_P = \hat{a}_0 \cdot \frac{1}{g} \cdot \upsilon + \hat{a}_1 \cdot \bar{f}_1(\mathbf{y}) + \hat{a}_2 \cdot \bar{f}_2(\mathbf{y}) + \hat{a}_3 \cdot \bar{f}_3(\mathbf{y} + \hat{a}_4 \cdot \bar{f}_4(\mathbf{y}). \tag{3.140}$$

The adaptation laws are chosen, according to [88], as follows

$$\begin{aligned} \dot{\hat{a}}_0 &= -\gamma_0 \cdot sign(g) \cdot \delta \cdot \bar{v} \cdot \frac{1}{g} \, , \\ \dot{\hat{a}}_i &= -\gamma_i \cdot sign(g) \cdot \delta \cdot \bar{f}_i(\mathbf{y}), \quad i = 1,2,3,4 \, , \end{aligned} \tag{3.141}$$

where the variable δ is defined in (3.133). According to [88], the adaptation rates $\gamma_i, i = \{0,1,2,3,4\}$ should be chosen reasonably small to avoid the parameter oscillations. The stability analysis of the selected adaptation rules is also provided in [88].

In this control design, without using of an observer, the feedback of the motor bent-axis angle is not available, therefore, a feedforward control is deployed instead for the hydraulic motor. By using the equation (3.128), the feedforward control can be determined by evaluating the inverse dynamics

$$u_M = \frac{1}{k_M}\tilde{\alpha}_{Md} + \frac{T_{uM}}{k_M}\dot{\tilde{\alpha}}_{Md} \ . \tag{3.142}$$

Here, again, an LTD2 is deployed for the estimation of $\dot{\tilde{\alpha}}_{Md}$ and an LTD3 is implemented for estimation of the derivatives for the motor angular velocity. For the evaluation of the function g and the functions in the linearization loop, the desired value $\tilde{\alpha}_{Md}$ is used. Fig. 3.11 shows the implementation of the whole control structure.

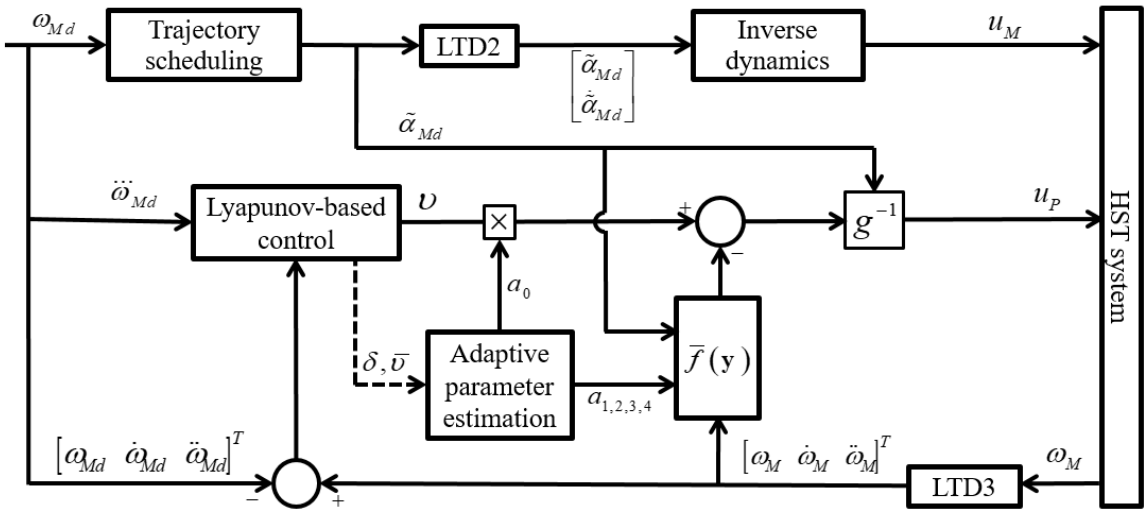

Figure 3.11: Feedback linearization implementation with APE.

3.2.3 Nonlinearity Compensation by a Neural Network

The following control approach using a neural network was developed by F. L. Lewis et al., see [93], where it is detailed for the control of rigid-link robotic systems and, then, generalized for the control of a class of nonlinear systems whose dynamics can be presented in the controller normal form. Therefore, an application of the approach to HST systems is possible.

There are many types of neural networks, such as radial basis function (RBF) neural networks, cerebellar model articulation controller (CMAC), Hopfield networks, multiple-layer perceptron (MPL) networks. They are also classified into feedforward and dynamic (recurrent) networks. The application of neural networks in technology is more and more widespread. Among them, MPL networks are perhaps the best known and widely used ones. Particularly in control systems, MPL networks are certainly most commonly employed [94, 95] exploiting the fact that they are able to approximate general nonlinear functions based on their universal function approximation property [93].

In the sequel, a two-layer feedforward perceptron network is deployed for nonlinearity compensation. The structure of the used network is depicted in Fig. 3.12.

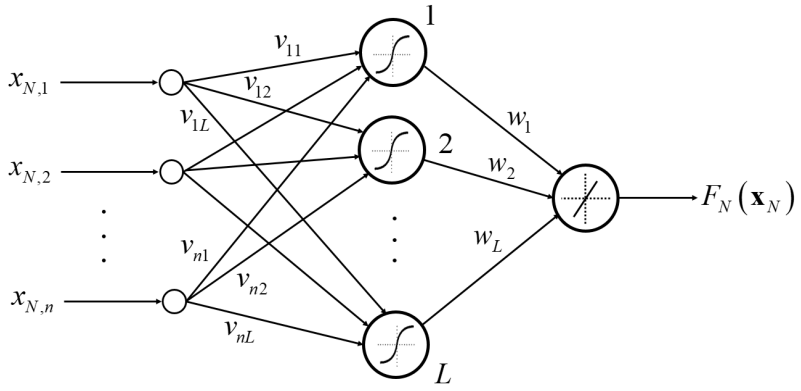

Figure 3.12: The MLP network structure.

The network comprises two layers in addition to the input layer. The first one is the hidden layer consisting of L neurons with sigmoid activation functions, the second one is the linear output layer with only one neuron corresponding to a single output signal. The general form of the neural network output can be stated as follows

$$F_N(\mathbf{x}_N) = \sigma\left(\mathbf{w}^T\left[\sigma\left(\mathbf{v}_1^T\mathbf{x}_N\right), ..., \sigma\left(\mathbf{v}_L^T\mathbf{x}_N\right)\right]^T\right), \tag{3.143}$$

where

- σ denotes the activation function. A logistic activation function is specified as follows

$$\sigma(u) = \frac{1}{1+e^{-u}}, \tag{3.144}$$

- $\mathbf{w} = [w_1, w_2, ..., w_L]^T$ is the weighting vector of the output layer,
- $\mathbf{V} = [\mathbf{v}_1, ..., \mathbf{v}_L]$ is the weighting matrix for the hidden layer,
- $\mathbf{x}_N = [\omega_M, \dot{\omega}_M, \ddot{\omega}_M]^T$ is the feedback state vector which serves as the synaptic inputs of the neural network.

In this implementation, a sigmoid function is applied to the hidden layer, whereas a linear one is employed in the output layer. Therefore, the description of the neural network output can be detailed as follows

$$F_N(\mathbf{x}) = \sum_{j=1}^{L} w_j \sigma\left(\mathbf{v}_j^T\mathbf{x}_N\right), \tag{3.145}$$

where L specifies the number of neurons, w_j presents the $j-th$ element of the output layer weighting vector $\mathbf{w}$, and $\mathbf{v}_j$ denotes the $j-th$ column of the hidden weighting matrix $\mathbf{V}$. The weighting matrix and vector of the network can be gathered in an augmented matrix

$$\Theta = \begin{bmatrix} \mathbf{V} & \mathbf{0} \\ \mathbf{0} & \mathbf{w} \end{bmatrix}. \tag{3.146}$$

By using the mentioned neural network, the approach allows for a reduction of the model knowledge required for the control design. Here, only the function g in the system equation

(3.99) remains to be known, whereas the lumped disturbance function $f(\mathbf{y}, q_U)$ is considered to be unknown and replaced by the estimation provided by the neural network. With this starting point, the system differential equation (3.99) is represented in a modified manner as follows

$$y_0^{(3)} = g \cdot u_P + \tilde{f}\left(\mathbf{y}\right) + \tilde{q}_U \ . \tag{3.147}$$

Under the realistic assumptions according to [93] that:

- the disturbance $\tilde{q}_U$ is bounded,
- the input gain g is bounded away from zero, i.e. $|g| > 0$,
- the reference $\mathbf{y}_d = [\omega_{Md}, \dot{\omega}_{Md}, \ddot{\omega}_{Md}]^T$ is designed satisfying the condition $\|\mathbf{y}_d\| \leqslant Q$ with the known bound Q and
- $\|\Theta\| \leqslant \theta_m$ holds with a known bound θ_m,

F. Lewis et al. [93] suggested the following feedback control

$$u_P = \frac{1}{g}\left[-\tilde{k} \cdot \delta + \tilde{\upsilon} - \tilde{f}\left(\mathbf{y}\right)\right], \tag{3.148}$$

where $\tilde{k}$ is a positive number, $\delta = \ddot{e} + \lambda_1 \dot{e} + \lambda_0 e$ which is identical to the one in (3.103) and $\tilde{\upsilon}$ is defined by

$$\tilde{\upsilon} = y_d^{(3)} - \lambda_1 \ddot{e} - \lambda_0 \dot{e} \ . \tag{3.149}$$

Here again, $y_d^{(3)} = \dddot{\omega}_{Md}$ is the reference value of $\dddot{\omega}_M$. The equivalence of this suggested control to the proposed feedback linearization (3.108) is easy to recognize. Substituting (3.149) into (3.148) and choosing $\tilde{k} = k$, where k is the parameter of the Lyapunov-based feedback-linearized control in (3.106), results in

$$u_P = \frac{1}{g}\left[y_d^{(3)} - \lambda_1 \ddot{e} - \lambda_0 \dot{e} - k\delta - \tilde{f}\left(\mathbf{y}\right)\right]. \tag{3.150}$$

By substituting (3.106) into (3.150), the following expression results

$$u_P = \frac{1}{g}\left[\upsilon - \tilde{f}\left(\mathbf{y}\right)\right]. \tag{3.151}$$

According to (3.151), if the estimated function $\tilde{f}\left(\mathbf{y}\right)$ is able to compensate both the nonlinearity and the disturbance $f\left(\mathbf{y}, q_U\right)$ in the original system. Then the system is linearized and the tracking performance is assigned. As the proposed feedback linearization control is equivalent to the suggested one using the neural network compensation, the adaptation law proposed in [93] can be directly applied under the assumptions above. The neural network is tuned in such a way that the envisaged tracking performance is achieved and the estimator stability is guaranteed – the proof is provided in [93]. The tuning rules are given by

$$\begin{aligned} \dot{w}_j &= M_w\left[\sigma\left(\mathbf{v}_j^T\mathbf{x}\right) - \sigma'\left(\mathbf{v}_j^T\mathbf{x}\right)\mathbf{v}_j{}^T\mathbf{x}\right]\delta - \kappa\left|\delta\right| M_w w_j, \\ \dot{\mathbf{v}}_j &= \boldsymbol{M}_v \delta \mathbf{x} w_j \sigma'\left(\mathbf{v}_j^T\mathbf{x}\right) - \kappa\left|\delta\right| \boldsymbol{M}_v \mathbf{v}_j, \end{aligned} \tag{3.152}$$

where the diagonal matrix $\boldsymbol{M}_v$, the scalar M_w and κ are positive tuning parameters. σ' denotes the derivative of the activation function σ. Finally, the control law is specified as follows

$$u_P = \frac{1}{g}\left[\upsilon - F_N\left(\mathbf{x}_N\right) + u_r\right], \tag{3.153}$$

where

- $F_N(\mathbf{x}_N)$ is the output of the MLP network
- u_r is a robustifying term, $u_r = -\kappa_r(\|\Theta\| + \theta_m)$, with $\kappa_r > 0$.

In this control design, a feedforward control – which is identical to the one used in (3.142) – is deployed for the hydraulic motor. Fig. 3.13 shows the implementation of the complete control structure.

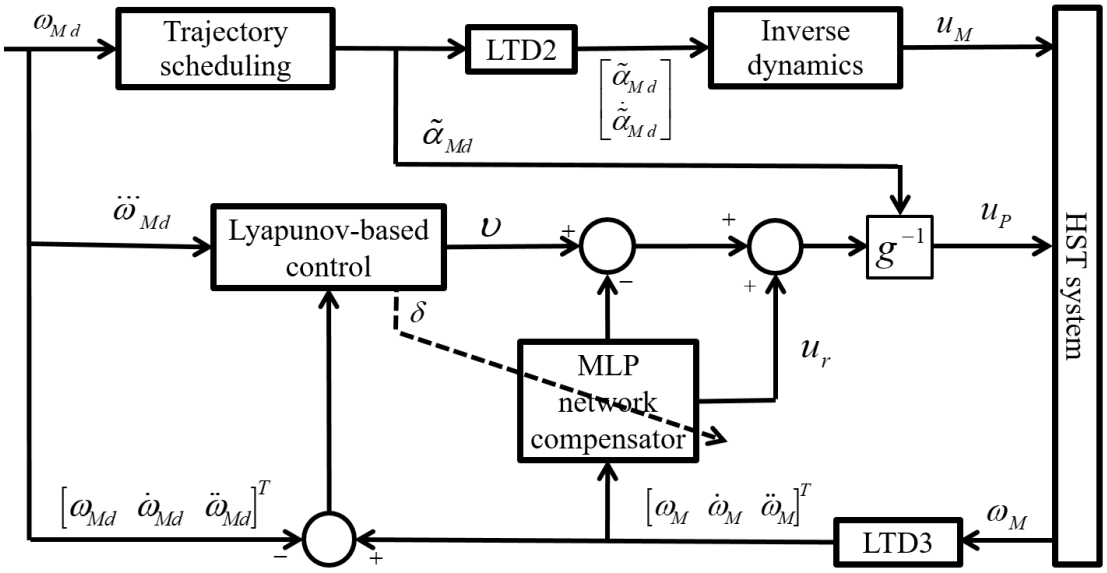

Figure 3.13: Feedback linearization with MLP networks.

3.3 Active Disturbance Rejection Approaches

Active disturbance rejection (ADR) control was introduced by J. Han during the late 1980s and 1990s to deal with the control of systems with vast uncertainty. ADR approaches reduce the complexity of a controlled system to a simple linear perturbed system which is affected by a total disturbance term. As a result, the system can be easily controlled by means of a linear output feedback control law [83, 96] and an estimator for the total disturbance. The robustness is guaranteed thanks to the low level of system knowledge required for the control design. The success of ADR control in practical engineering has been proved in several studies and applications [62, 83], which promises good result on HST systems as well. In this study, two versions of the ADR control approach – observer-based and flat-filtering-based version – are considered.

3.3.1 Observer-Based ADR Control Design

The key part of an observer-based ADR control is the extended observer (ESO). For a differentially flat system, the ESO estimates the output and its derivatives for the feedback loop as well as the total disturbance – which is estimated by an extended state of the observer – for the compensation loop. Disturbances can be classified in two categories: endogenous disturbances

that are dependent on internal variables – such as the system states, outputs, unmodeled dynamics, and nonlinearity – and exogenous disturbances that are generated by the environment. The ADR approaches treat both these two components jointly as a total or lumped disturbance $\tilde{F}$, which replaces the unknown function $f(\mathbf{y}, q_U)$ in the system model (3.99). For convenience, the HST system models (3.99) and (3.100) are reintroduced here in controller normal form with a replacement of $f(\mathbf{y}, q_U)$ by $\tilde{F}$:

$$\begin{aligned} \dot{y}_0 &= y_1 \\ \dot{y}_1 &= y_2 \\ \dot{y}_2 &= \tilde{F} + g \cdot u_P \ , \end{aligned} \tag{3.154}$$

and in companion form as follows

$$y_0{}^{(3)} = \tilde{F} + g \cdot u_P. \tag{3.155}$$

As mentioned by B. Z. Guo and Z. L. Zhao in [83], the conventional extended observer that is used for the ADR control is of the Luenberger-type. However, according to H. Sira-Ramirez et al. [96], the Luenberger-type extended observer is generally non-robust with respect to any practical system input perturbation. Therefore, they proposed a new extended observer structure with more extra states – for more robustness – which is deployed in this study.

According to the system model analysis and experimental studies, a state observer with two extended states is proposed as follows

$$\begin{aligned} \dot{\hat{y}}_0 &= \hat{y}_1 + l_4 (y_0 - \hat{y}_0) \\ \dot{\hat{y}}_1 &= \hat{y}_2 + l_3 (y_0 - \hat{y}_0) \\ \dot{\hat{y}}_2 &= g \cdot u_P + \chi_1 + l_2 (y_0 - \hat{y}_0) \\ \dot{\chi}_1 &= \chi_2 + l_1 (y_0 - \hat{y}_0) \\ \dot{\chi}_2 &= l_0 (y_0 - \hat{y}_0) \, , \end{aligned} \tag{3.156}$$

where $\hat{y}_0 = \hat{\omega}_M$, $\hat{y}_1 = \hat{\dot{\omega}}_M$ and $\hat{y}_2 = \hat{\ddot{\omega}}_M$ stand for the estimates of the system output and its time derivatives y_0, y_1 and y_2, respectively. The extended states χ_1 and χ_2 present the estimates of the total disturbance $\tilde{F}$ and its time derivative. $l_i, i \in \{0, 1, 2, 3, 4\}$ are the observer gains. Corresponding to the proposed observer structure, it is assumed that the second time derivative of the disturbance, i.e. $\tilde{F}^{(2)}$, is zero or at least bounded. Based on the definition of the estimation errors

$$\begin{aligned} \zeta_0 &= y_0 - \hat{y}_0, \\ \zeta_1 &= y_1 - \hat{y}_1, \\ \zeta_2 &= y_2 - \hat{y}_2, \end{aligned} \tag{3.157}$$

by using (3.154) and (3.156), the estimation error dynamics becomes

$$\begin{aligned} \dot{\zeta}_0 &= \zeta_1 - l_4 \zeta_0, \\ \dot{\zeta}_1 &= \zeta_2 - l_3 \zeta_0, \\ \dot{\zeta}_2 &= \tilde{F} - \chi_1 - l_2 \zeta_0, \\ \dot{\chi}_1 &= \chi_2 + l_1 \zeta_0, \\ \dot{\chi}_2 &= l_0 \zeta_0. \end{aligned} \tag{3.158}$$

Consider the equation system (3.158). Differentiating the first equation twice and using the second equation, integrating the last two equations, then, substituting into the third equation results in

$$\dddot{\zeta}_0 + l_4 \ddot{\zeta}_0 + l_3 \dot{\zeta}_0 + l_2 \zeta_0 + l_1 \int_0^t \zeta_0 d\tau_1 + l_0 \int_0^t \int_0^{\tau_1} \zeta_0 d\tau_2 d\tau_1 = \tilde{F}. \tag{3.159}$$

Transforming (3.159) into the Laplace domain yields

$$s^3\zeta_0 + l_4 s^2\zeta_0 + l_3 s\zeta_0 + l_2\zeta_0 + l_1\frac{1}{s}\zeta_0 + l_0\frac{1}{s^2}\zeta_0 = \tilde{F}(s), \tag{3.160}$$

which is equivalent to

$$\left(s^5 + l_4 s^4 + l_3 s^3 + l_2 s^2 + l_1 s + l_0\right)\zeta_0(s) = s^2\tilde{F}(s). \tag{3.161}$$

As the right hand side of (3.161) – the second derivative of the disturbance $\tilde{F}^{(2)}$ – is assumed to be bounded, the convergence toward zero of the estimation errors is guaranteed by a proper choice of the observer gains $l_i, i \in \{0,1,2,3,4\}$, which places the solutions of the characteristic polynomial

$$P_0(s) = s^5 + l_4 s^4 + l_3 s^3 + l_2 s^2 + l_1 s + l_0 \tag{3.162}$$

in the left half of the complex s-plane. With the reference value of the output $\omega_{Md} = y_d$, the following proportional-derivative feedback law is established to stabilize the system

$$u_P = \frac{1}{g}\left[y_d^{(3)} - \chi_1 - \sum_{j=0}^{2}\alpha_j\left(\hat{y}_j - y_d^{(j)}\right)\right]. \tag{3.163}$$

Substituting $\hat{y}_j = y_j - \zeta_j$ from (3.157) into (3.163) yields

$$u_P = \frac{1}{g}\left[y_d^{(3)} - \chi_1 - \sum_{j=0}^{2}\alpha_j e^{(j)} - \sum_{j=0}^{2}\alpha_j\zeta_j\right], \tag{3.164}$$

with $e = y_0 - y_d$ denoting the tracking error. Applying the control law (3.164) to the system dynamics (3.155) yields the dynamics of the tracking error as follows

$$\dddot{e} + \alpha_2\ddot{e} + \alpha_1\dot{e} + \alpha_0 e = \tilde{F} - \chi_1 + \sum_{j=0}^{2}\alpha_j\zeta_j. \tag{3.165}$$

By choosing properly a set of the feedback gains $\alpha_j, j \in \{0,1,2\}$, which places the solutions of the characteristic polynomial

$$P_e(s) = s^3 + \alpha_2 s^2 + \alpha_1 s + \alpha_0 \tag{3.166}$$

in the left half of the complex s-plane, the tracking error converges obviously toward the bounded perturbation on the right-hand side of (3.165). In order to determine both the feedback gains $\{\alpha_j, j = 0,1,2\}$ and the observer gains $\{l_i, i = 0,1,2,3,4\}$, pole-placement methods or the one proposed in [97] can be used.

A simple feedforward control is again deployed for the hydraulic motor. Fig. 3.14 depicts the implementation of the ESO-based ADR control.

3.3.2 Flat-Filtering ADR Control Design

Generalized-proportional-integral (GPI) control approach originates from the classical compensation networks [98]. The method was developed for differentially-flat linear systems. It can

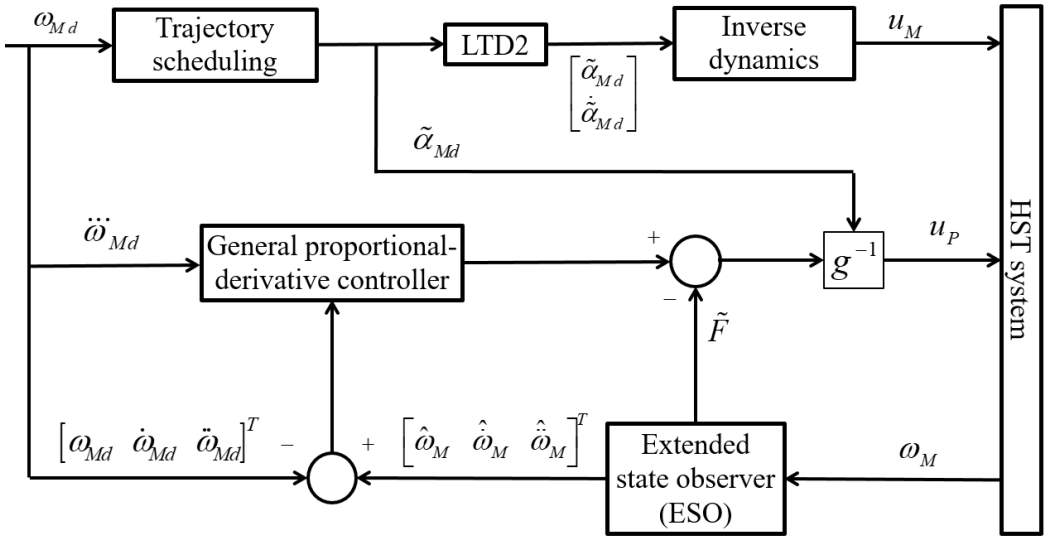

Figure 3.14: Implementation of the ESO-based ADR control.

be generalized toward nonlinear flat systems according to H. Sira-Ramirez in [96]. The flat-filtering GPI is a variation of the GPI control where the approximations in terms of the filtered output and input signals are used to replace all the variables in the compensation network. The approach is extended using ADR control ideas to handle efficiently the control tasks on perturbed differentially-flat SISO nonlinear systems affected by unknown nonlinearity in the presence of external disturbances and unmodeled dynamics [99]. H. Sira-Ramírez [100] showed that both ADR control and flat-filtering control are equivalent by means of an algebraic procedure involving a reduced-order observer structure. As can be seen from analysis of the HST model, the system is differentially flat. As a result, the flat-filtering approach – as proposed by H. Sira-Ramirez et al. [99] – can be applied to the system.

The design procedure starts with an introduction of the following nominal reference system

$$y_d^{(3)} = g \cdot u_{Pd}, \tag{3.167}$$

with $y_d = \omega_{Md}$ presenting the desired output value and u_{Pd} denoting the nominal control input. The tracking error is defined by

$$e = y_0 - y_d. \tag{3.168}$$

By using (3.155) and (3.167), the closed-loop error dynamics results in

$$e^{(3)} = g \cdot e_{u_P} + \tilde{F}, \tag{3.169}$$

where $e_{u_P} = u_P - u_{Pd}$ defines the control input error. The block diagram visualization of the dynamics (3.169) is shown in Fig. 3.15.

As presented in Fig. 3.15, the control input error e_{u_P} could be reconstructed using $\tilde{F}$ as well as the derivatives of the output error, which is measurable. However, it is practically impossible because the disturbance $\tilde{F}$ is unknown. Even in the case of known $\tilde{F}$, the time derivatives required - up to the third order - are also corrupted by the measurement noise. To tackle this practical issue, the derivatives of the tracking error are replaced by the estimations. For the purpose of an analysis, the disturbance term in (3.169) is discarded resulting in an

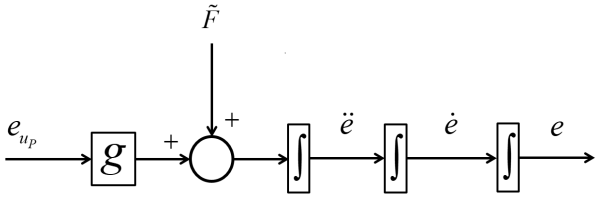

Figure 3.15: The closed-loop error dynamics of HST systems.

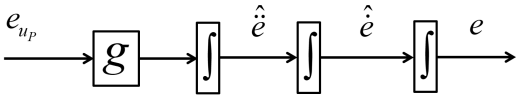

Figure 3.16: Signal reconstructions by multiple integration.

integrator chain as depicted in Fig. 3.16. Accordingly, the derivatives of the tracking error can be reconstructed as follows

$$\hat{\ddot{e}} = g \int_0^t e_{uP} \cdot d\tau_1, \quad \hat{\dot{e}} = g \int_0^t \int_0^{\tau_1} e_{uP} \cdot d\tau_2 d\tau_1. \tag{3.170}$$

As the derivatives of the error are reconstructed from the control input error, the system (3.169) can be stabilized using the following feedback control

$$e_{u_P} = -\frac{1}{g}\left(\beta_2 \hat{\ddot{e}} + \beta_1 \hat{\dot{e}} + \beta_0 e\right). \tag{3.171}$$

Nevertheless, taking into account the fact that the unknown disturbance $\tilde{F}$ has an impact on the system but is not compensated so far, the chosen control law (3.171) is no longer accurate. According to M. Ramírez-Neria et al. in [101], this issue can be handled by introducing m finite integrals of the tracking error. The choice of m depends on the assumption regarding the polynomial degree of the disturbance signals. In this work, based on experimental studies on the real HST system, $m = 3$ is chosen for a good tracking result. Accordingly, a new feedback control law results in as follows

$$e_{uP} = \frac{1}{g}\left(\beta_5 \hat{\ddot{e}} + \beta_4 \hat{\dot{e}} + \beta_3 e + \beta_2 \int_0^t e \; d\tau_1 + \beta_1 \int_0^t \int_0^{\tau_1} e \; d\tau_2 d\tau_1 + \beta_0 \int_0^t \int_0^{\tau_1} \int_0^{\tau_2} e \; d\tau_3 d\tau_2 d\tau_1\right). \tag{3.172}$$

Substituting (3.170) into (3.172) yields

$$\begin{aligned} e_{uP} = \frac{1}{g}\Bigg(& g \cdot \beta_5 \int_0^t e_{uP} \cdot d\tau_1 + g \cdot \beta_4 \int_0^t \int_0^{\tau_1} e_{uP} \cdot d\tau_2 d\tau_1 + \beta_3 e \\ & + \beta_2 \int_0^t e \cdot d\tau_1 + \beta_1 \int_0^t \int_0^{\tau_1} e \cdot d\tau_2 d\tau_1 + \beta_0 \int_0^t \int_0^{\tau_1} \int_0^{\tau_2} e \cdot d\tau_3 d\tau_2 d\tau_1 \Bigg), \end{aligned} \tag{3.173}$$

with the error signal e obtained directly from measurements. The expression (3.173) is in the form of a compensation network which can be visualized in the Fig. 3.21. For a realization

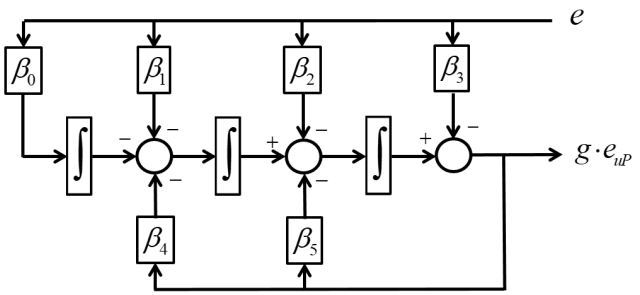

Figure 3.17: The compensation network.

of the control law in the implementation, a transformation of the expression (3.173) into the Laplace domain leads to

$$e_{u_P}(s) = -\frac{1}{g}\left(\frac{g\cdot\beta_5}{s}e_{u_P}(s) + \frac{g\cdot\beta_4}{s^2}e_{u_P}(s) + \beta_3 e(s) + \frac{\beta_2}{s}e(s) + \frac{\beta_1}{s^2}e(s) + \frac{\beta_0}{s^3}e(s)\right). \quad (3.174)$$

By rearranging the terms in (3.174), the following relation can be obtained

$$\left(1 + \frac{\beta_5}{s} + \frac{\beta_4}{s^2}\right)e_{uP}(s) = -\frac{1}{g}\left(\beta_3 + \frac{\beta_2}{s} + \frac{\beta_1}{s^2} + \frac{\beta_0}{s^3}\right)e(s). \quad (3.175)$$

Multiplying both sides of (3.175) by s^3 results in

$$\left(s^3 + \beta_5 s^2 + \beta_4 s\right)e_{uP}(s) = -\frac{1}{g}\left(\beta_3 s^3 + \beta_2 s^2 + \beta_1 s + \beta_0\right)e(s), \quad (3.176)$$

which leads to

$$e_{u_P}(s) = -\frac{1}{g}\left(\frac{\beta_3 s^3 + \beta_2 s^2 + \beta_1 s + \beta_0}{s^3 + \beta_5 s^2 + \beta_4 s}\right)e(s). \quad (3.177)$$

According to the error dynamics equation (3.169), the control input error can also be expressed related to the total disturbance $\tilde{F}$ as follows

$$e_{u_P}(s) = \frac{1}{g}\left(s^3 e(s) - \tilde{F}\right). \quad (3.178)$$

By comparing (3.177) and (3.178), the error dynamics results in

$$\left(s^6 + \beta_5 s^5 + \beta_4 s^4 + \beta_3 s^3 + \beta_2 s^2 + \beta_1 s + k_0\right)e(s) = \left(s^3 + \beta_5 s^2 + \beta_4 s\right)\tilde{F}(s). \quad (3.179)$$

As a small bounded derivative of the disturbance $\tilde{F}$ is assumed on the right-hand side of the equation (3.179), the convergence of the tracking error e is guaranteed by a proper choice of the set of gains $\beta_i, i \in \{0,1,2,3,4,5\}$, satisfying the Hurwitz criterion for the following characteristic polynomial

$$P_\beta(s) = s^6 + \beta_5 s^5 + \beta_4 s^4 + \beta_3 s^3 + \beta_2 s^2 + \beta_1 s + \beta_0\ . \quad (3.180)$$

Provided that the gain set is determined, the control input is finally given by

$$u_P = u_{Pd} + e_{u_P}\ , \quad (3.181)$$

with

$$u_{Pd} = \frac{1}{g}y_d^{(3)}\ . \quad (3.182)$$

Here, $y_d^{(3)}$ is available from the trajectory generator. Fig. 3.18 shows the block diagram of the implemented flat-filtering-based control for the hydraulic pump – in a combination with a feedforward control for the hydraulic motor – for the whole HST system.

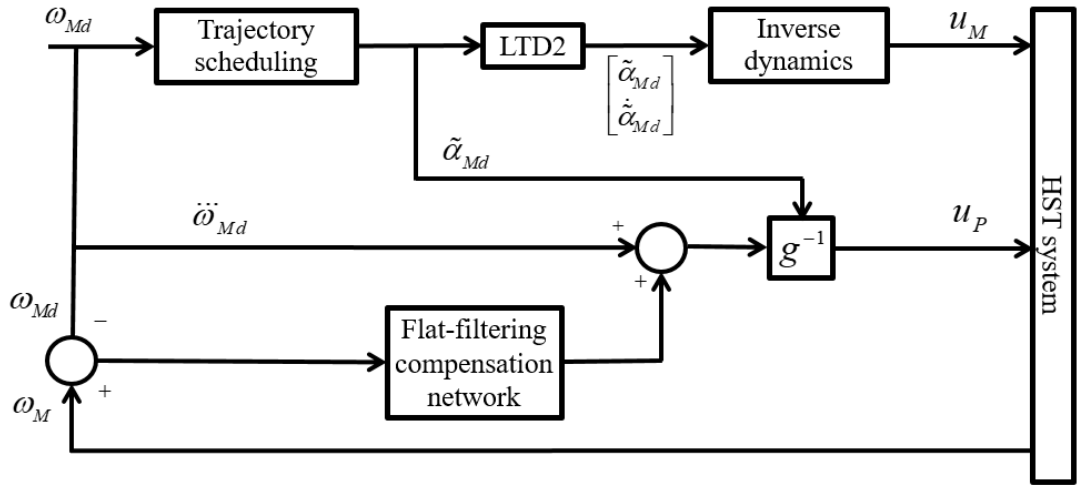

Figure 3.18: Flat-fitering-based control for HST systems.

3.4 Model-Free Approaches

Similar to the ADR approach, model-free control is also inspired by a practical motivation which relates a complex control problem with industrial control techniques such as P, PI or PID controllers. The approach originated from the techniques for black-box fast identification and estimation proposed by M. Fliess et al. [102]. A subsequent development resulted in the introduction of an intelligent PID controller [103], where the unknown parts of the plant are taken into account without any modeling procedure. The generalization of the approach was the origin of the so-called model-free control [104]. Despite the novelty of this approach, there are already many successful results in a variety of applications ranging from intelligent transportation systems to energy management [96].

The idea is that, instead of dealing with a complete system mathematical model, the approach uses a simpler phenomenological – or ultra-local – model of the following form

$$y^{(n)} = F + K \cdot u \ , \tag{3.183}$$

where K is a non-physical user-defined parameter and F is to be determined using estimation techniques. This system can then be stabilized by a linear feedback intelligent PID-type controller, where all the nonlinearity, uncertainty and disturbances in the system are compensated by an estimate for F which is considered as a piece-wise constant function relying on the algebraic differentiation [79]. Usually – as suggested in M. Fliess and C. Join [79] – $n = 1$ or $n = 2$ is chosen, where $n = 1$ results in a P- or PI-type controller, $n = 2$ leads to a PID controller. The choice of n and K is made by practitioners who know the system behavior well.

As the approach is tailored to a practical application, a high robustness on real systems belong to the advantages of the model-free design, which is obviously beneficial for uncertain systems like HSTs. However, the employment of the algebraic differentiation method, see [79], – as indicated by implementation on real HST systems – did not provide an acceptable tracking performance due to a large estimation error of F. Therefore, the work described in the sequel suggests several different approaches to deal with the disturbance for the control of HST systems in the framework of model-free control.

For the HST system, the ultra-local model for system approximation is be given by

$$y_0^{(3)} = K \cdot u_P + F \ , \tag{3.184}$$

i.e., $n = 3$ is chosen. The first reason for this choice comes from the prior knowledge of the HST model, which obviously provides the best match between the assumed model and the real system. The second reason is that, by experiments on real equipment, the choice of $n = 1$ or $n = 2$ is not appropriate for a good tracking result, which may be caused by the highly nonlinear behavior of HST systems. Similarly, for the parameter K, though the accuracy is not obligated, the value of K should be properly chosen. By simulation and experimental tests, $K = 11 \cdot 10^4$ turned out as appropriate. The following control approaches for the hydraulic pump control are studied and discussed in the sequel:

- Sliding mode control: the feedback iPID control is replaced by a sliding mode controller which provides robustness to overcome the estimation error of the term F.
- Feedback compensation by neural networks using the feedback-error-leaning technique: an intelligent PD-type feedback controller is used for stabilizing the system, whereas the estimation of the term F is replaced by a neural network.
- Feedforward compensation using neural networks: an intelligent PD-type feedback controller is used for stabilizing the system, and an adaptive feedforward neural controller reduces the tracking error instead of estimating the term F.

3.4.1 Sliding Mode Control

As the model-free approach relies on the derivatives of the system output signal, an estimator is the key part of the design. Many derivative estimators have been developed as mentioned in [96]. However, in this study an LTD is deployed, which provides the first and second time derivatives for the feedback control and the third time derivative for the disturbance estimation. It becomes obvious directly from the ultra-local model (3.184) that the estimate $\hat{F}$ of the unknown term F is given by

$$\hat{F} = \hat{y}_0^{(3)} - K \cdot u_P \ , \tag{3.185}$$

where $\hat{y}_0^{(3)}$ is the estimate of the third time derivative of the system output $y_0^{(3)}$.

Sliding mode control (SMC) is a robust control approach based on Lyapunov's direct stability method [88]. The simple structure of the control allows for a relaxation of the control parametrization, and the control can cope with uncertainties. Moreover, the discontinuity also provides a faster convergence toward the origin. For the design of an SMC for the HST system, the following integral sliding manifold is introduced

$$\vartheta = \ddot{e} + \rho_2 \dot{e} + \rho_1 e + \rho_0 \int_0^t e \ d\tau \ , \tag{3.186}$$

where the tracking error e is defined by $e = y_0 - y_d$, with $y_d = \omega_{Md}$ representing the desired value of the output y_0. The coefficients ρ_0, ρ_1, ρ_2 are chosen properly to specify solutions in the left half of the complex s-plane for the following characteristic polynomial

$$s^3 + \rho_2 s^2 + \rho_1 s + \rho_0 = 0. \tag{3.187}$$

By forcing the sliding variable ϑ to converge to zero in finite time, the tracking error e converges consequently toward zero as well according to (3.187). Differentiating the sliding variable ϑ w.r.t. time and using the dynamic equation (3.184) leads to

$$\begin{aligned} \dot{\vartheta} &= e^{(3)} + \rho_2 \ddot{e} + \rho_1 \dot{e} + \rho_0 e \\ &= -{y_d}^{(3)} + F + K \cdot u_P + \rho_2 \ddot{e} + \rho_1 \dot{e} + \rho_0 e \ . \end{aligned} \tag{3.188}$$

Accordingly, the following control input u_P can be chosen

$$u_p = \frac{1}{K} \left({y_d}^{(3)} - \rho_2 \ddot{e} - \rho_1 \dot{e} - \rho_0 e + \nu - \hat{F} \right) \ , \tag{3.189}$$

where the term ν is the discontinuous switching part, which dominates the system uncertainties. Substituting (3.189) into (3.188) results in

$$\dot{\vartheta} = \tilde{\xi} + \nu \ , \tag{3.190}$$

where $\tilde{\xi} = F - \hat{F}$ is the disturbance estimation error. In order to realize the witching part, the following Lyapunov function candidate is used

$$V = \frac{1}{2} \vartheta^2 \ . \tag{3.191}$$

Taking the time derivative of the Lyapunov function candidate results in

$$\dot{V} = \vartheta \dot{\vartheta} \ . \tag{3.192}$$

Substituting the expression (3.190) into the time derivative (3.192) yields

$$\dot{V} = \vartheta \left(\tilde{\xi} + \nu \right) = \vartheta \tilde{\xi} + \vartheta \nu \ . \tag{3.193}$$

To drive the sliding variable toward the origin, the switching control ν is chosen according to $\nu = -\bar{\rho} \ \mathrm{sign}(\vartheta)$, with $\bar{\rho} > 0$. Provided that the disturbance estimation error is assumed to be bounded, i.e., $\left| \tilde{\xi} \right| \leqslant \bar{L}$, the following inequality is obtained accordingly

$$\begin{aligned} \dot{V} &\leqslant |\vartheta| \, \bar{L} - \bar{\rho} \, |\vartheta| \\ &\leqslant |\vartheta| \left(\bar{L} - \bar{\rho} \right) . \end{aligned} \tag{3.194}$$

Given the reaching condition of the sliding variable

$$\dot{V} \leqslant -\bar{\eta} \, |\vartheta| \ , \tag{3.195}$$

with $\bar{\eta} > 0$, comparing (3.194) with the reaching condition (3.195) results in the switching gain $\bar{\rho}$ as follows

$$\bar{\rho} = \bar{L} + \bar{\eta} \ . \tag{3.196}$$

The SMC law becomes finally

$$\begin{aligned} u_p &= \frac{1}{K}\left({y_d}^{(3)} - \rho_2\ddot{e} - \rho_1\dot{e} - \rho_0 e - \bar{\rho}\,\mathrm{sign}(\vartheta) - \hat{F}\right) \\ &= \frac{1}{K}\left(u_{SMC} - \hat{F}\right) \ . \end{aligned} \tag{3.197}$$

For practical reasons, the chattering effect can be reduced by replacing the function sign$(\cdot)$ with a sigmoid one like

$$\mathrm{sign}\,(\vartheta) \triangleq \frac{\vartheta}{|\vartheta| + \bar{\gamma}}. \tag{3.198}$$

Here, $\bar{\gamma} \geqslant 0$ is a design parameter which allows for a trade-off between chattering reduction and uncertainty compensation.

As can be seen in the control law (3.197), the first and second derivatives of the output signal, $\dot{y}_0$ and $\ddot{y}_0$, are required for the error evaluation, while the third time derivative $y_0^{(3)}$ is needed for the estimation of the disturbance $\hat{F}$. The required derivatives of the measurement output are provided using the following forth-order linear tracking differentiator (LTD4) [65]

$$\begin{aligned} \dot{\varsigma}_1 &= \varsigma_2 \\ \dot{\varsigma}_2 &= \varsigma_3 \\ \dot{\varsigma}_3 &= \varsigma_4 \\ \dot{\varsigma}_4 &= -R_{\varsigma 4}^4\left[c_{\varsigma 4,1}\left(\varsigma_1 - y_0\right) + c_{\varsigma 4,2}\frac{\varsigma_2}{R_{\varsigma 4}} + c_{\varsigma 4,3}\frac{\varsigma_3}{R_{\varsigma 4}^2} + c_{\varsigma 4,4}\frac{\varsigma_4}{R_{\varsigma 4}^3}\right] \ . \end{aligned} \tag{3.199}$$

With all parameters of the LTD4 properly defined as recommended in [83], the derivatives are provided accordingly: $\dot{y}_0 = \omega_M = \varsigma_2$, $\ddot{y}_0 = \dot{\omega}_M = \varsigma_3$ and $y_0^{(3)} = \ddot{\omega}_M = \varsigma_4$.

For controlling the bent-axis angle of the hydraulic motor, as can be seen from the derivation of the hydraulic pump control, the method offers a model-free design procedure without any requirement of identified physical parameters. This inspires a model-free control for the hydraulic motor too. Therefore, a pure feedforward control is deployed. As obtained from the model knowledge, the proportional gain of the dynamical relation between the input u_M and the bent-axis angle $\tilde{\alpha}_M$ is equal to 1, hence, the feedforward control can be approximated by the desired trajectory value itself as follows

$$u_M \approx \tilde{\alpha}_{Md}, \tag{3.200}$$

where $\tilde{\alpha}_{Md}$ is provided by the trajectory scheduling module. This static feedforward control does not compensate for the lag behavior and leads to larger tracking errors in the motor bent-axis angle response, which may cause the saturation of the pump swash-plate angle. Nevertheless, this issue can be avoided by reducing slightly the maximal value of the desired motor angular velocity $\omega_{Md,max}$, which corresponds to a smaller value of the parameter b. This measure slightly narrows the working range of the HST system, however, the advantages of a completely model-free design can be exploited. Fig. 3.19 presents the implementation of the whole control system, which consists of a SMC for the hydraulic pump and a simple feedforward control for the hydraulic motor. In this implementation, the previous value of the control u_P is applied to avoid an algebraic loop.

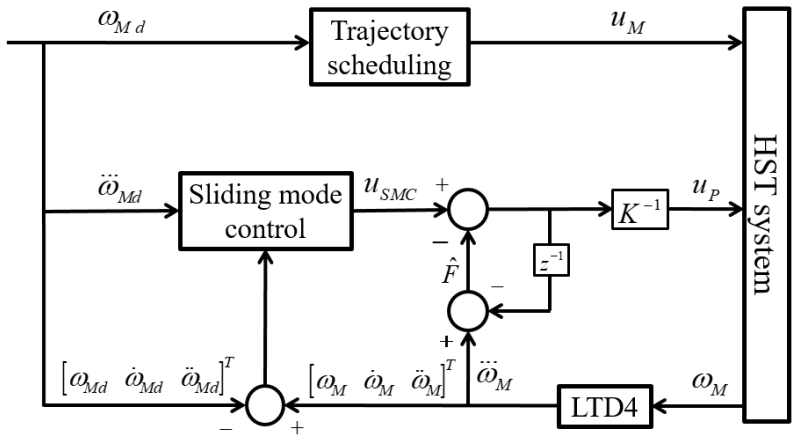

Figure 3.19: Implementation of the sliding mode control.

3.4.2 Neural Network Compensation Using Feedback Error Learning

Feedback error learning (FEL) approach is proposed by M. Kawato et al. [105] for voluntary movement control. In [107], the approach is generalized for nonlinear systems as an adaptive feedback control technique and for applications of motion control on mechanical systems. The success of the proposed control technique is also proved by many practical researches like in [112] for combustion engine control, in [111,113] for mobile robot control, in [114] for satellite control, etc. Fig. 3.20 shows a general principle of the feedback error learning technique. As proposed by M. Kawato et al. [105], the control structure consists of a conventional feedback stabilizer of the PD-type working in parallel with a neural network controller, which can be of any type of a universal function approximation.

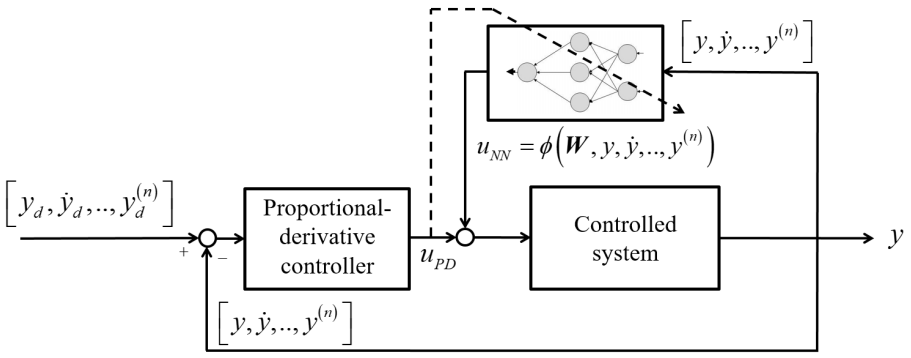

Figure 3.20: Principle of feedback error learning.

In the feedback error learning control scheme, the conventional feedback controller is supposed to assure the asymptotic stability and serves as the inverse reference model that regards the system response, whereas the neural network controller uses the output of the conventional feedback control as the training signal to learn the inverse dynamics of the HST system. The

controlled output – here generally presented by y – and its first n time derivatives are fed into the neural network as the synaptic inputs. Through the learning process, as the inverse dynamics is acquired by the neural controller, the output of the controlled system tracks the desired trajectory and, then, the conventional controller is relieved. As a consequence, any changes of the system dynamics can be captured, which provides an active compensation to the disturbance and uncertainties in the system.

As seen from the control scheme, the control signal part produced by the neural network is a nonlinear function of the synaptic inputs $y_0^{(j)}, j = 0, 1, 2, ..., n$, and the network weights $\boldsymbol{W}$, which can be expressed generally by the following function

$$u_{NN} = \phi\left(\boldsymbol{W}, y, \dot{y}, \ddot{y}, .., y^{(n)}\right). \tag{3.201}$$

Provided that the following assumptions are applied:

- The chosen learning rate η of the network is positive and small,
- The conventional controller – the PD-type one – is designed properly to assure the convergence of the system output y_0 toward the desired values y_d during the learning process,

the neural network weights can be updated during the learning process using the following gradient-type tuning law according to [105]

$$\frac{d\boldsymbol{W}}{dt} = \eta \frac{\partial \phi}{\partial \boldsymbol{W}} u_{PD} \ , \tag{3.202}$$

where the output u_{PD} of the PD-type controller presents the training error. The stability of the whole proposed control structure for a robotic application has been proved successfully in [107, 108] using averaging techniques in a stochastic setting and Lyapunov's second method. Further discussions based on Lyapunov theory analysis can be found in [109–111] as well.

Design of the PD-type Controller As the HST has a relative degree of three w.r.t. the angular velocity as the controlled output, a generalized PD-type controller with the additional second time derivative of the tracking error would be recommended to obtain a better performance. Moreover, the simulation and experimental tests also confirm a superior result of the proposed classical PD-type controller over the simple PD one which only uses the tracking error and its first time derivative. As the derivatives of the tracking error are impossible to implement directly by means of numerical calculations from the measurement due to the corruption of measurement noise, a third-order linear tracking differentiator (LTD3) with the same structure as presented in (3.114) is employed for the estimations, which provides the filtered signal of y_0, $\dot{y}_0$ and $\ddot{y}_0$ for tracking error evaluation. Accordingly, the proposed PD-type controller is given by

$$u_{PD} = k_0 e + k_1 \dot{e} + k_2 \ddot{e} \ , \tag{3.203}$$

where the tracking error $e = \omega_{Md} - \omega_M$, with ω_{Md} denoting the desired value of the motor angular velocity. The feedback gains k_0, k_1, k_2 can be chosen using trial-and-error approach or an improved one like Ziegler-Nichols [106]. However, as inspired by the model-free approach, the empirical tuning of the feedback gains can be avoided by using the idea of the intelligent PID controller [79]. Thereby, the PD-type controller (3.203) is modified as follows

$$\begin{aligned} u_{iPD} &= \dddot{y}_d + k_0 e + k_1 \dot{e} + k_2 \ddot{e} \\ &= \dddot{y}_d + u_{PD} \end{aligned} \tag{3.204}$$

with $\dddot{y}_d = \ddot{\omega}_{Md}$ supplied from the trajectory generator. A similar idea can be found also in [108]. Accordingly, the closed-loop error dynamics results in

$$\left[k_0 + k_1 s + k_2 s^2 + s^3\right] \; e(s) = \Delta(s), \tag{3.205}$$

where the lumped disturbance term $\Delta(s)$ on the right-hand side of (3.205) presents the excitation accounting for the remaining errors. The presence of $\dddot{y}_d$ does not affect the dynamics of proposed adaptation rule because it is a pure feedforward term. The tuning procedure for the control gains is now straightforward by using pole-placement methods to satisfy the Hurwitz criterion for the corresponding characteristic polynomial

$$s^3 + k_2 s^2 + k_1 s + k_0 = 0. \tag{3.206}$$

Design of the Neural Network Compensation As suggested by M. Kawato et al. [105], any type of neural networks with universal approximation properties can be used. However, in this design, a similar structure of the MLP network used in feedback linearization control is again employed. As a well-known network structure in control, the MLP network represents a popular universal approximation method which allows for a straightforward practical implementation [115] using the well-established back-propagation training technique. The implemented neural network structure, as shown in Fig. 3.21, consists of a hidden layer with P neurons using sigmoid activation function and the linear output layer with a single neuron. The corresponding

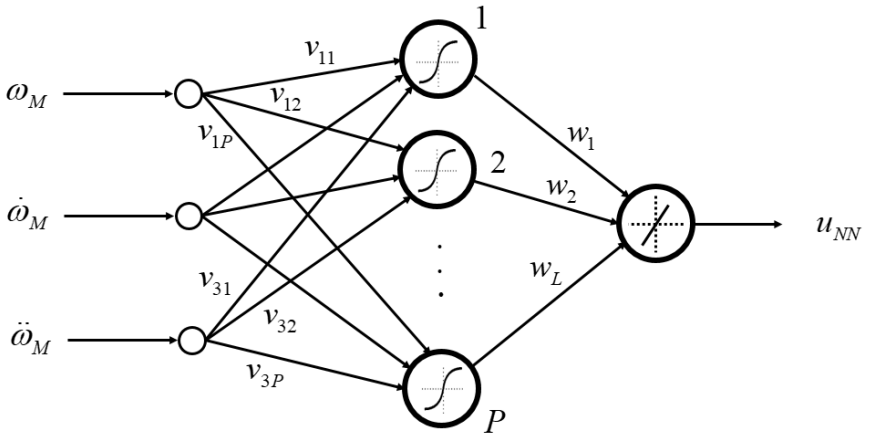

Figure 3.21: The implemented MLP network.

structure allows to describe the network output u_{NN} as follows

$$u_{NN} = \phi\left(\boldsymbol{W}, \mathbf{x}_N\right) = \sum_{j=1}^{P} w_j \sigma\left(\mathbf{v}_j^T \mathbf{x}_N\right), \tag{3.207}$$

where $\sigma(\cdot)$ denotes the activation function, w_j is the j-th element of the output weight vector $\boldsymbol{w}$ and $\mathbf{v}_j$ presents the j-th column of the input weight matrix $\mathbf{V}$ corresponding to the j-th neuron. The input vector $\mathbf{x}_N$ is defined by

$$\mathbf{x}_N = \left[\begin{array}{ccc} y_0 & y_1 & y_2 \end{array}\right]^T = \left[\begin{array}{ccc} \omega_M & \dot{\omega}_M & \ddot{\omega}_M \end{array}\right]^T, \tag{3.208}$$

which corresponds to $n = 2$, and these synaptic input signals are provided by the LTD3.

For using the back-propagation technique in the network training, the gradients of the objective function ϕ w.r.t. each individual weight can be stated as follows

$$\begin{aligned} \frac{\partial \phi}{\partial \mathbf{w}} &= \boldsymbol{\delta}_1, \\ \frac{\partial \phi}{\partial \mathbf{V}} &= \mathbf{x}_N \cdot \mathbf{w}^T \cdot \boldsymbol{\delta}_2 \ . \end{aligned} \tag{3.209}$$

Here, $\boldsymbol{\delta}_1$ and $\boldsymbol{\delta}_2$ are defined by

$$\begin{aligned} \boldsymbol{\delta}_1 &= \sigma\left(\mathbf{V}^T \mathbf{x}_N\right), \\ \boldsymbol{\delta}_2 &= diag\left[\sigma'\left(\mathbf{V}^T \mathbf{x}_N\right)\right]. \end{aligned} \tag{3.210}$$

In the expression (3.210), $\sigma'(\cdot)$ stands for the derivative of the activation function $\sigma(\cdot)$ w.r.t. its inputs. According to (3.202), the tuning laws for the weights become

$$\begin{aligned} \dot{\mathbf{w}} &= \eta_w \cdot \boldsymbol{\delta}_1 \cdot u_{PD}, \\ \dot{\mathbf{V}} &= \eta_v \cdot \mathbf{x}_N \cdot \mathbf{w}^T \cdot \boldsymbol{\delta}_2 \cdot u_{PD} \ . \end{aligned} \tag{3.211}$$

The overall control for the tracking of the motor angular velocity is evaluated with the sum of the contributions from both the iPD controller and the neural network

$$u_P = u_{iPD} + u_{NN}. \tag{3.212}$$

Fig. 3.22 shows the details of the proposed control structure in combination with a feedforward control law for the motor bent-axis angle.

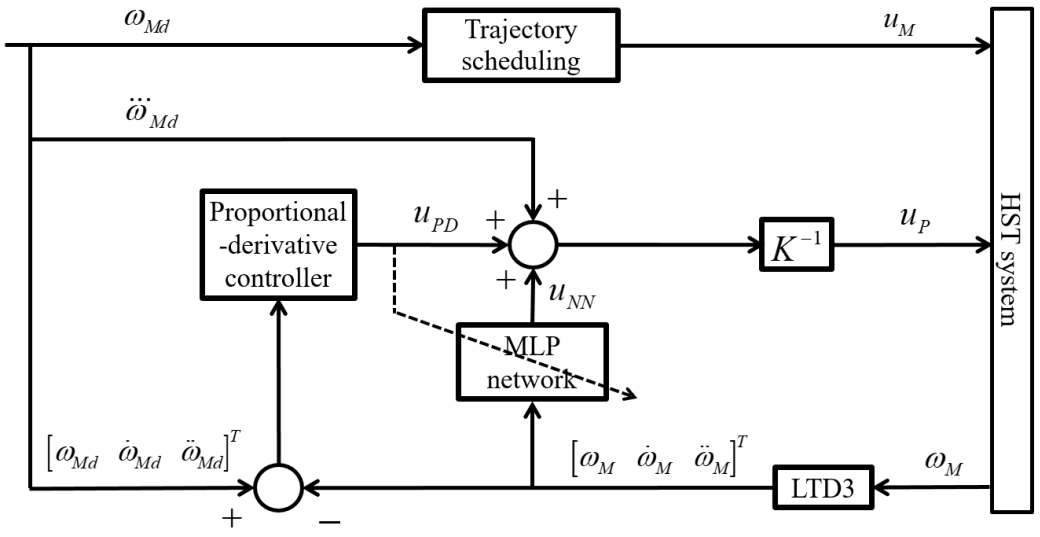

Figure 3.22: The model-free approach using feedback error learning.

3.4.3 Adaptive Feedforward Compensation Using Neural Networks

The idea of adaptive feedforward compensation (AFC) using a neural network comes from the adaptive feedforward neural controller that is mentioned in the works of F. Damak et al. [116],

L. Shi et al. [117] and X. Cui et al. [118]. In these control structures, only the neural network directly controls the plant using the tracking error as training signal to adapt the network weights. Y. Pan et al. [119] proposed an improvement for adaptive feedforward control by a combination of a neural network in parallel connection with a PD error feedback. The same control idea can be found in previous research conducted by D. Psaltis in [120].

N. Ommer et al. [121] proposed a purely feedforward adaptive control for the velocity tracking of an unmanned ground vehicle. The adaptive control law relies on a correction policy which provides an improvement of the tracking accuracy using the desired value of the velocity as the input and the current value of the tracking error as the adaptation signal. However, the idea of this method is not to learn the complete inverse dynamics which determines the transient response of the controlled system during the trajectory tracking. Instead, only a proper correction input is learned to compensate for the possible future tracking errors. As stated in [121], the adaptive feedforward controller predicts only the compensating actions, therefore, a combination with any existing feedback controller is possible.

In the current work, the mentioned idea is deployed for HST systems. Here, however, a neural network is used to imitate the adaptation policy [66] working in parallel with an iPD feedback control, where the output tracking error is directly used as the training signal. The iPD controller reduces the initial tracking error and stabilizes the system whereas the MLP network learns to produce a correcting input to the system that reduces the future error caused by the feedforward control signal. A similar implementation can also be found in D. Psaltis et al. [120].

iPD Feedback Stabilizing An iPD controller – which is already introduced in previous section for feedback error learning control – is again deployed in this control design. The iPD control is used to stabilize the system. Moreover, it reduces the initial tracking error in the learning phase of the neural network controller, which provides an improvement of the tracking performance. Accordingly, the output signal of the iPD control is given by

$$\begin{aligned} u_{iPD} &= \dddot{y}_d + k_P e + k_D \dot{e} + k_{2D} \ddot{e} \\ &= \dddot{y}_d + u_{PD}, \end{aligned} \tag{3.213}$$

where the tracking error e is also defined by $e = \omega_{Md} - \omega_M$ and the feedback gains k_P, k_D and k_{2D} are determined using pole-placement methods satisfying the Hurwitz criterion for the following characteristic polynomial

$$s^3 + k_{2D} s^2 + k_D s + k_P = 0 \ . \tag{3.214}$$

Here, an LTD3 yields the filtered derivatives of the error signal.

The Feedforward Neural Compensation The structure of an MLP neural network used for the compensator is shown in Fig. 3.23 The hidden layer of network comprises M neurons with the corresponding weights v_1, v_2, ... v_M. The output layer consists only one single neuron with the output weights w_1, w_2, ... w_M. Either the hyperbolic tangent or the logistic function can be used as activation function for the hidden layer, whereas the linear function is applied to the output layer. The MLP neural network processes the desired value of the angular velocity ω_{Md} as the synaptic input. Accordingly, the output of the neural network u_{NN} can be expressed as follows

$$u_{NN} = \sum_{i=1}^{n} \left(w_i \cdot \sigma \left(v_i \cdot \omega_{Md} \right) \right) \ , \tag{3.215}$$

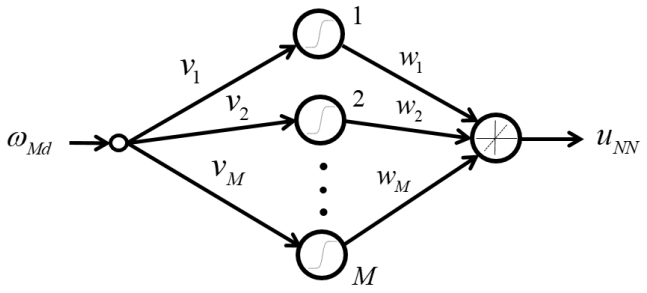

Figure 3.23: The neural network structure.

with $\sigma(\cdot)$ denoting the activation function. As the tracking error e is used as the training signal, the back-propagation training technique alters the network weights in such a way as to minimize the following quadratic cost function

$$E = \frac{1}{2}e^2. \tag{3.216}$$

This results in a gradient-descent law that updates the neural network weights in each correction step k according to

$$\begin{aligned} v_i(k+1) &= v_i(k) - \eta_1 \frac{\partial E}{\partial v_i(k)} \quad , \\ w_i(k+1) &= w_i(k) - \eta_2 \frac{\partial E}{\partial w_i(k)}, \end{aligned} \tag{3.217}$$

where η_1 and η_2 denote the learning rates. The gradients of the cost function w.r.t. the individual weights in (3.217) can be determined by applying the chain rule resulting in

$$\begin{aligned} \frac{\partial E}{\partial v_i} &= \frac{\partial E}{\partial e}\frac{\partial e}{\partial \omega_M}\frac{\partial \omega_M}{\partial u_{NN}}\frac{\partial u_{NN}}{\partial v_i}, \\ \frac{\partial E}{\partial w_i} &= \frac{\partial E}{\partial e}\frac{\partial e}{\partial \omega_M}\frac{\partial \omega_M}{\partial u_{NN}}\frac{\partial u_{NN}}{\partial w_i}. \end{aligned} \tag{3.218}$$

According to the mathematical definitions, some terms of the gradient chain (3.218) can be specified easily as follows

$$\begin{aligned} &\frac{\partial E}{\partial e} = e, \frac{\partial e}{\partial \omega_M} = -1, \\ &\frac{\partial u_{NN}}{\partial w_i} = \sigma\left(v_i \cdot \omega_{Md}\right), \\ &\frac{\partial u_{NN}}{\partial v_i} = \omega_{Md} \cdot \sigma'\left(v_i \cdot \omega_{Md}\right) \cdot w_i, \end{aligned} \tag{3.219}$$

where $\sigma'(\cdot)$ denotes the corresponding partial derivative of the activation function.

Only one remaining term $\frac{\partial \omega_M}{\partial u_{NN}}$ – which regards the system dynamics – is not defined yet because the system is considered to be unknown. For a monotonic response system, this obstacle can be overcome by a replacement of the gradient with its sign, according to X. Cui et al. in [118] and M. Saerens et al. in [122]. The magnitude of the gradient is not important because it can be incorporated in the learning rate. The mentioned idea is also applicable on the HST system by supposing a small adaptation rate which produces such a small change of u_{NN} so that the system response becomes over-damped, thereby, the system output ω_M behaves monotonically to the

input u_{NN}. This method has been successfully applied in several recent studies as presented in [123–125]. For HST systems, the sign of the gradient term can be easily recognized from physical considerations

$$\frac{\partial \omega_M}{\partial u_{NN}} \triangleq sign(\frac{\partial \omega_M}{\partial u_{NN}}) = 1 \ . \tag{3.220}$$

Finally, substituting (3.220) and (3.219) into (3.218) results in the update law

$$\begin{aligned} v_i(k+1) &= v_i(k) + \eta_1 \cdot e \cdot \omega_M \cdot \sigma'\left(v_i \cdot \omega_{Md}\right) \cdot w_i(k), \\ w_i(k+1) &= w_i(k) + \eta_2 \cdot e \cdot \sigma\left(v_i(k) \cdot \omega_{Md}\right). \end{aligned} \tag{3.221}$$

The overall control for the tracking of the motor angular velocity is evaluated with the sum of the contributions from all the control components

$$u_P = \ddot{y}_d + u_{PD} + u_{NN}. \tag{3.222}$$

A feedforward control is again applied to the hydraulic motor. Fig. 3.24 shows the whole structure of the proposed control. Comparison between the control structures with the application of

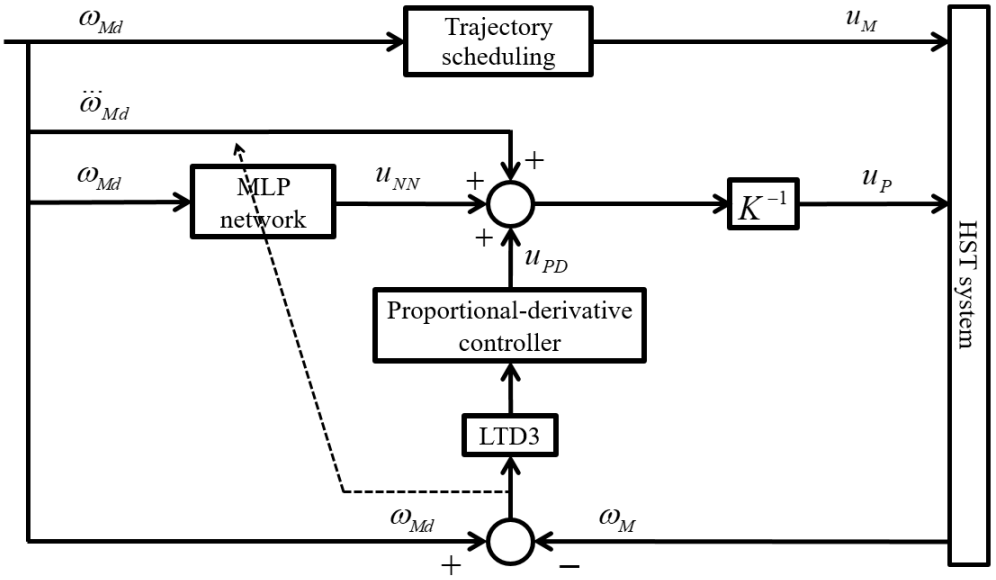

Figure 3.24: The model-free approach with AFC using neural network.

neural network – adaptive feedforward compensation using neural network (AFC), neural network compensation using feedback error learning (FEL) and feedback linearization using neural network (MLP), it can be seen that these designs result in basically similar control structures, where the system is stabilized by linear feedback controllers, while the neural networks approximately capture the inverse dynamics of the system to compensate the nonlinearity. The difference among these designs is the way that the neural networks learn the model. In feedback linearization with MLP, see Fig. 3.13, the training law is derived based on the direct Lyapunov theory analysis, which results in a specific update rule. In FEL (Fig. 3.22) and AFC (Fig. 3.24) control structure, the neural networks are trained by the well-established method – the general back propagation training technique. The difference between these two controls is that, in FEL, the learning of the neural network takes into account the dynamics of the feedback controller, whereas in AFC the dynamics of the feedback controller is not regarded, only the tracking error is used for the neural network learning.

4 Control Design Validation

In this section, the control approaches previously designed are validated. The control designs are firstly analyzed in simulations to derive the proper setting of design parameters, after a successful result in simulations, the control structures are implemented and perform in real time on the real equipment for validation. The control performance, then, is analyzed and compared by means of root-mean-square error evaluation.

4.1 Synchronization of the Displacement Units

The displacement unit of the hydraulic motor is controlled synchronically with the desired trajectory of the motor angular velocity. As mentioned before, the displacement of the hydraulic motor is kept as large as possible to produce a high possible torque at the motor output shaft. However, the motor displacement must reduce accordingly to the increase of desired motor angular velocity in order to gain proper transmission ratios. The limit of the motor angular velocity is defined at a nominal value of the hydraulic pump velocity of $\omega_P = 70\ rad/s$. According to the experiments, the possible maximum of the motor velocity is $\omega_{M,max} = 160\ rad/s$. With the limiting parameter $b = 0.95$, the maximum of the desired output angular velocity should be defined not to exceed $\omega_{Md,max} = b \cdot \omega_{M,max} = 150\ rad/s$.

In simulations, a good control result can be achieved with the motor control activated at $a = 80\ rad/s$. On the test rig, however, the value of $a = 80\ rad/s$ results in a very fast decrease of the motor bent-axis angle, that causes the oscillation in the system, therefore, a should be reduced to 60 rad/s for a better performance.

Fig. 4.1, 4.2 and Fig. 4.3 show the synchronized behavior of the motor bent-axis angle to the variation of different desired trajectories on the test rig. A can be seen, with a high desired

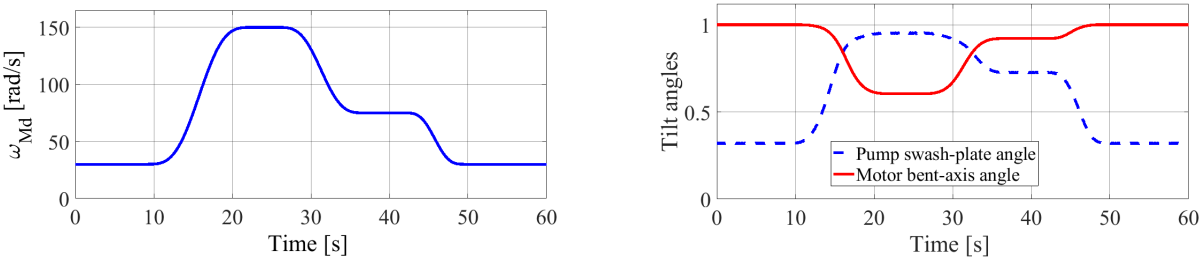

Figure 4.1: Synchronization of displacement units with the full range trajectory.

motor angular velocity – which covers the whole working range of the HST system – the motor displacement unit is fully activated from its minimum to maximum whereas the displacement unit of the hydraulic pump also increases from zero to the predefined maximal level to control the output angular velocity but not to get saturation which allows for the control authority. In Fig. 4.2 when a very low desired trajectory is applied, only the hydraulic pump displacement

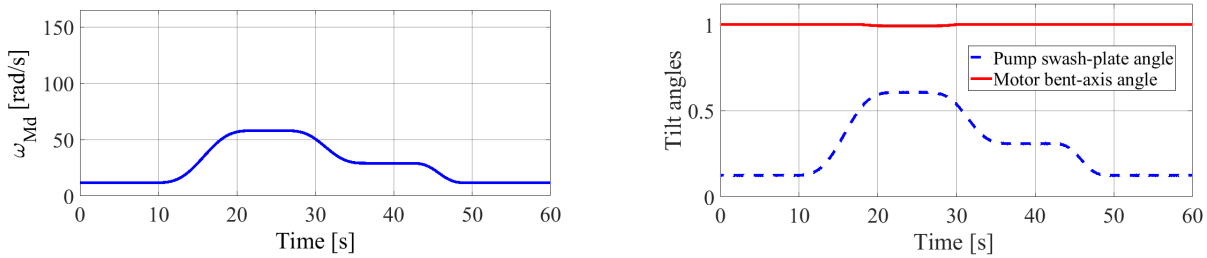

Figure 4.2: Synchronization of displacement units with the small range trajectory.

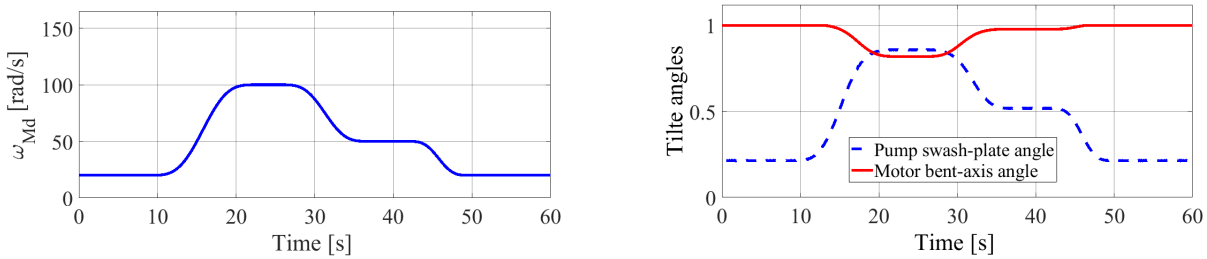

Figure 4.3: Synchronization of displacement units with the medium range trajectory.

takes the control action while the motor displacement maintains its maximal value. With a medium desired trajectory as seen in Fig. 4.3, both displacement units are activated in their operation range to follow the desired value of the controlled output while the hydraulic torque is still kept as high as possible at the output shaft.

4.2 Control Performance

Aiming at realistic and reliable simulation results, the output signals – the motor angular velocity and the difference pressure – are extended by the additive measurement noise. Moreover, the disturbance torque and the leakage volume flow are modeled as follows [73]

$$q_U = 1 \cdot 10^{-12} \Delta p \ ,$$
$$\tau_U = 0.1 J_V \dot{\omega}_M + 7 \tanh\left(\frac{\omega_M}{0.1}\right) \ .$$

Fig. 4.4 presents the desired trajectory of the motor angular velocity which is used for the velocity control design validation. The control designs are studied in two application scenarios

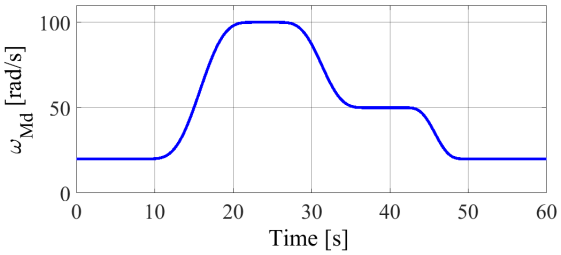

Figure 4.4: The desired angular velocity for testing.

- In the first scenario, the angular velocity of the hydraulic pump and the load torque applied to the motor shaft are constant.

- In the second scenario, both the pump angular velocity and the load torque are harmonically varying.

In the first scenario, the hydraulic pump speed is set to 70 rad/s and the load torque is held constant at 0 $N.m$. For the second test scenario, both the hydraulic pump angular velocity and external load torque acting on the motor output shaft are assumed to vary periodically as shown in Fig. 4.5 and Fig. 4.6. This mimics the working conditions in real applications where the prime mover changes the angular velocity due to external effects or due to the commands of the operator. In addition, the load may also vary due to external resistances. Such conditions happen frequently in applications of hydrostatic transmissions in wind turbines or in working machines.

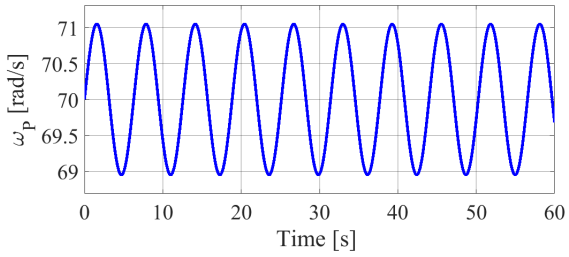

Figure 4.5: Variation of prime mover angular velocity.

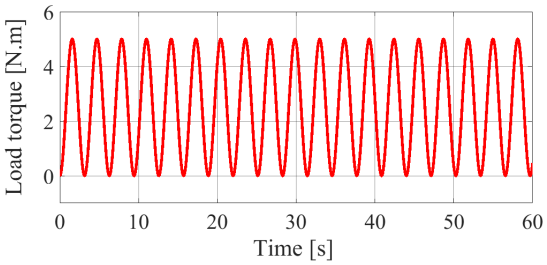

Figure 4.6: Variation of external disturbance load torques.

4.2.1 Optimization-Based Approaches

Model Predictive Control

Optimization-based controls rely on the real-time optimization process which usually results in a high computational load, therefore, a larger sampling time is required for completing calculation cycles. For the proposed optimization-based controllers, the sampling time $T_s = 50\ ms$ is chosen for implementation. The prediction horizon of the NMPC is selected with $N = 5$ by trial-and-error methods but in compliance with the stability analysis.

In the first scenario, the hydraulic pump speed is set to 70 rad/s and the load torque is held constant at 0 $N.m$. Moreover, the weights of the cost function are selected as follows

$$w_1 = 8 \cdot 10^4, w_2 = 1 \cdot 10^{-6}, w_3 = 10 \cdot 10^5, w_4 = 11 \cdot 10^4$$

and the empirical parameter $p = 0.6$. The Kalman filter – which is deployed for states and

disturbance estimation – is utilized with following parameters

$$\mathbf{Q}_K = diag\left(\left[10^{-3}\ 10^{-6}\ 10^{-6}\ 10^{-6}\ 10^{-10}\ 10^{2}\right]\right),$$
$$\mathbf{R}_K = diag\left(\left[10^{5}\ 10^{2}\right]\right),\ \alpha = 1,\ \kappa = 1,\ \beta = 2.$$

The estimation performance of the Kalman filter with the chosen sampling time is shown in Fig. 4.7. As can be seen, the estimates of system disturbances are not perfectly match with the simulated ones, however, the smoothness and the accuracy are sufficient for the envisaged control purpose. The simulation result for the velocity tracking of the proposed control is shown

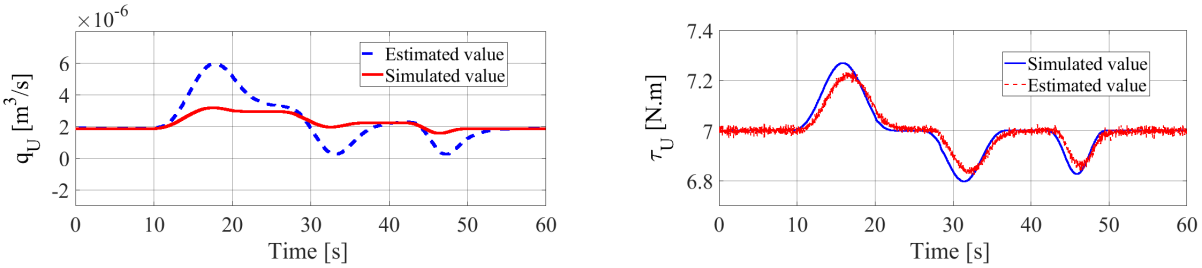

Figure 4.7: Disturbance estimation performance of the Kalman filter.

in Fig. 4.8. A very high tracking performance is achieved with only small errors between the controlled output and the desired value.

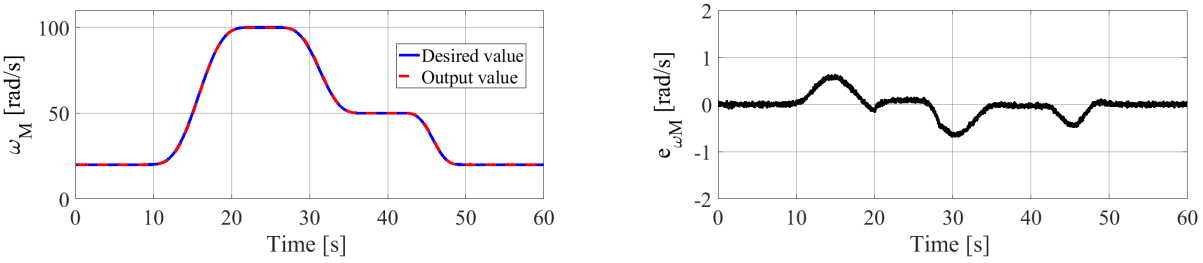

Figure 4.8: Simulation velocity tracking result of NMPC in the first test case.

As mentioned in the design section, the stability of the NMPC controller is confirmed by evaluating the stability criterion (3.9) during the tracking process. The numerical result is presented in Fig. 4.9. As the criterion is satisfied with strictly negative values, the equation (3.9) implies a decreasing Lyapunov function candidate over the control horizon, which indicates the stability of the control system according to [131].

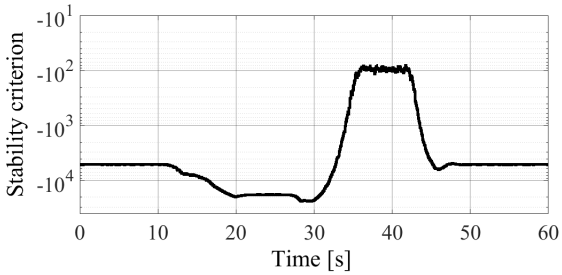

Figure 4.9: Numerical evaluation of the NMPC stability criterion

The variations of both displacement units, see Fig. 4.10, meet the constraints and show the envisaged characteristics. When the pump swash-plate angle is still within its admissible working range, the motor maintains its maximal volume displacement. If the pump displacement unit reaches the saturation value, the motor displacement decreases to enlarge the angular velocity for an accurate tracking.

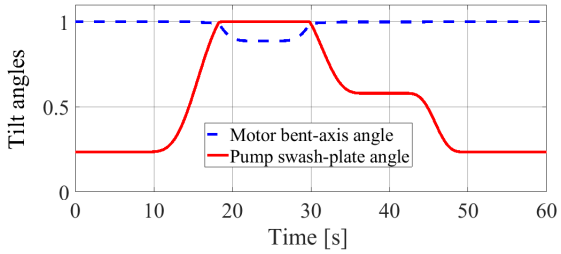

Figure 4.10: Variation of displacement units in simulation of the NMPC.

The simulation result for the velocity tracking control in the second test scenario is shown in Fig. 4.11. Under the effects of oscillating disturbances, the controlled output also exhibits an oscillation, however, the accuracy is till maintained well.

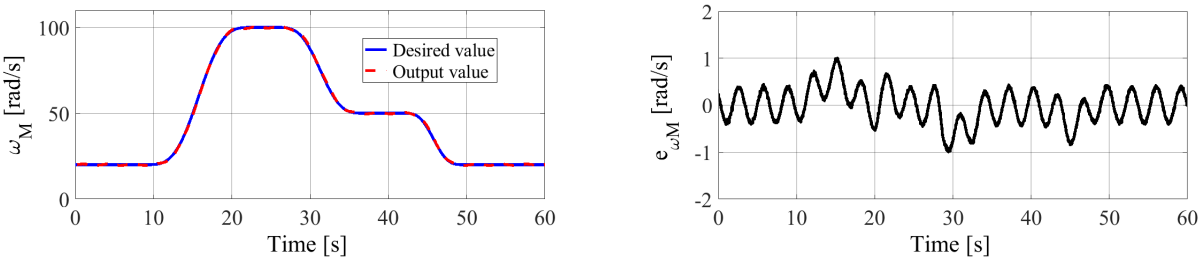

Figure 4.11: Simulation velocity tracking result of NMPC in the second test case.

The control structure is implemented on the dedicated test rig using an identical sampling time of $T_s = 50\ ms$. The parameters implemented on the test rig are based on simulations but slightly altered for a better performance:

$$w_1 = 2.3 \cdot 10^4, w_2 = 4 \cdot 10^{-6}, w_3 = 3.1 \cdot 10^5, w_4 = 2.5 \cdot 10^4, p = 0.6.$$

Experimental results for the velocity tracking in the first test case are shown in Fig. 4.12, the accuracy is comparable to the one in the simulation study. Fig. 4.13 depicts the behavior of the

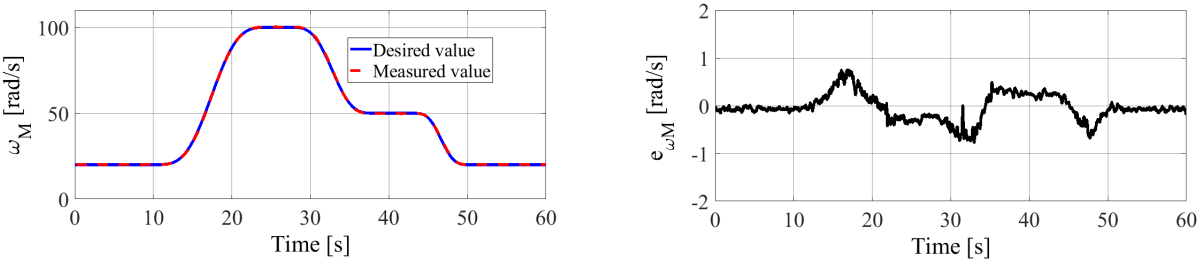

Figure 4.12: Experimental velocity tracking result of NMPC in the first test case.

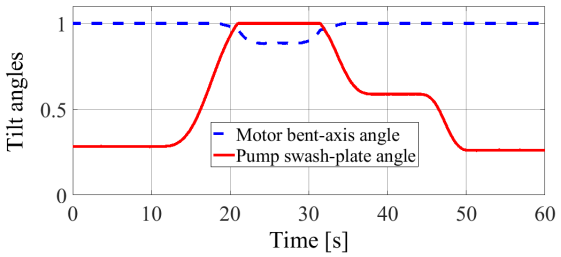

Figure 4.13: Variation of displacement units of the NMPC on the test rig.

displacement units in experiments on the real system, which are also similar to the simulation results.

For the second test scenario, which is subject to the disturbance effects, the velocity tracking result is shown in Fig. 4.14. A slightly increase of the tracking error can be recognized accompanied by oscillations similar to the simulation results. Nevertheless, a high tracking accuracy is still achievable which indicates the capability of the proposed control design.

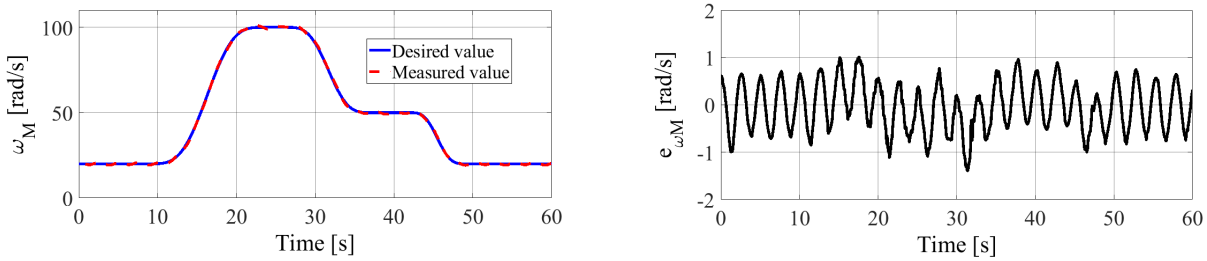

Figure 4.14: Experimental velocity tracking result of NMPC in the second test case.

As detailed in the control design section, the proposed NMPC can be adapted for the control of the hydraulic torque by simply modifying the cost function accordingly where the first term in the cost function – which penalizes the tracking error – is altered w.r.t. the hydraulic torque output. The corresponding weights are selected as follows

$$w_{\tau 1} = 4.5 \cdot 10^7, w_{\tau 2} = 5.1 \cdot 10^{-7}, w_{\tau 3} = 1.5 \cdot 10^7, w_{\tau 4} = 9 \cdot 10^6,$$

and $p_\tau = 0.6$. Fig. 4.15 and Fig. 4.16 depict the simulation results for the hydraulic torque tracking in the first and second test scenarios respectively.

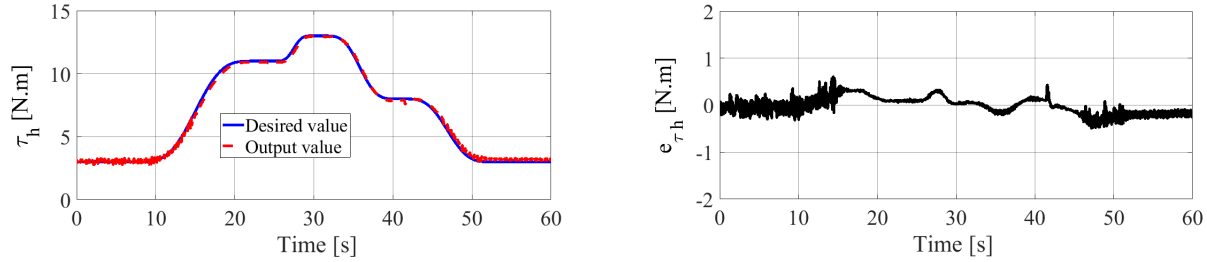

Figure 4.15: Simulation torque tracking result of NMPC in the first test case.

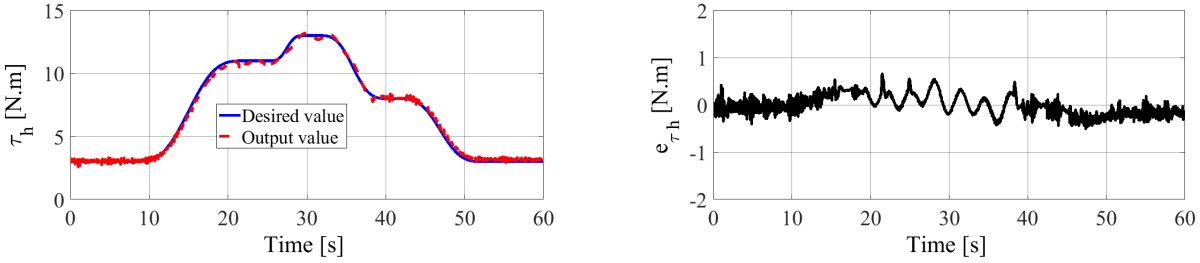

Figure 4.16: Simulation torque tracking result of NMPC in the second test case.

On the test rig, the parameters for the torque tracking control are implemented using the following values

$$w_{\tau 1} = 9.3 \cdot 10^6, w_{\tau 2} = 5.1 \cdot 10^{-7}, w_{\tau 3} = 5.3 \cdot 10^7, w_{\tau 4} = 2 \cdot 10^6, p_\tau = 0.6.$$

The experimental results in the first test case can be found in Fig. 4.17, whereas Fig. 4.18 presents the tracking result of the controller under the impacts of external disturbances in the second test scenario.

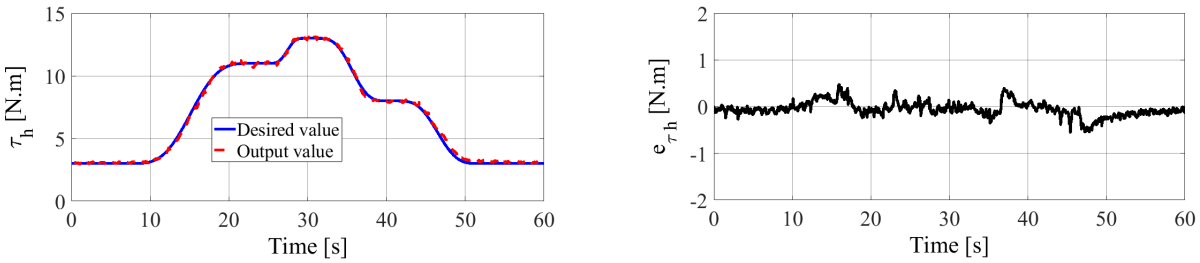

Figure 4.17: Experimental torque tracking result of NMPC in the first test case.

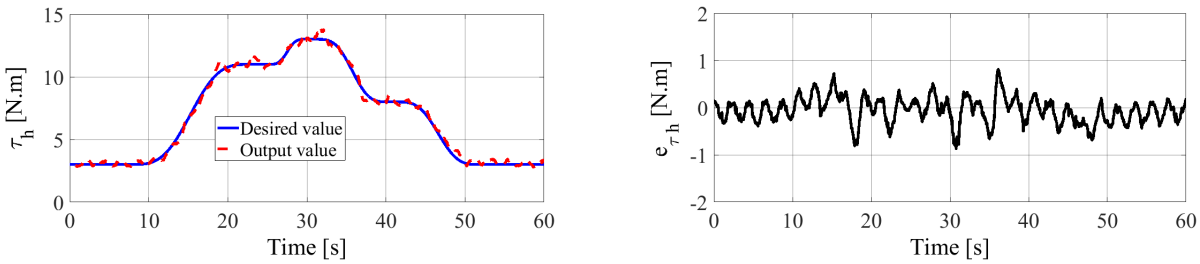

Figure 4.18: Experimental torque tracking result of NMPC in the second test case.

Takagi-Sugeno Fuzzy-Based Optimal Control

The implemented structure of the Takagi-Sugeno fuzzy-based optimal (FBO) control consists of three parts, as depicted in Fig. 3.5. An optimal control is directly applied for the control of hydraulic motor, whereas for the control of the hydraulic pump, the LQR control is involved by deploying the Takagi-Sugeno fuzzy technique. A Kalman filter – which is already implemented for the NMPC – is reemployed in this control study for the feedback of states and disturbances which are required by the controllers.

The control is implemented at sampling time $T_s = 50\ ms$ with the following control parameters

$$\mathbf{Q} = \begin{bmatrix} 10^2 & \\ & 10^{-12} \end{bmatrix},\ r = 10^2,$$
$$q_M = 1, r_M = 1.$$

The simulation results for the hydraulic torque tracking control in the first and second test scenarios are presented in Fig. 4.19 and Fig. 4.20 respectively.

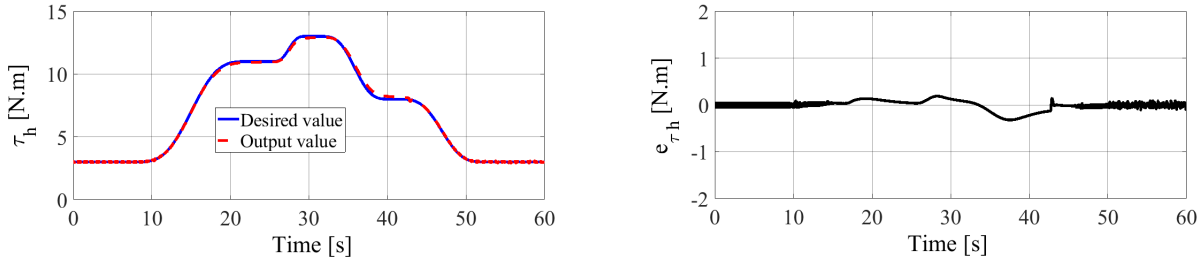

Figure 4.19: Simulation torque tracking result of FBO control in the first test scenario.

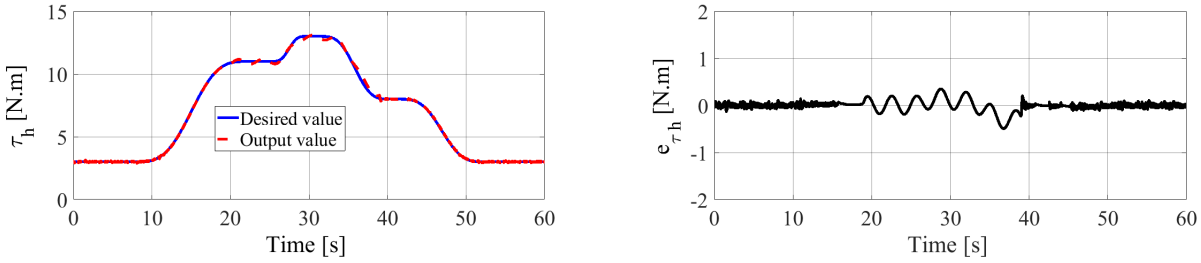

Figure 4.20: Simulation torque tracking result of FBO control in the second test scenario.

An identical parameter setting is also implemented on the test rig. The control performance in the first test case can be found in Fig. 4.21.

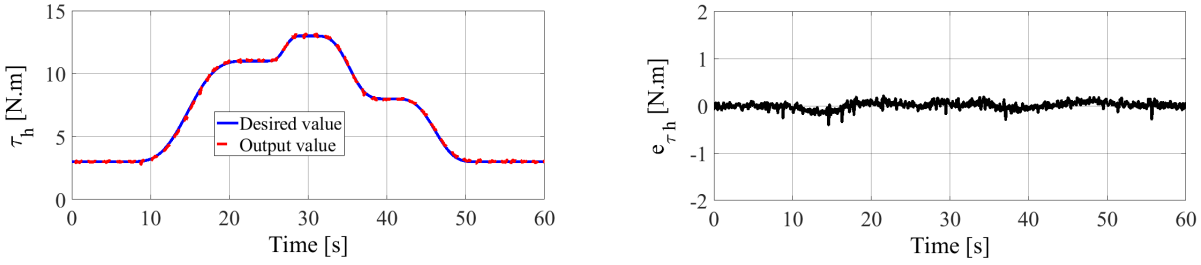

Figure 4.21: Experimental torque tracking result of FBO control in the first test case.

According to the desired torque trajectory, the motor angular velocity varies in a wide range, the displacement unit of the hydraulic motor is controlled synchronically with the pump displacement unit to guarantee the control authority. Their behaviors are visualized in Fig. 4.22

Under the impacts of external disturbances, the controller is still able to maintain an accurate tracking result as presented in Fig. 4.23

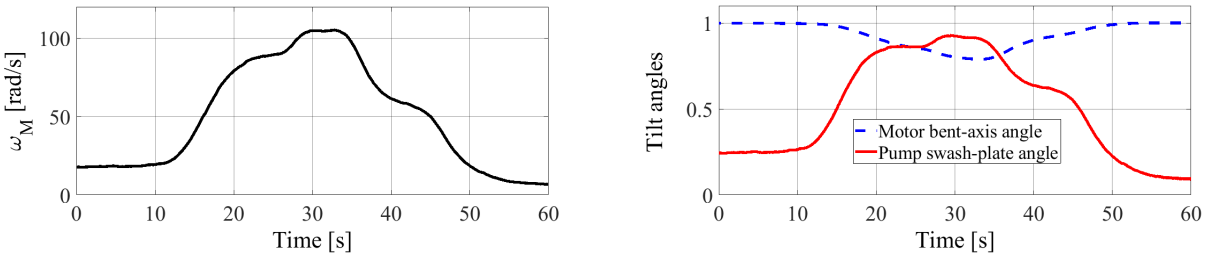

Figure 4.22: Variation of motor angular velocity and displacement units for FBO control.

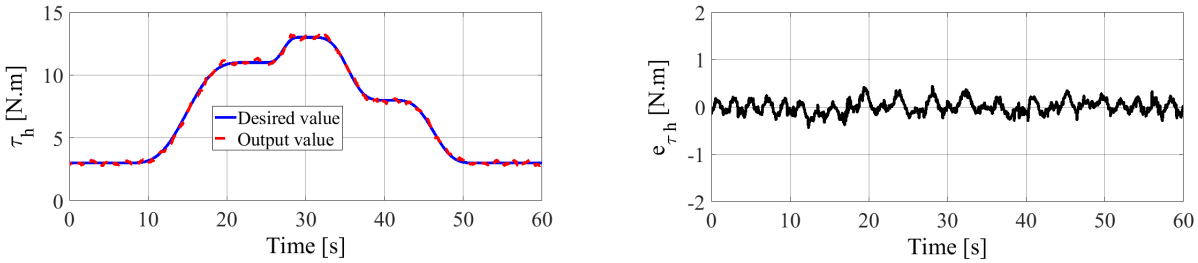

Figure 4.23: Experimental torque tracking result of FBO control in the second test case.

State-Dependent Integral State Feedback Control

The state-dependent integral state feedback (SIF) control also uses the LQR technique as the FBO control does. However, in SIF control, the LQR is deployed to solve the optimal control problem online in real time. The control structure comprises three parts: An optimal control for the hydraulic motor, a state-dependent optimal control for the hydraulic pump and a state-dependent optimal observer for state and disturbance estimations. The sampling time of $T_s = 50\ ms$ is chosen for implementation with the following parameter setting

$$\begin{aligned}
&\mathbf{Q}_e = diag\left(\left[10^{-5}\ 10^{-10}\ 10^{4}\ 10^{4}\ 10^{-9}\ 10^{4}\right]\right),\\
&\mathbf{R}_e = diag\left(\left[10^{10}\ 10^{4}\right]\right),\\
&\bar{\mathbf{Q}} = diag\left(\left[1\ 10^{-8}\ 10^{8}\right]\right),\ \bar{r} = 1,\\
&q_M = 1,\ r_M = 1.
\end{aligned}$$

The performance of the state-dependent observer for disturbance estimations is shown in Fig. 4.24. As can be seen, the estimation provides sufficient accuracy for the control design.

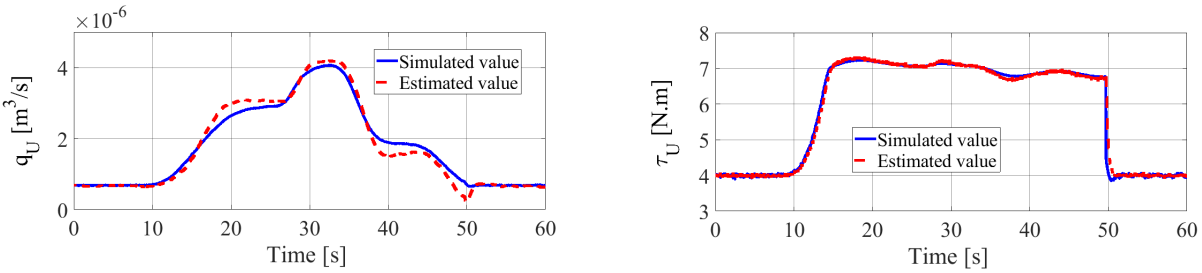

Figure 4.24: Disturbance estimations of the state-dependent observer.

Fig. 4.25 and Fig. 4.26 show the simulation results of the proposed controller in the first and second test cases respectively.

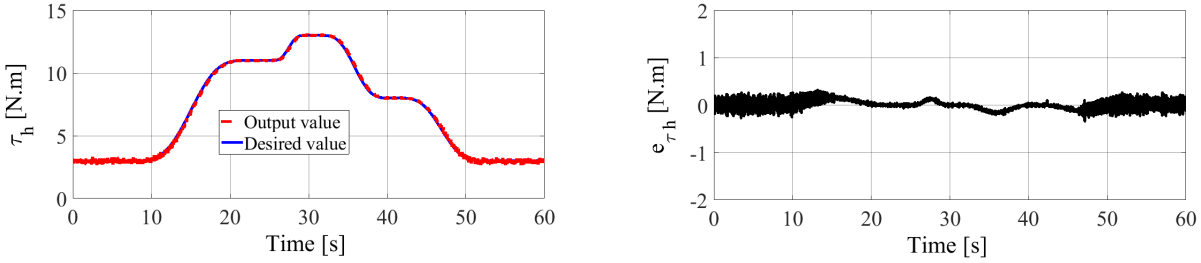

Figure 4.25: Simulation torque tracking result of SIF control in the first test case.

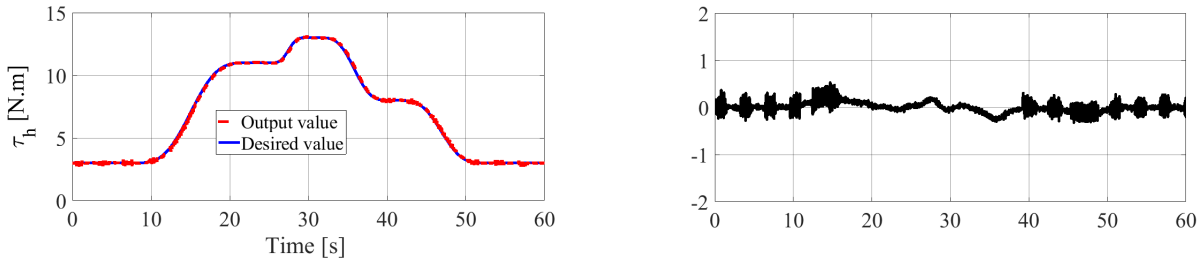

Figure 4.26: Simulation torque tracking result of SIF control in the second test case.

The experimental results on the test rig can be found in Fig. 4.27 and Fig. 4.28 for the first and second test scenarios respectively. As depicted, the controller performs quite well in both test cases, the accuracy is achievable with small tracking errors.

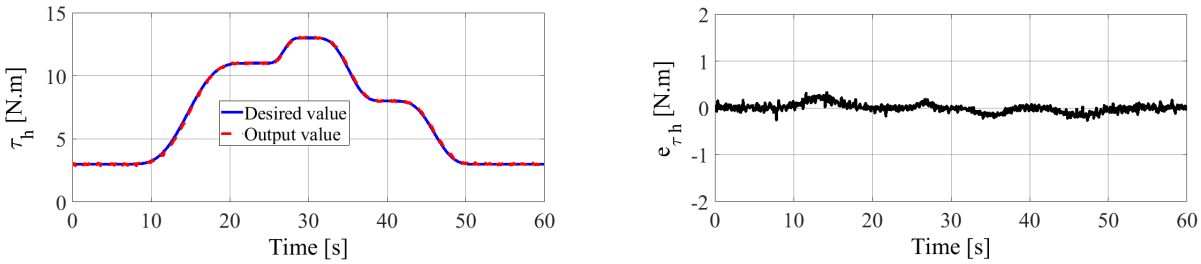

Figure 4.27: Experimental torque tracking result of SIF control in the first test case.

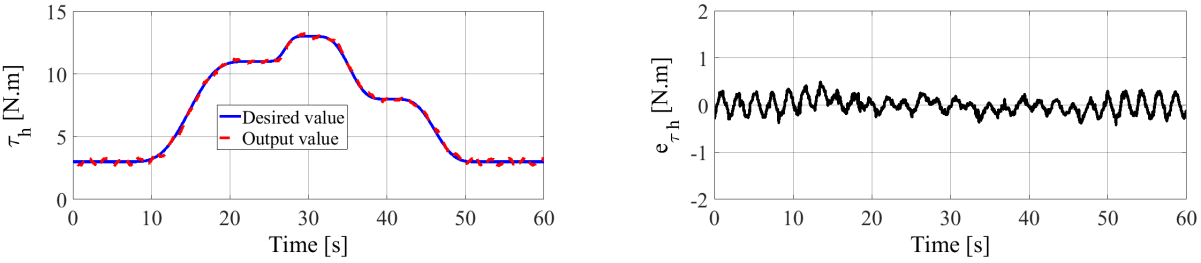

Figure 4.28: Experimental torque tracking result of SIF control in the second test case.

Summary

The performance of optimization-based control structures is summarized and analyzed in the Tab. 4.1, 4.2 and Tab. 4.3. As can be seen from the Tab. 4.1, the NMPC – for the velocity

control – performs equivalently both in simulation and on the real system for the first test case where the prime mover angular velocity and external torque disturbance are constant. However, in the second test case where the external disturbances impact on the system, the performance on the real equipment degrades dramatically in comparison to the performance in simulations. This may come from the fact that some physical characteristics of the real system under the effect of disturbances are not fully reflected in the mathematical model, therefore, the model based design could not fully compensate the disturbances.

Table 4.1: RMS error evaluation for velocity control of the nonlinear MPC

	The first test scenario	**The second test scenario**	**Increasing error**
Simulation	$2.371 \cdot 10^{-1}$	$3.674 \cdot 10^{-1}$	54.9%
Experiment	$2.790 \cdot 10^{-1}$	$5.181 \cdot 10^{-1}$	85.7%

In the Tab. 4.2 and Tab. 4.3, the tracking performance of the hydraulic torque control for the three control structures are compared. As can be concluded from the data statistics, the FBO and SIF controls provide better tracking results in comparison to the nonlinear MPC. In simulation, they perform quite equivalently in both test cases. Nevertheless, on the real system the tracking accuracy reduces significantly under the impact of disturbances in the second test case, that seems to confirm the above comments regarding the model-based design.

Table 4.2: Comparison of simulation RMS error for optimization-based control designs

	The first test scenario	**The second test scenario**	**Increasing error**
MPC	$1.805 \cdot 10^{-1}$	$2.097 \cdot 10^{-1}$	16.2%
FBO	$1.068 \cdot 10^{-1}$	$1.153 \cdot 10^{-1}$	8.0%
SIF	$1.058 \cdot 10^{-1}$	$1.210 \cdot 10^{-1}$	14.4%

Table 4.3: Comparison of experimental RMS error for optimization-based control designs

	The first test scenario	**The second test scenario**	**Increasing error**
MPC	$1.609 \cdot 10^{-1}$	$2.758 \cdot 10^{-1}$	71.4%
FBO	$0.800 \cdot 10^{-1}$	$1.392 \cdot 10^{-1}$	74.0%
SIF	$0.886 \cdot 10^{-1}$	$1.590 \cdot 10^{-1}$	79.5%

4.2.2 Estimator-Based Feedback Linearization

Feedback Linearization Using the RDO

The control structure consists of two components – a flatness-based control for the hydraulic motor and a feedback linearization control for the hydraulic pump. The control of hydraulic pump comprises two control signals – the stabilizing control signal generated by a linear PD-type controller and the linearizing signal obtained from the linearization loop. The controller is implemented with sample time $T_s = 20\ ms$. The linear PD-type stabilizing controller is set up with the following design parameters

$$\lambda_1 = 100, \lambda_2 = 20, k = 10$$

and the parameter setting of the tracking differentiator LTD3 for signal derivatives filtering is given as follows

$$R_{\vartheta 3} = 12, c_{\vartheta 3,1} = 27, c_{\vartheta 3,2} = 27, c_{\vartheta 3,3} = 9.$$

For the control of the hydraulic motor, the flatness-based controller is implemented using the following parameter setting for the LTD2 and for the feedback gain

$$R_{\vartheta 2} = 15, c_{\vartheta 2,1} = 10, c_{\vartheta 2,2} = 25, k_{\alpha M} = 10.$$

With these specifications, the performance of the linear feedback stabilizer is shown in Fig. 4.29 where the nonlinearity and disturbance compensation is not activated. As can be seen, the nonlinearity and disturbance in the system cause a large difference between the output and the desired value of the motor angular velocity. That simply means the system could not be accurately controlled by a simple linear controller.

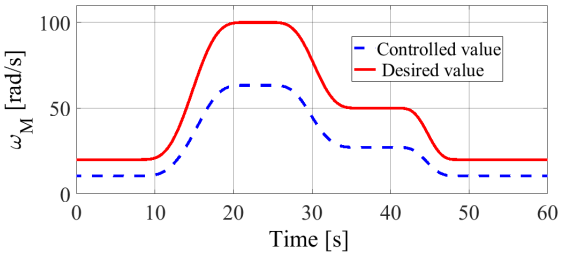

Figure 4.29: Performance of the simple linear feedback controller.

In the feedback linearization control using the RDO, the feedback linearization loop requires the estimates of the motor bent-axis angle and the leakage flow disturbance to construct the linearization signal. These two variables are estimated by the RDO whose characteristic specifications according to 3.127 are chosen as follows

$$s_1 = 10, s_2 = 10, s_3 = 20, s_4 = 20.$$

The estimation accuracy of the RDO is shown in Fig. 4.30 and the tracking performance of the whole control structure in the first test scenario is presented in Fig. 4.31. As can be seen, a good matching between the output value and the desired value is recognizable with a very small tracking error. In the second test scenario where the pump angular velocity and the external load torque are intensively varying, the simulation result in Fig. 4.32 presents a good maintenance of the tracking performance despite of a small oscillation in the output.

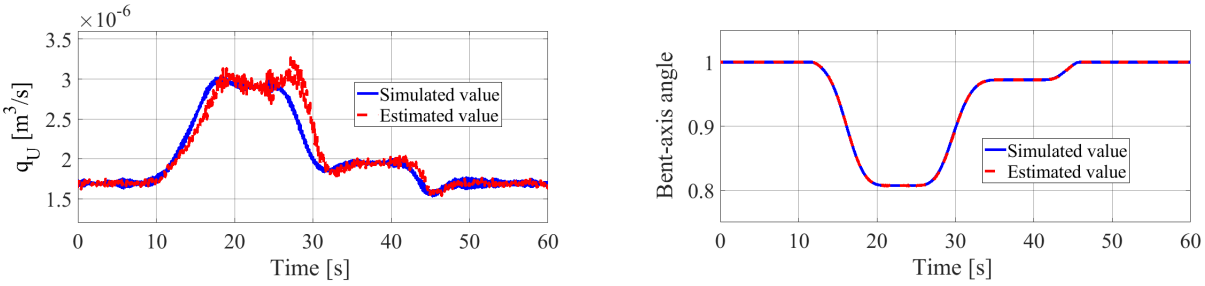

Figure 4.30: Estimation of disturbance q_U and the bent-axis angle $\tilde{\alpha}_M$ by the RDO.

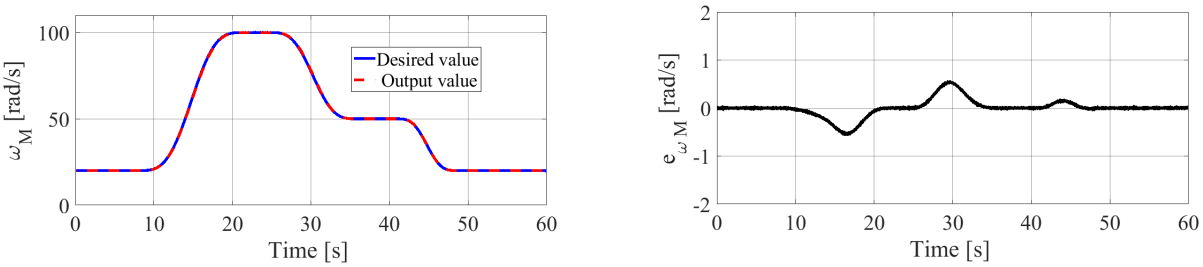

Figure 4.31: Simulation velocity tracking result using the RDO in the first test case.

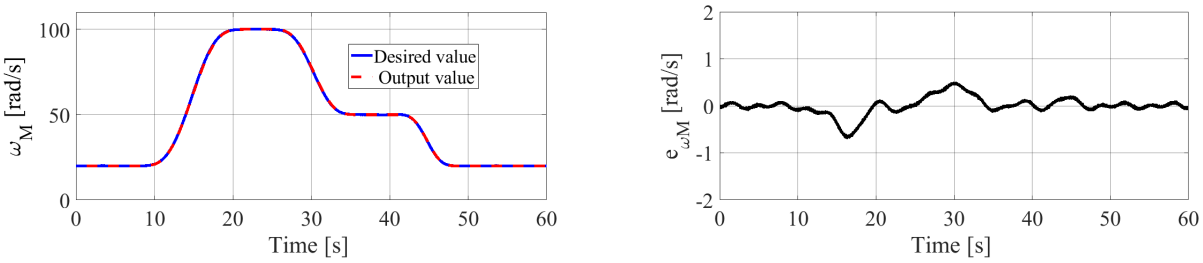

Figure 4.32: Simulation velocity tracking result using the RDO in the second test case.

Based on the successful results in simulation, the control structure is implemented on the test rig. Due to the mismatch between simulation model and the real system, the implemented parameter setting generally requires a bit further tuning for a good performance. In this control design, the following control parameter setting is adapted on the test rig

$$\begin{aligned}
&\lambda_1 = 54, \lambda_2 = 10, k = 22,\\
&R_{\vartheta 3} = 5, c_{\vartheta 3,1} = 8, c_{\vartheta 3,2} = 12, c_{\vartheta 3,3} = 6,\\
&R_{\vartheta 2} = 15, c_{\vartheta 2,1} = 10, c_{\vartheta 2,2} = 25, k_{\alpha M} = 10,\\
&s_1 = 5, s_2 = 5, s_3 = 10, s_4 = 10.
\end{aligned}$$

The experimental tracking result in the first test scenario is shown in Fig. 4.33. The result in the second test scenario under the effect of external disturbances is visualized in Fig. 4.34, as can be seen, in comparison to the first test case, the tracking error becomes larger with intensive oscillations, however, the tracking accuracy is still maintained.

As the main obstacle in using derivative terms for control designs is the noise caused by measurement signal, noisy derivatives of measurement signal raise the vibration of mechanical actuators, that reduces the lifetime of system components. In this control design, the derivatives of the measured angular velocity are estimated by the tracking differentiator, therefore, the vibration of the pump displacement unit can be reduced. The detail shown in Fig. 4.35 analyzes the

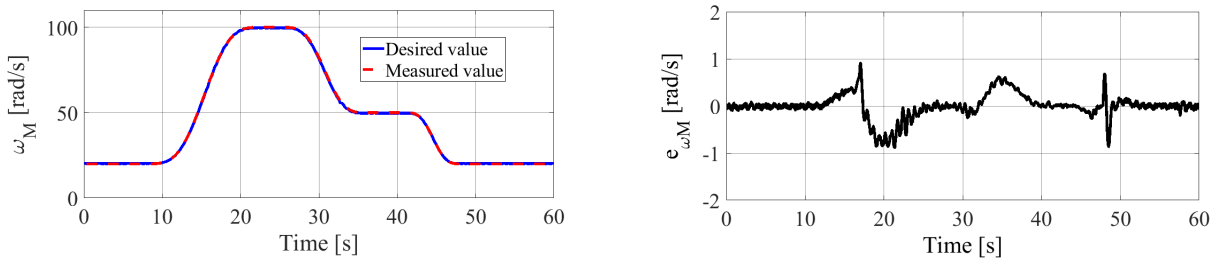

Figure 4.33: Experimental velocity tracking result using the RDO in the first test case.

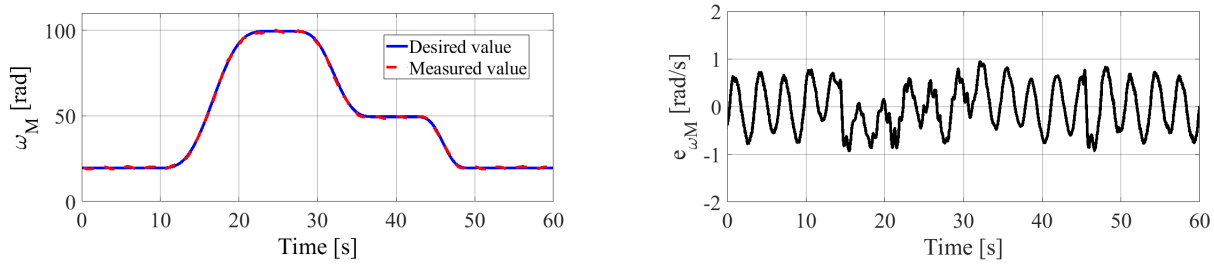

Figure 4.34: Experimental velocity tracking result using the RDO in the second test case.

resulting control signal on the test rig, as can be seen, the noise is mostly filtered out, only small vibration is visible.

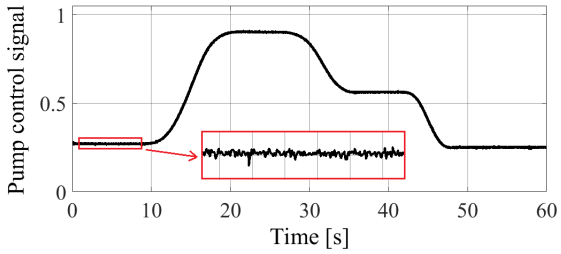

Figure 4.35: Analog control signal of the hydraulic pump.

However, this is the electrical vibration, under the filtering effect of the hydraulic pump displacement unit – whose dynamics is presented by a first-order lag system – this vibration will be filtered out further and is not very visible at the mechanical parts as demonstrated in Fig. 4.36. This proves the capability of using filtered derivatives for feedback designs for HST applications.

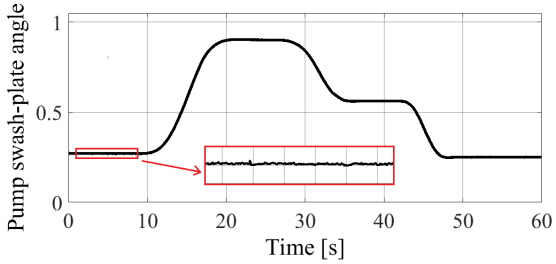

Figure 4.36: Smooth motion of the pump swash plate.

Feedback Linearization with APE

The simulation of the feedback linearization control using APE also uses the same setting for the feedback controller as used in the RDO case. The sampling time $T_s = 20\ ms$ is used as well

$$\lambda_1 = 100, \lambda_2 = 20, k = 10,$$
$$R_{\vartheta 3} = 12, c_{\vartheta 3,1} = 27, c_{\vartheta 3,2} = 27, c_{\vartheta 3,3} = 9,$$
$$R_{\vartheta 2} = 15, c_{\vartheta 2,1} = 10, c_{\vartheta 2,2} = 25$$

and the adaptation rates for the APE are set as follows

$$\gamma_0 = 10^{-5}, \gamma_1 = 4 \cdot 10^{-4}, \gamma_2 = 10^{-5}, \gamma_3 = 10^{-5}, \gamma_4 = 4 \cdot 10^{-6}.$$

The adaptive parameters can be initialized according to the nominal model of the HST system

$$a_0 = 1, a_1 = 1, a_2 = 1, a_3 = 1, a_4 = 0.$$

Fig. 4.37 shows the simulation result of the implemented controller in the first test scenario. As can be seen, an excellent tracking performance can be achieved with a good matching between the output and the desired value, which results in a very small tracking error.

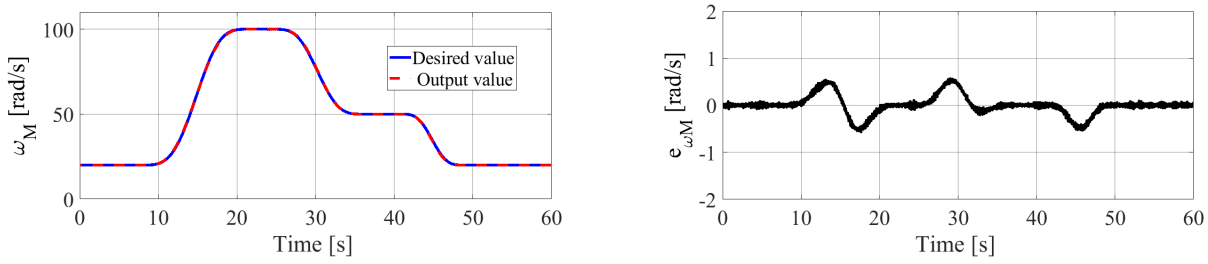

Figure 4.37: Simulation velocity tracking result using APE in the first test case.

The behavior of adaptive parameters corresponding to the given adaptive rates and initialization is depicted in Fig. 4.38. The results show that the parameters a_1 and a_4 take the most action to compensate the uncertainty and the disturbance in the system whereas the parameters a_2, a_3 and a_0 mostly stay constant.

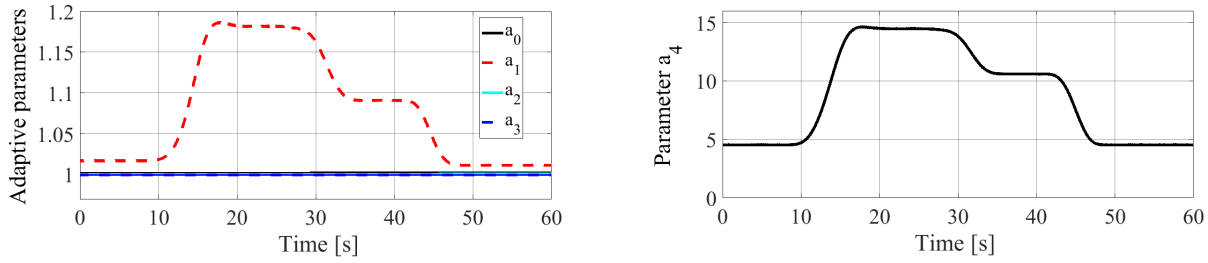

Figure 4.38: Variation of adaptive parameters.

The simulation of the controller in the second test scenario is presented in Fig. 4.39. As can be seen, the output motor angular velocity suffers a small oscillation as the pump angular velocity and the external load torque change, however, the performance is quite equivalent to the result in the first test case.

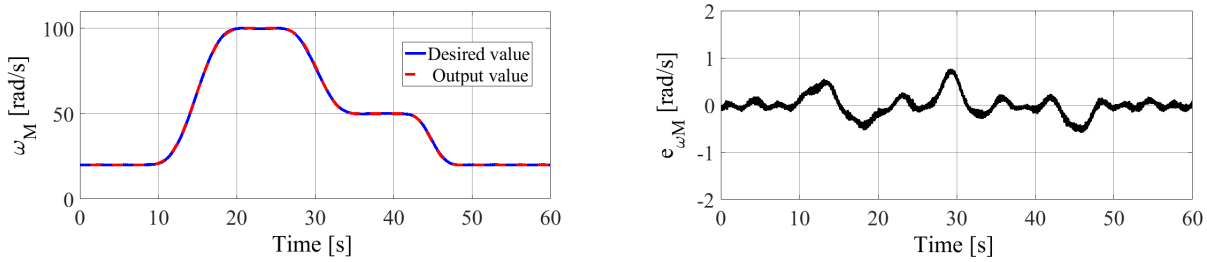

Figure 4.39: Simulation velocity tracking result using APE in the second test case.

On the test rig, the controller is implemented with the same sampling time $T_s = 20\ ms$. Similarly to the previous implementation, the parameters are also further adapted on the real system with the following setting

$$\lambda_1 = 54, \lambda_2 = 10, k = 22,$$
$$R_{\vartheta 3} = 5, c_{\vartheta 3,1} = 8, c_{\vartheta 3,2} = 12, c_{\vartheta 3,3} = 6,$$
$$R_{\vartheta 2} = 15, c_{\vartheta 2,1} = 10, c_{\vartheta 2,2} = 25, k_{\alpha M} = 10,$$
$$\gamma_0 = 10^{-6}, \gamma_1 = 7 \cdot 10^{-3}, \gamma_2 = 10^{-6}, \gamma_3 = 10^{-6}, \gamma_4 = 2 \cdot 10^{-3},$$
$$a_0 = 1, a_1 = 1, a_2 = 1, a_3 = 1, a_4 = 0.$$

The experimental result in first test scenario is shown in Fig. 4.40, the small tracking error indicates a good tracking performance of the implemented controller. In the second test scenario, a good accuracy is also achieved, however, the controlled output oscillates with higher amplitudes in comparison to the one in simulation. The result is shown in Fig. 4.41

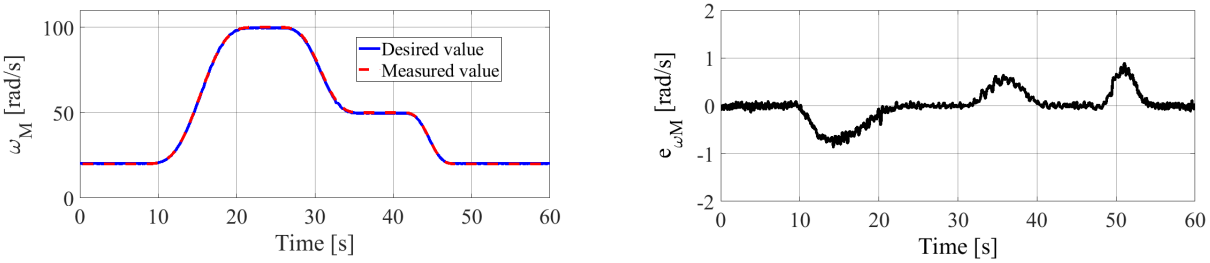

Figure 4.40: Experimental velocity tracking result using APE in the first test case.

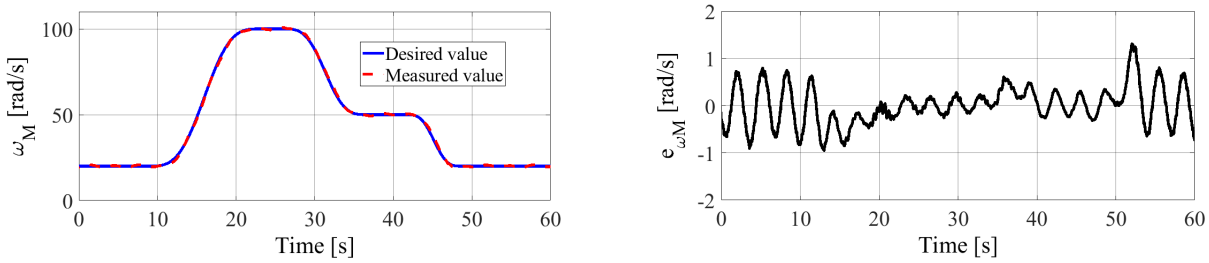

Figure 4.41: Experimental velocity tracking result using APE in the second test case.

Feedback Linearization Using MLP Networks

In this control approach, an MLP network is used for nonlinearity and disturbance compensation. The neural network processes the measurement vector $\begin{bmatrix} \omega_M & \dot{\omega}_M & \ddot{\omega}_M \end{bmatrix}^T$ as the synaptic

inputs. However, as indicated by tests, the synaptic input $\ddot{\omega}_M$ should not be activated due to the noise, which is not completely removed by the LTD3, to avoid causing the neural network noisy. Therefore, only ω_M and $\dot{\omega}_M$ are supplied into the neural network. With the simulation sampling time $T_s = 20\ ms$, the parameter setting for the hydraulic motor controller and for the linear feedback controller of the hydraulic pump are given as follows

$$\begin{aligned}
&\lambda_1 = 100, \lambda_2 = 20, k = 10,\\
&R_{\vartheta 3} = 12, c_{\vartheta 3,1} = 27, c_{\vartheta 3,2} = 27, c_{\vartheta 3,3} = 9,\\
&R_{\vartheta 2} = 15, c_{\vartheta 2,1} = 10, c_{\vartheta 2,2} = 25.
\end{aligned}$$

The neural network consists of $L = 10$ neurons using the following tuning parameters

$$\boldsymbol{M}_v = \begin{bmatrix} 10 & & \\ & 4 & \\ & & 0 \end{bmatrix}, M_w = 12, \kappa = 2 \cdot 10^{-6}, \theta_m = 2 \cdot 10^4, k_r = 0.2$$

and the neural network weights are initialized as follows

$$\begin{aligned}
&\mathbf{V} = \mathbf{0},\\
&\mathbf{w} = 100 + 50 \cdot rand\,(10, 1)\,,
\end{aligned}$$

where $rand()$ is a random generator generating random vector in the range $\{0...1\}$.

Fig. 4.42 shows the tracking performance of the controller in the first test scenario. Similarly to two previous controllers, a good match between the output and the desired values can be achieved. The variation of network weights corresponding to the chosen settings is depicted in Fig. 4.43.

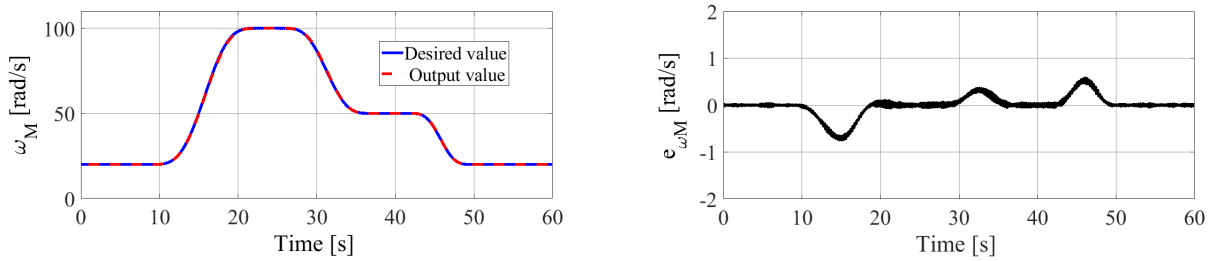

Figure 4.42: Simulation velocity tracking result using MLP networks in the first test case.

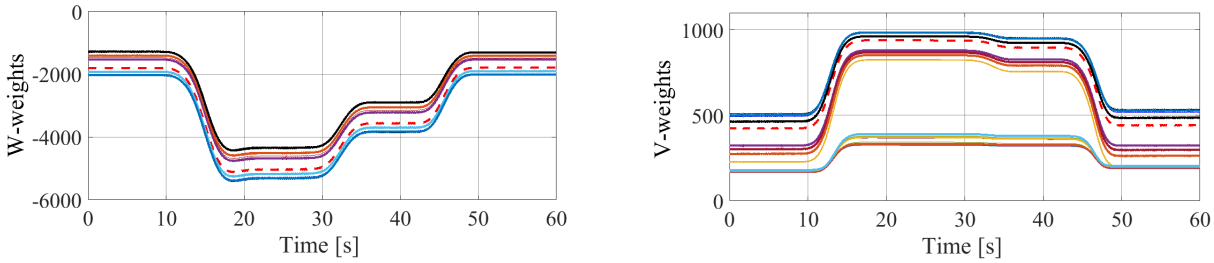

Figure 4.43: Variation of the MLP network weights.

The tracking performance in second test scenario is presented in Fig. 4.44. As can be seen, in comparison to previous controllers, the output motor angular velocity also suffers a small oscillation, however, the magnitude is much lower.

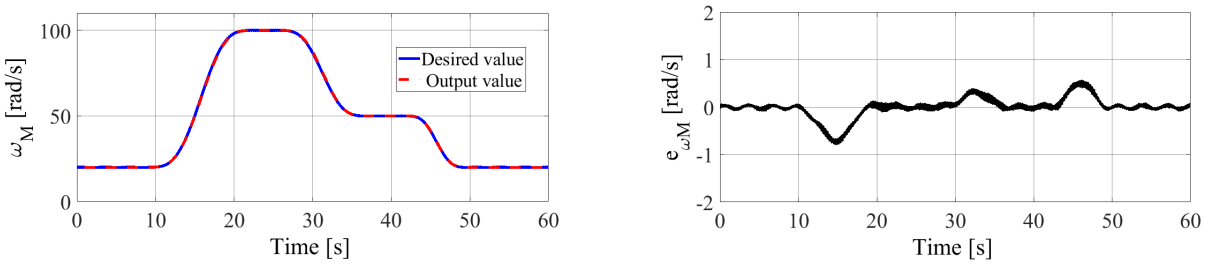

Figure 4.44: Simulation velocity tracking result using MLP networks in the second test case.

On the test rig, the controller is implemented with the same sampling time $T_s = 20\ ms$. As the conditions on the real equipment are different from those in simulation, the setting of some parameters is adjusted for a good control performance. They are given as follows

$$
\begin{aligned}
&\lambda_1 = 54, \lambda_2 = 10, k = 22,\\
&R_{\vartheta 3} = 5, c_{\vartheta 3,1} = 8, c_{\vartheta 3,2} = 12, c_{\vartheta 3,3} = 6,\\
&R_{\vartheta 2} = 15, c_{\vartheta 2,1} = 10, c_{\vartheta 2,2} = 25, k_{\alpha M} = 10,\\
&\boldsymbol{M}_v = \begin{bmatrix} 5 & & \\ & 5 & \\ & & 0 \end{bmatrix}, M_w = 5.5, \kappa = 2 \cdot 10^{-6}, \Theta_m = 2 \cdot 10^4, k_z = 0.1,\\
&\mathbf{V} = \mathbf{0}, \mathbf{w} = 100 + 50 \cdot rand\,(10, 1)\,.
\end{aligned}
$$

The experimental results for the first and second test scenarios are shown in Fig. 4.45 and Fig. 4.46 correspondingly, the small tracking error indicates an excellent tracking performance of the implemented controller with MLP networks on the real equipment.

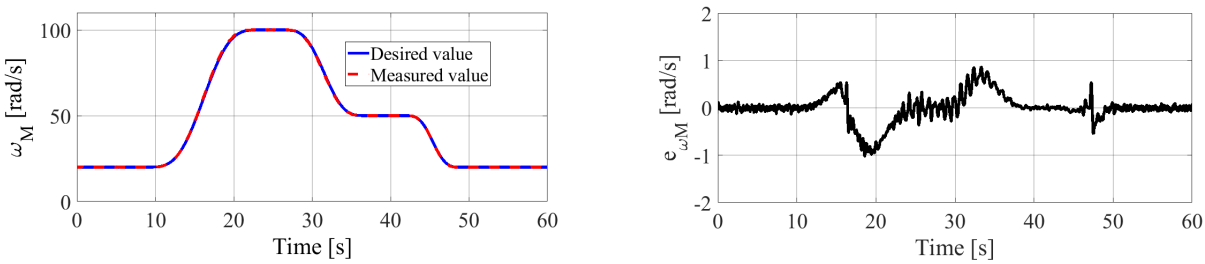

Figure 4.45: Experiment velocity tracking result using MLP networks in the first test case.

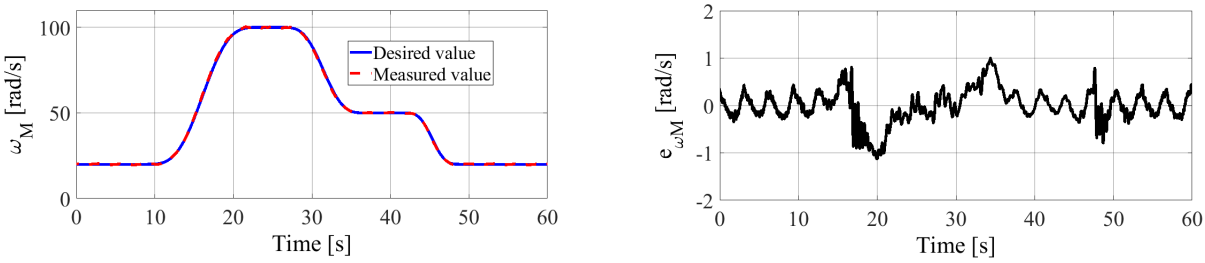

Figure 4.46: Experiment velocity tracking result using MLP networks in the second test case.

Summary

The feedback linearization approaches – with three alternative methods for nonlinearity and disturbance compensation – seem efficient for the control of HST systems. The results show a good tracking performance for all proposed feedback linearization control structures, however, a slight difference is visible in the test results which is summary in the Tab. 4.4 and Tab. 4.5 using root-mean-square (RMS) error for evaluation. As the feedback stabilizer uses the same setting as indicated before, this difference obviously comes from the different linearizing approaches used in the nonlinearity and disturbance compensation loop.

Table 4.4: Simulation RMS errors of feedback linearization control with alternative compensation approaches

	The first test scenario	**The second test scenario**	**Increasing error**
RDO	$1.795 \cdot 10^{-1}$	$1.895 \cdot 10^{-1}$	5.3%
APE	$2.044 \cdot 10^{-1}$	$2.216 \cdot 10^{-1}$	7.4%
MLP	$2.108 \cdot 10^{-1}$	$2.121 \cdot 10^{-1}$	0.6%

Table 4.5: Experimental RMS errors of feedback linearization control with alternative compensation approaches

	The first test scenario	**The second test scenario**	**Increasing error**
RDO	$2.607 \cdot 10^{-1}$	$4.761 \cdot 10^{-1}$	82.5%
APE	$3.039 \cdot 10^{-1}$	$4.060 \cdot 10^{-1}$	33.6%
MLP	$2.927 \cdot 10^{-1}$	$3.476 \cdot 10^{-1}$	18.7%

From Tab. 4.4 it can be concluded that the control with the RDO provides the best tracking performance, the APE and MLP approaches follow behind. This result may come from the perfect match between the simulation model and the model-based design. However, the increasing errors under the effects of external disturbances show that the approach with the MLP network provides more robustness for the control structure. The APE approach is also based on the system model with the use of an adaptation mechanism, however, the small adaptation rate – which is required for stability – may result in a slow response of the controller to the variation of external disturbances.

The situation changes a bit on the real system as seen in Tab. 4.5. Under the effects of external disturbances, the tracking performance of the RDO approach degrades significantly whereas the adaptive methods such as APE and MLP maintain the accuracy pretty much better.

4.2.3 Active Disturbance Rejection Controls

ESO-Based ADR Control

The ESO-based control is the standard structure of the ADR approach, which consists of an ESO for the state and disturbance estimations and a linear feedback controller. The ESO gains are defined using the characteristic ratio assignment method proposed in [97]

$$l_0 = 9.4 \cdot 10^5, l_1 = 2.4 \cdot 10^5, l_2 = 2.7 \cdot 10^4, l_3 = 1.7 \cdot 10^3, l_4 = 60$$

and the gains of the feedback control are also defined in the same way

$$\alpha_0 = 271, \alpha_1 = 92, \alpha_2 = 14.$$

The feedforward control for the hydraulic motor is implemented with the LTD2 using the following parameters

$$R_{\vartheta 2} = 15, c_{\vartheta 2,1} = 10, c_{\vartheta 2,2} = 25, k_{\alpha M} = 10.$$

The simulation is performed at sampling time of 20 ms. With the given specifications, the tracking performance of the ESO-based ADR control structure in the first test scenario is presented in Fig. 4.47. As can be seen, the controller can accurately track the desired trajectory of the system output.

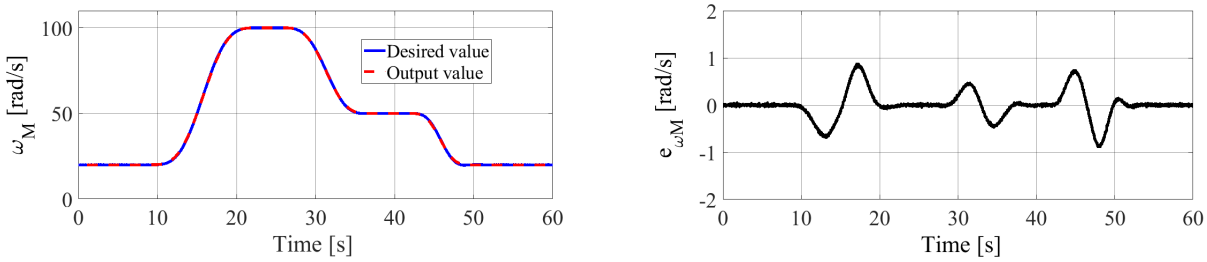

Figure 4.47: Simulation velocity tracking result of ESO-based ADR control in the first test case.

In the second test scenario where the pump angular velocity and the external load torque are intensively varying, the simulation result shown in Fig. 4.48 presents a very good maintenance of tracking performance.

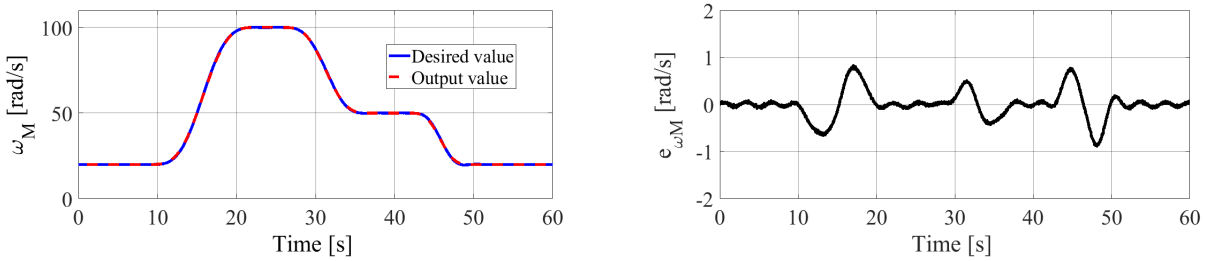

Figure 4.48: Simulation velocity tracking result of ESO-based ADR control in second test case.

Based on the successful results in simulation, the ESO-based ADR control structure is implemented on the test rig with the same sampling time of $T_s = 20$ ms, the feedback controller and

the ESO gains are further tuned for a good result on the real equipment, their values are given as follows

$$\alpha_0 = 350, \alpha_1 = 120, \alpha_2 = 30,$$
$$l_0 = 8.7 \cdot 10^5, l_1 = 1.7 \cdot 10^5, l_2 = 2.5 \cdot 10^4, l_3 = 1.1 \cdot 10^3, l_4 = 30.$$

Fig. 4.49 shows the tracking error of the control in the first test scenario on the real HST system. A similar tracking accuracy in comparison to the one of simulation is achievable.

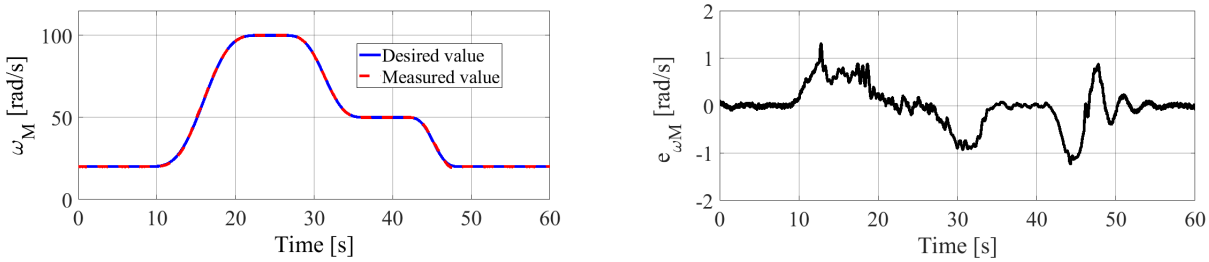

Figure 4.49: Experimental velocity tracking result of ESO-based ADR control in the first test case.

The tracking result under the effects of the varying pump angular velocity and external torque is visualized in Fig. 4.50. As can be seen, the controller responds with more oscillations on the real system than in simulation, however, the tracking accuracy still can be achieved.

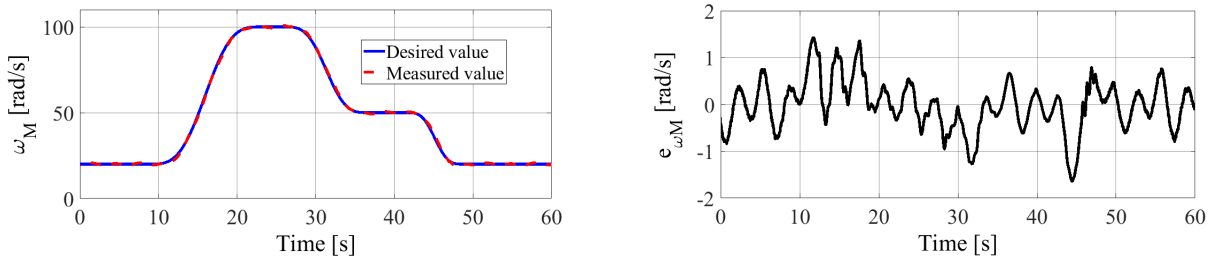

Figure 4.50: Experimental velocity tracking result of ESO-based ADR control in the second test case.

Flat-Filtering-Based ADR Control

The simulation is conducted with sampling time $Ts = 20\ ms$, the compensation network parameters are determined using the characteristic ratio assignment method [97] as follows

$$\beta_0 = 5.6 \cdot 10^7, \beta_1 = 1.4 \cdot 10^7, \beta_2 = 1.6 \cdot 10^6, \beta_3 = 1.1 \cdot 10^5, \beta_4 = 4.2 \cdot 10^3, \beta_5 = 96$$

and the previous setting for the feedforward control of the hydraulic motor and the LTD2 is used

$$R_{\vartheta 2} = 15, c_{\vartheta 2,1} = 10, c_{\vartheta 2,2} = 25, k_{\alpha M} = 10.$$

Fig 4.51 shows the tracking performance of the controller in the first test scenario with a small tracking error. The tracking performance in the second test scenario is presented in Fig. 4.52. It is recognizable that the output motor angular velocity can still track the desired value very accurately, the effects of external disturbances are almost invisible in the tracking result.

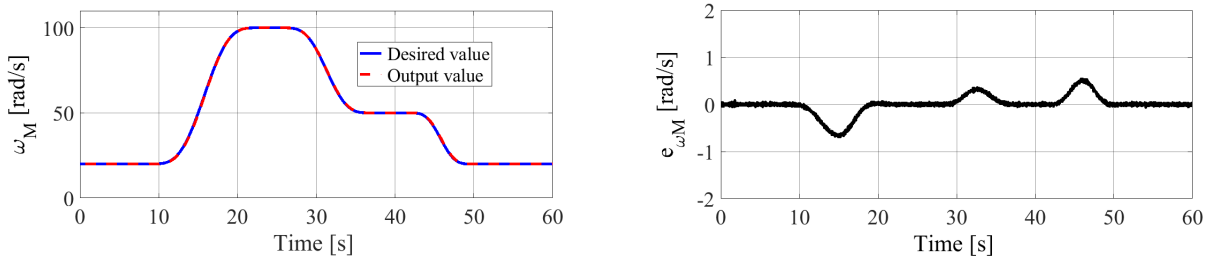

Figure 4.51: Simulation velocity tracking result of flat-filtering-based ADR control in the first test case.

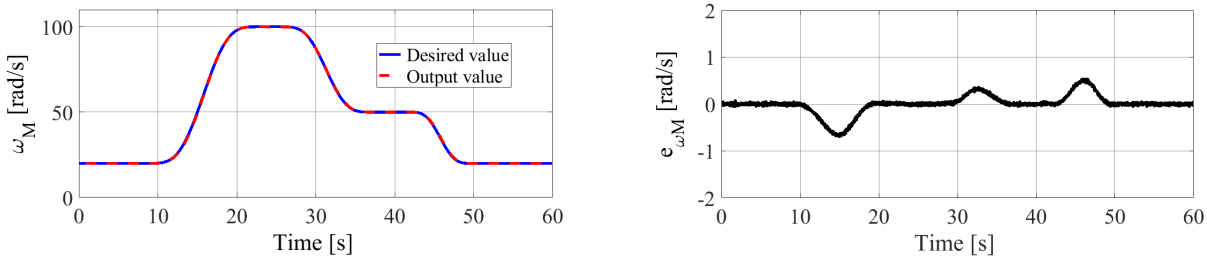

Figure 4.52: Simulation velocity tracking result of flat-filtering-based ADR control in the second test case.

On the test rig, the controller is implemented with the same sampling time $T_s = 20\ ms$ using the following parameter setting

$$\begin{aligned}
&\beta_0 = 9.5 \cdot 10^6, \beta_1 = 6.5 \cdot 10^5, \beta_2 = 9.2 \cdot 10^5,\\
&\beta_3 = 9 \cdot 10^4, \beta_4 = 3.5 \cdot 10^3, \beta_5 = 80,\\
&R_{\vartheta 2} = 15, c_{\vartheta 2,1} = 10, c_{\vartheta 2,2} = 25,\\
&k_{\alpha M} = 10.
\end{aligned}$$

The experimental result for first test scenario is shown in Fig. 4.53. A very good tracking result on the real system with a small tracking error indicates the efficiency of the implemented controller. In the second test scenario, a good accuracy is also achieved, however, the controlled output oscillates with a visible amplitude but much better in comparison to the ESO-based controller. The result is shown in Fig. 4.54

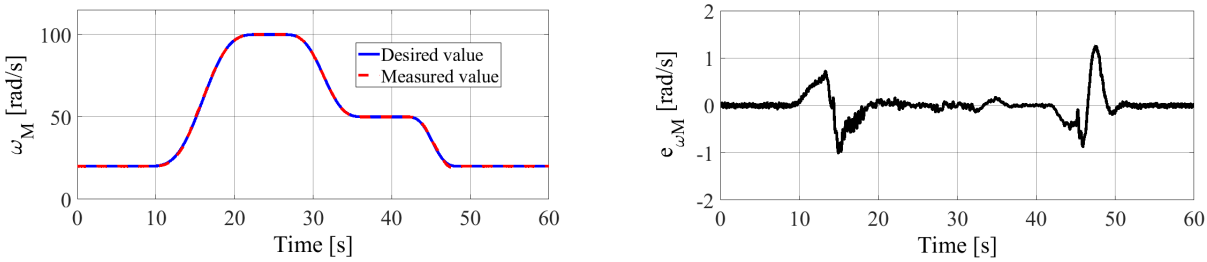

Figure 4.53: Experimental velocity tracking result of flat-filtering-based ADR control in the first test case.

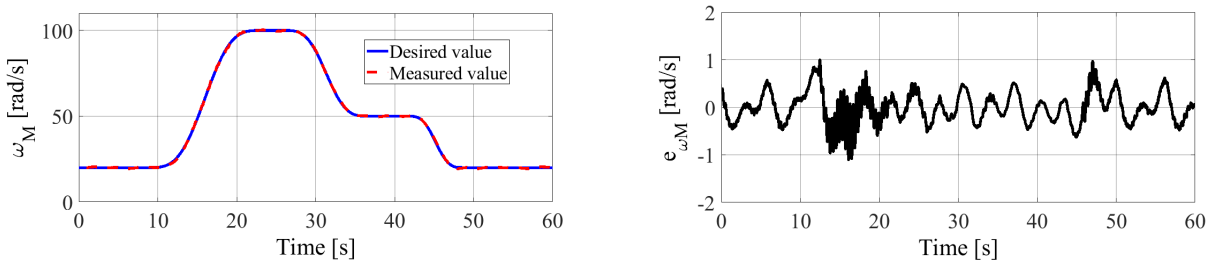

Figure 4.54: Experimental velocity tracking result of flat-filtering-based ADR control in the second test case.

Summary

The simulation and experimental results of the two ADR control approaches prove the capability of these control structures on the HST system. The performance evaluation using the RMS error is summarized in the Tab. 4.6 and Tab. 4.7. As can be seen from the data statistics, both the simulation and experiments confirm a better performance of the velocity tracking for the flat-filtering-based ADR control in comparison to the ESO-based approach.

Table 4.6: Comparison of simulation RMS error for ADR controllers

	The first test scenario	**The second test scenario**	**Increasing error**
ESO-based	$2.904 \cdot 10^{-1}$	$2.938 \cdot 10^{-1}$	1.2%
Flat-filtering	$1.973 \cdot 10^{-1}$	$1.991 \cdot 10^{-1}$	0.9%

Table 4.7: Comparison of experimental RMS error for ADR controllers

	The first test scenario	**The second test scenario**	**Increasing error**
ESO-based	$4.219 \cdot 10^{-1}$	$5.354 \cdot 10^{-1}$	26.9%
Flat-fitering	$2.711 \cdot 10^{-1}$	$3.300 \cdot 10^{-1}$	21.7%

4.2.4 Model-Free Approaches

Sliding Mode Control

The sliding mode control design in the model-free frame work consists of a feedforward control for the hydraulic motor and a TD-based sliding mode control for the hydraulic pump. As depicted in Fig. 3.19, the feedforward control signal for the motor bent-axis angle is generated directly from the trajectory scheduling module. For the control of the pump swash-plate angle, an LTD4 is used to filter the signal derivatives. These signals are supplied into the sliding mode control. The LTD4 also provides the third time derivative signal of the system output for disturbance estimation.

As recommended in the model-free approach, the parameter K is chosen based on system understanding

$$K = 11 \cdot 10^4.$$

The parameters of the LTD4 are determined using the pole-placement method as follows

$$c_{\vartheta 4,1} = 81, c_{\vartheta 4,2} = 108, c_{\vartheta 4,3} = 54, c_{\vartheta 4,4} = 12$$

and $R_{\vartheta 4} = 12$. The parameters of sliding manifold are obtained based on the characteristic ratio assignment method and further tuned for a good tracking result whereas the parameters of switching part are chosen empirically as follows

$$\rho_0 = 700, \rho_1 = 120, \rho_2 = 15,$$
$$\bar{\rho} = 400, \bar{\gamma} = 50.$$

The simulation result of the tracking control in the first test scenario is shown in Fig. 4.55

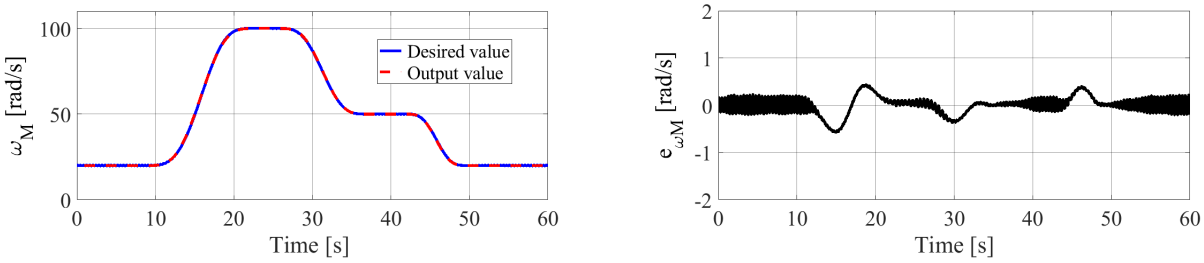

Figure 4.55: Simulation velocity tracking result of SMC in the first test case.

Fig. 4.56 analyzes the analog control signal of the sliding mode controller. As can be seen, the switching happens when the tracking error reaches zero, however, by deploying the sigmoid function this chattering effect is significantly reduced to an acceptable level.

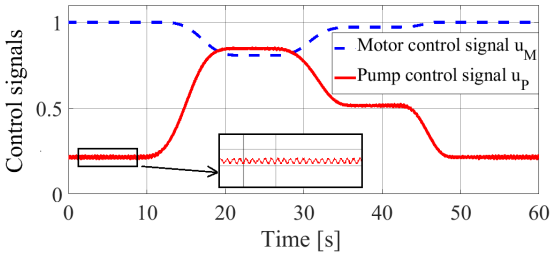

Figure 4.56: Analog control signals using SMC.

Under the effects of external disturbances, though the tracking error slightly increases, a good tracking performance is still maintained well. The simulation result is presented in Fig. 4.57

The experiments are performed on the test rig using the following parameter setting

$$c_{\vartheta 4,1} = 81, c_{\vartheta 4,2} = 108, c_{\vartheta 4,3} = 54, c_{\vartheta 4,4} = 12, R_{\vartheta 4} = 12,$$
$$\rho_0 = 614, \rho_1 = 216, \rho_2 = 25, \bar{\rho} = 400, \bar{\gamma} = 50.$$

The results in the first and second test cases are presented in Fig. 4.58 and Fig. 4.59 respectively.

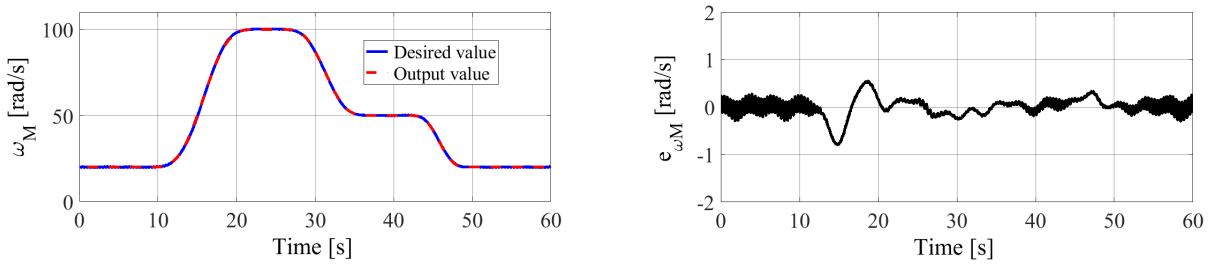

Figure 4.57: Simulation velocity tracking result of SMC in the second test case.

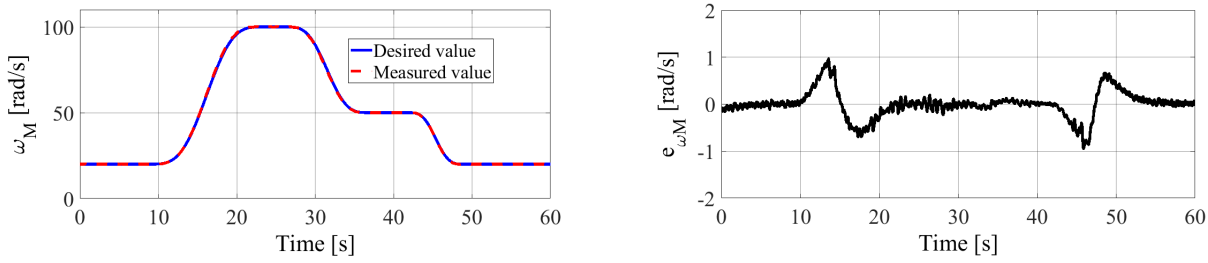

Figure 4.58: Experimental velocity tracking result of SMC in the first test case.

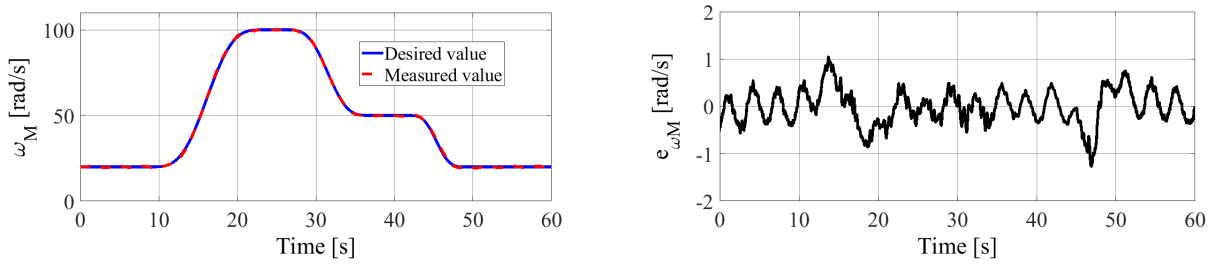

Figure 4.59: Experimental velocity tracking result of SMC in the first test case.

Feedback Error Learning

The model-free control structure with the use of the feedback error learning approach consists of a stabilizing control signal from the iPD controller and the compensation signal from the neural network. The iPD controller is set up with the following feedback gains defined by the characteristic ratio assignment method

$$k_0 = 2200, k_1 = 368, k_2 = 29$$

and the parameter $K = 11 \cdot 10^4$ is also used.

An LDT3 is deployed for the output signal derivative filtering with the following setting

$$R_{\vartheta 3} = 5, c_{\vartheta 3,1} = 8, c_{\vartheta 3,2} = 12, c_{\vartheta 3,3} = 6.$$

The MLP network is constructed with $P = 10$ neurons and the learning rates

$$\eta_v = 0.5, \eta_w = 0.75$$

are chosen. The network is initialized as follows

$$\mathbf{V} = \mathbf{0}, \ \mathbf{w} = 1000 + 50 \cdot rand\,(10, 1)\,.$$

The simulation result in the first test scenarios is shown in Fig. 4.60 and the corresponding adaptation of the neural network weights is visualized in Fig. 4.61. Fig. 4.62 presents the tracking performance of the control structure under the effects of external disturbances in the second test scenario.

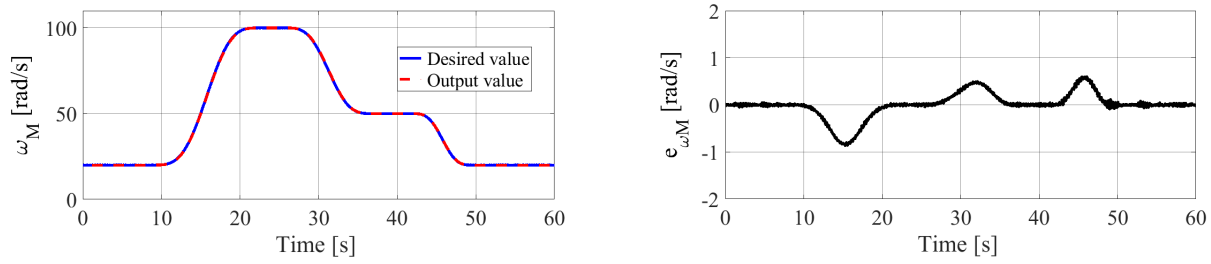

Figure 4.60: Simulation velocity tracking result using FEL in the first test case.

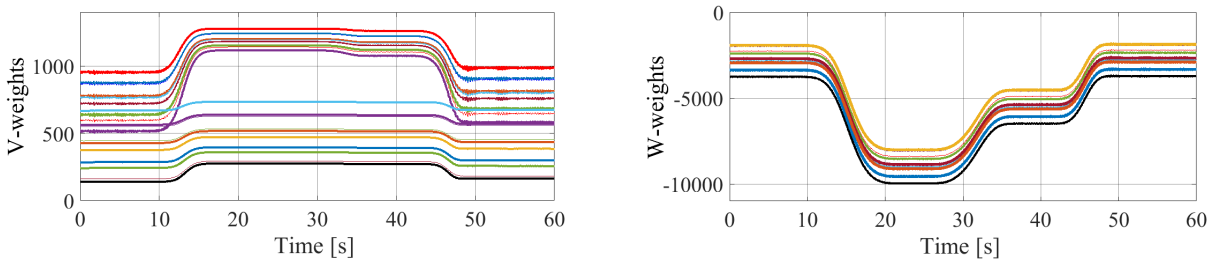

Figure 4.61: The network weight adaptation using FEL.

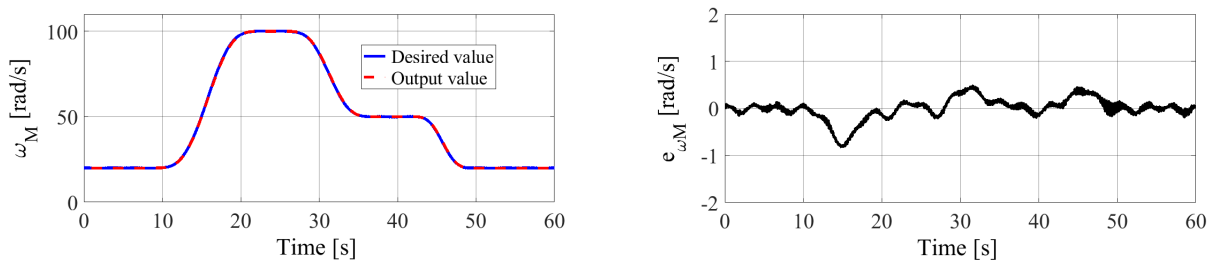

Figure 4.62: Simulation velocity tracking result using FEL in the second test case.

On the test rig, the control parameters are utilized as follows

$$
\begin{aligned}
&k_0 = 1200, k_1 = 140, k_2 = 25,\\
&R_{\vartheta 3} = 5, c_{\vartheta 3,1} = 8, c_{\vartheta 3,2} = 12, c_{\vartheta 3,3} = 6,\\
&\eta_v = 0.4, \eta_w = 0.8\ .
\end{aligned}
$$

The experimental result of the velocity tracking in the first test scenario is shown in Fig. 4.63

Under the effects of external disturbances, the neural network weights adapt very fast to the variations of the system disturbances resulting in a good tracking performance despite of a small oscillation. The result is presented in Fig. 4.64

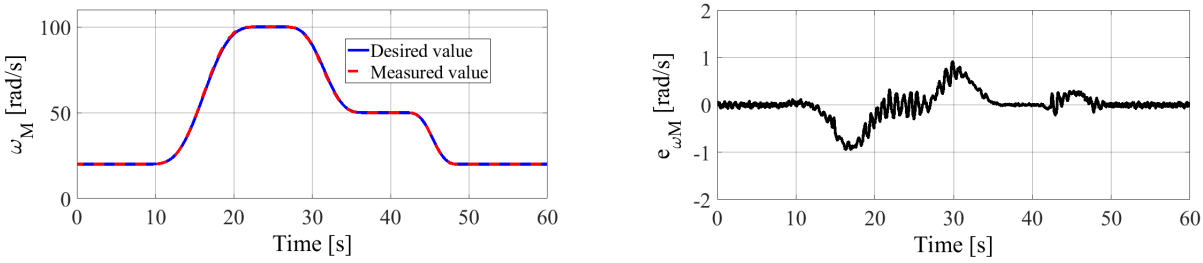

Figure 4.63: Experimental velocity tracking result using FEL in the first test case.

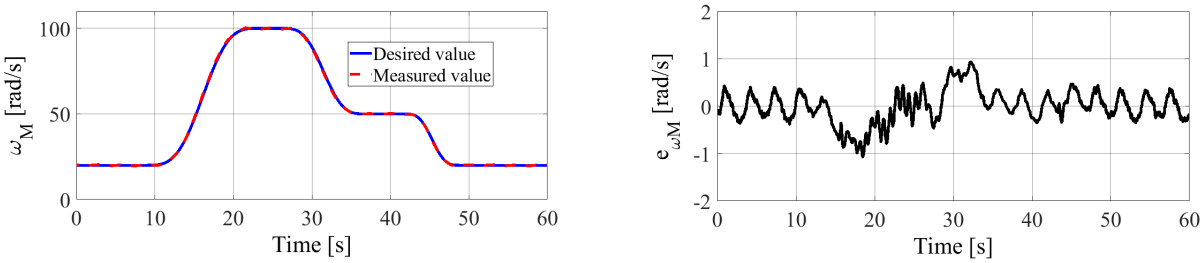

Figure 4.64: Experimental velocity tracking result using FEL in the second test case.

Adaptive Feedforward Compensation Using Neural Networks

Similar to the control with the FEL approach, the simulation of adaptive feedforward compensation (AFC) using neural networks is also deployed with the same setting of parameters as follows

$$k_P = 2200, k_D = 368, k_{2D} = 29,$$
$$R_{\vartheta 3} = 5, c_{\vartheta 3,1} = 8, c_{\vartheta 3,2} = 12, c_{\vartheta 3,3} = 6,$$
$$K = 11 \cdot 10^4 \ .$$

The neural network is utilized using the following setting

$$M = 10, \eta_1 = 10, \eta_2 = 35$$
$$\mathbf{V} = \mathbf{0}, \mathbf{w} = 1000 + 50 \cdot rand\,(10, 1)\,.$$

The simulation result in the first test scenario is shown in Fig. 4.65, Fig. 4.66 depicts the corresponding variations of neural network weights in the compensation process. Fig. 4.67 shows the simulation result of the tracking performance of the controller in the second test scenario. As can be seen, despite of the disturbances, a very good tracking result is still achievable.

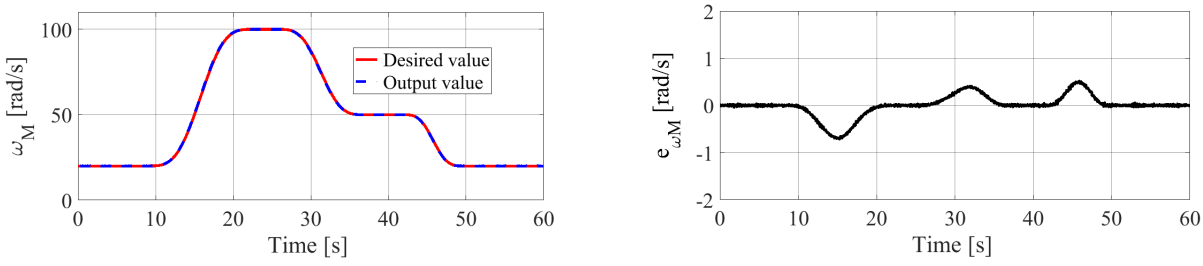

Figure 4.65: Simulation velocity tracking result using AFC in the first test case.

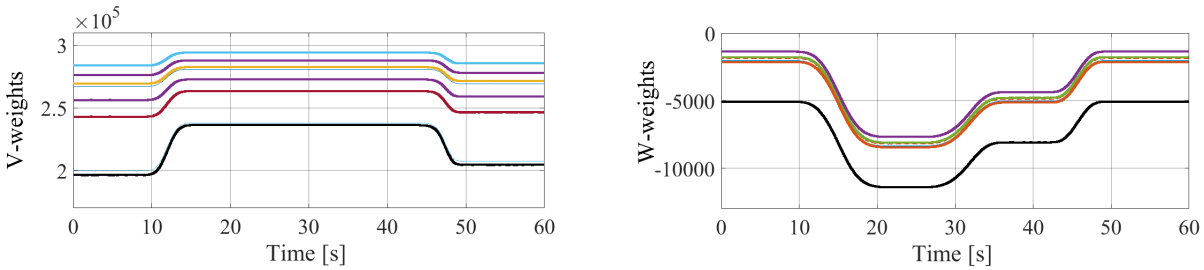

Figure 4.66: Adaptation of network weights in AFC control.

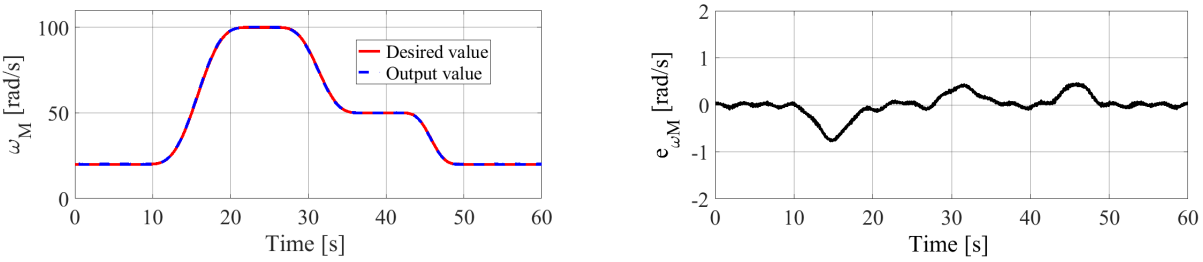

Figure 4.67: Simulation velocity tracking using AFC in the second test case.

On the real system, the controller is implemented using the following parameter setting

$$k_P = 1200, k_D = 140, k_{2D} = 25,$$
$$R_{\vartheta 3} = 5, c_{\vartheta 3,1} = 8, c_{\vartheta 3,2} = 12, c_{\vartheta 3,3} = 6,$$
$$K = 11 \cdot 10^4, \ \eta_1 = 7, \eta_2 = 30 \ .$$

The experimental results of the tracking control in the first and second test scenarios are shown in Fig. 4.68 and Fig. 4.69 correspondingly. An equivalent performance of the proposed control in comparison to the FEL case is recognizable.

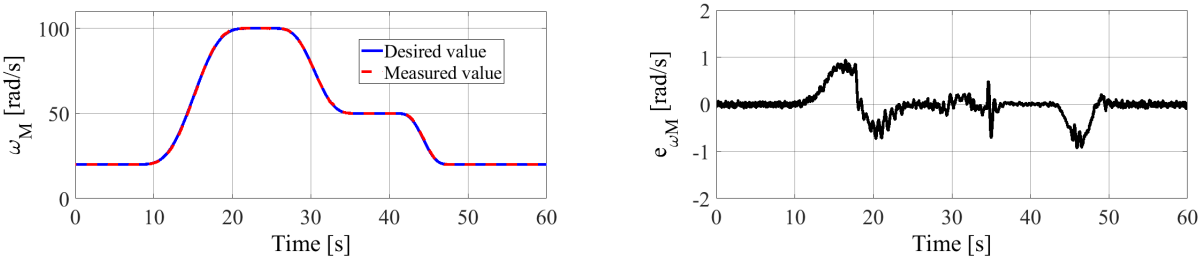

Figure 4.68: Experimental velocity tracking result using AFC in the first test case.

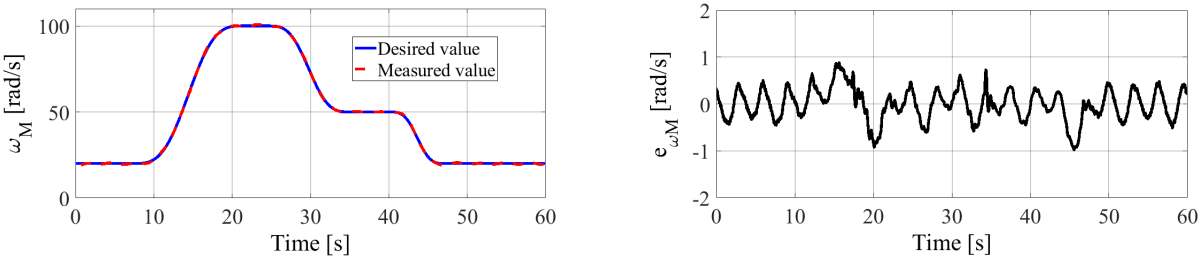

Figure 4.69: Experimental velocity tracking result using AFC in the second test case.

Summary

The model-free approach provides a simple framework for the robust control designs. The three proposed control structures corresponding to three alternative methods for nonlinearity and disturbance compensation present the simple but efficient control approaches for HST systems. The results show a good tracking performance for all proposed control structures in both test cases. The robustness is one of the most impressive properties, which is recognizable from the statistic evaluation in the Tab. 4.8 and Tab. 4.9, especially for the results of the FEL and AFC controllers.

Table 4.8: Comparison of simulation RMS error for control designs in model-free framework

	The first test scenario	**The second test scenario**	**Increasing error**
SMC	$1.854 \cdot 10^{-1}$	$2.015 \cdot 10^{-1}$	8.7%
FEL	$2.507 \cdot 10^{-1}$	$2.529 \cdot 10^{-1}$	0.9%
AFC	$2.226 \cdot 10^{-1}$	$2.248 \cdot 10^{-1}$	1.0%

Table 4.9: Comparison of experimental RMS error for control designs in model-free framework

	The first test scenario	**The second test scenario**	**Increasing error**
SMC	$2.783 \cdot 10^{-1}$	$3.631 \cdot 10^{-1}$	30.5%
FEL	$2.960 \cdot 10^{-1}$	$3.516 \cdot 10^{-1}$	18.8%
AFC	$2.814 \cdot 10^{-1}$	$3.423 \cdot 10^{-1}$	21.6%

5 Conclusions

The work in this dissertation addresses both design and validation of several advanced control approaches for the output tracking of HST systems. These control designs can be roughly classified into four control categories: (1) optimization-based controls – model predictive control (MPC), Takagi-Sugeno fuzzy-base optimal control (FBO) and state-dependent integral state feedback control (SIF); (2) estimator-based feedback linearization with the use of a reduce-order disturbance observer (RDO), with online adaptive parameter estimation (APE) and with a multiple-layer perceptron network (MLP) for nonlinearity and disturbance compensation; (3) active disturbance rejection controls with two variants – extended state observer (ESO) based and flat-filtering based designs; (4) model-free approaches with three robust control structures – sliding mode control (SMC), feedback error learning (FEL) and adaptive feedforward compensation using a neural network (AFC). Except the case of MPC where both control inputs for the hydraulic motors and pumps are derived by the multiple-input single-output optimization algorithm, the remaining control designs are based on a decentralized scheme where the hydraulic motor and pump are controlled separately regarding the control structure but synchronized w.r.t. the trajectory planning.

The control designs with the proposed control plan provide efficient methods for the control of HST systems in a wide working range, their performance has been analyzed and validated by means of both simulation using the validated mathematical model and experiments on the real equipment. The summary of the results shows an equivalent control performance for all control structures, which include both model-based and model-free design approaches. However, there are distinctions between them regarding the control performance in different test cases on the real system. The corresponding performance is evaluated by a common criterion – the RMS error – for both velocity and hydraulic torque controls. From the error statistics, taking the most focus on the experimental results, it can be concluded that the proposed control designs can be divided into two groups regarding their robustness under the impacts of external disturbances.

The first group consists of RDO, MPC, FBO and SIF approaches, which rely on the complete mathematical model of the HST system. The RMS error evaluation shows very accurate control results in the first test case, where the prime mover speed and disturbance load torque are constant. Those achievements obviously prove a high quality of the system model – which was developed in early work, see [11], and employed in this application research. In the second test case, where the prime mover speed and external load torques vary intensively, the model-based designs exhibit their limits. The tracking accuracy is still maintained, however, the performance degrades significantly with the increasing RMS error of 71.4% up to 85.7%. The robustness of these controls relies on the disturbance observer or Kalman filter as analyzed in [73], however, it does not seem enough to completely reject the disturbance acting on the HST system.

The second group comprises active disturbance rejection approaches with either ESO-based or flat-filtering-based designs, feedback linearization with MLP, APE and the model-free approaches with SMC, FEL and AFC. In the first test case, these approaches provide an equivalent control accuracy in comparison to the one of the first group controls. In the second test case under the impacts of disturbances, however, they show a superior behavior with more robust-

ness and a smaller increase in the RMS error of 18.7% up to 33.6%. Though the disturbances are not completely rejected, the tracking accuracy is much improved. These results certainly are closely related to the design method of these controls, where the requirement for a complete model is reduced – as in the cases of MLP, APE, ESO-base and flat-filtering-based ADR controls – or even not necessary as in the cases of model-free designs – SMC, FEL and AFC.

From an overall perspective, all of the proposed control designs have shown their applicability for an accurate control result of HST systems. With two test cases investigated in this application study, the principle characteristics of each designed control are revealed to a certain extent. However, for a practical application objective in the future, the controls should be tested under more realistic working conditions and, especially, over a long time horizon that increases the level of uncertainty in the system, e.g., due to varying oil temperatures or varying ambient temperatures. This research conducts the tests in a short time, therefore, the changes of the physically-related aspects such as temperature, viscosity, elasticity are small and may not enough to have a significant impact on the controllers.

Further improvement of the tracking performance may be achievable on HST systems with machine learning techniques. As indicated by the study results in this work, learning controls provide a high robustness, accuracy and simplicity of the control design.

Bibliography

[1] G. K. Costa and N. Sepehri, Hydrostatic transmissions and actuators: Operation, modelling and applications. John Wiley & Sons, Ltd., 2015.

[2] https://hydra-tech.com/hydraulic-circuits-open-vs-closed/. Published on 7.04.2017, accessed on 01.04.2021.

[3] M. S. A. Ibrahim, Investigation of Hydraulic Transmissions for Passenger Cars. Ph.D. dissertation, Shaker Verlag, Aachen, 2011.

[4] V. Šušteršič, D. Gordić, M. Josijević and V. Vukašinović, Application and design of hydro transmission for tractors. *Mobility & Vehicle Mechanics*, Vol. 42(2), pp. 55-65, 2016.

[5] M. Martelli and L. G. Zarotti, Hydrostatic Transmission with a Traction Control. In *22nd International Symposium on Automation and Robotics in Construction (ISARC)*, Ferrara, Italy, 2005.

[6] H. Schulte, Control-Oriented Modeling of Hydrostatic Transmissions considering leakage losses. In *IFAC Workshop on Advanced Fuzzy-Neural Control*, Valenciennes, France, 2007.

[7] J. Backas, Energy Efficient Control of Hydrostatic Drive Transmissions: A Nonlinear Model-Based Approach. Ph.D. dissertation, Tampere University of Technology, Vol. 1559, 2018.

[8] N. D. Manring and R. C. Fales, Hydraulic control systems - Second edition. John Wiley & Sons, Inc. , 2020.

[9] H. Schulte and S. Georg, Nonlinear control of wind turbines with hydrostatic transmission based on Takagi-Sugeno model. *Journal of Physics: Conference Series 524*, 012085, 2014.

[10] M. E. Hasan, S. K. Ghoshal and K. Dasgupta, Speed Control of a Hydraulic Motor. Applied Mechanics and Materials, Vols. 592-594, pp 2239-2243, 2014.

[11] H. Aschemann, J. Ritzke and H. Schulte, Model-based nonlinear trajectory control of a drive chain with hydrostatic transmission. In *IFAC Proceedings Volumes*, Vol. 42, 13, pp. 461-466, 2009.

[12] D. Gordić, V. Šušteršič, M. Babić, D. Končalović and D. Jelić, Computer application in hydrostatic transmission technology. In *3rd International conference power transmissions*, Chalkidiki, Greece, 2009.

[13] https://www.boschrexroth.com/, A6VM hydraulic motor data sheet.

[14] K. E. Rydberg, Concepts and development trends for efficiency improvement of hydrostatics in mobile applications. *SAE International Off-Highway Congress*, Nevada, USA, 2002.

[15] N. Kumar, B. K. Sarkar and S. Maity, Recent development and application of the hydrostatic transmission system. Advances in Mechanical Engineering, pp. 1613-1625, 2020.

[16] https://www.harsle.com/Disadvantages-of-hydraulic-transmission-id8779743.html, Published on 14.01.2020, accessed on 10.04.2021.

[17] S. Ahn, J. Choi, S. Kim, J. Lee, C. Choi and H. Kim, Development of an integrated engine-hydro-mechanical transmission control algorithm for a tractor. Advances in Mechanical Engineering, Vol. 7(7) 1–18, 2015.

[18] M. Jelali and A. Kroll, Hydraulic servo-systems: modelling, identification, and control. SpringerLink, 2003.

[19] A. Nawrocka and J. Kwasniewski, "Advanced algorithm for stabilization rotational speed in hydrostatic transmission," Intern. Journal of Mechanics, Vol. 4, pp. 164–168, 2006.

[20] J. Kwaśniewski, J. Pluta and A. Piotrowska, "Research on the properties of a hydrostatic transmission with different controllers," In Acta Montanistica Slovaca, Vol. 8, pp. 240–244, 2003.

[21] H. W. Wu and C. B. Lee, "Self-tuning adaptive speed control for hydrostatic transmission systems," In Internationnal Journal of Computer Aplications in Technology, Vol. 9, pp. 18–33, 1996.

[22] H. T. Do, H. G. Park, K. K. Ahn, "Application of an adaptive fuzzy sliding mode controller in velocity control of a secondary controlled hydrostatic transmission system". Mechatronics, Vol. 24(8), pp. 1157-1165, 2014.

[23] L. V. Larsson, Control of hybrid hydromechanical transmissions. Ph.D. dissertation, LiU-Tryck, Linköpings, 2019.

[24] H. Berg and M. Ivantysynova, Design and testing of a robust linear controller for secondary controlled hydraulic drive. *Proceedings of the Institution of Mechanical Engineers, Part I: Journal of Systems and Control Engineering*, Vol. 213(5), 1999.

[25] L. Liebenberg and J. J. Krüger, Computer controlled hydrostatic transmission with traction control for vehicles. SAE Transactions Section 2: Journal of commercial vehicles, Vol. 99, pp. 306-317, 1990.

[26] L. Dubonjić, N. Nedić, V. Filipović, and Dragan Pršić, Design of PI controllers for hydraulic control Systems. Mathematical Problems in Engineering, Vol. 2013.

[27] J. Ambuel, L. Steenhoek, R. Smith and T. Colvin, Control of hydrostatic transmission output speed: Development and comparison of PI and hybrid fuzzy-PI controllers. American Society of Agricultural Engineers, Vol. 36(4): 1057-1064, 1993.

[28] K. Huhtala, Modeling of hydrostatic transmission - steady state, linear and nonlinear models. Ph.D. dissertaiton, Acta Polytechnica Scandinavica, Mechanical Engineering Series, Me; No. 123, 1996.

[29] S. Tikkanen, K. Huhtala and M. Vilenius, Fuzzy controllers in hydrostatic transmission. *IEE Colloquium on Innovative Actuators for Mechatronic Systems*, pp. 15/1–15/3, London, 1995.

[30] I. A. Njabeleke, R. F. Pannett, P. K. Chawdhry and C. R. Burrows, Self-organising fuzzy logic control of a hydrostatic transmission. In *UKACC International Conference on Control*, Vol. 1, pp. 66-72, Swansea, UK, 1998.

[31] A. V. Akkaya, Effect of bulk modulus on performance of a hydrostatic transmission control system. Sādhanā, Vol. 31, Part 5, pp. 543–556, 2006.

[32] A. Q. Hussien and A. J. Hamidi, Speed control of hydraulic motor system with swashplate DC-controlled pump. *Advanced Materials Research*, Vols. 403-408, pp 4828-4840, 2012.

[33] J. Lennevi and J. 0. Palmberg, Application and implementation of LQ design method for the velocity control of hydrostatic transmissions, *Proceedings of the Institution of Mechanical Engineers, Part I: Journal of Systems and Control Engineering*, Vol. 209(4), 1995.

[34] H. W. Wu and C. B. Lee, "Self-tuning adaptive speed control for hydrostatic transmission systems," In Internationnal Journal of Computer Aplications in Technology, Vol. 9, pp. 18–33, 1996.

[35] I. A. Njabeleke, R. F. Pannett, P. K. Chawdhry and C. R. Burrows, Modelling and control of a high speed hydrostatic transmission. *International Mechanical Engineering Congress and Exposition (ASME)*, Anaheim, California, 1998.

[36] L. D. Re, A. Goransson and A. Astolfi, Enhancing hydrostatic gear efficiency through nonlinear optimal control strategies. In *Proceedings of IEEE International Conference on Control and Applications*, 1994.

[37] A. Nawrocka and J. Kwasniewski, Predictuve neural network controller for hydrostatic transmission control. Mechanics, Vol. 27(2), 2008.

[38] A. J. Humadi, A. Q. Hussein and M. M. Farjo, Improvement of a hydrostatic transmission control system performance using radial basis neural network. Journal of Engineering, Vol. 17(3), 2011.

[39] H. T. Do and K. K. Ahn, Velocity control of a secondary controlled closed-loop hydrostatic transmission system using an adaptive fuzzy sliding mode controller. Journal of Mechanical Science and Technology, Vol. 27(3), pp. 875 884, 2013.

[40] C. S. Kim and C. O. Lee, Robust speed control of a variable-displacement hydraulic motor considering saturation nonlinearity. Journal of dynamic systems, measurement and control. Vol. 122(1), pp. 196-201, 2000.

[41] J. Ritzke and H. Aschemann, Design and Experimental Validation of Nonlinear Trajectory Control of a Drive Chain with Hydrostatic Transmission, /in *The 12th Scandinavian International Conference on Fluid Power*, Tampere, Finland, 2011.

[42] H. Sun and H. Aschemann, Robust Inverse Dynamics Control for a Hydrostatic Transmission with Actuator Uncertainties, In *6th IFAC Symposium on Mechatronic Systems*, Hangzhou, China, 2013.

[43] H. Sun and H. Aschemann, Adaptive Inverse Dynamics Control for a Hydrostatic Transmission with Actuator Uncertainties. In *IEEE International Conference on Mechatronics (ICM)*, pp. 676 - 681, 2013

[44] H. Sun and H. Aschemann, Sliding-mode control of a hydrostatic drive train with uncertain actuator dynamics. In *European Control Conference (ECC)*, Zürich, Switzerland, 2013.

[45] H. Aschemann and H. Sun, Decentralized Flatness-Based Control of a Hydrostatic Drive Train Subject to Actuator Uncertainty and Disturbances. In *18th International Conference on Methods & Models in Automation & Robotics (MMAR)*, Miedzyzdroje, Poland, 2013.

[46] H. Sun and H. Aschemann, Experimental validation of robust nonlinear tracking control for a hydrostatic transmission with unknown disturbances. *American Control Conference (ACC)*, Chicago, IL, USA, 2015.

[47] H. Sun, T. Meinlschmidt and H. Aschemann, Comparison of two nonlinear model predictive control strategies with observer-based disturbance compensation for a hydrostatic transmission. In *19th International Conference on Methods and Models in Automation and Robotics (MMAR)*, Miedzyzdroje, Poland, 2014.

[48] H. Sun, T. Meinlschmidt and H. Aschemann, Nonlinear Model Predictive Control for a Hydrostatic Drive Train with Unknown Disturbances. *8th European Nonlinear Dynamics Conference (ENOC)*, 2014

[49] H. Sun, T. Meinlschmidt and H. Aschemann, Passivity-Based Control of a Hydrostatic Transmission with Unknown Disturbances. *IEEE Intl. Conference on Methods and Models in Automation and Robotics (MMAR)*, pp. 94–99, 2014.

[50] H. Sun, T. Meinlschmidt and H. Aschemann, Optimal Tracking Control with Observer-Based Disturbance Compensation for a Hydrostatic Transmission. *IEEE Multi-conference on Systems and Control (MSC)*, pp. 1936 - 1941, 2014.

[51] H. Sun, T. Meinlschmidt and H. Aschemann, An Experimental Study of Decentralized Backstepping Approaches for a Hydrostatic Drive Train with Unknown Disturbances. *American Control Conference (ACC)*, pp. 874 - 879, 2014.

[52] H. Sun and H. Aschemann, Quasi-continuous sliding mode control applied to a hydrostatic transmission. *Control Conference (ECC)*, pp. 691-696, 2015.

[53] H. Sun and H. Aschemann, Sliding Mode Control for a Hydrostatic Transmission in Combination with a Sliding Mode Observer. Variable-structure approaches, pp. 155-188, 2016.

[54] H. Sun, R. Prabel and H. Aschemann, Cascaded control design for the tracking control of a hydrostatic transmission based on a sliding mode state and disturbance observer. *21st International Conference on Methods and Models in Automation and Robotics (MMAR)*, pp. 432-437, 2016.

[55] H. Sun and H. Aschemann, A Backstepping Sliding Mode Control for a Hydrostatic Transmission with Unknown Disturbances. *Journal IFAC-PapersOnLine*, Vol. 49(18), pp. 879-884, 2016.

[56] R. Prabel and H. Aschemann, Torque control of a hydrostatic transmission using extended linearization techniques. *The 15th Scandinavian International Conference on Fluid Power (SICFP)*, Linköping, Sweden, 2017.

[57] N. D. Dang and H. Aschemann, Comparison of Estimator-Based Compensation Schemes for Hydrostatic Transmissions with Uncertainties. In *23rd International Conference on Methods & Models in Automation & Robotics (MMAR)*, pp 692-697. Międzyzdroje, Poland, 2018.

[58] N. D. Dang and H. Aschemann, Design of a Takagi-Sugeno State and Disturbance Observer for a Torque-Controlled Hydrostatic Transmission. In *24th International Conference on Methods and Models in Automation and Robotics (MMAR)*, pp. 378-383, Międzyzdroje, Poland, 2019.

[59] N. D. Dang and H. Aschemann, Discrete-Time Takagi-Sugeno Tracking Control Design for the Motor Torque of a Hydrostatic Transmission. In *15th European Workshop on Advanced Control and Diagnosis (ACD)*, Bologna, Italy, 2019.

[60] N. D. Dang and H. Aschemann, Neural Network Control by Error-Feedback Learning for Hydrostatic Transmissions with Disturbances and Uncertainties. Contemporary Control,

SpringerLink, 2020.

[61] N. D. Dang and H. Aschemann, Discrete-Time State-Dependent Proportional-Integral Control for Torque Tracking of Hydrostatic Transmissions. In *21st International Federation of Automatic Control World Congress (IFAC)*, Berlin, Germany, 2020.

[62] N. D. Dang and H. Aschemann, Design and Comparison of Active Disturbance Rejection Approaches for the Velocity Tracking Control of Hydrostatic Transmissions. In *European Control Conference (ECC)*, Rotterdam, Netherlands, 2021.

[63] N. D. Dang and H. Aschemann, Real-Time Implementation of Model Predictive Multivariable Tracking Control for Hydrostatic Transmissions. In *24th International Conference on System Theory, Control and Computing (ICSTCC)*, Sinaia, Romania, 2020.

[64] N. D. Dang and H. Aschemann, Application Study of Newton-Raphson-Type Nonlinear MPC for Hydrostatic Transmissions Under Disturbance and System Uncertainty. System Theory, Control and Computing Journal, 1(1), pp. 21–29. 2021.

[65] N. D. Dang and H. Aschemann, Differentiator Based Sliding Mode Control Design for Velocity Tracking of a Hydrostatic Transmission. *The 25th International Conference on Methods and Models in Automation and Robotics (MMAR)*, Międzyzdroje, Poland, 2021.

[66] N. D. Dang and H. Aschemann, Adaptive Feedforward Compensation Using Neural Network for Velocity Control of Hydrostatic Transmissions. *The 29th Mediterranean Conference on Control and Automation (MED)*, Puglia, Italy, 2021.

[67] P. Zeman, W.Kemmetmüller and A.Kugi, Model predictive speed control of axial pistion motors. In *10th IFAC Symposium on Nonlinear Control Systems (NOLCOS)*, Monterey, California, USA, 2016.

[68] P. Zips, A. Lobe, A. Trachte and A. Kugi, Torque control of a hydrostatic transmission applied to a wheel loader. In *IEEE 58th Conference on Decision and Control (CDC)*, Nice, France, 2019.

[69] E. Carlsson, Modeling hydrostatic transmission in forest vehicle. Research thesis, Linköpings University, 2006.

[70] T. H. Ho and K. K. Ahn, Modeling and simulation of hydrostatic transmission system with energy regeneration using hydraulic accumulator. *Journal of Mechanical Science and Technology*, Vol. 24(5), pp. 1163–1175, 2010.

[71] Y. Wang, Z. Zhang and X. Qin, Modeling and control for hydraulic transmission of unmanned ground vehicle. Central South University Press and Springer-Verlag Berlin Heidelberg, Vol. 21, pp. 124–129, 2014.

[72] L. Zao, J. Wang and Z. Zhang, Research on Travel Control System of Hydrostatic Transmission Chassis. MATEC Web of Conferences 139, 00212, 2017.

[73] H. Sun, Decentralized nonlinear control for a hydrostatic drive train with unknown disturbances. Ph.D. dissertation, University of Rostock, Shaker, 2015.

[74] https://www.hydraulicspneumatics.com/fluid-power-basics/hydraulics/article/21882804/engineering-essentials-hydrostatic-transmissions. Published on 08.07.2016, accessed on 14.04.2021.

[75] B. Vanwalleghem, C. Dousy, G. Pinte and B. Vanseveren, Optimization of the efficiency of hydrostatic drives. In *8th International Fluid Power Conference*, Dresden, Germany, 2012.

[76] M. Ijas and E. Makinen, Improvement of total efficiency of hydrostatic transmission by using optimized control. In *Proceedings of the JFPS International Symposium on Fluid Power*, Vol. 2008(7-2), pp. 271-276, Toyama, Japan, 2008.

[77] J. Rapp and J. Turesson, Hydrostatic Transmission in Wind Turbines - Development of Test Platform. Master thesis, Linköping, 2015.

[78] D. Coombs, Hydraulic efficiency of a hydrostatic transmission with a variable displacement pump and motor. Master thesis, University of Missouri-Columbia, 2012.

[79] M. Fliess and C. Join, Model-free control. International Journal of Control, Vol. 86(12), pp. 2228–2252, 2013.

[80] A. Levant, Robust exact differentiation via sliding mode technique, Automatica, Vol. 34, No. 3, pp. 379—384, 1998.

[81] A. Levant, Higher order sliding modes and arbitrary-order exact robust differentiation. In *Proceeding of the European Control Conference (ECC)*, 2001.

[82] M. Reichhartinger, S. K. Spurgeon, M. Forstinger and M. Wipfler, A robust exact differentiator toolbox for Matlab/Simulink. In *IFAC-PapersOnLine*, Vol. 50(1), pp.1711-1716, 2017.

[83] B. Z. Guo and Z. L. Zhao, Active disturbance rejection control for nonlinear systems: an introduction, John Wiley & Sons (Asia) Pte Ltd, 2016.

[84] X. W. Bu, X. Y. Wu, Y. X. Chen and R. Y. Bai, Design of a class of new nonlinear disturbance observers based on tracking differentiators for uncertain dynamic systems. International Journal of Control, Automation, and Systems, Vol. 13(3), pp. 595–602, 2015.

[85] Z. Yang, J. Ji, X. Sun, H. Zhu and Q. Zhao, Active disturbance rejection control for bearingless induction motor based on hyperbolic tangent tracking differentiator. IEEE Journal of Emerging and Selected Topics in Power Electronics, Vol. 8(3), 2020.

[86] C. Hua, K. Wang, J. Chen and X. You, Tracking differentiator and extended state observer-based nonsingular fast terminal sliding mode attitude control for a quadrotor. Nonlinear Dynamics, Vol. 94, pp. 343–354, 2018.

[87] I. K. Ibraheem and W. R. Abdul-Adheem, On the improved nonlinear tracking differentiator based nonlinear PID controller design. International Journal of Advanced Computer Science and Applications, Vol. 7(10), 2016.

[88] J. J. E. Slotine and W. Li, Applied nonlinear control, Prentice Hall, New Jersey, 1991.

[89] A. N. Atassi and H. K. Khalil, A Separation principle for the control of a class of nonlinear systems. IEEE Transactions on Automatic Control, Vol. 46(5), 2001.

[90] A. E. Golubev, A. P. Krishchenko and S. B. Tkachev, Separation principle for a class of nonlinear systems. *15th Triennial world congress*, Barcelona, Spain, 2002.

[91] B. Friedland, Advanced Control System Design. Prentice Hall, 1996.

[92] H. K. Khalil, Nonlinear Control. Pearson Education, 2015.

[93] F. L. Lewis, S. Jagannathan and A. Yesildirek, Neural network control of robots and nonlinear systems. Taylor and Francis, London, 1999.

[94] A. E. de Barros Ruano, Applications of neural networks to control systems. Ph.D. disser-

tation, University of Wales, Bangor, 1992.

[95] Y. Shin, Neural network based adaptive control for nonlinear dynamic regimes. Ph.D. dissertation, Georgia Institute of Technology, 2005.

[96] H. Sira-Ramírez, A. Luviano-Juarez, M. H. Ramírez-Niera and E. W. Zurita-Bustamante, Active disturbance rejection control of dynamic systems: A flatness-based approach, Butterworth-Heinemann, Oxford, UK, 2017.

[97] Y. C. Kim, L. H. Keel and S. P. Bhattacharyya, Transient response control via characteristic ratio assignment. IEEE Transactions on Automatic Control , Vol. 48(12), 2003.

[98] M. Fliess, R. Marquez, E. Delaleau and H. Sira-Ramirez, Correcteurs proportionnels-integraux generalises. ESAIM: Control, optimisation and calculus of variations, Vol. 7, pp. 23–41, 2002.

[99] H. Sira-Ramírez, A. Luviano-Juarez, M. Ramírez-Neria and R. Garrido-Moctezuma, Flat filtering: A classical approach to robust control of nonlinear systems. *American Control Conference (ACC)*, Boston, MA, USA, 2016.

[100] H. Sira-Ramírez, E. W. Zurita-Bustamante and C. Huang, Equivalence among flat filters, dirty derivative-based PID controllers, ADRC, and integral reconstructor-based sliding mode control. IEEE Transactions on Control Systems Technology, Vol. 28(5), 2020.

[101] M. Ramírez-Neria, A. Luviano-Juarez, N. Lozada-Castillo, G. Ochoa-Ortega and H. Sira-Ramirez, Flat filtering cascade control of fourth order systems. *IFAC-PapersOnLine*, Vol. 53(2), pp. 9068-9073, 2020.

[102] M. Fliess, C. Join and H. Sira-Ramirez, Complex continuous nonlinear systems: their black box identification and their control. IFAC Proceedings, Vol. 39 (1), pp. 416–421, 2006.

[103] M. Fliess and C. Join, Intelligent PID controllers. *16th Mediterranean conference on control and automation (MCA – IEEE – GdR MACS)*, Ajaccio, France, 2008.

[104] M. Fliess and C. Join, Model-free control and intelligent PID controllers: towards a possible trivialization of nonlinear control. *15th IFAC symposium on system identification*, Saint-Malo, France, 2009.

[105] M. Kawato, K. Furukawa and R, Suzuki, A hierarchical neural-network model for control and learning of voluntary movement. Biological Cybernetics, Vol. 57, pp. 169–185, 1987.

[106] J.G. Ziegler and N. B. Nichols, Optimum Settings for Automatic Controllers. Journal of Dynamic Systems Measurement and Control-transactions of The Asme, Vol. 115, pp. 759–765, 1942.

[107] H. Gomi and M. Kawato, Learning control for a closed loop system using feedback-error learning. In *Proc. of 29th IEEE Conf. on Decision and Control*, Vol. 6, pp. 3289–3294, Honolulu, Hawaii, 1990.

[108] J. Nakanishia and S. Schaal, Feedback error learning and nonlinear adaptive control. Neural Networks, Vol. 17, pp. 1453–1465, 2004.

[109] A. Miyamura, H. Kimura, Stability of feedback error learning scheme. Systems & Control Letters, Vol. 45, pp. 303 – 316, 2002.

[110] A. K. Ishihara, J. van Doornik and T. D. Sanger, Feedback error learning with basis func-

tion networks. *Proceedings of the IEEE International Symposium on Intelligent Control*, Munich, Germany, 2006.

[111] F. Jinhui, J. Songmin and L. Xiuzhi, Direct adaptive control based on improved RBF neural network for omni-directional mobile robot. *International Conference on Mechatronics, Electronic, Industrial and Control Engineering (MEIC)*, Atlantis Press, 2015.

[112] E. S. Widayaka and H. Ohmori, Combustion control of diesel engine using feedback error learning with kernel online learning approach. Journal of Physics: Conference Series. Vol. 744, 2016.

[113] F. Passold and M. R. Stemmer, Feedback Error Learning Neural Network Applied to a Scara Robot. *Proc. of Fourth International Workshop on Robot Motion and Control (RoMoCo'04)*, pp.197 - 202, Puszczykowo, Poland, 2004.

[114] M. A. Khanesar, E. Kayacan, M. Reyhanoglu and O. Kaynak, Feedback error learning control of magnetic satellites using type-2 fuzzy neural networks with elliptic membership functions. IEEE Transactions on Cybernetics, Vol. 45(4), 2015.

[115] A. Pinkus, Approximation theory of the MLP model in neural networks. Acta Numerica, pp. 143–195, 1999.

[116] F. Damak, M. B. Nasr and M. Chtourou, Indirect adaptive neural control using a hybrid learning algorithm. ICIC Express Letters Part B: Applications, Vol. 9(11), pp. 1125–1132, 2018.

[117] L. Shi and X. C. Wang, The application of neural network in nonlinear system. Advanced materials Research Online, Trans Tech Publications Ltd, Switzerland, Vols. 179-180, pp. 128-134, 2011.

[118] X. Cui and G. S. Kang, Direct control and coordination using neural networks. IEEE Transactions on System, Man and Cybernetics, Vol. 23(3), pp. 686–697, 1993.

[119] Y. Pan, Y. Liu, B. Xu and H. Yu, Hybrid feedback feedforward: An efficient design of adaptive neural network control. Neural Networks, Vol. 76, pp. 122–134, Elsevier Ltd, 2016.

[120] D. Psaltis, A. Sideris, and A. A. Yamamura, A multilayered neural network controller. IEEE Control Systems Magazine, Vol. 8(2), 1988.

[121] N. Ommer, A. Stumpf and O. V. Stryk, Real-time online adaptive feedforward velocity control for unmanned ground vehicles. RoboCup 2017: Robot World Cup XXI, pp. 3–16, SpringerLink, 2018.

[122] M. Saerens and A. Soquet, A neural controller. *First IEE Intern. Conf. on Artificial Neural Networks*. Conf. Publ. No. 313, pp. 211–215, 1989.

[123] A. Gómez-Espinosa, R. C. Sundin, I. L. Eguren, E. Cuan-Urquizo, and C. D. Treviño-Quintanilla, Neural network direct control with online learning for shape memory alloy manipulators, Sensors, Vol. 19(11), 2019.

[124] A. N. Ponce, A. A. Behar, A. O. Hernández and V. R. Sitar, Neural networks for self-tuning control systems. Acta Polytechnica, Vol. 44(1), pp. 49–52, 2004.

[125] R. Hernández-Alvarado, L. G. García-Valdovinos, T. Salgado-Jiménez, A. Gómez-Espinosa and F. Fonseca-Navarro, Neural network-based self-tuning PID control for underwater vehicles. Sensors, Vol. 16(9), 2016.

[126] A. Jezierski, J. Mozaryn and D. SuskiA, Comparison of LQR and MPC control algorithms of an inverted pendulum. Advances in Intelligent Systems and Computing, Vol. 577, pp. 65–76, 2017.

[127] S. Boyd and L. Vandenberghe, Convex Optimization. Cambridge University Press, 2009.

[128] R. Hooke and T. A. Jeeves, "Direct search" solution of numerical and statistical problems. Journal of the ACM, Vol. 8(2): pp. 212–229, 1961.

[129] R. K. Arora, Optimization: Algorithms and Applications. Taylor & Francis Group, 2015, New York, USA.

[130] W. H. Chen, Stability analysis of classic finite horizon model predictive control. *In International Journal of Control, Automation, and Systems*, vol. 8(2), Springer, pp. 187-197, 2010.

[131] A. A. Ahmadi and P. A. Parrilo, Non-monotonic Lyapunov functions for stability of discrete time nonlinear and switched systems, *In Proc. of IEEE Conf. on Decision and Control*, pp. 614-621, Cancun, Mexico, 2008.

[132] E. Wan and R. Van der Merwe, The unscented Kalman filter for nonlinear estimation. In *Proc. of IEEE Conf. on Adaptive Systems for Signal Processing, Communications, and Control Symposium*, pp. 153–158, 2000.

[133] S. J. Julier and J. K. Uhlmann, Unscented filtering and nonlinear estimation. Proceeding of the IEEE, Vol. 92(3), pp. 401–422, 2004.

[134] K. Tanaka and H. O. Wang, Fuzzy Control Systems Design and Analysis: A Linear Matrix Inequality Approach. John Wiley & Sons, Inc., 2001.

[135] J. A. Coetsee, Control of nonlinear systems represented in quasilinear form. Ph. D. dissertation, Massachusetts Institute of Technology, 1994.

[136] H. Schulte, Control-oriented modeling of hydrostatic transmission using Takagi-Sugeno fuzzy systems, In *Proc. of IEEE Intern. Fuzzy Systems Conference*, pp. 1–6, 2007.

[137] S. Boyd, L. E. Ghaoui, E. Feron, and V. Balakrishnan, Linear matrix inequalities in system and control theory. SIAM, 1994.

[138] J. Löfberg, YALMIP: A toolbox for modelling and optimization in MATLAB. In *Proc. of Intern. Symp. on Computer Aided Control Systems Design (CACSD)*, pp. 284–289, New Orleans, LA, USA, 2004.

[139] J. F. Sturm, Using SeDuMi 1.02, A Matlab toolbox for optimization over symmetric cones. Optimization Methods and Software, Vol. 11-12, pp. 625–653, 1999.

[140] J. R. Cloutier and P. H. Zipfel, Hypersonic guidance via the state-dependent Riccati equation control method, *Proceedings of the 1999 IEEE International Conference on Control Applications*, Vol.1, pp. 219-224, 1999.

[141] T. Çimen, State-Dependent Riccati Equation (SDRE) Control: A Survey. IFAC Proceedings Volumes, Vol. 41(2), pp. 3761-3775, 2008.

[142] E. B. Erdem and A. G. Alleyne, Experimental real-time SDRE control of an underactuated robot, *Proceedings of the 40th IEEE Conference on Decision and Control*, Vol. 3, pp. 2986-2991, 2001.

[143] K. J. Åström and R. M. Murray, Feedback Systems: An Introduction for Scientists and

engineers. Princeton University Press , Princeton, NJ, 2008.

[144] A. S. Dutka and M. J. Grimble, State-dependent Riccati equation control with predicted trajectory. *Proceedings of the 2004 American Control Conference*, Vol. 2, pp. 1563-1568, 2004.

[145] B. A. Steinfeldt and P. Tsiotras, A state-dependent Riccati equation approach to atmospheric entry guidance, *AIAA Guidance, Navigation, and Control Conference*, Toronto, Ontario, Canada, 2010.